DOE/ER/40085--16

DE89 014935

An Underground Search for an Excess Muon Flux from the Direction of Cygnus X-3

Joseph Alfred Kochocki

(Ph.D. dissertation)

AN UNDERGROUND SEARCH FOR AN EXCESS MUON FLUX FROM THE DIRECTION OF CYGNUS X–3

A Thesis

submitted by

Joseph Alfred Kochocki

In partial fulfillment of the requirements
for the degree of

Doctor of Philosophy

in

Physics

TUFTS UNIVERSITY

May, 1989

To My Wonderful Family
and
Our Newest Member
Liam

ABSTRACT

During the period July, 1987 through March, 1988 (livetime 0.5 year) an array of 128 proportional wire modules, arranged in two planes (each of two crossed layers) separated by 10 m, and with effective overlap areas of 35 m^2, was operated as an underground muon detector. The detector is located at a depth of 2100 meters of water equivalent in northern Minnesota (92.2° W, 47.7° N). The response time for the proportional tubes is 1 μs and the overall angular resolution is 2°. Absolute timing information ($\sim 1\ ms$) was available for most of the 250,000 recorded triggers. A sample of the total data consisting of 103,000 reconstructed, single muon tracks, was used to search for an excess muon flux from the direction of the astronomical point source, Cygnus X-3. We report an integrated excess flux from that direction of $(6 \pm 2) \times 10^{-11}\ cm^{-2}s^{-1}$. The vertical muon flux was also measured and found to be $(1.2{\pm}0.3){\times}10^{-3}\ m^{-2}s^{-1}sterad^{-1}$.

PREFACE

This dissertation is about a cosmic ray experiment that took place at the bottom of an iron mine in northern Minnesota between 1987 and 1988. The experiment, conducted under the auspices of the Soudan 2 collaboration (see Appendix A), made several independent physical observations that included a measurement of the vertical muon flux at the underground site and a determination of the muon flux from the direction of the astronomical source Cygnus X–3. Chapter 1 is an introduction to the characteristics of the source and observations of it by various experiments since its discovery over 20 years ago. The detector used in this experiment is called the Tracker and it is thoroughly described in Chapter 2. Several Monte Carlo calculations that were required in order to derive results from the data are described in Chapter 3. The results are presented in two separate chapters, one dealing with observations of general interest, such as the muon flux (Chapter 4), and the other dealing exclusively with an analysis of muons from the Cygnus X–3 direction (Chapter 5). References are listed at the ends of each chapter in the order in which they appear in the text.

Since I joined the Soudan 2 collaboration six years ago, its membership has nearly doubled. My experiment would have been next to impossible to perform were it not for the efforts of a large number of people. In particular, for their diligent work in the design, installation and maintainence of the various systems necessary to operate the Soudan 2 experiment and the Tracker, I wish to thank Dave Ayres, Don Jankowski and Earl Peterson. I would also like to thank Ken Johns and Marvin Marshak. The many enlightening conversations I have had with each of them concerning muon astronomy has certainly expedited my education and for that I am very grateful.

The installation of the Tracker was difficult at best. Just getting the 23 ft-long modules down the 6 ft × 6 ft shaft was a chore. Most times, the work required one to crawl on hands and knees under several tons of steel or to walk on 8 inch steel beams 30 ft in the air. This would not have been so bad if one didn't have to carry 40 pounds of aluminum under one arm at the same time. Frustrating still was the fact that installation required several rounds at gas leak checking, cabling, more testing...*etc.* Fortunately, we have an excellent crew at the mine to help us with all of these problems. I am very grateful to my friends Brian Dahlin, Bill Miller and Barbara Miller for their efforts over the past four years.

I want to acknowledge the help of two Tufts undergraduates in this research. My thanks to Josh Renkin for his work on the installation of the Tracker extension and thanks to Steve Wilmarth for his excellent work on graphics which led to the fine pictures of the Tracker in Chapter 2.

Many thanks to my friends and fellow students, Sundar Nakamuthu and Ken Shaw. I thank Sundar for his continuing effort over the past few years in testing the electronics used in the shield. Before turning his sights to optics, Ken worked for several years on the quality control of veto shield modules. I thank him for this work and also for his sense of humor; it pulled me through some difficult times during the course of this research. Good luck to you Ken.

My grateful thanks to another friend at Tufts, Larry McMaster. He has been with the Soudan 2 veto shield project since the beginning and his work has been pivotal to the successful design, manfacture and installation of the shield. He has always been very helpful and has gone out of his way to see that things got done right and on time.

Thanks also to Larry Porzio, Amanda Mees and Dorothy DeStefano.

I have had several advisors over the past few years at Tufts that I would like to acknowledge. Thanks to Tony Mann for his excellent organization of the Tufts veto shield effort. Veto shield installation has proceeded on schedule largely because of his push. I also thank him for his careful reading of this dissertation. Thanks also to Austin Napier for many fruitful discussions and again for his careful reading of this text. The implementation of the veto shield has been a team effort. I wish to thank a few other members of the HEP group at Tufts for their work on the shield. Thanks to Tomas Kafka, Rick Milburn and Gino Saitta.

I am very grateful to my advisor, Bill Oliver. I have learned a lot from him during my stay at Tufts. Bill's knowledge and experience of electronics and physics is responsible for the successful design of the shield. This work would have been very difficult without his help. His assistance at each step along the learning curve will always be remembered. He is a top-notch physicist and I am sure I won't be the last grateful student under his direction. Thanks Bill!

Finally, I want to thank my family. They have given me encouragement and hope throughout my graduate career. I am very grateful to my wife Hazel for her help in preparing this dissertation and for her encouragement over the past eight years. Our new son Liam has given us high hopes for a joyous future.

LIST OF FIGURES

Chapter 1

Chapter 2

Chapter 3

Chapter 4

Chapter 5

Appendix B

Appendix C

LIST OF TABLES

TABLE OF CONTENTS

APPENDICES

CHAPTER 1. INTRODUCTION

Underground muon astronomy is a subfield of high energy astrophysics that seeks to use secondary muons, created by interactions of primary cosmic rays in the atmosphere, as a probe to study the physics of astronomical sources and perhaps even fundamental particle interactions. This chapter begins with a description of the Cygnus X–3 star system and a summary of observations of this source by various experiments over the past 20 years. (Only topics relevant to this research will be considered; the details of individual experiments can be found in references at the end of this chapter.) The interactions of primary cosmic rays in the atmosphere will be discussed briefly in order to expose a current and perplexing problem in the field: the muon content of photon induced showers. The observation of an astronomical source, using the flux of underground muons as a signal, would contradict the current understanding of photon initiated atmospheric showers. The chapter concludes with the goals of this thesis.

1.1 A Review of Cygnus X–3 Observations

The Source: Cygnus X–3

Cygnus X–3 (Cyg X–3) is generally believed to be a binary star system consisting of a dense degenerate star (either a black hole or a neutron star) in orbit with a companion star. Several models have been proposed to explain the energy source for the system. The accretion of matter from the companion star onto the compact one, is thought to be the primary energy source for X–ray and gamma–ray emissions. The system is located in the galactic plane at equatorial coordinates $\alpha \simeq 308^\circ$ and $\delta \simeq 41^\circ$. Measurements of the distance to Cyg X–3 are difficult to make because the line of sight is obscured by interstellar matter in the optical range; current estimates place it at d $\sim$ 8.5–12 kpc. Since its discovery in a 1966 rocket flight [1], it has been observed as a source of radio waves, infrared radiation, X–rays and gamma–rays. This source has some very distinguishing features and hence is one of the most studied objects in the celestial sphere at high energies [2]. Its total luminosity is $\approx 5 \times 10^{37}$ ergs/s (8.5 kpc). The source is marked by flaring radio outbursts. A precise measurement of the location of the source was made in 1972 during a burst when it became the brightest radio source in the sky. Another giant radio outburst occurred in October, 1985, during which time many experiments claimed to have detected a high energy signal from the direction of this source. Most of the energy comes out in the form of X–rays that are modulated with a characteristic 4.8 h period.

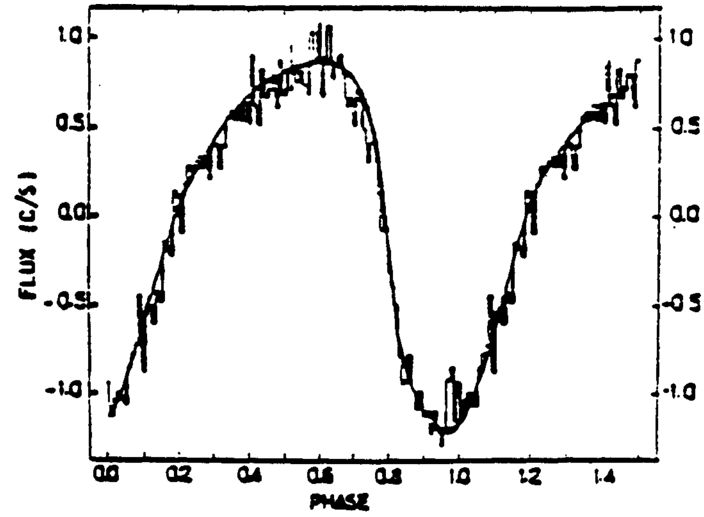

Fig. 1-1. Modulation of the X–ray Source Cyg X–3. X–ray measurements by satellites over the past two decades have established an extremely stable period ($\dot{P} \approx 10^{-9}$) for the compact binary system. The curve shows the modulation of X–ray intensity as a function of the phase of the system.

The X–ray light curve, which shows an extremely stable 4.8 h modulation [3], is thought to be due to the orbital period of the binary system. Figure 1-1 shows the modulation of the X–ray intensity from Cyg X–3 as a function of its phase. Note that the minimum in the X-ray emission is used to define the zero in phase. During the first 10 years of observation no detectable change in the period was observed. However, during the years 1978–1985, a series of satellite experiments confirmed a positive period derivative of $\dot{P} \approx 10^{-9}$. The best fit to the 1972–1985 data was made in 1988 by van der Klis and Bonnet–Bidaud [4].[1] The period P, its derivative, $\dot{P}$ and the time of initial measurement T_0, are given by (quadratic fit):

$$P = 0.199\,683\,54 \pm 0.000\,000\,15\ d, \tag{1.1}$$

$$\dot{P} = (0.90 \pm 0.05) \cdot 10^{-9}, \tag{1.2}$$

$$T_0 = 2\,440\,949.896\,2 \pm 0.000\,9\ HJD, \tag{1.3}$$

where HJD refers to heliocentric Julian day ($T_0 = 9.509$ h UT on 29 Dec 1970). No other periodicities of the source have been firmly established. There is some indication of a steady decrease of $\dot{P}$ over the past 15 years. Also, there is a claimed observation of a 12.59 ms pulser period but this has not been confirmed.

VHE and UHE Experimental Observations

The VHE (very high energy) experiments are atmospheric Čerenkov detectors that rely on the production of Čerenkov radiation as an electromagnetic or hadronic shower develops and passes through the atmosphere. In either type of shower, electrons and positrons, travelling faster than the speed of light in air, are responsible for the signal. These experiments are limited to observations in a clear, moonless, nighttime sky since they depend on measurement of a light signal with photomultiplier tubes. The angular resolution is typically a few degrees and threshold energies are in the range 0.1 to 2 TeV (10^{12} eV). The showers of interest are assumed to be initiated by high energy gamma-rays that get absorbed by the atmosphere, though this has never been verified directly. The observation of a signal from Cyg X–3 has been recorded in this energy regime by several experiments between 1973 and 1985. All of the experiments show some degree of

---

[1] For future reference, the 1981 and 1988 ephemerides by van der Klis and Bonnet-Bidaud will be called vdKBB-81 (quadratic fit) and vdKBB-88 (cubic fit).

modulation of their shower detection times as a function of phase but not all show a surplus at the same absolute phase. The first VHE experiment [5] to claim a Cyg X–3 signal showed signal enhancement in the [0.2,0.3] phase region. Most of the later experiments (1980 and on) [6-8] show it closer to the maximum in the X–ray light curve, [0.5,0.7]. Before a phase analysis, no experiments show a significant excess in their data when a right ascension scan is performed at the Cyg X–3 declination, except for one group [5], which declared a 3.5 σ excess above expected background. The other experiments depend on a phase analysis of the data to increase the signal-to-noise ratio and report signals significant at the 2.5–4 σ level.

The UHE (ultrahigh energy) experiments are extensive air shower arrays (EAS) that use a different technique to measure the energy and direction of a shower created by a primary particle interacting in the atmosphere. Whereas the Čerenkov detectors measure the light spread across the sky from a shower, EAS experiments are capable of detecting the particles in the showers themselves (mainly $e^{\pm}$ and $\mu^{\pm}$) and this results in a higher threshold energy of detection. The typical energy range in these experiments is 300 TeV to 1 PeV (10^{15} eV). There is a low number of detected events for experiments of this type (the differential cosmic ray spectrum falls off as $\mathrm{E}^{-2.7}$). Two experiments [9,10] reported enhancements in the [0.1,0.3] phase region while others [11-13] reported it closer to the maximum in the X–ray curve, [0.5,0.8]. Only one group [9] reported a significant excess of events from the source direction (31 events to a background of 15).

A noteworthy observation in the context of this work, is the report by the Kiel group [9] of an enhanced muon content in their detected showers that approaches 80 % of the expected number of muons from hadronically initiated showers. Recent results from the Cygnus experiment [14] also report that no significant excess in events is present in their data. However, they too report an anomalous muon signal in a subset of their data. Finally, the Fly's Eye (VHE) experiment has recently claimed to have found evidence for ≥ 1 EeV (10^{18} eV) neutral particles from the Cyg X–3 direction [15]. This is the first sighting of cosmic ray particles of such high energy from a specific source. Their data show a distinct dc excess at a galactic longitude of 80°, close to the source coordinates. Using an ephemeris by Molnar ($T_0 = JD\ 2443052.9750 \pm 0.00006$, $P_0 = 0.19968513 \pm (1.1 \times 10^{-7})\ d$, $\dot{P} = (9.6 \pm 0.7) \times 10^{-10}$), they report a slight modulation of their data with the 4.8 h period in the phase region near zero.

Underground Muon Observations

Grand unified theories developed over the past decade leave open the possibility of nonconservation of baryon number; no symmetry has been found to indicate such a conservation principle exists. Several experiments have therefore been set up with the goal of measuring the lifetime of the nucleon. The flux of cosmic rays on the surface of the Earth presents a large source of background to these experiments so that an underground environment is preferred. Two types of detectors are in use. Water Čerenkov detectors use a large mass of pure water as the source of nucleons and rely on phototubes to record Čerenkov rings generated by charged tracks that pass through the detector. Calorimeter experiments use a large mass of iron as the nucleon source and record tracks by detecting ionization losses. Besides searching for nucleon decay, these detectors are also capable of recording muon tracks with energy thresholds set by the amount of rock overburden at the site.

Interest in the field of muon astronomy was sparked by the nearly simultaneous observations of the Soudan 1 [16] and NUSEX (NUcleon Stability EXperiment) [18] groups in 1985 of secondary muons from the direction of Cyg X–3 that were modulated with the characteristic 4.8 h phase.

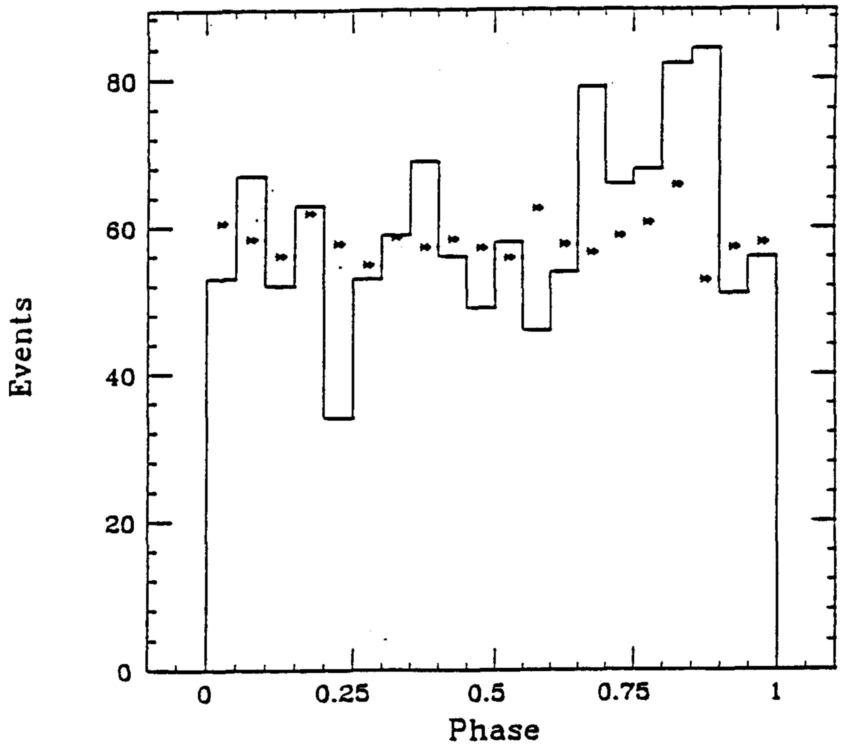

Fig. 1-2. The phase of muon time signals arriving at the barycenter of the solar system as observed by Soudan 1. An abundance of muons is seen in the [0.65,0.90] phase region. The expected background per bin is shown as an asterisk.

Between the years 1981 and 1983 (livetime 0.94 years), the Soudan 1 first generation nucleon decay calorimeter, at a depth of 1800 meters of water equivalent (mwe), collected a total of $\sim 800,000$ muons. The overall angular resolution for muons is about 1.5°. Their muon signal was optimized by maximizing the χ^2 for the phase plots in 3° right ascension and declination scans about the source direction. Phase analysis using the vdKBB-81 ephemeris showed an excess of 84 ± 20 events above an expected 295 in the phase region [0.65,0.90] (a 3.6 σ enhancement), corresponding to an integrated flux[2] of $7 \times 10^{-11} cm^{-2} s^{-1}$ (Fig. 1-2). Since photon induced showers are thought to be muon poor, the Soudan 1 group postulated, for the first time, that either new physics would be required to explain an increase in the photoproduction cross section above a new (as yet undetected) energy threshold or a different (and new) primary particle would be required to explain their results (explained further below).

---

[2] Integrated flux here refers to the excess flux, above that expected from an isotropic cosmic ray background, as measured over the entire observation period.

Further evidence for an underground signal in the Soudan 1 detector came in October, 1985, during a radio outburst of Cyg X–3 [17]. A phase plot for the period 24 September through 7 October, 1985 shows an accumulation of muons in the same phase region reported earlier (Fig. 1-3).

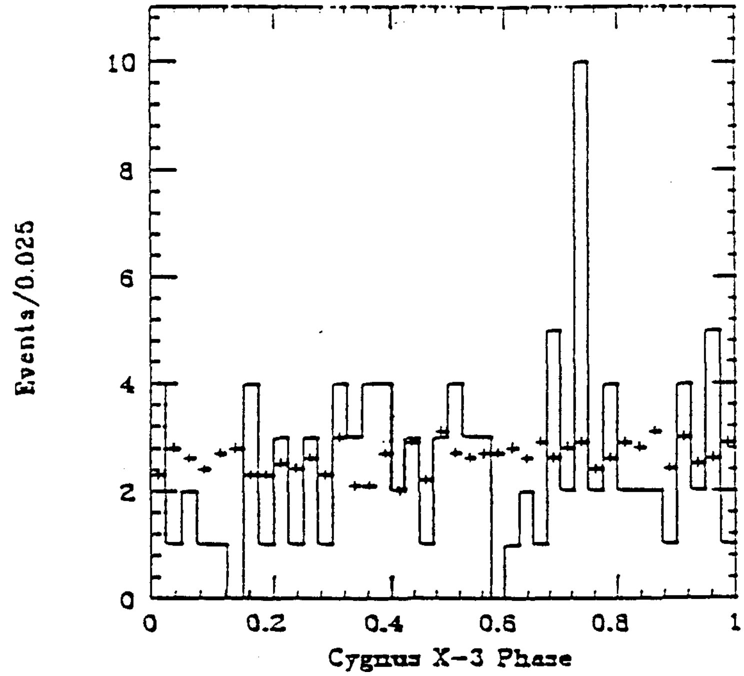

Fig. 1-3. Cyg X–3 phase plots within 5° of the source observed by Soudan 1 between 24 September and 7 October, 1985. The solid curve is data and the crosses indicate the background as determined from 23 off-source directions.

A signal enhancement resulted by increasing the size of the cone cut about the source from 3° to 5° and increasing the number of bins in the plot from 10 to 40. Monitoring the number of detected events per week in a narrow range of phase [0.725,0.775] (Fig. 1-4), they again saw a large fluctuation in their data, 16 events when only 6.3 were expected.

In the same year, the NUSEX group [18] reported on their search for underground muons during a period between 1982 and 1985, (livetime 2.4 years). Their detector is also of the calorimeter type, is located at a depth of ~ 5000 mwe and has ~ 1° angular resolution. The result seems, however, to depend highly on the size of the angular cut placed around the source. When an angular window close to the resolution of the detector

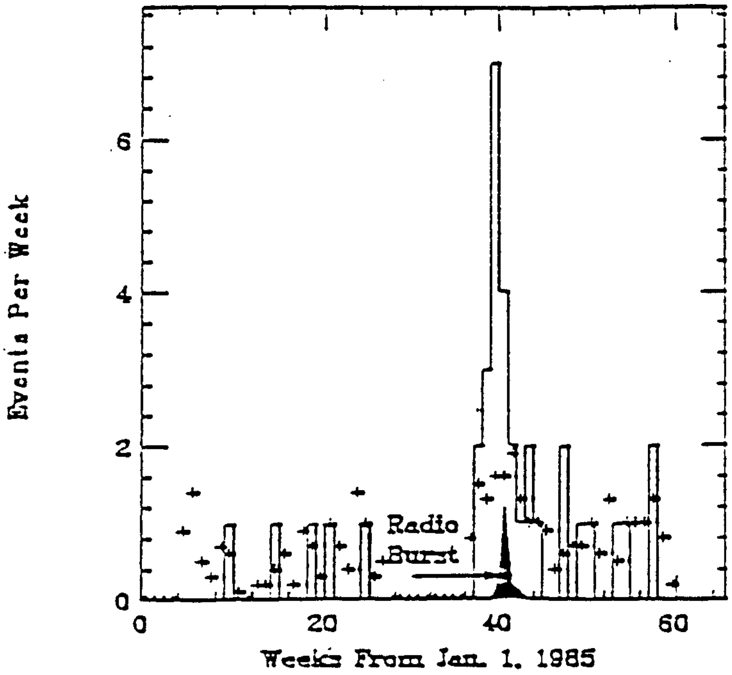

Fig. 1-4. A large increase in the rate of muons from the source direction was observed by the Soudan 1 group during the 1985 radio outburst. The solid histogram is for data observed within 5° of the source and the dashes are the expected background per bin as determined by 23 off-source directions.

is used, no signal is seen. Their reported signal was made with a 5° half-angle cone cut about the source. Using 10 bins to unfold the phase with the vdKBB-81 ephemeris, they reported a 5 σ peak in the [0.7,0.8] phase region, an excess of 19 ± 3.6 events above a background of 13 events. Their integrated flux measurement of $\sim 3 \times 10^{-12} cm^{-2} s^{-1}$, taken at the deeper location, is consistent with the Soudan 1 result.

A third calorimeter-type detector also made measurements of underground muons. The Frejus experiment [19], at a depth of ~ 4800 mwe, collected ~ 170,000 muons between 1984 and 1986. Their angular resolution was 0.4° and they used the same ephemeris in the time-dependent analysis. They reported no significant excess of muons in any phase bins and an integrated flux limit of $0.8 \times 10^{-12} cm^{-2} s^{-1}$. The flux recorded at this depth is still consistent with the Soudan 1 result. A search for an increased flux during the 1985 radio outburst was carried out but none was found.

Two other nucleon decay experiments of the water Čerenkov type have also reported flux limits and phase analysis results. Both of these analyses again made use of the vdKBB-81 ephemeris. The IMB experiment [20], using a 7° half-angle cone, reported that a set of $\sim 3.6 \times 10^4$ single on-source muons showed no significant dc excess from the source direction nor did it show any phase enhancement. They set a flux limit for muons from the source direction of $6.9 \times 10^{-11} cm^{-2} s^{-1}$ at a depth of 1570 mwe, a result consistent with the Soudan 1 measurement. The Kamioka nucleon decay experiment [21], has an average angular resolution of 2.7°and their analysis uses a 7° × 7° (α vs δ) window. Based on a data sample of nearly 2 million single muons, no significant signal is seen in their detector. Their upper flux limit of $2.2 \times 10^{-12} cm^{-2} s^{-1}$ measured at 2400 mwe contradicts the Soudan 1 result. This experiment also searched for evidence in their data of the 1985 outburst and reported a null result [22].

Recently, the Soudan 1 group has reported on data collected over the entire livetime (1.64 yr) of the experiment between 1981 and 1988 [23]. They have combined their previous data set with the newer one and have performed both a time-independent analysis of the data to determine the flux of muons from the source direction and a time-dependent analysis based on a cubic fit of the vdKBB-88 ephemeris and on quadratic fits using the vdKBB-81 and Mason ($T_0 = JD\ 2442946.739$, $P_0 = 0.1996851\ d$, $\dot{P} = 7.84 \times 10^{-10}$), ephemerides. The background for both of these studies was determined by an analysis of 35 3° half-angle cones in right ascension at a declination of 41°. (Presumably, the detector livetime is the same for all background directions as for the source direction.) A sinusoidal fit to the number of muons in each of the background bins was used to determine the expected number of muons in the Cyg X-3 bin. The deviation from the fit in this bin does not appear to be significant. They see 2922 events above a background of 2885, an excess of 37 ± 54 events corresponding to a flux of $5.7 \pm 8.4 \times 10^{-12} cm^{-2} s^{-1}$. When the vdKBB-88 ephemeris is used to unfold the phase plot, the bin centered in the [0.70,0.75] phase region is seen to contain 60 % of the signal, corresponding to a flux of $6 \times 10^{-12} cm^{-2} s^{-1}$ (3 σ).

1.2 The Muon Content of Photon Induced Showers

The large distance between the Earth and the source and the temporal structure maintained by the primary indicates that it must be either massless or extremely relativistic. In addition, in order to maintain its directionality through the galactic magnetic field ($\sim$ 3 μG), it must be neutral. The only known particles which could satisfy these criteria are the photon, the neutrino, or the neutron. Since free neutrons are unstable, they must acquire energies on the order of those detected in the most recent Fly's Eye report or else they will decay in flight. Neutrinos are known to interact only weakly. At least in the known energy regimes, their cross sections in the atmosphere (and even in rock) are much too low to produce the effects claimed. Furthermore, studies by the Soudan 1, IMB and the Kamioka groups show a drop in muon flux from the Cyg X–3 direction with increase in overburden as expected for a normal muon background (a neutrino primary would show no zenith angle dependence). Considering these facts, it is hard to find evidence that supports the neutrino as the primary involved in signals detected from Cyg X–3. This leaves the photon as the only viable candidate among the known particles. This has been a standard assumption in the VHE and UHE experiments.

Calculations [24] have been made of the photoproduction cross section of pions in air (*i.e.*, the cross section for the production of pions in gamma–nucleon interactions). The cross section for pion production is shown in Fig. 1-5. The production cross section is small and shows only a slight logarithmic rise in production with photon energy. This indicates that electromagnetic showers should be "muon poor", having muon densities of only $\sim$ 10 % of those initiated by hadrons. In fact, low muon content has been used as a signature for electromagnetically initiated showers. Since the report by the Soudan 1

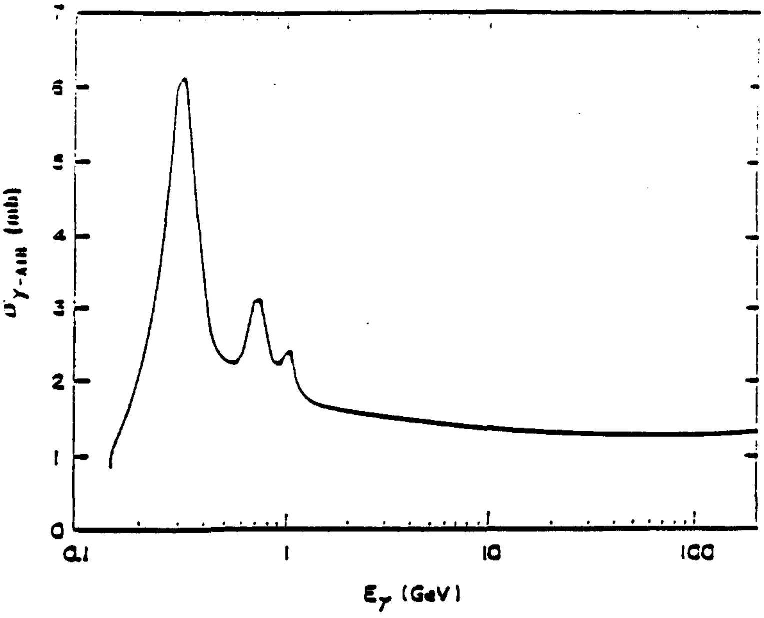

Fig. 1-5. The cross section for pion photoproduction in air as a function of photon energy.

group in 1985 of underground muons from the direction of Cyg X–3, several authors [25-27] have taken up the question of the muon content of these showers. No disagreement with previous calculations is found. In light of the theoretical argument, the measurements by the Soudan 1 and NUSEX groups are taken with some skepticism. (Since the authors of the CYGNUS experiment themselves find little significance in the anomalous muon content found in a subset of their gamma–ray data, not much can be said of that result.)

The ability to distinguish photonic showers in a sky full of hadronic ones is very important if we wish to learn more about astronomical phenomena through the only (indirect) means we know (using the atmosphere as a target). Based on the above observations of the source, it appears that the window of underground muon astronomy has not been shut (at least not too tightly). Future and better experiments are being built and these should produce answers with an unambiguous degree of statistical significance.

1.3 The Goals of the Present Thesis

The main goal of this research is a search for radiation from Cyg X–3 using muons detected underground with a section of the Soudan 2 active shield known as the "Tracker".

The detector is located in the same mine as the Soudan 1 experiment but at slightly greater depth. In addition, this detector and the Soudan 1 detector ran concurrently during the lifetime of the Tracker. We report on a flux and phase analysis of muons from the direction of Cyg X–3 for comparison with other experiments.

A measurement of the vertical muon flux at a depth of 2100 meters of water equivalent is reported.

Results of this work are presented in two separate chapters, one dealing with observations of general interest (the vertical muon flux, background rates due to radioactivity, parallel muons, *etc.*) and another providing a detailed analysis of the source Cyg X–3.

Chapter 1 References

[1] Giacconi,R., *et al.*, Ap. J. 148, L19 (1967).

[2] see 'Cygnus X–3: A Critical Review', J.-M. Bonnet-Bidaud and G. Chardin, Phys. Rep. 170, No. 6 (1988).

[3] M. van der Klis and J.-M. Bonnet-Bidaud, Astron. Astrophys. 101, 299 (1981).

[4] M. van der Klis and J.-M. Bonnet-Bidaud, Astron. Astrophys. 214, 203 (1989).

[5] Vladimirsky, B. M., *et al.*, Proc. 13^{th} Int. C. R. Conf. Denver, 1, 456 (1973).

[6] Weekes, T. C., *et al.*, T. C., Astrophys. J. 104, L4 (1981).

[7] Lamb, R. C., *et al.*, Nature 296, 543 (1982).

[8] Dowthwaite, J. C., *et al.*, Astron, Astrophys. 126, 1 (1983).

[9] Samorski, M. and Stamm, W., Ap. J. (Letters) 268, L17 (1983).

[10] Lloyd-Evans, J., *et al.*, Nature 305, 784 (1983).

[11] Alexeenko, V. V., *et al.*, Rev. Nuovo Cimento 10, 151 (1987).

[12] Kifune, T., *et al.*, Astrophys. J. 301, 230 (1986).

[13] Morello, C. G., *et al.*, Proc. Intern. Conf. C. R. Vol. 1, 127 (1983).

[14] Dingus, B. L., *et al.*, Phys. Rev. Lett. 60, 1785 (1988).

[15] Cassiday, G. L., *et al.*, Phys. Rev. Lett. 62, 383 (1989).

[16] Marshak, M., *et al.*, Phys. Rev. Lett. 54, 2079 (1985).

[17] Marshak, M., *et al.*, in *Proceedings of the XXIII International Conference on High Energy Physics*, Berkeley, California, 1986, edited by S. Loken (World Scientific, Singapore, 1987).

[18] Battistoni, G., *et al.*, Phys. Lett. B 160, 465 (1985).

[19] Berger, Ch., *et al.*, Phys. Lett. B 174, 118 (1986).

[20] Bionta, R. M., *et al.*, Phys. Rev. D 36, 30 (1987).

[21] Oyama, Y., *et al.*, Phys. Rev. Lett. 56, 991 (1986).

[22] Oyama, Y., *et al.*, Phys. Rev. D 36, 3537 (1987).

[23] Johns, K. A., *et al.*, *Proceedings of the International Conference on High Energy Physics*, Munich, 1988.

[24] Karakula, S. and Wdowczyk, J., Acta. Phys. Pol. 24, 231 (1963).

[25] Stanev, T., *et al.*, Phys. Rev. D 32, 1244 (1985).

[26] Dar, A., *et al.*, Phys. Rev. D 33, 303 (1986).

[27] Halzen, F., *et al.*, Phys. Rev. D 34, 2061 (1986).

CHAPTER 2. TRACKER DESIGN AND EXPERIMENTAL DETAILS

The Tracker is a section of the Soudan 2 active shield that was installed as a muon tracking system. It consists of 128 proportional tube modules arranged in two planes of crossed layers, separated by 10 m, with an effective overlap area of ~ 35 m^2. The detector is shown in Fig. 2-1. Each layer contains 32 proportional tube modules each consisting of eight individual proportional tube cells. Anode wires from the four cells in each of the upper and lower rows of a module are ganged together to form a detection element or channel. As measured on a cosmic ray test stand, individual channels are capable of responding to minimum ionizing radiation within 1 μs. The identification of a coincidence (1 μs) between any adjacent upper and lower channels within a layer forms a trigger signal for that layer. The logical AND of the trigger signals generated by a set of three layers is used to form the signal for a penetrating muon in this experiment. Absolute timing information, accurate to 1 ms was provided by the WWVB signal generated in Fort Collins, Colorado.

As is the case here, proportional counters are normally designed to meet the needs of a specific measurement. The specific details of the proportional counters used in the Tracker detector have been described elsewhere [1]. Some further explanation will be given here, however, in order to close the gap between the description of an individual component of a large system and incorporation of that component in a fully implemented detector. In particular, a complete description of the Tracker will cover: a brief history, location and overburden, the electronics and gas systems, and the basic element—a multiwire proportional chamber. The chapter will conclude with a description of the data acquisition system. First, for pedagogical reasons, the theory of operation of proportional counters is presented.

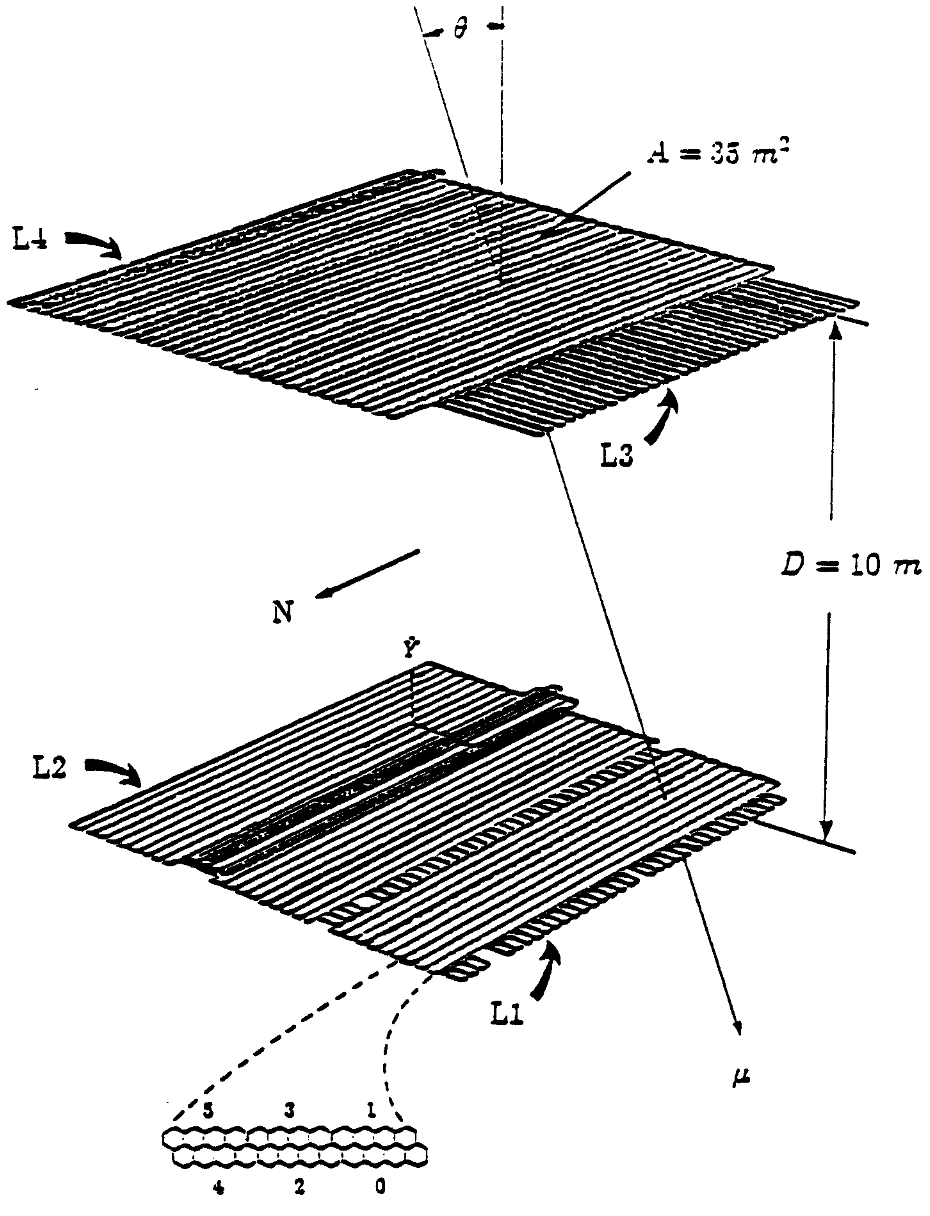

Fig. 2-1. The Tracker. The Tracker consists of four layers of 32 proportional tubes each, arranged in two crossed planes as shown. The planes are separated by 10 m and the overlap region in each is 35 m^2. A two-fold in-time coincidence (1 μs) from each of 3 out of 4 layers is used to form the signal for a penetrating muon. The channel numbering scheme for each layer is also shown.

2.1 Theory of Proportional Counter Operation

Energy Loss

Proportional counter operation [2] relies entirely upon the fact that charged particles traversing matter deposit energy there. The phenomenon is described by the Bethe–Block equation which gives the mean rate of energy loss, per unit path length x, of charged particles undergoing Coulomb scattering in the medium:

$$\frac{dE}{dx} = 4\pi N_0 r_e^2 m_e c^2 \rho \frac{Z}{A}\left(\frac{z}{\beta}\right)^2 \left\{ ln\left(\frac{2m_e\gamma^2\beta^2c^2}{I}\right) - \beta^2 \right\} \tag{2.1}$$

where N_0 is Avogadro's number and e, m_e and r_e are the electron charge, mass and radius respectively. The medium is described by atomic number Z, atomic mass A, density ρ, and effective ionization potential I. The particle passing through the medium has charge z, and velocity β (in units of c).

Ionization

The process which contributes to the above energy loss in the medium of a gas ionization chamber, is the creation of an ion pair, or pairs, by removal of one or more electrons from the atoms of the gas filling. Let W represent the energy required to create a single ion pair in the gas filling of the counter. For the inert gas Ar, $W \simeq 26$ eV, independent of the energy of the charged particle. In the absence of an external electric field, a 2.6 keV electron will then create about 100 ion pairs in the gas.

In a proportional counter, however, a force is applied to the electrons and positive ions so formed, allowing them to create additional ion pairs, the total number of pairs formed being "proportional" to the initial energy lost by the particle. This driving force is an externally applied electric field that accelerates the ions.

Amplification

For further discussion, it is useful to introduce a simple model of a proportional counter based on a cylindrical design (which closely resembles the counter used in the actual experiment). Consider a conducting cylinder with radius b down the axis of which is stretched a wire with radius a. The capacitance of the system is given by $C = 2\pi\epsilon_0/ln(b/a)$. A typical value for C (per unit length) is 10 pf/m. Then, the 100 ion pairs created by the 2.6 keV electron represent a potential difference of $V = 100\ e/C, \simeq 1\ \mu$V between the electrodes. If an external field is now applied between the anode (wire) and cathode (cylinder), these 100 ion pairs can create still more pairs causing an avalanche effect to take place, boosting the total number of ion pairs created and hence the signal, V. The ratio of the total charge collected at one of the electrodes, to the number of ion pairs initially formed in the chamber, is a proportionality constant, M, which is the multiplication (or amplification) factor for the system. Most of the amplification occurs within 1 ns and takes place near the anode where the electric field ($\propto 1/r$) is greatest. The electrons drift a short distance in this high field region so they reach the anode very rapidly; they are responsible for the initial rapid rise of the detected voltage pulse. The positive ions have to drift a relatively large distance since most of them are created close to the wire. The voltage signal is then due mostly to the positive ions which drift between (essentially) the wire and the cathode. Under proper circumstances, multiplication factors of 10^4 can be achieved. An expression for the amplification factor is derived in the work by Sauli [2] and will not be repeated here. Rather, in order to stress the importance of knowing and maintaining the operational parameters of the device, we simply remark that M scales as $e^{\sqrt{N}\cdot V}$ where N represents the molecular density of the gas, (sensitive to changes in pressure, volume, temperature *and purity*) and V is the applied voltage.

2.2 The Soudan 2 Active Shield Module

Design Considerations

The initial design goals of the shield were to provide for a highly efficient veto with full geometrical coverage (including the floor) of the Soudan 2 detector. Also, because the experiment was designed to run for a decade or so, the veto shield elements must be rugged, long-lived, readily serviceable and must allow ready access to the main detector. In addition, it was hoped that the shield would be able to provide pulse height information (dE/dx) to distinguish radioactivity from through-going muons in the detector, have good spatial resolution in order to associate wall spray with tracks penetrating the main detector and have very good time resolution (10-25 ns) in order to determine track directionality. Only the former goals have been met.

"To be effective the shield must have very high efficiency. Furthermore, to minimize false vetoing, its time resolution should equal or exceed the time resolution of the central calorimeter. Practicality dictates that the shield be constructed of modules which are small enough to be brought down the Soudan mine shaft and rugged enough to withstand rough handling as they are brought into the mine and installed on the walls. These considerations led to the design of the shield as an array of extruded-aluminum honeycomb proportional tube modules. Fine spatial resolution is not essential for the shield so the honeycomb modules were made as long as possible to reduce the number of (expensive) electronics channels required."[1] Several attempts at satisfying these requirements were made before a final design was eventually selected.

Components and Assembly

The basic element of the detector is an extruded aluminum proportional tube with eight individual cells. A cross sectional view of the chosen honeycomb design is shown in

---

[1] See reference [1].

Fig. 2-2 along with a view of one of the 7 m modules used in the experiment. When nested together as shown in Fig. 2-3, this cross section allows no cracks through which penetrating particles could pass undetected. This avoids a costly gap–filler layer of detector.

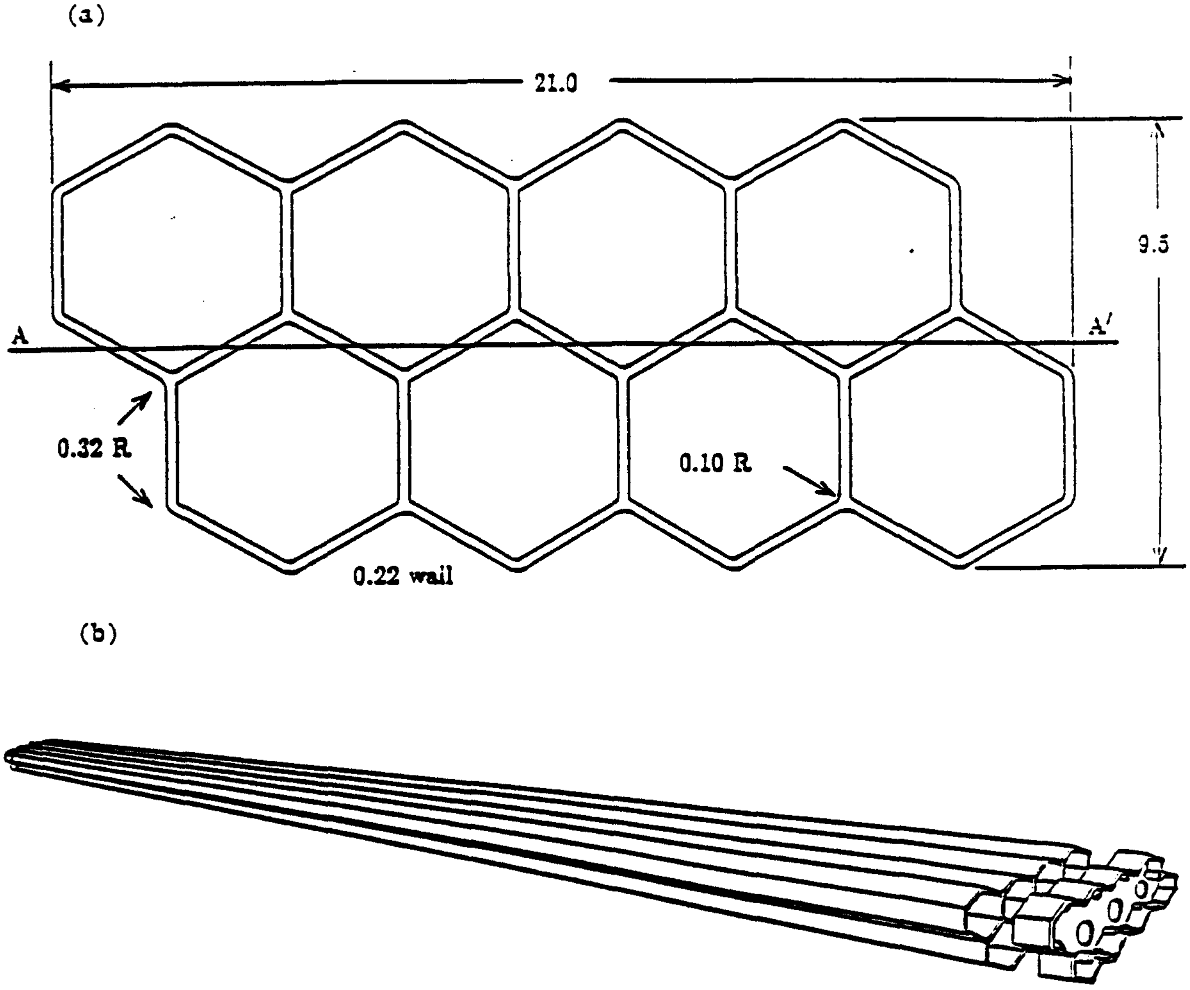

Fig. 2-2. The Honeycomb Design. A cross sectional view of an active shield module is shown. Also shown is one of the 7 m proportional tubes used in the experiment. Dimensions are in cm.

Sandcast aluminum endcaps (Fig. 2-4) are machined to provide a threaded gas port hole, eight sense wire holes and threaded mounting holes for later installation of preamps and ground shields. A deep well in the endcap provides protective housing for a preamp to be mounted to the outside of the module. A shallow well on the inside face provides

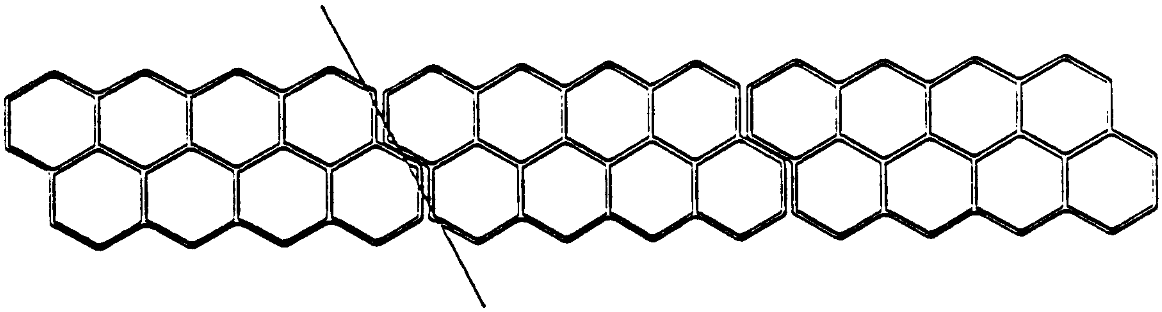

Fig. 2-3. Shield modules nested together as shown allow no crack regions through which a charged particle could pass undetected.

a common volume at the ends of the honeycomb cells for gas to flow. Two endcaps are required for each module, one endcap being a mirror image of the other. After thorough cleaning, these are TIG–welded (tungsten inert gas) to the extrusion by faculty, graduate students and technicians who have been trained by a professional welder. The welded unit is checked for internal debris, overpressured (1 bar), then checked for leaks. Repairs are made at the welding station if required.

Each of the eight cells in a module is strung with a resistive (0.45 kΩ/m) wire [3]. The wire diameter was chosen to be 60 μm, slightly greater than the usual 50 μm wire in order to raise the plateau voltage and decrease drift time to the wire. The wire is supported at both ends with a plastic molded insulating mounting disk [4]. At the center of this disk is a small tube through which the wire passes. The tubes are crimped with the wire under 2.0 N of tension. The surfaces of the plastic molded feedthroughs and nearby aluminum are then cleaned before being sealed with epoxy [5].

Before a module can be certified for shipment to the mine, it must undergo a set of quality control checks. Experience has shown that a visual inspection of the module followed by a gas leak test and high voltage tests ensures a properly operating counter. Modules may be rejected at any stage of the quality control check and returned to the appropriate station for repair. In the visual inspection, bent crimp pins and improperly seated feedthroughs are identified and repaired if necessary. Next, the module is again

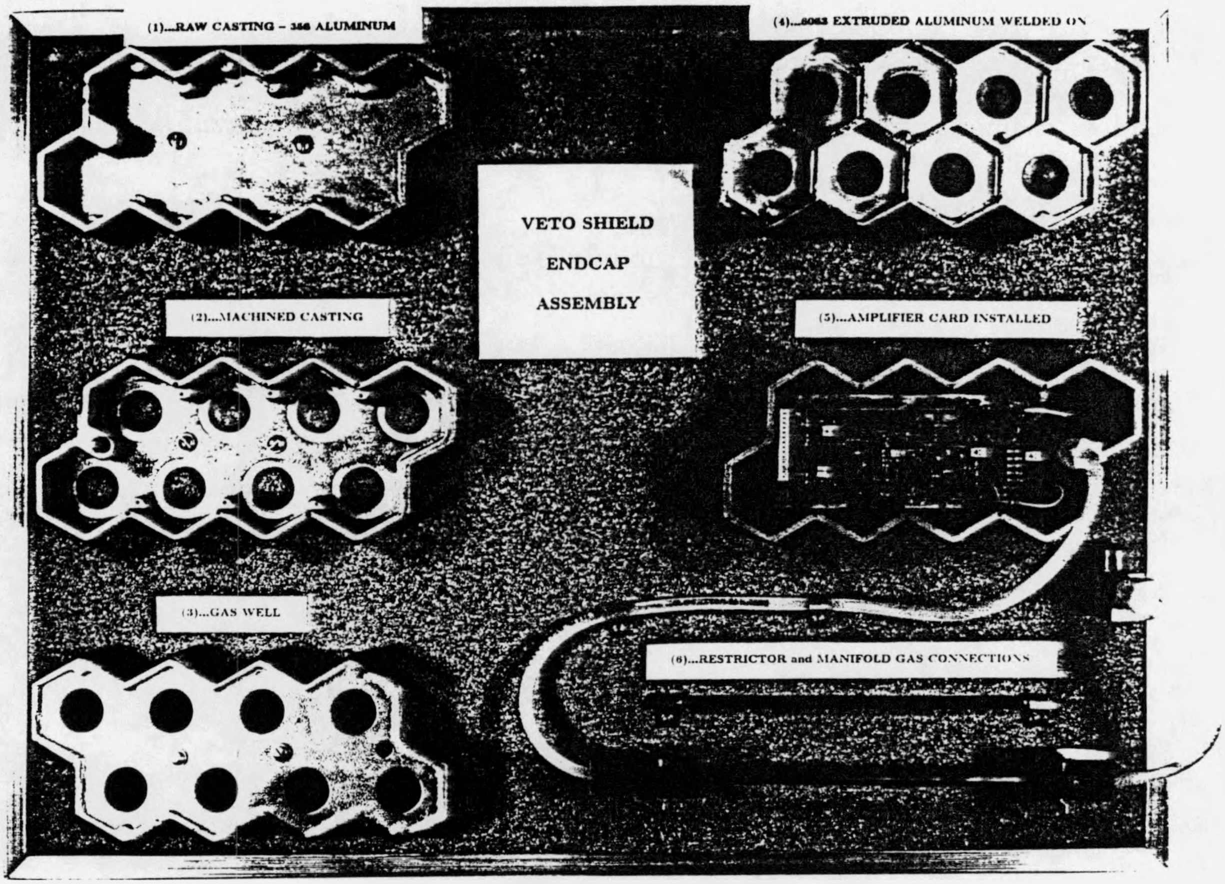

Fig. 2-4. Endcap Assembly. Endcaps must be machined and cleaned before being welded to the aluminum honeycomb extrusions. Mounting disks for the anode wires are installed in the stringing procedure. A digital output card (see text) senses the anode wires and informs the experiment when a 'hit' occurs in one or both channels of the module.

overpressured (0.35 bar) and checked for leaks. This time the ends of the crimp pins, the feedthrough–aluminum epoxy seal, the gas ports and the weld area are all inspected. Since it is time consuming and costly to return the module to the welding station for repair (all wires and plastic feedthroughs would have to be removed), leaks in the weld area are sealed by first drilling a small cavity around the hole and filling it with optically–hardened cement. Other leaks are sealed with epoxy. If the module passes the leak check, it is gas conditioned with a 90–10 Ar–CO_2 gas mixture, then checked for current draw at 2.0 kV and 2.5 kV. The check at 2.0 kV, below the measured plateau, measures current leakage. Modules are required to draw less than 10 nA at this voltage. For modules with low current leakage, a second measurement is made on plateau to check the counter's ability to respond to cosmic rays and natural radioactivity in the room. Current draws in the range 0.02 – 0.01 μA are acceptable at this voltage.

A picture of the end of a completed module is shown in Fig. 2-5.

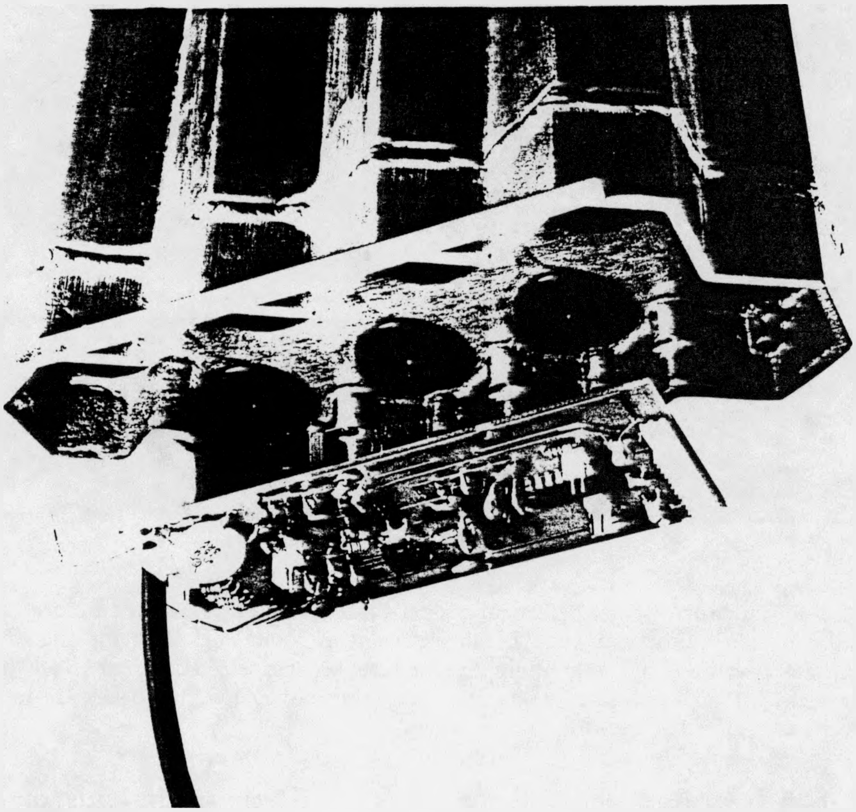

Fig. 2-5. End View of A Completed Active Shield Module.

Operational Characteristics and Performance of a Four–cell Element

In addition to the standard checks just described, several modules were selected to undergo more extensive testing. A four–panel scintillator telescope was constructed to make efficiency and plateau measurements of these modules (see Fig. 2-6). The telescope included 10 cm of lead in order to form a trigger on the hard component of surface cosmic rays. One of the panels in the telescope was small enough so that all particles passing through it had to pass through the test module thus enabling the efficiency measurement.

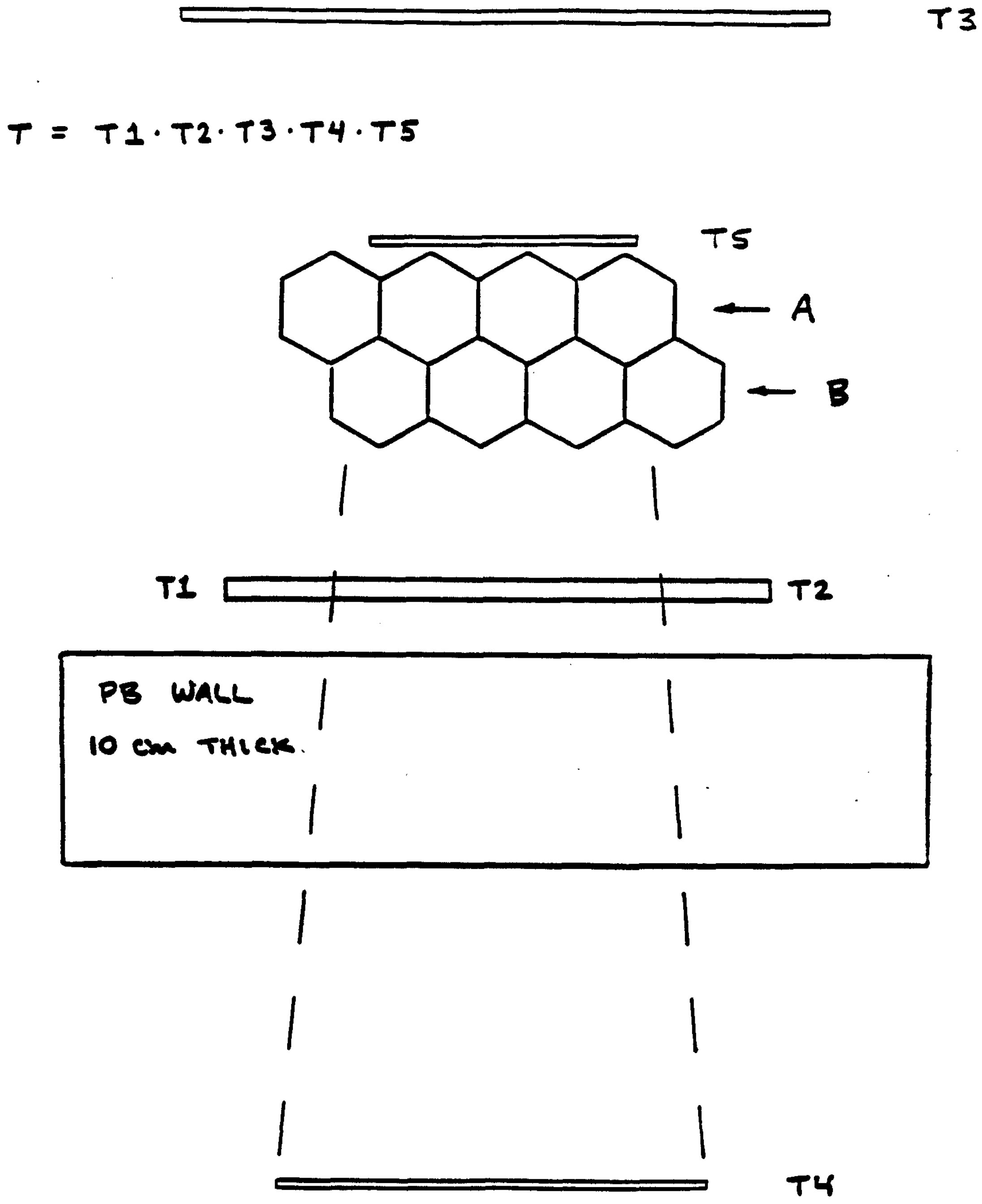

Fig. 2-6. The Cosmic Ray Telescope. Four scintillator panels with 10 cm of lead between them are used to form a trigger on the hard component of cosmic rays. This test set up was used extensively in prototype plateau and efficiency studies.

Measurements of the efficiency of a module versus operating voltage and drift time were made for two gas mixtures, 90–10 and 95–5 Ar–CO_2. The four wires in each row of the module are ganged together at one end to form a single channel. A trigger by the telescope creates a 2 μs window in which the modules must respond to cosmic rays. The results presented in Fig. 2-7 show the 95–5 mixture to have a plateau width of 90 V at roughly 2400 V. The 90 V plateau width allows us to operate the entire shield at the same voltage since there is a card–to–card uniformity of the response of the digital output cards over this voltage range. At the plateau voltage, channels respond to cosmic rays within 1 μs for this gas mixture.

Performance of a Panel of Modules

A 16 module test array was operated at Tufts to study the performance of a section of shield. The goal was to test the efficiency of a panel as a whole so that inefficiencies in crack regions (should they exist) could be determined. The coincidence of six plastic scintillation counters provided a cosmic ray muon trigger for two layers of eight 7 m long modules. The setup is shown in Fig. 2-8. Efficiencies of the rows of cells in each of the two layers were then measured. One of the rows in the setup, having a broken wire, allowed us to test the efficiency of the shield under these (less than satisfactory) conditions. From top to bottom, the rows operated with efficiencies of 97.1 ± 0.2 %, 97.2 ± 0.2 %, 97.5 ± 0.2 % and 92.1 ± 0.3 %. The OR efficiency of a layer (upper row + lower row) was measured to be 99.91 ± 0.03 % for the top layer and 99.82 ± 0.04 % for the bottom layer.

The efficiency for muon detection by a coincidence between the upper and lower rows in a layer can be inferred from the measurements of the OR efficiencies of each row. Using an average of the above measurements, this efficiency is 94.6 ± 0.3 %. This allows for muon trajectories which pass through any region of the layer, including the crack regions between modules (provided they are within the acceptance of the test setup). If one requires

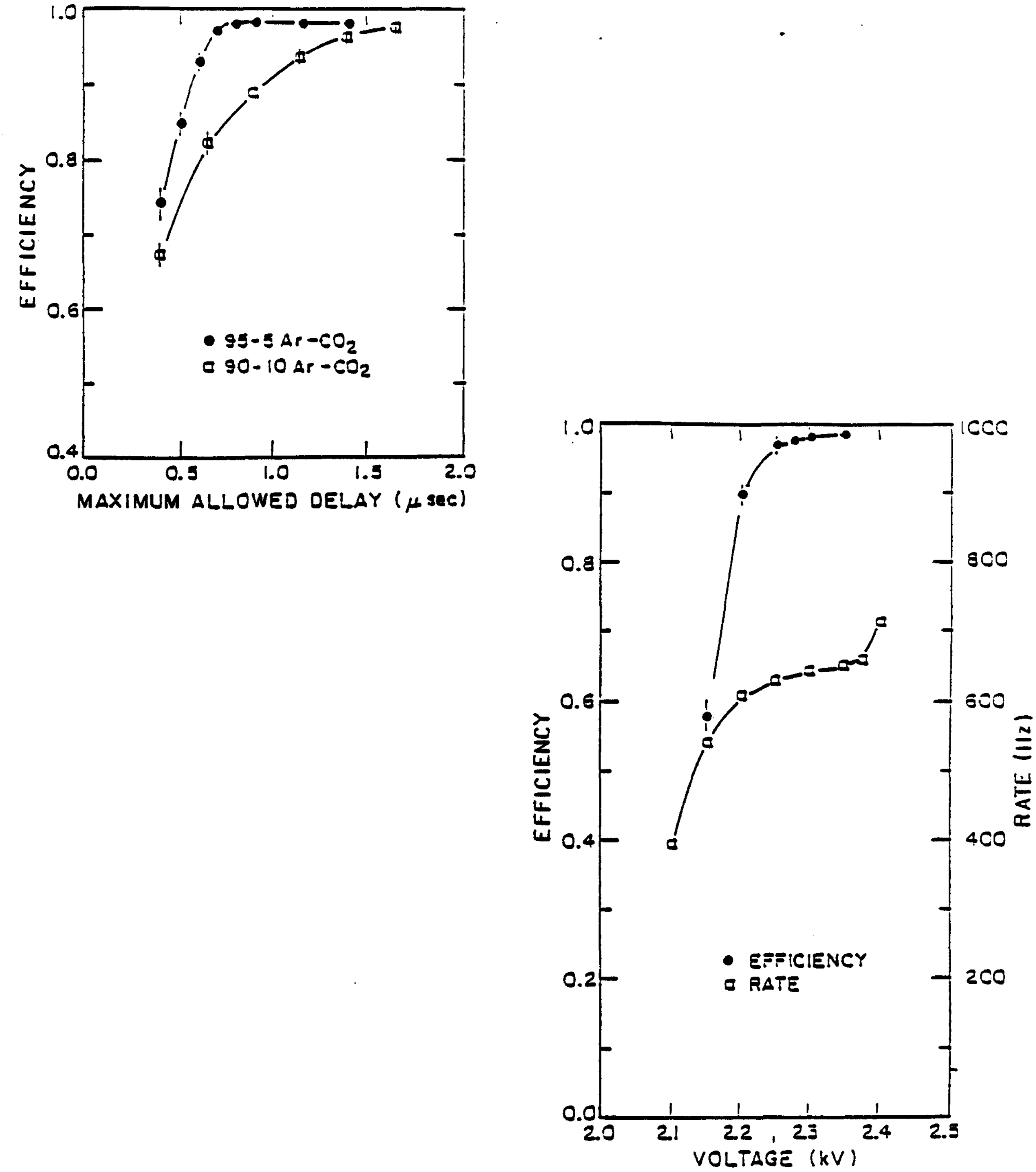

Fig. 2-7. Active Shield Module Performance. Dependence of the 4-cell element efficiency on the maximum allowed drift time for the 95–5 Ar–CO_2 mixture (circles) and for the 90–10 mixture (squares). High-voltage dependence of the counting rate (squares) and the efficiency (circles) for an individual 4-cell element using a 95–5 Ar–CO_2 mixture.

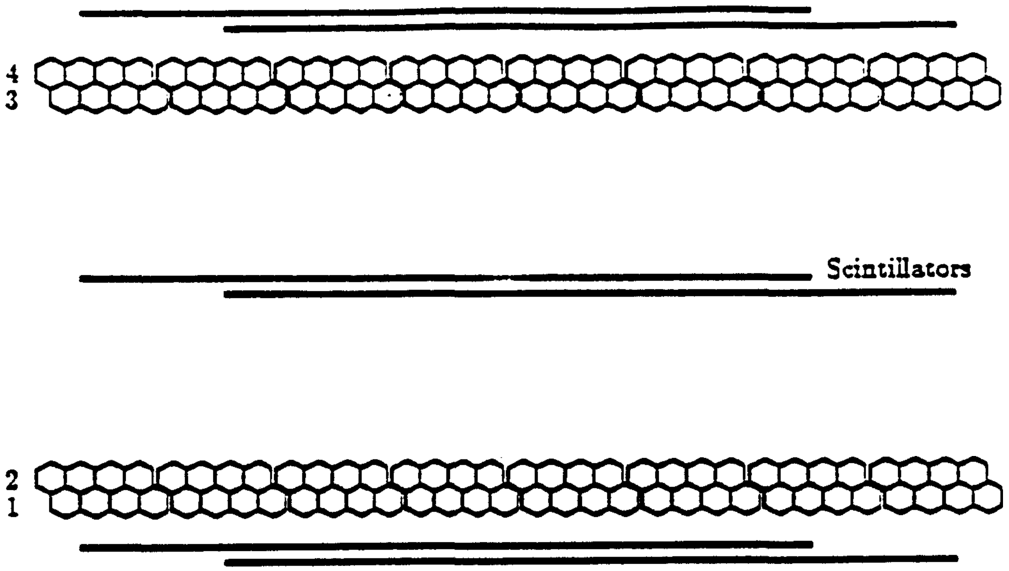

Fig. 2-8. The 16 Module Test Array at Tufts. A six-fold coincidence from the scintillator panels forms the cosmic ray trigger used to make efficiency measurements of each of the four rows in the two layers of proportional tubes.

muon trajectories not to be in the crack regions, however, the efficiency for detection of a coincidence is 97.0 ± 0.2 % as measured on the cosmic ray telescope described in the last section. This latter number is important in calculating the vertical muon flux at the underground site (see Chapter 3).

2.3 The Tracker Muon Telescope

A General Description and Brief History of the Tracker

The Tracker consists of 128 of the proportional tube modules just described. These are arranged as shown in Fig. 2-1. Layers in the detector are labeled L1 through L4, L1 being closest to the floor and L4 closest to the ceiling. Modules for the Tracker were extruded in two lengths: modules in layer L1 have lengths 6.62 m and modules in all other layers have lengths 7.03 m. The alignment of the modules matched that of the steel framework used to support the central calorimeter so that the two layers in each plane run parallel to the steel in the east-west (L1 and L3) and north-south (L2 and L4) directions. The criss-crossed $(x - z)$ geometry of each plane allows for muon tracking.

The veto shield trigger is formed by the OR of all possible combinations of coincidences between sets of two adjacent channels in a layer: $T = 0\cdot1 + 1\cdot2 + \cdots + 62\cdot63$. Then, the individual trigger formed by each layer is brought to a special CAMAC trigger module where various combinations of layers in coincidence can be formed. The usual cosmic ray trigger was the three-fold coincidence $T1\cdot T2\cdot T3$. Since 17 % of layer L3 is not overlapped by layer L4, not requiring L4 in the on-line trigger resulted in a higher trigger rate. An XZ readout was not available for muons which passed through this non-overlapped area and so they could not be used in muon astronomy. However, the higher rate allowed for greater illumination of the central calorimeter which was being installed and tested at that time.

The Tracker represents about ten percent of the entire shield and was installed as a muon detector. It was proposed to the Soudan 2 collaboration (see Appendix A) in June of 1986 with four goals: to provide a testing of the complete veto shield design, to serve as an unbiased muon trigger to the main detector, to provide a detector close to the Soudan 1 depth for muon astronomy, and to provide physics data at an early stage. All of these goals have been met.

The formal proposal to install initial portions of the veto shield as a muon detector was written in May, 1986, and presented to the entire Soudan 2 collaboration the following month when it was accepted. Initial installation of the various layers took longer than expected due to the learning process in an unfamiliar laboratory. L1 was installed between October and December, 1986, while L4 was installed in April, 1987. Layer L5, an extension to layer L3, was installed in December, 1987. The Tracker stopped operation in March, 1988, when it was deemed necessary to upgrade the prototype readout modules with production ones. Analysis of the data has proceeded between the summer of 1987 and the present.

Site Location and Overburden Description

The history of the Soudan Mine in Soudan, Minnesota [6], as an active iron ore mining operation, spans the period between the end of the last century and the middle of the present one. The first miners arrived from Michigan in 1883 to begin open pit mining of the hard hematite ore from the surface. The open pits soon became dangerously steep and in the early 1890s, the mining operation was brought underground. Electricity was brought into the mine in 1924 and this changed the mining operation drastically. A new hoist was added on the surface and modern equipment was brought in to step up the ore production. Although the hematite ore is extremely rich in iron (up to 70 %) it became clear that extraction of iron from taconite was much less expensive, and the industry switched to mining taconite ore in the 1950s. The last mining in the Soudan took place in 1963 and shortly thereafter the mine was donated to the State of Minnesota to become the Tower-Soudan State Park. The park still operates the hoist and schedules hourly tours between Memorial Day and Labor Day.

The topology of the surface near the site is presented in Fig. 2-9; the detector is located at 'T' in the figure. The underground laboratory is situated directly below a 40 m–wide ridge that runs along an east–west axis. Ore veins in the mine were usually cut along this same axis. In addition to the hematite ore that was mined, two other types of rock are prevalent in the mine: jasper and Ely greenstone. The Soudan 2 cavity was excavated out of mostly greenstone type rock. Chemical analyses [7] of rock composition have determined the average density to be 2.93 g/cm^3. The radiation length is 25 g/cm^2 and $Z^2/A = 6.0$.

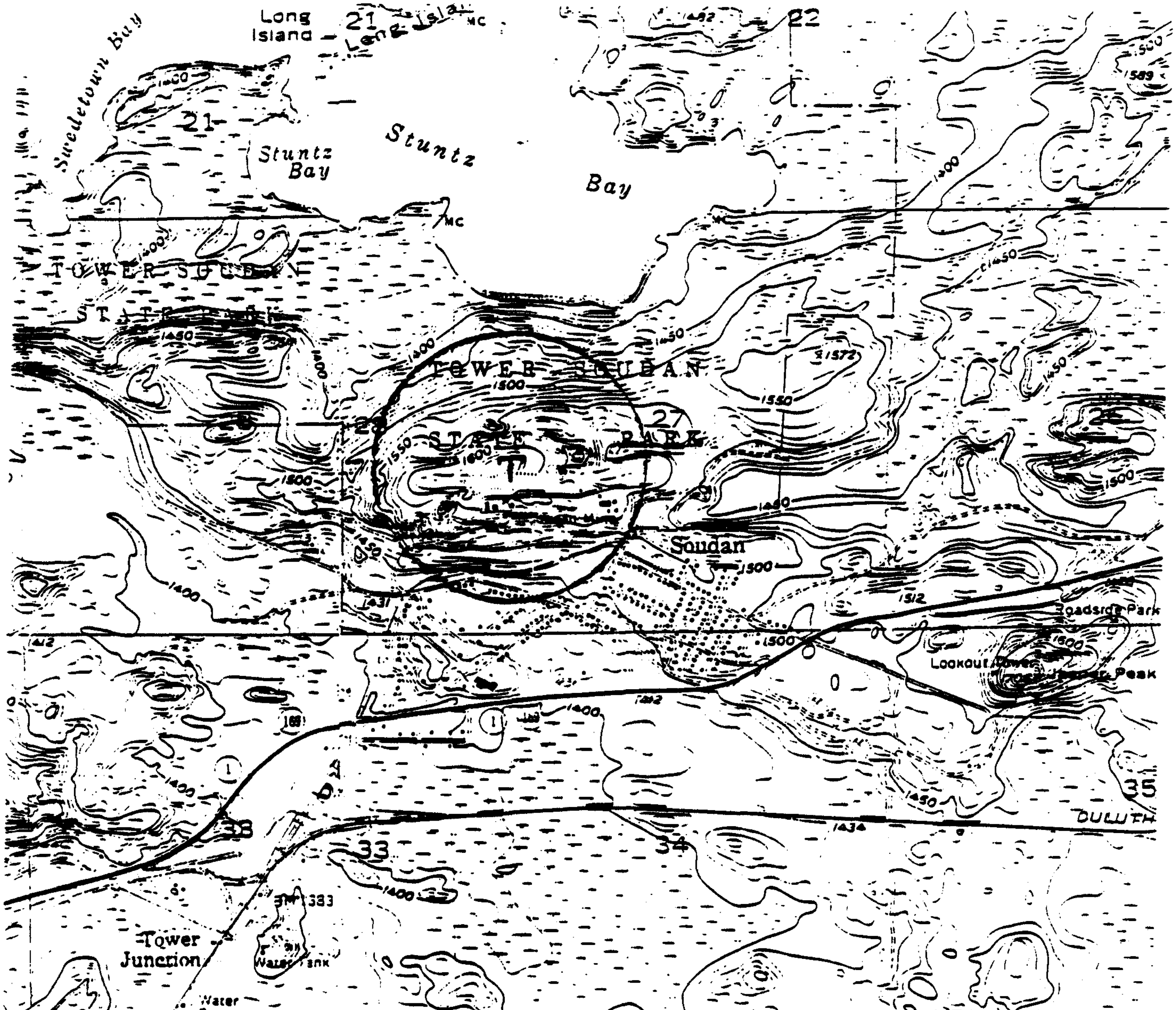

Fig. 2-9. Topology of the Soudan Mine Site. The Tracker is located at 'T' in the figure. It lies just below a hill that slopes off rapidly to the north and south. A 40 m-wide ridge that runs along an east-west axis is seen. The variation in the amount of overburden traversed by muons penetrating to the underground lab must be corrected for (see Chapter 3). The acceptance limit of the Tracker is approximated by the circle drawn.

The experiment was set up in the Tower-Soudan State Park on the bottom level of the Soudan mine (level 27). The coordinates of the park are 92.2° west longitude and 47.8° north latitude. The depth at level 27 is 715 m below the surface or 2100 mwe. A private contractor was hired to excavate a cavity ($72 \times 14 \times 11\ m^3$) for the Soudan 2 Nucleon Decay Experiment between 1984 and 1985. The first testing of veto shield modules took place in December of 1985 when measurements of the local singles rate due to radioactivity were carried out [8]. During the following year, steel to support the main detector and crane structure was fabricated, delivered to the site and installed. The Tracker muon telescope was installed below the main detector support structure and above the crane support structure.

Geometry

To set up a coordinate system for muon tracking, it was necessary to determine two orthogonal directions in the cavity. The vertical direction was determined by simply hanging a plumb bob over the 10 m separation between the upper and lower layers.[2] Then, modules in both layers could be referenced to a coordinate system origin and hence to each other. The coordinate system for the experiment has $\hat{x}$ in the west direction, $\hat{y}$ in the zenith direction and $\hat{z}$ in the north direction. The origin, marked on a steel beam that supports the central calorimeter, is located about 1 m above L1, close to the center of the overlap area for the bottom plane. The direction of north in the cavity was determined using a gyroscopic surveying theodolite [9]. The direction of the north-south axis of the steel is $9' \pm 1.5'$ west of true north. The coordinates of a single point on each of the four layers was determined relative to this origin. Next, the relative locations of all modules within a layer was determined with respect to that single point. The error for each of these

---

[2] This procedure assumes that the local gravitational field points toward the center of the Earth.

measurements is $\pm\sqrt{2}\cdot(1/16)''$. (The error in the angular resolution of the detector will be described in Chapter 4.)

2.4 The Electronics System

The electronics system for the Tracker is comprised of several parts: a ground scheme, low voltage and high voltage power distribution mechanisms, a means for distributing test signals and a means for reading out the data. A separate system to monitor and control the Oxford gas recirculation and purification unit is noted but will not be discussed here.

The readout system is depicted in Fig. 2-10. The front end of the readout system consists of digital output preamp cards. One card services the two channels on each proportional tube module in the Tracker. All of the backend electronics are CAMAC designed and include digital readout modules, a trigger module, a pulser module and a WWVB clock interface module. Detailed descriptions of the trigger and pulser can be found in Appendix B. A general description of the role of each is presented below.

The Ground Plan

Proper grounding is critical in systems (such as this one) which measure small signals. For that reason, two separate grounds are supplied at the experimental site. One is a power ground supplied for normal use (power hand tools, large equipment such as the overhead crane, pumps, welding stations, *etc.*) and the other is a quiet power ground reserved for use by electronics systems. The quiet power ground and the normal power ground are kept separate near the experiment, but both are tied together under the counting house and then run out to the rails in the shaft used to carry the hoist. The rails extend down the shaft into the Earth and are submerged in a variable amount (5-20 ft) of water providing the ground for the Soudan 2 experimental laboratory. A measurement of the resistance between the two grounds yields 1-2 Ω, just the ohmic drop across the conductors which carry the two grounds back to their common point under the counting house. The main detector support

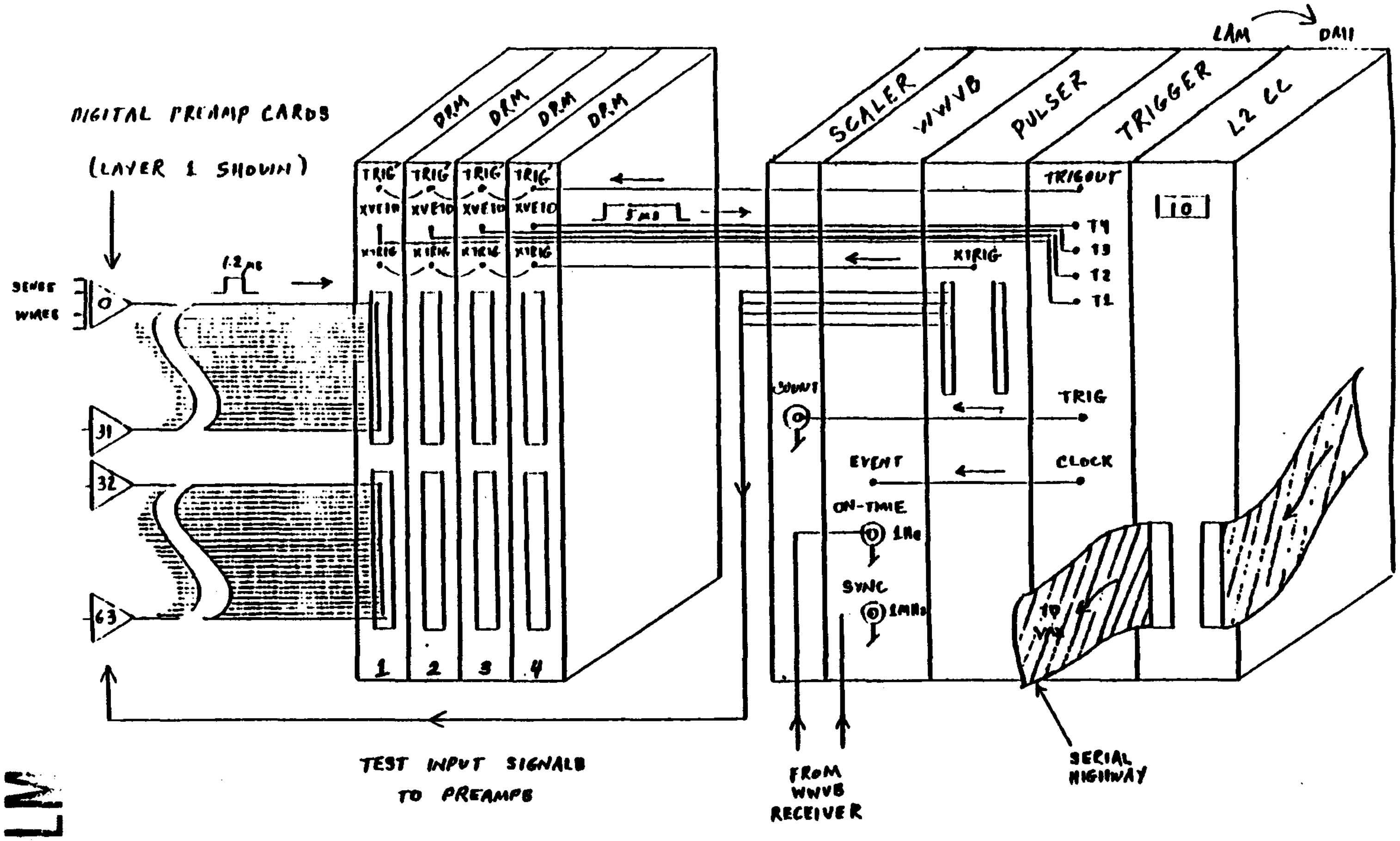

Fig. 2-10. Readout Electronics. Digital output cards monitor sense wires and send digital signals over twisted-pairs to a CAMAC crate up to 100 feet away. Readout modules in the crate sample the states of each channel at 1 MHz. When a coincidence (0·1 + 1·2 + ··· + 62·63) occurs between the upper and lower channels of a layer, the readout module that services that layer generates the trigger signal XVETO. The trigger signals from each readout module, designated T1–T4, are monitored by the trigger module. When the cosmic ray trigger requirement (T1·T2·T3) is met, the signal, TRIGOUT, is generated and used to trigger the readout modules.

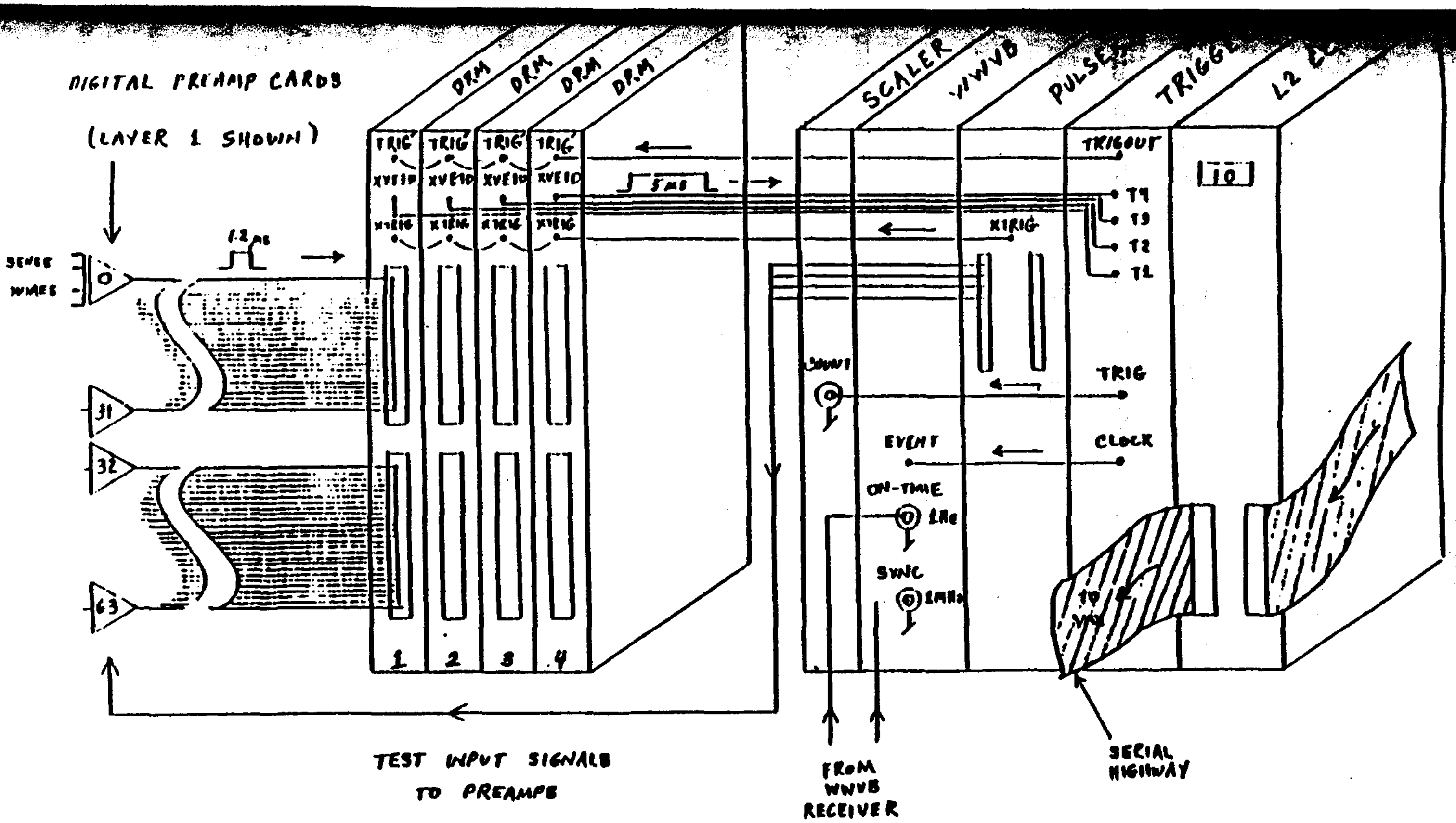

Fig. 2-10. Readout Electronics. Digital output cards monitor sense wires and send digital signals over twisted-pairs to a CAMAC crate up to 100 feet away. Readout modules in the crate sample the states of each channel at 1 MHz. When a coincidence (0·1 + 1·2 + ··· + 62·63) occurs between the upper and lower channels of a layer, the readout module that services that layer generates the trigger signal XVETO. The trigger signals from each readout module, designated T1–T4, are monitored by the trigger module. When the cosmic ray trigger requirement (T1·T2·T3) is met, the signal, TRIGOUT, is generated and used to trigger the readout modules.

structure and the crane support structure are both kept at the normal power ground. Since the signal ground of the Tracker is the aluminum modules themselves, it is necessary to provide insulation between steel and aluminum. This separation was carried out for all sections of the shield in operation. A cross between the two grounds at any point ruins the quiet ground not only for the active shield, but also for the entire experiment. The computer and serial highway used for data acquisition are kept on quiet power ground as well.

Low Voltage Power

Low voltage power must be provided to the digital output cards on the ends of each veto shield module. Five components are needed to carry this out: a +5 V power supply, a −7 V power supply, a cable with four conductors to carry power from control racks to repeater boxes near the modules, repeater boxes, and parallel bus cables to carry power from the repeater boxes to the preamps.

Two Accopian low voltage supplies were required: one provides +5 V to the digital circuits on the output card as well as to the amplifier, and the other provides −7 V to the amplifier at the front end of the card. To keep the noise level on the card down at a tolerable level, two separate +5 V supplies are provided to the cards. These are designated 5·T and 5·S. 5·T provides a power for the TTL circuitry (high current) and 5·S provides power for the amplifier (low current). At the relay rack the power and signal grounds are tied to the quiet power ground and 5·T = 5·S.

As a first check for proper operation of the shield units, one can simply measure the low voltage current draw since this is a well-defined and stable number (80 mA per output card at +5 V). Short circuits and improperly operating output cards are turned up rapidly using this procedure. Under these same conditions, one can then measure the singles rate with no applied voltage (zero) by randomly triggering the digital readout modules and reading them out. Channels which give spurious counts can then be repaired and replaced.

High Voltage Power

High voltage power is distributed using a Bertan positive high voltage supply, a coaxial cable to carry power from this supply to the repeater boxes and return the signal ground to the relay rack through its outer shield, repeater boxes (also used to distribute low voltage and test input signals), and a single cable to bus high voltage from the repeater boxes to each preamp card. A low impedance path for return of the signal current is provided by a ground strap which ties together all the modules in a layer and is connected to the outer conductor of the high voltage coaxial cable.

As a second check for proper operation of the shield, one can look at the current draw at high voltage. Modules sent to the mine for installation are first recertified by requiring them to pass the same quality control checks on site that are required before shipment. The current draw is measured at 2000 V (where leakage current dominates) and at 2500 V (where signals are seen due to radioactivity and cosmic rays). These currents have been measured for every module in the Tracker and are $\leq .01\ \mu$A at 2000 V and 0.10–0.20 μA at 2500 V. The average current draw for a section of 32 installed modules is $\sim 1.5\ \mu$A at 2500 V. Measurement of the singles rates at various voltages allows one to plateau the units and check operation once again. A plateau such as this is on radioactivity but the shape of the plateau curve will be similar to one done on cosmic rays and will allow one to observe the gross operation of the card and determine a plateau voltage (2450 V) and plateau width (90 V). (Plateau curves are presented in Chapter 4.)

Test Signal Distribution

Test input signals are generated by a CAMAC pulser module and are carried over twisted pair to repeater boxes near the modules. Line receiver/driver pairs located in these repeater boxes are used to repeat the test signal which is then bussed along a single twisted pair to all preamps in a layer.

The Veto Shield Pulser Module [12] was designed to provide a number of functions. When data collection was not in progress, it served as a diagnostic tool in readout module checkout. Also, it could send test signals to sections of modules in the Tracker thus providing an assessment of digital output card performance. During data taking, its use was more passive in that it simply held various voltage levels at well defined states.

During data collection, the pulser module was used to tie the test signal inputs on the digital output cards to their off state preventing spurious signals from mimicking a real event. A test input signal was provided for each section of 32 modules in the Tracker. A test signal register on the pulser was used to apply a level to each of the four test signal cables. This level is delivered to repeater boxes where the line receiver/driver pairs boost the signals along a bussed test signal input cable to the preamps. Another register was used to bus a set of control signals, ABORT, TRIG, XTRIG, and XVETO, to/from the digital readout modules. The ABORT signal was to be used when the complete active shield system was installed but was not crucial to Tracker operation. Nevertheless, because it is carried over a twisted pair line, it was necessary for the pulser to tie the line low to prevent undesirable results.

When the system was not collecting data, the pulser module could be used to access the state of the electronics. To test preamp operation, the pulser could strobe the test inputs on the preamp cards. In addition, one may vary the delay between the time this voltage is applied and the time that the digital readout modules are triggered. This feature allows one to test the ability of the readout modules to scan their 128 μs time buffers looking for a signal. In this way, a complete test of the installed electronics system could be achieved. In addition, the Pulser could be used to perform diagnostic tests on the digital readout modules directly. This was very useful in the (arduous) process of debugging the prototype readout modules. In this mode, a special set of cables was used to bus the test signals from the test register on the front of the pulser to an individual readout module hence bypassing the front end preamps. Signals of varying width and trigger delay can then be presented to the readout modules on register T0. This feature also allows one to test the veto shield trigger (XVETO) feature of the readout modules since one may generate in–time signals on adjacent channels.

Finally, the Pulser served in one other way as an integral part of this system. By providing an external trigger signal, XTRIG, to the digital readout modules, it was possible to trigger the electronics through software and thus make measurements of the singles rates due to natural radioactivity in the mine.

The Readout System

The Digital Output Card The role of the digital output card is threefold. First, the card must amplify the small ($\sim 0.5\ \mu$A) signals generated by avalanches at the anode wires of the proportional tubes. Second, the amplified signals are discriminated with a threshold level set at 0.1 V. Third, for signals above threshold the card must transmit a digital signal to a readout module up to 100 feet away.

One channel of an output card is shown in Fig. 2-11. The amplifier at the front end of the card was designed by Peter Shields of Oxford University. The amplifier uses feedback to stabilize the current gain and to achieve low input impedance.[3] The input to the preamp is ac–coupled to the anode wires which are at high voltage and to the test input point on the card. The amplifier converts a current pulse from the wires into a voltage pulse. The gain is set by resistor values to 190 mV/μA. The threshold at the comparator is set at 100

---

[3] See the Art of Electronics by Horowitz and Hill [10] for a discussion of high–speed/high–frequency amplifiers.

mV and hysteresis is provided by the resistor in its feedback loop. The multivibrator has an RC circuit set to provide a 1.1 μs pulse at the output when a pulse above threshold is detected. The output of the multivibrator is transformed into a pulse capable of driving a 100 Ω twisted pair by a differential line driver.

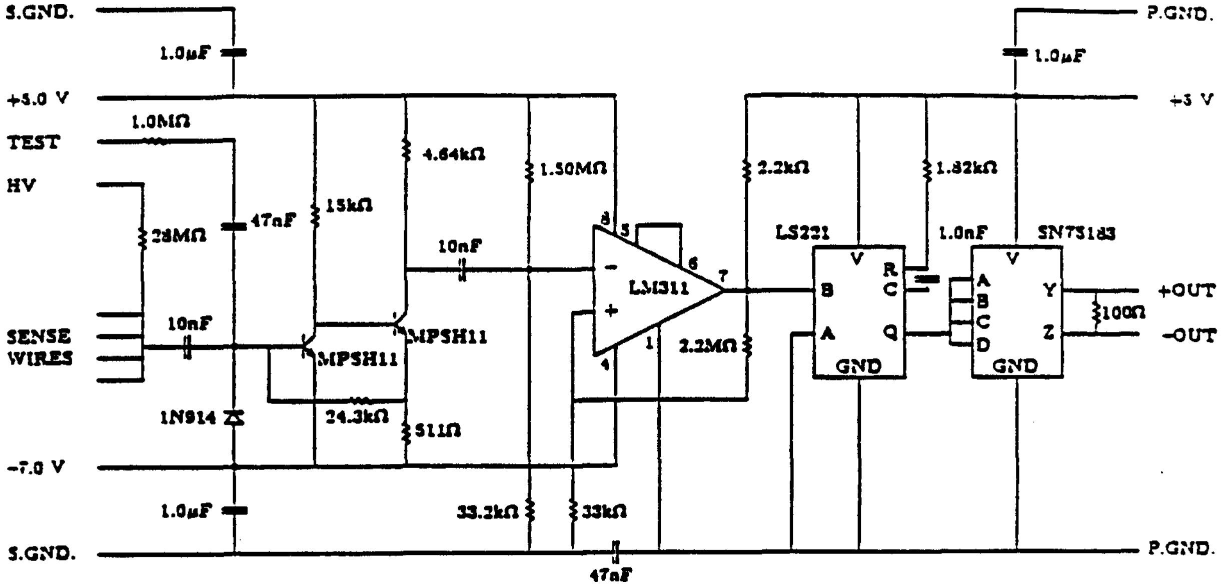

Fig. 2-11. One Channel of a Digital Output Card.. The two-transistor (MPSH11) amplifier at the front end converts a current pulse on the anode wire to a voltage signal with the gain set by resistor values. A comparator (LM311) checks to see if the signal surpasses a preset threshold and then fires a multivibrator (LS221) that generates a 1.1 μs-wide pulse. A line driver (SN75183) sends the pulse over twisted pair to a readout module.

Early attempts at preamp design suffered from lack of sufficient isolation of the low-current signal ground and the high-current TTL ground. Separate ground planes with appropriate ac-coupling between them allowed for good signal structure without oscillation problems caused by feedback from the TTL circuitry to the preamp input.

The Veto Shield Readout Module Each layer of the Tracker was serviced by its own Veto Shield Readout Module [11]. Readout modules operate in one of three states: Sample-and-Store, Data Scan, and CAMAC Readout. In the Sample-and-Store state, the digital readout module restores the differential line signals sent out from 32 digital output cards (64 channels) in a layer to TTL levels, samples the state of each channel at 1 MHz and stores the information in a buffer. The state of each channel is stored in a 128–element delay line. When triggered, the readout modules enter the Data Scan state and begin compactification of the data, looking for hit channels within the 128 μs time window preceding the trigger. Data compactification takes $\sim$ 1 ms at which time the module sets its LAM indicating it is ready for CAMAC readout.

The special feature of the readout modules relevant to the operation of the Tracker was the ability to generate the veto shield trigger signal, XVETO. XVETO is generated whenever a coincidence is detected in a set of two adjacent channels in a layer: $0 \cdot 1 + 1 \cdot 2 + \ldots + 62 \cdot 63$. A set of programmable array logic chips on the readout modules monitors the states of all channels looking for this coincidence.

Five prototype readout modules were acquired from a commercial vendor. Much diagnostic work went into preparing these modules for use in the experiment. The Veto Shield Pulser Module greatly simplified this work.

The Tracker Trigger Module The Tracker Trigger [13] is a CAMAC module used to form a coincidence between any or all of the four layers in the system (see Figs. 2-10 and 2-12). When a coincidence occurs between adjacent channels of a particular Tracker layer, the corresponding readout module servicing that layer generates a 5 μs–wide XVETO signal. The XVETO signals from layers L1 through L4 are referred to as T1 through T4 respectively. These signals, T1–T4, one from each of the readout modules, were carried over twisted pair to the front of the trigger module. There, their levels were restored to TTL and used to form the trigger for the experiment. The trigger requirement was formed using a set of switches (S1–S4 in the figure) under software control. By requiring a logical OR between a switch and the corresponding trigger signal, one may remove a layer from the trigger requirement by turning that switch *on*. When coincident triggers were enabled

(ENCT true) and the preset coincidence requirement met, an internal signal, TRIG, was generated. This signal, not under computer control, provided a means of scaling the total trigger count. TRIG was fanned out first to a lemo connector on the front panel of the module and then to a JK flip–flop which could be enabled/disabled using another switch (ENTR) under computer control. A CAMAC scaler module was used to count TRIG and hence provide a means of measuring the experimental deadtime created when data was ready and waiting to be read out by the VAX. The latched signal, under computer control, provided a number of functions. First, a multivibrator circuit was used to provide a 110 μs-wide signal at the front panel of the module to be sent by twisted pair to each of the readout modules (this signal is called TRIG in the sections on the readout module and the pulser module). The falling edge of this signal provided the trigger for the experiment. Second, a prompt trigger signal was sent directly to the WWVB CAMAC Interface Module in order to latch the WWVB clock time at the earliest possible moment. Third, the latched trigger signal set the LAM line for the module. The trigger module LAM line is the only one that was strapped to the DMI (Demand Initiate) line on the back of the Jorway L2 crate controller. When it was set, a demand was sent out on the serial highway to inform the the VAX that a trigger had just occurred.[4] After readout of the data, the trigger module LAM line was reset ($\overline{\text{LRST}}$) in order to allow further triggers to interrupt the VAX.

Another important feature of the module is its status register, TTSR. At begin-run time and for each event, this register was used to record the current settings of the trigger requirement in the data files. This proved to be very useful in later analysis since runs and triggers not satisfying a cosmic ray type trigger could quickly be barred from further analysis.

---

[4] In this case, the experiment was interrupt driven. A program could however simply monitor the state of the trigger module LAM line to determine when a trigger had occurred.

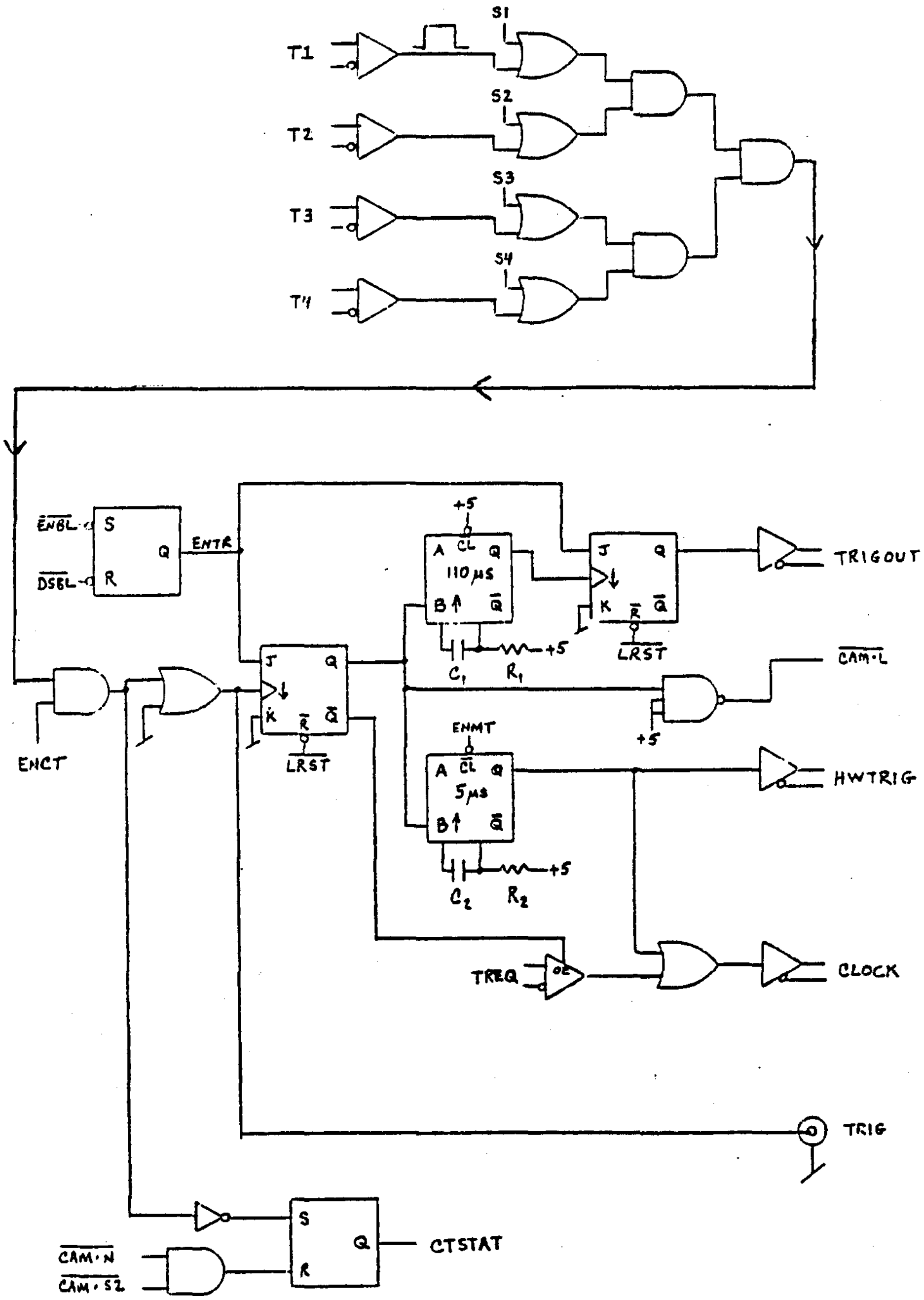

Fig. 2-12. The Tracker Trigger Module. A simplified schematic describes the basic functions of the module. Trigger signals T1–T4 from the readout modules and corresponding software switches S1–S4 are logically ORed setting the trigger requirement. When the requirement is met, the signals TRIG and TRIGOUT are generated. TRIG, not under computer control, is used to increment a counter and hence provide a determination of the deadtime during a run. TRIGOUT is used to trigger the readout modules.

Finally, we note that the trigger module was used in ways other than as a cosmic ray muon trigger. Since the coincidence level could be set through software, it was possible to require any number of layers in the trigger and hence change the trigger rate. Trigger rates faster than the muon rate were useful in both software and hardware development for the on-line system.

The WWVB Clock and CAMAC Interface The WWVB Clock Receiver is a Spectracom Corp., Model 8170 synchronized clock [14]. It is used to measure the Universal Coordinated Time (UTC) of events by monitoring the WWVB time signal. This signal, carried over a 60 kHz carrier frequency, is generated in Fort Collins, Colorado, received by an antenna mounted on the surface at the site, and transmitted down the half-mile mine shaft on coaxial cable. The signal contains time of day information to be decoded by the clock receiver and a 1 Hz on-time pulse used for synchronization. Binary coded data, containing the time of day information, is formed and placed on a back panel parallel port. The binary formatted data, the 1 Hz on-time pulse and the 1 MHz clock signal are all provided to the WWVB CAMAC Interface module [15]. Each second, the on–time pulse latches the coded data from the clock into a set of flip–flops. When an event trigger signal (TRIGOUT) is received at the front panel of the WWVB CAMAC Interface, the WWVB time is stored by strobing the latched time into a second set of flip–flops. This time is then available to be read out through CAMAC. The interface also provides a software trigger to strobe the time, allowing for daily synchronization of the VAX and WWVB times. Accurate measurement of the time is crucial in muon astronomy since astronomical sources, such as pulsars, may have periods on the order of a millisecond. The accuracy of the Spectracom Model 8170 Clock Receiver is ±1 ms.

2.5 The Gas System

It is desired to operate the shield under known stable conditions to reduce the number of experimental uncertainties. The operating characteristics of proportional counters depend on gas pressure, temperature, concentration and purity as well as on the geometry involved and the choice of the gas filling. In a mine environment it is easy to control the ambient temperature. Pressure, purity and concentration are more difficult to control. Small changes in gas purity, for example, can cause drastic changes in performance by affecting the amplification process. The gas system must therefore be designed to minimize any changes in these operational characteristics. In order to ensure that the demands placed upon the shield are met, it must:

- provide a high purity gas *mixture* to the individual units of the shield;
- maintain a fixed absolute pressure independent of changes in the local ambient pressure;
- monitor the purity and pressure of the system and effect changes when necessary;
- remove impurities which diffuse into the system;
- ensure a uniform gas mixture throughout the gas volume;
- operate continuously over a long period of time;
- provide these objectives at a reasonable cost.

The main components of the gas system are: a supply of pure Ar, a supply of (premixed on site) 85–15 Ar–CO_2, a gas mixing unit, a recirculation and purification unit, restrictors, the shield modules themselves, and a volume of hose, used to connect all the pieces. The gas mixer uses a simple set of pressure gauges to control the flow of each of the supplies thereby adjusting the mixture to achieve the 95–5 mix desired. The rest of the system is essentially a closed loop.

The recirculation and purification unit performs a number of vital functions. The pressure is maintained at an absolute level of 1.12 bar, approximately 4 % above the average ambient pressure in the laboratory. A recirculation pump is used to move gas through the system ensuring a uniform mix. The flow is regulated by small restrictors which take almost all of the pressure drop across the input and output manifolds of the recirculation unit. This minimizes the static pressure drop across the individual shield modules, thus maintaining a uniform gain along the length of the anode wires. Gas purity is maintained by removal from the system of electronegative molecules such as oxygen. Oxygen is removed by combining it with small amounts of hydrogen and filtering the product (water). The content of O_2 and CO_2 in the system is monitored daily.

Our system used a 95–5 mixture of Ar–CO_2, the CO_2 being used as a 'quenching' agent that changes the drift properties of electrons. The electrons are slowed down in this way in order to avoid what is known as the Ramsauer effect–a condition in which the electron's wavelength approaches that of the electron shells of the molecules in the gas. Under those circumstances, quantum–mechanical processes take place that can cause ultraviolet emission. If this secondary radiation exceeds the work function of the material of which the counter is built (Al), more electrons can be created via the photoelectric effect and after–pulsing will occur. The amount of quenching agent must be chosen carefully since too much will increase the average drift time to the wire and hence change the desired properties.

2.6 The Online Data Acquisition System

The readout electronics for the Tracker are CAMAC based. A serial CAMAC highway was used that allowed the readout of up to 64 crates on a single highway controller. A Jorway Model 411 PDP 11 CAMAC Interface was used to facilitate communications between the serial highway and the host computer, a Digital Equipment Corporation VAX 11/750 running under VMS. Jorway Model L2 Serial Crate Controllers were used to control each of the crates on the highway.

The software used to execute CAMAC instructions at any address on the highway is called MIDAS (Multi–user Interactive Data Acquisition System) [16]. It is a set of

VAX/VMS utilities developed at Argonne National Laboratory that interprets CAMAC instructions and sends the appropriate commands to the 411 branch driver for execution. The utilities may be linked to a user–written Fortran program which specifies a list of instructions to be executed at begin-run time, at event time and at end-run time. The executable image then becomes a separate program allowed to run with other programs that access the CAMAC system at the same time. All communications between the highway and the computer are monitored with a separate program, DAQ, that polls the highway waiting for demands and then issues the appropriate instructions generated by the routines that service those demands. DAQ, running at a higher priority than all other processes that access the highway, distinguishes the priority of each of those processes and places demands generated by them in a stack. When time permits, each demand on the stack is (priority) serviced by its own routine.

During the course of data collection, the Tracker process ran at a priority lower than that of the Soudan 2 experiment (but higher than the priority set for interactive users of the system). Two different sets of Fortran routines were used to collect data during this period. The first program continually monitored the LAM status word of the L2 controller for the Tracker crate. A set of instructions to read out the data was executed when the Tracker Trigger Module set its LAM. After readout, the digital readout modules were set back to their sample–and–store state and the LAM in the trigger module was reset. The instructions were issued as a set of calls to a Fortran subroutine in the MIDAS package that executed appropriate FNAC (function, station, sub–address, crate) commands. The second program was slightly different from the first in that no polling of the L2 LAM status word was done. Instead, when a trigger occurred, the trigger module LAM line (strapped to the L2 DMI line) was set, causing a demand (DMI) to be initiated on the highway. DAQ, monitoring the highway, then placed a demand on the stack which was later serviced by a list of CAMAC instructions specified in a command file. The only essential difference between the two programs was that the interrupt driven one had a smaller dead time associated with it (1 % *vs.* 1.5 %). For both programs, the format of the data files written to disk was the same in order to facilitate later analysis. The data file format was very compact (typically 100 bytes/trigger) so that disk storage was not a problem. Testing and other system startup problems made it necessary to run the former program from time to time.

Measurement of the total livetime for the experiment was carried out by noting the begin-run time (when the detector became active) and the time for the last trigger taken during the run. A scaler, not under computer control, was incremented each time a trigger occurred. The ratio of the number of triggers recorded by the detector under computer control to the number of triggers recorded by the scaler determines the deadtime. The time accumulated between the time the run began and the time of the last trigger in the run determines the total livetime for the run. By summing over all the runs, we calculate the total livetime of the experiment to be 0.50 years representing an ontime duty cycle of 75 % over the course of eight months. The livetime includes the deadtime caused by computer control. The average deadtime during runs for the experiment was measured to be 1.2 %. The scaler was not always available at the end of a run because of computer crashes, power outages and other inconveniences.

Chapter 2 References

[1] Oliver, W. P., *et al.*, *A Rugged 1700* m^2 *Proportional Tube Array Nuclear Instruments and Methods* 276, A (1989).

[2] Sauli, F., 'Principles of Operation of Multiwire Proportional and Drift Chambers', CERN preprint 77–09 May, 1977.

[3] Stabalohm 800 wire manufactured by the California Fine Wire Co, Grover City, CA.

[4] NORYL resin (^{TM}General Electric Co.) by Mikros Engineering Co., Minneapolis, MN.

[5] TRA-BOND #BC-2133, Tracon Inc., Medford, MA.

[6] Tower Soudan the State Park Down Under, Minnesota Parks Foundation (1976).

[7] Ruddick, K., 'Radioactivity in the Soudan', PDK-114, March, 1984 and 'Multiple Scattering of Underground Muons', PDK-201, May, 1985.

[8] Kochocki, J. A., *et al.*, 'Testing of the First 126 Veto Shield Modules at Soudan', PDK-247, January, 1986.

[9] H. Courant (Univ. of Minnesota) and the U. S. Forest Service, private communication, July, 1987.

[10] Horowitz P. and Hill W., The Art of Electronics Cambridge University Press, (1980).

[11] Oliver, W. P., 'Veto Shield Readout Module', PDK-289, August, 1986.

[12] Kochocki, J. A., 'Veto Shield Pulser', PDK-315, March, 1987.

[13] Kochocki, J. A. and Oliver, W. P., 'The Tracker Trigger', PDK-314, January, 1987.

[14] Spectracom Corporation, Model 8170 WWVB Synchronized Clock.

[15] Oliver, W. P., 'WWVB CAMAC Interface', PDK-322 (1987).

[16] Schlereth, J., 'MIDAS - A Multi-user Interactive Data Acquisition System', PDK-209, June, 1985.

CHAPTER 3. MONTE CARLO DETECTOR SIMULATION

To obtain the results presented in the following chapters, it is necessary to model the geometry and location of the Tracker and thereby determine its acceptance for penetrating muons. A Monte Carlo program has been developed to perform the acceptance calculation. In addition to the acceptance correction, underground experiments which study interactions that (presumably) occur above the surface of the Earth must correct for effects caused by differences in the rock overburden for the various trajectories within the acceptance. The Monte Carlo program treats each of these problems so that a comparison with results from other experiments and theory can be made. Results from the single muon Monte Carlo program will be used to calculate both the vertical muon flux at the site and the excess muon flux from the Cyg X–3 direction. Data is compared to the model in Chapter 4.

3.1 Overburden

The topology of the surface at the mine site was given in Fig. 2-9. The detector is located at the position marked 'T', directly below a hill which slopes off rapidly to the north and south and less rapidly toward the east and west. The acceptance limit of the Tracker is indicated as a circle with radius $\sim$ 1700 feet on the surface. The amount of overburden as a function of zenith angle, θ, and azimuthal angle[1], φ, has been determined by subdividing the contour plot into 100 ft × 100 ft squares and estimating the average height above the detector in each bin.[2] The variation in the amount of overburden as a function of θ and φ is shown in Fig. 3-1 for various cutoffs in θ. The vertical scale indicates the amount of overburden above the detector. A cutoff was imposed on the overburden data at $\theta > 85°$; in any case, only the overburden for $\theta < 45°$ is applicable here.

---

[1] Here, φ is a local coordinate system azimuthal angle that increases from west to north.

[2] The overburden was first calculated for the Soudan 1 detector by K. Ruddick [1]. His overburden data and the translation vector between the Tracker origin and the Soudan 1 detector was used to calculate the overburden at level 27 of the Soudan mine. The translation vector is given by ($-6\,\hat{x}$, $123\,\hat{y}$, $66\,\hat{z}$ m).

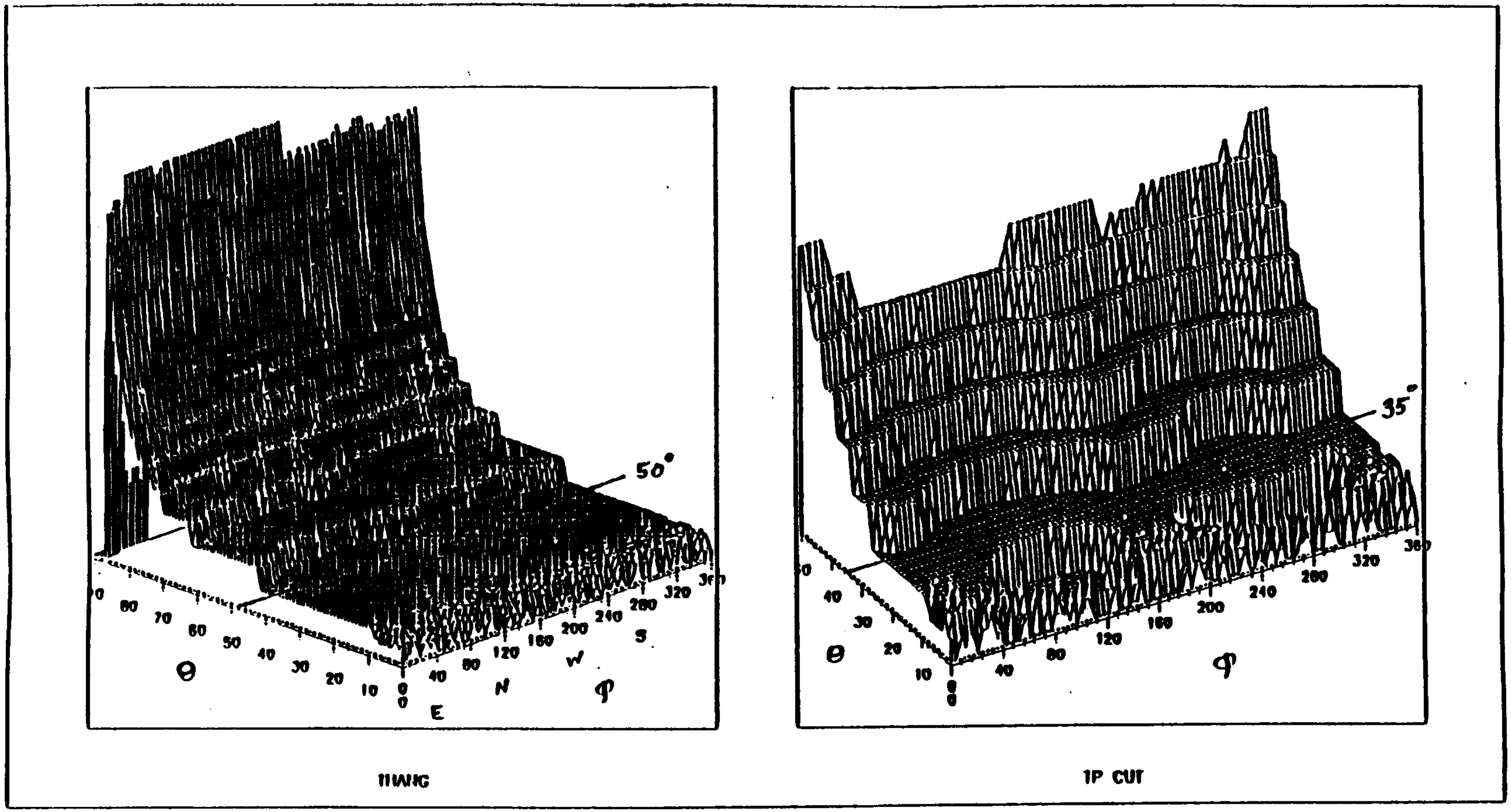

HANG

IP CUT

Fig. 3-1. Overburden. The amount of overburden as a function of local coordinates θ, the zenith angle, and ϕ, an azimuthal angle. Acceptance in the Tracker is limited to $\theta < 45°$.

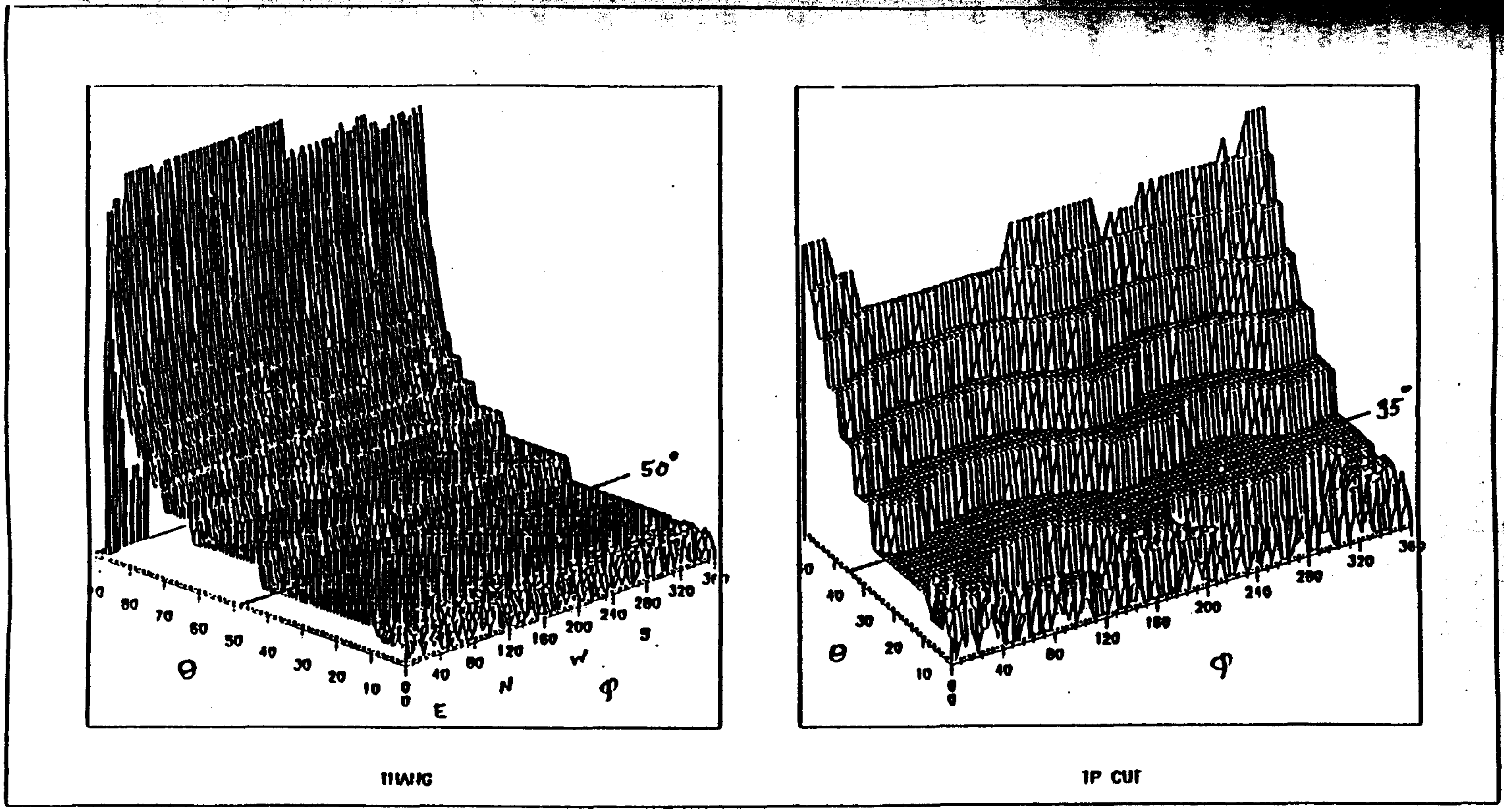

HANG

IP CUT

Fig. 3-1. Overburden. The amount of overburden as a function of local coordinates θ, the zenith angle, and ϕ, an azimuthal angle. Acceptance in the Tracker is limited to $\theta < 45°$.

To use this information, a lookup table is made of the amount of overburden as a function of $\cos\theta$ and φ. Then, the overburden can be determined for muons tracked through all layers at any angles. Each muon has its $\cos\theta$ and φ bin inversely weighted by an amount that depends on the threshold energy of a muon to pass through the amount of overburden at these angles. Calculation of this threshold energy included the effects of ionization, pair production and bremsstrahlung losses in the rock overburden [2, 3]. The rock composition above the Tracker is taken to be the same as that above Soudan 1. Then, the rate of energy loss in $TeV/(g/cm^2)$ of a muon with energy E_μ, as a function of slant depth y, is given by:

$$-\frac{dE_\mu}{dy} = a + bE_\mu \tag{3.1}$$

with

$$a = 2.5 \times 10^{-6} TeV\ cm^2 g^{-1}, \tag{3.2}$$

$$b = 4.0 \times 10^{-6}\ cm^2 g^{-1}, \tag{3.3}$$

and the slant depth, y, given by

$$y = \rho D \sec\theta. \tag{3.4}$$

The average rock density is $\rho = 2.93\ g/cm^3$ and the detector is at a vertical depth $D = 715\ m$. This equation can be integrated over the distance from the surface to the detector at slant depth y to yield the threshold energy for a muon to penetrate to the depth:

$$E_t(y) = \frac{a}{b}\left(e^{by} - 1\right). \tag{3.5}$$

The slant depth is looked up for each value of $\cos\theta$, E_t is calculated and used to determine the statistical weight of the muon.

3.2 Single Muon Simulation

A simple form has been chosen to describe the angular distribution of single muons at the detector. The number of muons, N_μ, at zenith angle, θ, is given by:

$$\frac{dN_\mu}{d(\cos\theta)} \propto \cos^n \theta. \tag{3.6}$$

The value of n, was adjusted to fit the data. This model does not explicitly include phenomena such as muon energy loss in the rock overburden or the spectrum of the primary cosmic ray flux at the surface. Instead, the severe limitation in zenith angle acceptance ($\theta \leq 45°$) has prompted us to try a simple power law spectrum for comparison with the data.

Distributions were generated for $n = 1$, $n = 2$ and $n = 3$. First, a value for $\cos\theta$ is generated. Muons with $\theta > 45°$ are counted and rejected. The muon is required to pass through a $10 \times 10\ m^2$ plane above the Tracker. The plane is centered on the Tracker origin and is large enough and close enough to layer L4 so that all muons which may trigger the detector must pass through it. The ratio of the number of muons triggering the detector, to the number passing through this plane, will be used later to determine the flux of muons through the Tracker. An azimuthal angle, φ, is randomly generated between 0 and 2π. A unit vector in the direction of the muon is constructed and the muon is tracked through each layer of the detector. The tracking procedure checks the location of the muon at the central height of each channel in each layer. If the muon passes within half a channel width (nominal 18.16 cm) of the center of a channel the tracking algorithm registers a hit for that channel. It will be recalled from Chapter 2 that the usual cosmic ray trigger required that three of the four layers in the Tracker record coincident adjacent channel hits ($0{\cdot}1 + 1{\cdot}2 + \cdots + 62{\cdot}63$), *i.e.*, T1·T2·T3.[3] The same trigger requirement is imposed on muons

---

[3] Requiring all four layers in the trigger would have lowered the rate by $\sim$ 15 %. Since part of the effort was to illuminate the central calorimeter with muons, only three layers were required in the on-line trigger.

generated in the Monte Carlo and those which satisfy it are counted. Next, muons which satisfy the off-line trigger requirement, at least one channel hit in layer L4, are counted.

As just described, this Monte Carlo model does not take into account several factors. Channels do not have an infinitesimally thin height and they do not all have the same nominal width, though these are reasonable approximations. More importantly, real channels are not 100 % efficient at detecting radiation. The efficiency of a row of cells within a layer was measured in the 16 module test array (previously described) and found to be ~ 0.972. The inferred efficiency for detection of a coincidence between upper and lower rows within a layer was then estimated at 0.946. In the Monte Carlo model, muons which pass through the crack regions within a layer are counted but do not contribute to the on-line trigger count, $T1 \cdot T2 \cdot T3$. Therefore, it would be incorrect to use 0.946 as the efficiency of a layer for detection of a coincidence. The appropriate efficiency to use here is the one measured in the cosmic ray telescope (see Fig. 2-6). It will be recalled that the efficiency for detection of a coincidence is 0.970 ± 0.002 when tracks are not allowed to pass through the crack regions within a layer. Since there are three layers involved in forming the on-line trigger, calculation of the muon flux from the observed muon rate, using results from this Monte Carlo model, will have to be scaled by a factor $(0.970)^{-3}$. The off-line trigger requirement is a hit channel in either row of layer L4. Since the efficiency to detect a hit in either the upper OR the lower rows of a layer was measured to be ≥ 0.998, the efficiency of layer L4 will be taken to be 1.0 in the model.

3.3 Cyg X–3 Flux Monte Carlo

A separate Monte Carlo program was also developed to perform the acceptance correction for muons which arrive from the Cyg X–3 direction.[4] A muon is generated with a random Cyg X–3 hour angle, h, and a fixed declination, $\delta = 40.9°$. Remembering that the

---

[4] See Appendix C for a thorough description of the astronomical terms used here.

lab is at north latitude, $\phi = 47.7°$, and west longitude, $\lambda = 92.2°$, we can then calculate the altitude, a, and the azimuth, A for the muon. The transformation equations, symmetric under $(a, A) \rightleftharpoons (\delta, h)$, are given by:

$$\cos\delta \sin h = -\cos a \sin A \tag{3.7}$$

$$\sin\delta = \sin a \sin\phi + \cos a \cos A \cos\phi \tag{3.8}$$

$$\cos\delta \cos h = \sin a \cos\phi - \cos a \cos A \sin\phi. \tag{3.9}$$

A unit vector in the direction of the muon is formed and the muon is required to pass through the same 100 m^2 plane used in the vertical flux calculation. The tracking algorithm described above is again used to determine which channels the muon passed through, if any. If the on-line and off-line trigger requirements are met, the hour angle of the muon, weighted by $\cos\theta$, is recorded. This weighting is done to correct the solid angle subtended by the horizontal plane to the solid angle subtended by a plane with the same area but normal to the Cyg X–3 direction. The ratio of the weighted number of muons that are tracked through the detector, to the number of muons generated, will be used to scale the observed rate (s^{-1}) of muons from the Cyg X–3 direction and hence determine a flux ($cm^{-2}s^{-1}$). Results of this Monte Carlo calculation will be presented in Chapter 5 where the excess muon flux from the Cyg X–3 direction will be determined.

3.4 Multiple Muon Simulation

Multiple muon events are characterized by the number of muons in the event, M_μ, and the average distance, $\langle r \rangle$, of muons from the core of the event. The core of the event is defined by the trajectory of the primary particle just before it interacts. Distances from the event core are measured in the plane perpendicular to this line and depend on the depth of the observation site. Underground measurements of muon multiplicity and lateral displacement are important because they shed light on the energy and composition of the primary involved in the atmospheric interaction. Determination of values of M_μ and $\langle r\rangle$ from Tracker data requires a Monte Carlo model of multiple muon events in the detector. Parameterizations of the average number of muons in events and the lateral distribution of multiple muons have been derived and compared with data from other experiments at different depths [4].

A Monte Carlo program was written to determine the Tracker acceptance for two-muon ($M_\mu = 2$) events, the most prevalent type of multiple muon event in the data. Two muons are generated in the calculation. The first muon is generated with differential spectrum $dN/d(\cos\theta) \propto \cos^2\theta$. The second muon is generated with a random azimuthal angle relative to the first and parallel to the first. In the model, no information is known about the average distance of muons from the core of the event. Rather, the average separation, $\bar{s}$, between muons is studied for two cases.

i) The number of two-muon events with average separation $\bar{s}$, was chosen to be random between 0 and 10 m:

$$\frac{dM_\mu^{(2)}}{ds} = R \cdot 10\ m\ ;\ R \in [0,1]. \tag{3.10}$$

ii) The number of two-muon events with average separation $\bar{s}$, was chosen to be inversely proportional to s:

$$\frac{dM_\mu^{(2)}}{ds} = \frac{R \cdot 10\ m}{s}\ ;\ R \in [0,1]. \tag{3.11}$$

Both muons were required to pass through the 100 m^2 plane above the detector. The same tracking algorithm used in the Monte Carlo for single muons was applied here as well. All events were counted. If the first track satisfied the on-line trigger requirement, the second one was tracked to see if it, too, would have been detected. For those events in which both tracks passed through all four layers, a data file was written containing all of the hit channels in the event. This data file was then read by a program that made use of the same off-line filter used to scan the data. Tracks were reconstructed using the same cuts for parallelism that were applied on the data (see Chapter 4).

Chapter 3 References

[1] Ruddick, K., program TERCALC – private communications.
[2] Ruddick, K., 'On the Origin of the Species Multiple Muon', PDK–32, May, 1982.
[3] Ruddick, K., 'Multiple Scattering of Underground Muons', PDK–201, May, 1985.
[4] Gaisser, T. K. and Stanev, T., 'The Physics of Multiple Muons in Underground Detectors', *Proceedings of the Workshop on Very High Energy Cosmic Ray Interactions*, University of Pennsylvania, April, 1982.

CHAPTER 4. PHYSICS OBSERVATIONS WITH THE TRACKER

Chapter 4 is a survey of general muon physics results obtained with the Tracker. We begin by considering natural radioactivity, a source of background to the detected muon signal. Background rates and plateau curves will be shown and accidental rates in the muon trigger calculated. Next is a description of the off-line filter used in the analysis. This is a two step filter in which triggers first had to pass a strict set of cuts before being allowed to enter the pattern recognition and track fitting algorithms. As a consequence of these requirements, the definition of a muon in the experiment will be made evident. Muon events are categorized according to their multiplicity and directional certainty. The features of the single and multiple muon data samples selected for Cyg X–3 analysis will be described and compared to the Monte Carlo models in Chapter 3. An analysis of multiple muon events will be done in order to determine the overall angular resolution of the detector. Upper and lower limits for the vertical muon flux at 2100 mwe will be set. An examination of the muon rate will be conducted to search for any day–night or seasonal variation in the muon rate.

4.1 The Background to Through–going Muons

Natural Radioactivity

Natural radioactivity in the Soudan mine has been extensively studied [1–4]. Predictions have been made and compared to actual measurements of natural radioactivity in order to estimate the amount of background expected in the nucleon decay experiment. Some of the relevant findings of these studies will be highlighted here for comparison with rates found in the Tracker.

The most prevalent forms of natural radioactivity in the mine come from photons generated by decays in the U^{238} and Th^{232} chains, and from K^{40} decay. The photons produce electrons mainly by Compton scattering and the photoelectric effect. These processes take place in rock, or in the materials (*e.g.*, aluminum) which make up the detector. Also present is Rn^{222} gas. This is created in the rock walls and may diffuse into the lab directly or be absorbed in water which then leaks into the cavity. Its concentration is sensitive to pressure changes and rock porosity and it must be vented off to avoid buildup ($\tau_{\frac{1}{2}}$ = 3.8 d).

Measurements and Monte Carlo calculations have been carried out by fellow collaborators in order to predict electron fluxes and counting rates. Studies of radioactivity in the mine by Keith Ruddick give the expected electron flux seen by shield modules in the lab from rock in the cavern walls: 48 e^-/m^2s plus an additional 10 expected from Rn^{222}. This number is based on actual measurements of gamma radiation from rock samples using a NaI crystal and assumes a 1" thickness of the concrete used to line the walls of the cavern. The attenuation length for gamma rays was taken as 20 g/cm^2. An independent calculation by Giles Barr arrived at 79 e^-/m^2s. We now wish to compare these predictions with measurements carried out by the Tracker.

Singles Rates and the Plateau on Singles

The first plateau curve on singles in the cavern using a veto shield element[1] was obtained in December, 1985, before any of the structural support for the detector was installed but after the cement floor was poured and after the final coating of shotcrete was sprayed on the walls. Figure 4-1 shows the singles rate as a function of high voltage as measured in the cavity. Two channels (A and B in the figure) of a single module were plateaued. No reliable measurement of atmospheric pressure could be made at the time; the module was bubbled with 91–9 Ar–CO_2 at slightly above ambient pressure. The curves show a plateau width of ~ 50–100 V (*cf.*, Fig. 2-7) and an average counting rate of about 450 Hz per channel (corresponding to 112 Hz per cell).

---

[1] *Ibid.*, [Chapter 2, ref. 8]

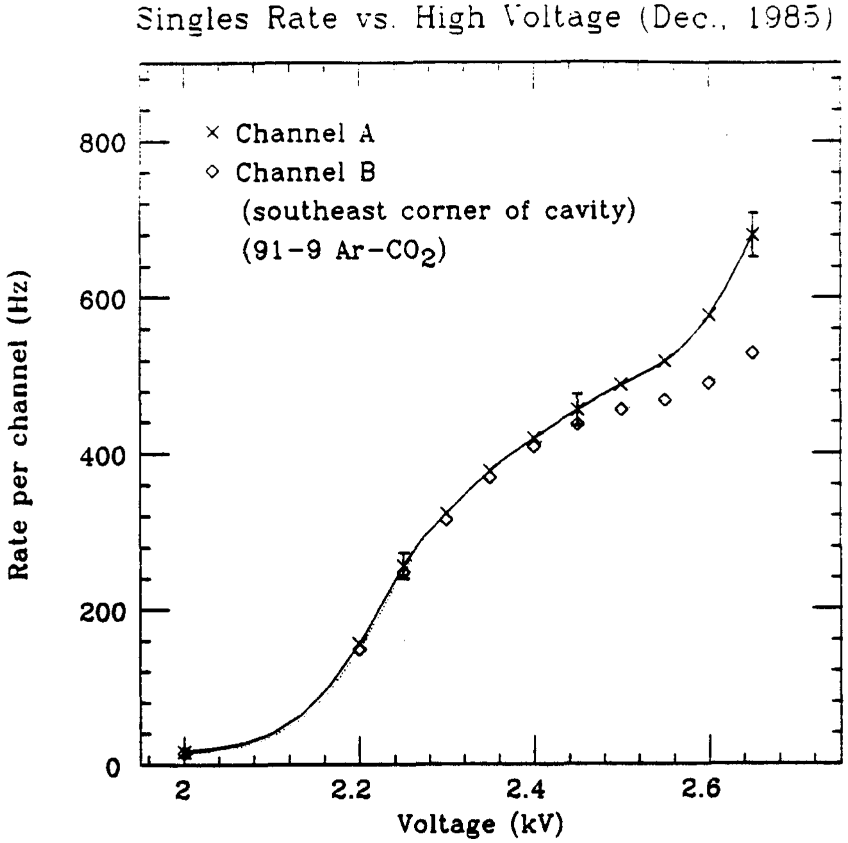

Fig. 4-1. Plateau on Singles (Dec., 1985). The plot shows the counting rate as a function of high voltage for two channels (A and B) in one of the first modules shipped to the mine. A small plateau is observed at 2450 V.

Better measurements of singles rates were made when the final gas system was installed. This allowed for better gas conditioning and a fixed absolute pressure for the measurement. Plateau curves on singles were obtained for every channel in the Tracker (except the extension) using a 95–5 gas mixture at a fixed absolute pressure of 1.12 bar. Some typical plateaus are shown in Fig. 4-2; a few channels (not shown) were found to be in need of repair. When the plateau measurement is performed on singles as it is here, the shape of the plateau region is not as well defined as when the measurement is made on through-going radiation. The plateau widths are usually smaller than the 100 V width measured in the cosmic ray test stand using through-going muons. The singles rate on plateau for modules near the floor is about 320 Hz or 80 Hz per cell. The surface area of a cell is (7×0.027) m^2/side $\times 6$ sides $= 1.13$ m^2, so the measured flux is ~ 70 $e^-/m^2 s$, in agreement with the above the predictions.

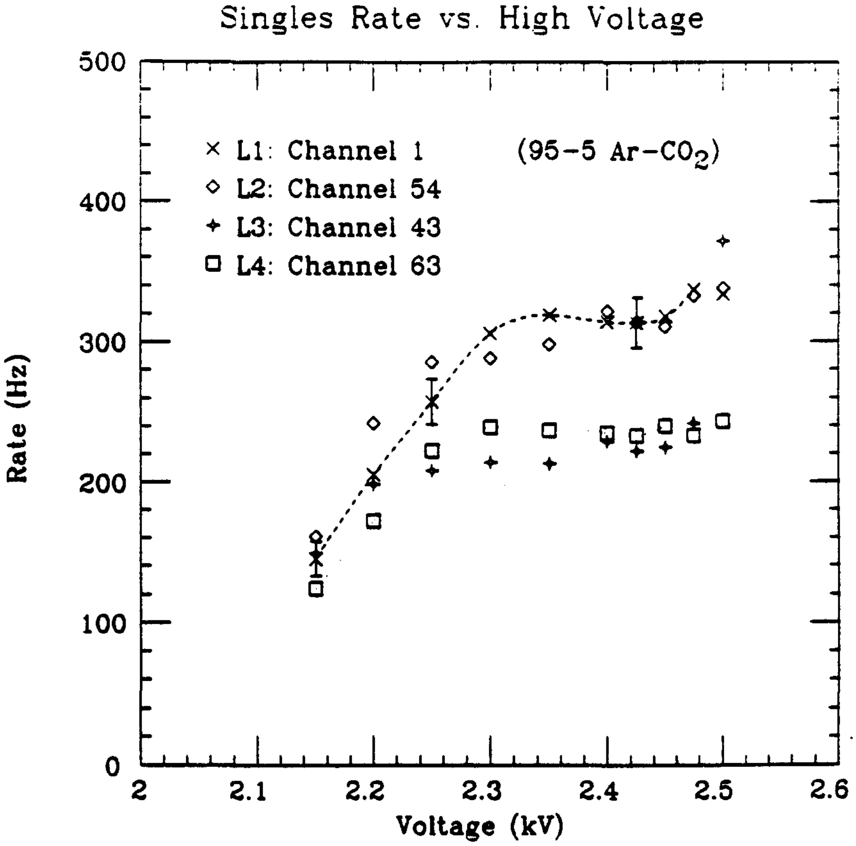

Fig. 4-2. Plateau Curves for Installed Modules. Singles counting rates *vs.* high voltage are shown for some typical channels in the Tracker.

Average singles rates for each run, integrated over all channels in the Tracker, have been compiled in the rate history shown in Fig. 4-3. Rates were calculated by scanning a 100 μs window in the readout module buffer that excluded the trigger. The horizontal axis corresponds to the number of hours since data-taking began and the vertical axis gives the singles rate in kHz averaged over the entire detector. The large fluctuations in counting rate are due to short data runs with poor statistics. A single trigger provides only 100 μs for counts to accumulate and there were typically 500 triggers per run. At a nominal rate of 300 Hz per channel, this corresponds to only 100×10^{-6} s $\times 300$ Hz $= 0.03$ counts/trigger for a single channel. The expected rate, summed over 256 (320) channels, is 77 (96) kHz for 4 (5) layers. From the singles rate history it is easy to see when the extension was added ($\sim$ 4500 hours). A steady decrease (12 %) in the counting rate is seen to have occurred, during the pre-extension era. The only explanation for the decrease in performance is gas poisoning over an extended period of time. Although this has a discernable effect on the singles rate (*e.g.*, low energy electrons that have to drift out of corners), the effect on the muon trigger rate (as will be shown below) was not so great.

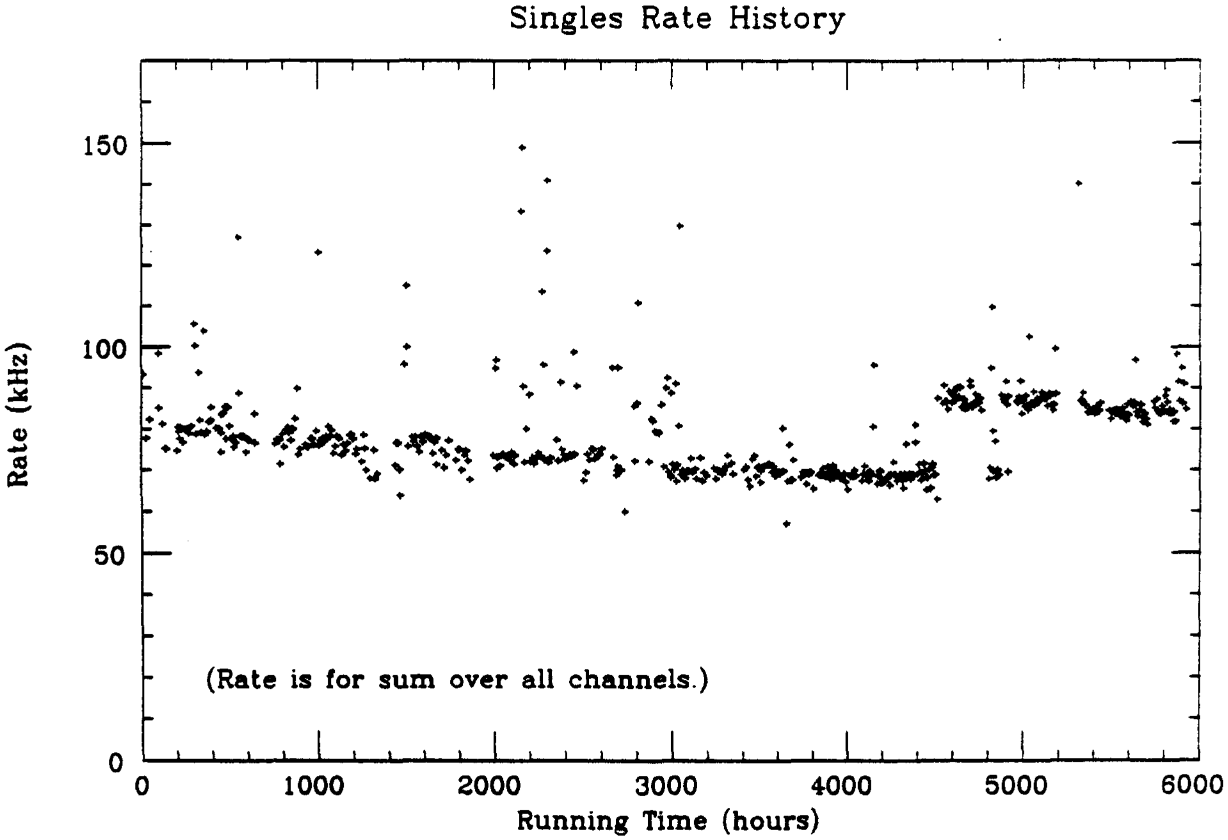

Fig. 4-3. Singles Rate History. The horizontal axis is the number of hours since the start of data collection and the vertical axis is the counting rate in kHz. The counting rate, summed over all channels in the Tracker and averaged over a run, shows a distinct drop in rate with time – evidence for slow gas poisoning of the system.

Average singles rates per channel, measured during the early stages of data taking, are shown in Table 4.1 for the different layers. It is clear from this data that modules near the floor detect a larger flux of electrons than the modules near the ceiling (as predicted in [4]). For an isotropic source of gammas, the difference in length between layers L1 (6.6 m) and L2 (7.0 m) should correspond to a 6 % difference in counting rates with L1 counting *less* than L2. Rather, the singles rate in layer L1 is seen to be greater than in any other layer in the detector. This effect is due to high activity in the concrete floor and it has provided us with a means of estimating the attenuation length of the gamma rays. Average counting rates for the bottom row of channels in layer L1 were calculated and compared to average rates for the top row in that layer. These averages were calculated by scanning the time history buffers of the readout modules and counting the single hits found in them. By scanning a subset of the data runs, it was found that the even-numbered channels in L1, closest to the floor, had an average counting rate of 327 ± 26 Hz and the odd-numbered channels had an average counting rate of 306 ± 27 Hz (these rates were measured in 95–5 Ar–CO_2). The 6.6 % reduction in rate corresponds to a photon attenuation length of $\lambda_0 \simeq 18\ g/cm^2$ and an average photon energy on the order of 1–2 MeV ($\rho_{Al} = 2.7\ g/cm^3$, and wall thickness $t = 0.216\ cm$). The *active* shield provides *passive* shielding of gammas at the level of 10–15 %.

RATES IN THE TRACKER

Layer	Singles Rate† (Hz)	Coincidence Rate‡ (Hz)
1	334 ± 33	95 ± 2
2	314 ± 24	111 ± 2
3	266 ± 21	80 ± 2
4	269 ± 17	82 ± 2

† Singles rate per channel averaged over all channels in layer.
‡ Average coincidence rate per layer.

Table 4-1. Rates in the Tracker. The table lists the average singles rate per channel and the average coincidence (0·1 + 1·2 + ⋯ + 62·63) rate per layer. Modules in layer 1 are 6.6 m long while those in the other layers are 7.0 m long. The above rates were measured at 2.45 kV using a 91-9 Ar-CO_2 gas mixture.

Coincidence Rates in the Tracker

Using the Tracker Trigger Module, coincidence rates (0·1 + 1·2 + ⋯ + 62·63) could be measured for each layer by monitoring the trigger signals, T1 through T4 from each readout module. The counting rate per layer as a function of high voltage is shown in

Fig. 4-4 for the 95–5 Ar-CO_2 gas mixture. The nominal rate on plateau is about 100 Hz per layer or 3 Hz per module. The coincidence rates per layer are also compiled in Table 4-1. The layers closest to the floor show higher coincidence rates as well.

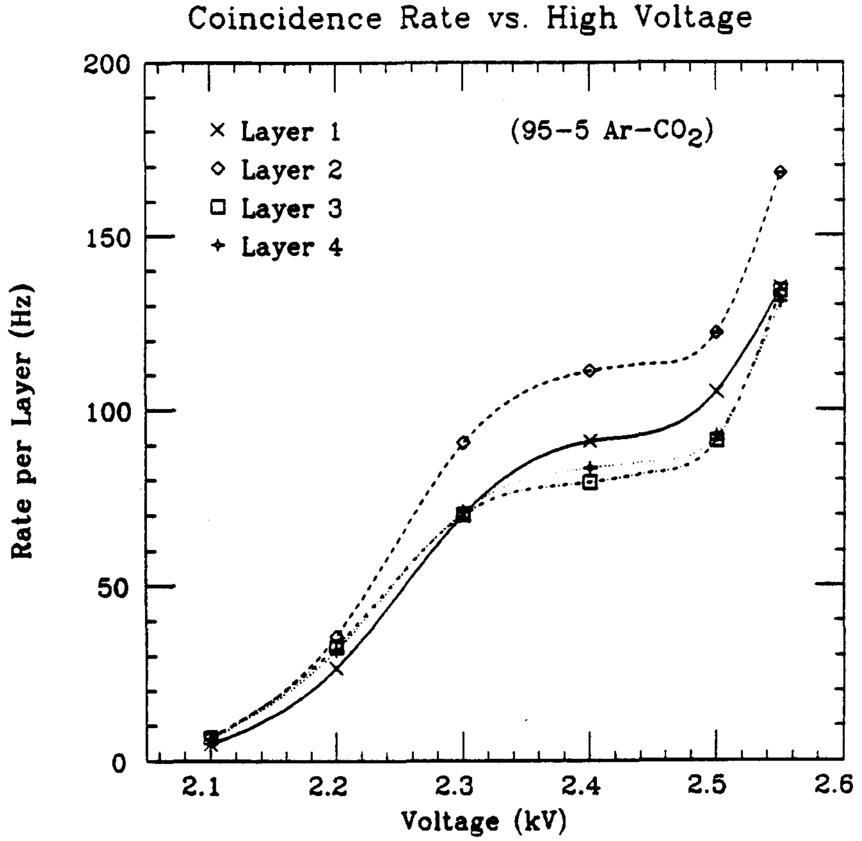

Fig. 4-4. Coincidence Plateau. The coincidence rate for $0\cdot1 + 1\cdot2 + \cdots + 62\cdot63$ in Tracker layers is shown as a function of high voltage. A nominal value of 3 Hz per module is used to determine the accidental rate in the muon trigger (see text).

Accidental Rates in the Muon Trigger

Using the (nominal) singles and coincidence rates just calculated, we are now ready to predict the expected background rates in the muon trigger. As will be shown in the next section, for 95% of all muon triggers, the muon could be located within a 3 μs window of the time buffer. From the measured singles rate, the accidental rate for uncorrelated coincidences in 3 μs is $(300/s)^2 \cdot 3 \times 10^{-6} s = 0.27$ Hz, less than the measured coincidence rate of 3 Hz. Based on the measured value, the chance of an extra coincidence being observed in *any* module in the Tracker, within the trigger window, is 3 μs $\times 3$ Hz/module $\times 128$ modules $= 1.1 \times 10^{-3}$. The chance probability of a single hit appearing anywhere in the Tracker within this same window is 3 μs $\times 300$ Hz/channel $\times 256$ channels $= 0.23$. So, one out of every four triggers can be expected to contain an extra single hit while one out of every thousand can be expected to contain an extra coincidence hit.

Finally, the accidental rate in the muon trigger can be now be calculated. The nominal coincidence rate in each layer is 100 Hz. Three layers are required in the trigger. The accidental rate in the muon trigger is therefore $(100\ \mathrm{Hz})^3 \times (3 \times 10^{-6}\ s)^2 = 9.0 \times 10^{-6}$ Hz.

4.2 Data Reduction: The Off-line Filter

Data Decoding and Cuts

Figure 4-5 describes how cuts were placed on the data. Analysis begins by examining the header record for each run. The settings of the Tracker Trigger Module status register (TTSR) were written into this record at begin-run time for all runs. Runs with a cosmic ray setting (621 out of 705 total runs) are selected for further analysis before examination of individual triggers takes place.

The total number of triggers recorded is 248,576. Cuts on this total data set were applied as follows. First, the TTSR, recorded for every trigger, is examined to determine the trigger settings in place when the event occurred. There were 2,980 events with inappropriate trigger settings that were discarded. A total of 245,596 (100 %)[2] events have been identified as cosmic ray type triggers. Each trigger is required to pass a noise cut. The size of the cut was chosen to be proportional to the total number of readout modules in use. A total of 8,534 (3.5 %) triggers having a word count greater than 32 times the number of readout modules were removed. Many of these 'noisy' triggers were caused by rf signals generated in the cavity (*e.g.*, by cranes, pumps and relays turning on and off)

---

[2] Numbers in parenthesis refer to the percentage of cosmic ray triggers.

CUTS APPLIED TO THE DATA

248,576	RECORDED TRIGGERS
- 2,980	NON–COSMIC RAY TRIGGERS
- 8,534	NOISE TRIGGERS
- 17,153	DATA BUFFER ERRORS
- 1,010	READOUT ERRORS (CAMAC)
- 6,977	NO IN-TIME HITS
- 57,164	MISSED LAYER L4
- 3,814	FALSE TRIGGERS
- 3,775	MISSED LAYER L3 (POST-EXTENSION)
- 115	TIME ERRORS
147,054	TRIGGERS ENTERED THE PATTERN-RECOGNITION AND TRACK-FITTING ALGORITHMS

~ 103,000	~ 900	~ 43,000
GOLDEN SINGLE MUON SAMPLE	GOLDEN MULTIPLE MUON SAMPLE	AMBIGUOUS OR BLOB-SIZE TOO BIG OR > 100 TRACKS

Fig. 4-5. The Cuts Applied to the Data.

and hence were unavoidable. Next, the data buffer for each trigger is rigorously examined for a number of possible errors. Data buffers with: a) exactly the same data and time as the previous trigger, b) word count register[3] errors, c) inconsistent word counts (redundancy check), or d) trailer word errors, were rejected from further analysis. The number of triggers that did not survive this cut is 17,153 (7.0 %). Two further checks were imposed after the raw data buffers from the readout modules are decoded. There were 29 (0.01 %) triggers recorded that had at least one unrecognizable readout module identification (unique switch settings, used to identify modules within a crate, that are hard–wired when modules are placed into service). There were 981 (0.4 %) triggers that showed no hits in their time buffers even though a cosmic trigger was formed. Most of the triggers removed by these last three cuts were real muon events that were discarded because of CAMAC or readout electronics failures.

Cosmic ray triggers with a reasonable word count and error–free data buffers then have their time buffers scanned for a trigger signal. The time delay between recognition of a muon trigger by the Tracker Trigger Module and receipt of this trigger (TRIGOUT) by the readout modules, was set by an RC circuit in a multivibrator. During the course of the experiment, the properties of this circuit, and hence the time of arrival of TRIGOUT at the readout modules changed slightly. A first pass through the data was then required in order to extract an average value for the trigger time within any given run. This was accomplished by histogramming the number of hits in each 1 μs slot of the time buffers for all readout modules required in the trigger. Then the mean for each histogram is calculated and an average trigger time determined. Figure 4-6 shows the readout module time buffers for layers L1–L4 for a typical cosmic ray run. The horizontal axis shows

---

[3] The word count registers and the trailer words, read for every trigger, provide the status, identification and the size of the data buffer for each readout module.

one half of the complete buffer (0–64 μs) and the vertical axis shows the number of hits recorded over the entire run for each microsecond. The delayed muon trigger signal shows up at about 6–7 μs, above a small background caused by random hits from radioactivity that were also detected by the shield. The time history buffer for layer L4, *not* included in the trigger, shows a large, clear signal, in time coincidence with the other layers—evidence for detection of a penetrating muon.

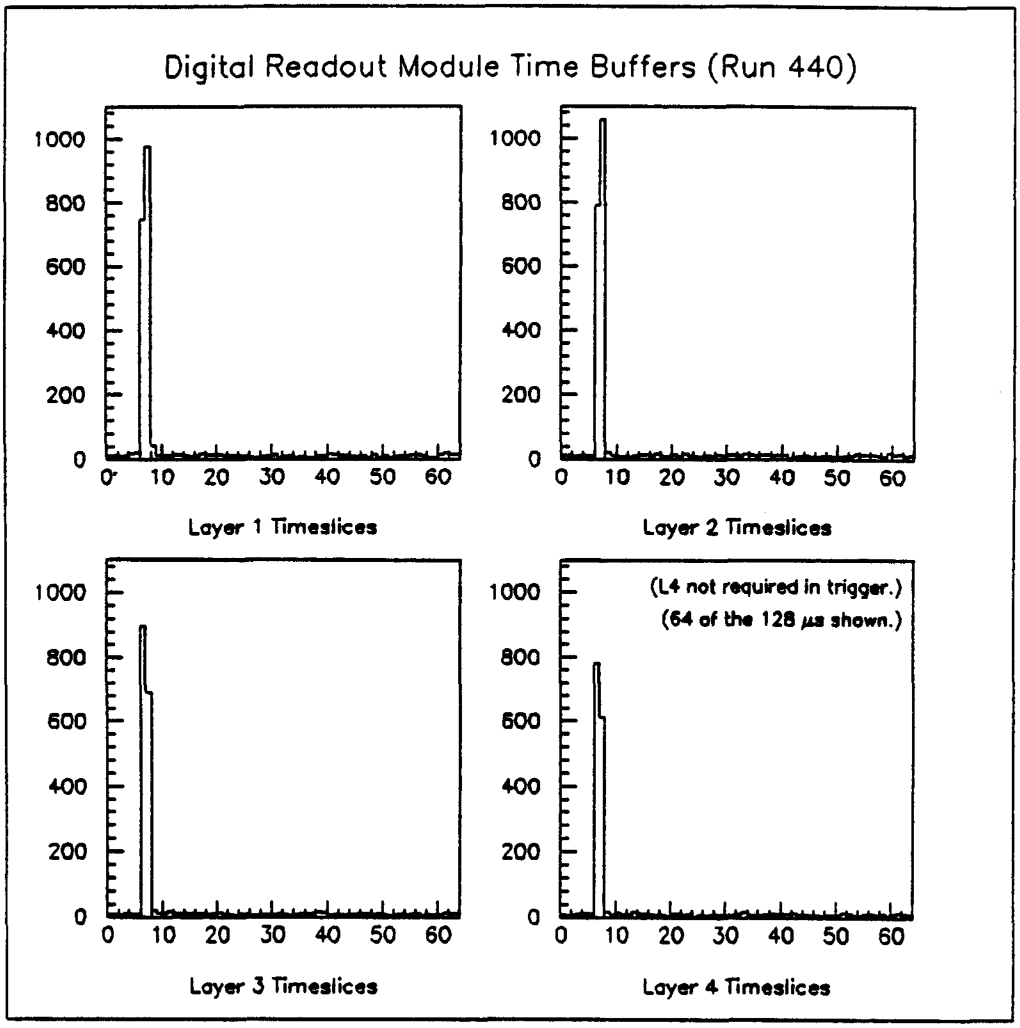

Fig. 4-6. Readout Module Time Buffers. Layers L1, L2 and L3 were required in the cosmic ray trigger. Their signals appear at about 6-7 μs in the buffer. The sharp peak seen in L4, not required in the trigger, is evidence for a penetrating muon.

The scan proceeded by opening up a 4 μs window around the trigger time selected in the first pass. The scan was performed on an event–by–event basis in order to improve efficiency. A total of 6,478 (2.6 %) triggers with no hits within this window were rejected. Then, an attempt was made to tighten the time window for the muon, thus lowering the accidental background rate for the trigger. In approximately 95% of the accepted cosmic ray triggers, it was possible to locate the muon within a 3 μs window of the 128 μs time buffer. For the other 5%, the window remained at 4 μs. A total of 6,977 (2.8 %) events had to be rejected because they showed no in-time hits in any layer in either the 4 or 3 μs window cuts. The width of this time window was calculated for each cosmic ray run by averaging over all triggers in the run. As shown in Fig. 4-7 the average trigger width is 3.25 μs. In the cosmic ray test stand, channels were capable of responding to muons within 1 μs. The larger 3 μs window required here is due to several factors which include the 1 MHz digitization by readout modules of the 1.1 μs pulses from the output cards and small variations in the overlap of the 5 μs-wide T1–T3 signals used in formation of TRIGOUT.

The next stage of processing checked to see if any hits were recorded in layer L4 within the trigger window. Over the course of the *entire* data run, 57,164 (23.3 %) triggers had no hits in layer L4 within a 3 or 4 μs window centered about the trigger, thus precluding an XZ readout for a ceiling hit. This is substantially larger than the Monte Carlo prediction of 14.7 %. Part of the reason for the discrepancy is the addition of the Tracker extension halfway through the data taking. The number of triggers that miss layer L4 has been monitored and plotted in Fig. 4-8 for the pre-extension era. The plot shows an average miss ratio of 17.3 %, still larger than the predicted value. A possible explanation for some of the remaining discrepancy is that the trigger window selected was not wide enough to include T4 in some of the triggers. Based on the survey measurements, the overlap region is 16.8 % in agreement with the data. The model therefore underestimates the miss ratio by 2 %.

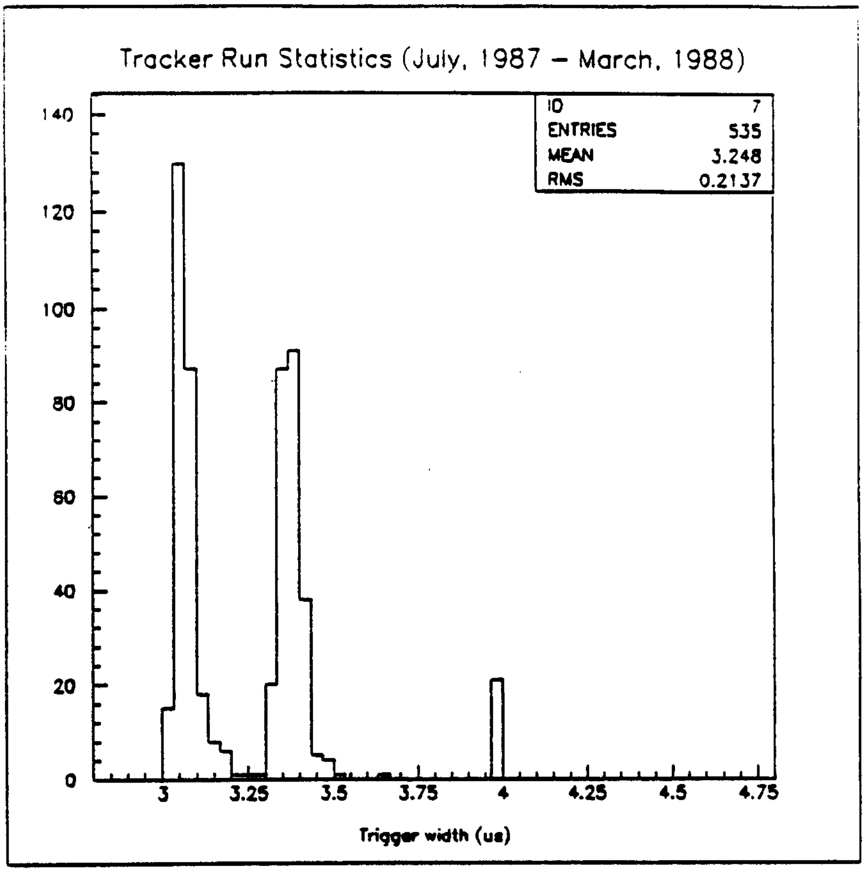

Fig. 4-7. The Trigger Width. For 95 % of the cosmic ray triggers the muon could be located in a 3 μs wide window.

Next an examination is made to ensure that at least one coincidence occurred in all layers required in the trigger. Triggers not passing this cut were deemed false triggers and removed from the analysis chain. A total of 3,814 (1.5 %) false triggers were recorded. Again, a possible explanation for this type of event is the tight trigger window.

After addition of the Tracker extension, L5, an additional 3775 (1.5 %) muons were recorded that had hits in L5 and L4 but no hits in L3. These events were not used in further analysis.

Tracking celestial objects requires a precise measurement of the time of the event as recorded in the lab. An algorithm was setup to extract WWVB and VAX times from the raw data buffer. The algorithm monitored the status of the WWVB and VAX times, calculated the absolute difference between them whenever both were available and flagged

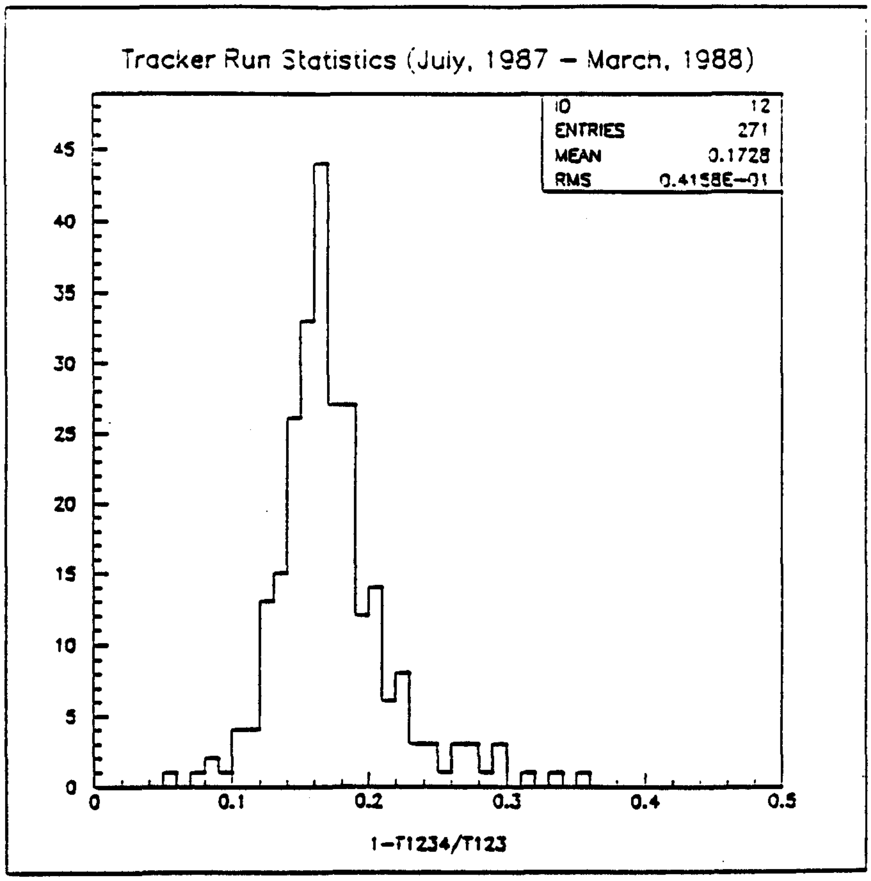

Fig. 4-8. Trigger Miss Ratio for L4. Since L3 and L4 do not completely overlap each other, 17 % of all triggers miss layer L4 altogether and have to be rejected.

events for which no WWVB time was available. A total of 115 (0.05 %) events were excluded from further analysis because of various problems with the time measurement.

A total of 147,054 (60 %) triggers passed all of these cuts and were allowed to enter the pattern–recognition and track fitting algorithms. This number represents the accumulated sum of all triggers satisfying the (T1·T2·T3) trigger *or* the (T1·T2·T3 + T1·T2·T5) trigger.[4] Further cuts were later applied to this data set in order to maintain a high angular resolution for track pointing.

Pattern Recognition and Track Fitting

Only two other cuts were applied to triggers that made it this far. First, a cut was made on the spatial extent of any hit in the shield. All hit patterns having a multiplicity

---

[4] Here, T5 refers to the XVETO signal generated by the readout module that serviced the Tracker extension.

(defined to be the number of adjacent in-time channels that make up a hit) of five channels or more were rejected from the analysis. This amounted to 15,629 (6.4 %) of the original 245,596 cosmic ray triggers. Second, whenever more than 100 tracks were found in either projection during the track finding process, the algorithm tossed out the event. There were only 88 (0.03 %) events that had to be excluded here.

The program for setting up and fitting tracks is very simple [5]. As shown above, the accidental single hit probability within a 3 μs window for all channels in the Tracker is 0.23 while the coincident hit probability is only 1.1×10^{-3}. Single hits, representing a high source of background in the muon signal, were therefore excluded from track reconstruction initially and only used later to resolve ambiguities in track direction or event multiplicity (if possible). Coincidence hits, on the other hand, are almost surely to be associated with the muon since the accidental probability for these is very small.

Treating each projection separately, all possible tracks were then constructed from the hits in each projection. Since layer L4 was not required in the trigger, it was sometimes necessary to use single hits in that layer in order to form a track. A simple least squares algorithm was used to determine the slopes, intercepts, errors and χ^2 for each track with special attention paid to layers L1 and L2 which have elevated sections of modules (see Fig. 4-9).

The remaining muons are then classified first in terms of their multiplicity and second in terms of their directional certainty (or ambiguity). Multiplicity is calculated by determining the number of parallel pairs of tracks found in each projection, choosing the largest (if different) and adding 1. For example, for a single muon, no parallel pairs of tracks would be found so the multiplicity is 1. For a three–muon event in which two parallel pairs were found in one projection but only one parallel pair was found in the other, the multiplicity would be $2 + 1 = 3$. Care was taken to avoid double counting of tracks. An

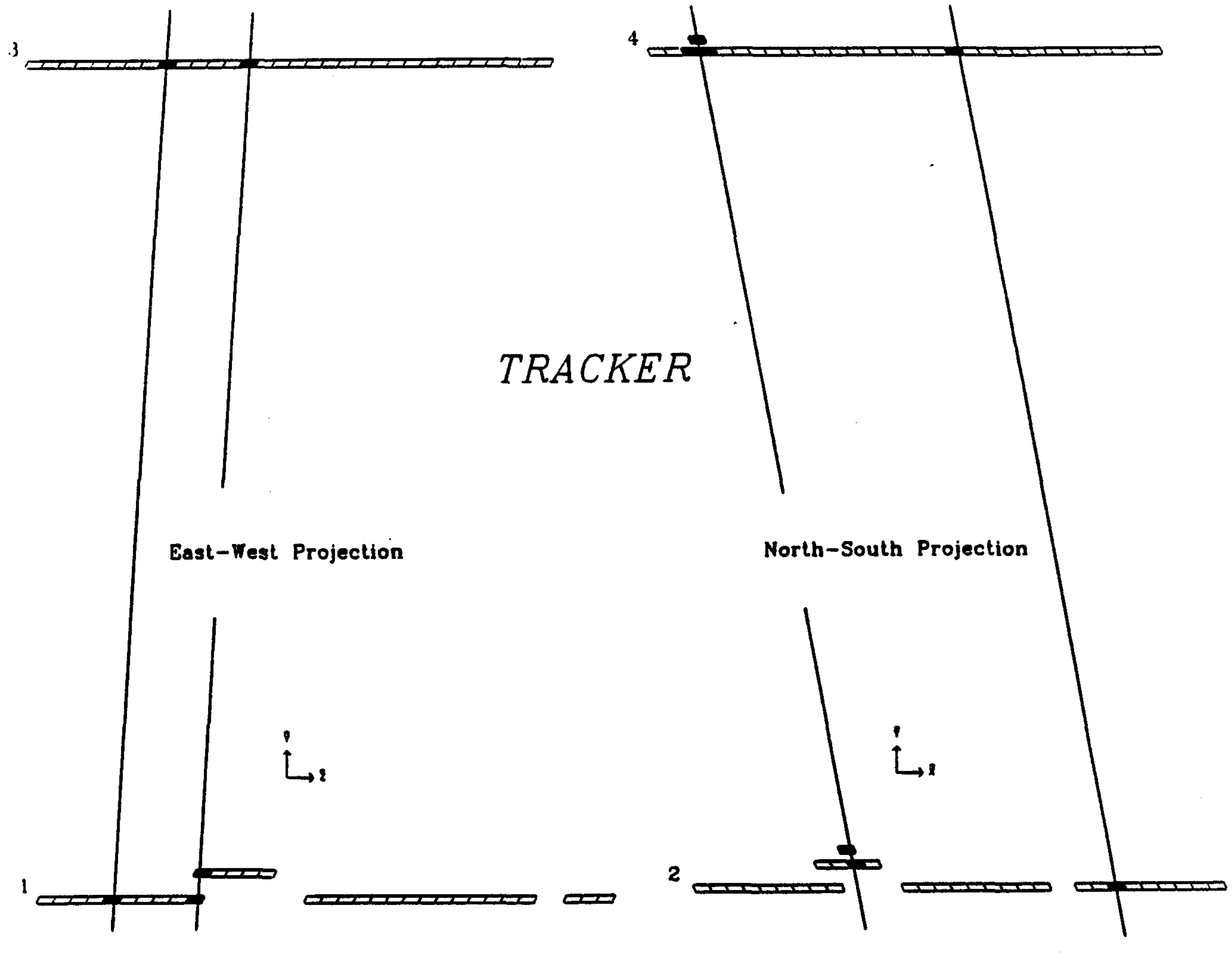

Fig. 4-9. Projections of the Tracker. Shown is a two-muon event as it appears in each projection. The track fitting routine carefully treats the elevated sections in the floor layers so that the maximum number of hits can be used in track formation.

event is ambiguous if an examination of the hit pattern in either layer yields no conclusive direction for the track. As an example, let the multiplicity of an event be 1. If two coincident hits with a separation between them is found in one of the layers in a projection while a single coincident hit is found in the other layer, then the true muon direction is lost and the event is counted as an ambiguous single muon.

Triggers for which there are no ambiguities in *direction* are called 'golden muons'.[5] A golden single muon data sample and a golden multiple muon data sample were extracted from the data for further analysis. Table 4-2 summarizes the run statistics for data collected by the Tracker.

4.3 The Golden Single Muon Data Sample

General Features of the Data Sample

The golden single muon data set consists of $\sim$ 103,000 muons with no ambiguities in track direction. A plot of the relative error in the slopes of all tracks (errors for both the XY and ZY projections are plotted), expressed in milliradians, is shown in Fig. 4-10. The rms (root mean square) width of this distribution is 26 mrad or 1.5°; from this we calculate the angular resolution for single muon tracking to be $\sqrt{2} \cdot 1.5^\circ = 2.1^\circ$. The largest error in track direction, found in a small percentage of the muons, is 7°. The peaks seen in the tail reflect the granularity ($\sim 1^\circ$) of the detector.

---

[5] *N.B.* These muons included those triggers for which *only* the VAX time was recorded as well as those for which both the WWVB and VAX times were recorded. Data summary files included a flag noting this difference so that point source analysis could be done with or without the VAX-time-only events.

TRACKER RUN STATISTICS

	July, 1987 - March, 1988 Total livetime: 0.5044 years
Total runs	705
Cosmic ray runs	621
Interrupt-mode runs (MIDAS)	443
Unanalyzable runs	5
Total triggers read	248,576
Non-cosmic ray triggers	2,980
Cosmic ray triggers	245,596
Noisy triggers	8,534
False triggers	3,814
Data buffer errors	17,153
Switch decoding errors	29
No quartet hits on decode	981
Triggers with $> 32\cdot$NDRM[†] hits in-time	321
Triggers with no in-time hits	6,656
Triggers which missed layer 4	57,164
Triggers with coincidence T1·T2·T5	3,775
Triggers with coincidence T1·T2·T3	147,169
Triggers with VAX time	248,571
Triggers without VAX time	5
Triggers with WWVB time	190,719
WWVB error - no time sync (receiver)	57,727
WWVB error - inoperative (interface)	130
Changes in WWVB status	290
Triggers with VAX-WWVB time $>$ 1 day	10
Triggers with no time	4
Triggers with same UTC time	188
Entries to tracking algorithm	147,054
Triggers with blob multiplicity ≥ 5	15,629
Triggers with $>$ 100 tracks/projection	88
Golden one muon triggers	102,943
Golden two muon triggers	638
Golden three muon triggers	33
Golden four muon triggers	4
One muon triggers	25,943
Two muon triggers	1,597
Three muon triggers	149
Four muon triggers	21
Five muon triggers	8
Six muon triggers	1

[†] NDRM refers to the number of digital readout modules that were in use.

Table 4-2. Tracker Run Statistics.

The VAX time was recorded for all muons and the WWVB time was recorded for 83 % of them. The distribution of the time separation between muons for the total data set is shown in Fig. 4-11 while the WWVB subset is shown in Fig. 4-12. The horizontal axis is the time (in one-second bins) between triggers. As expected, both distributions are of a Poisson process. The solid curve in Fig. 4-11 is an exponential fit to the data with $\chi^2 = 642$ for the 600 points fit. From this fit, we infer the mean muon rate for this *clean*

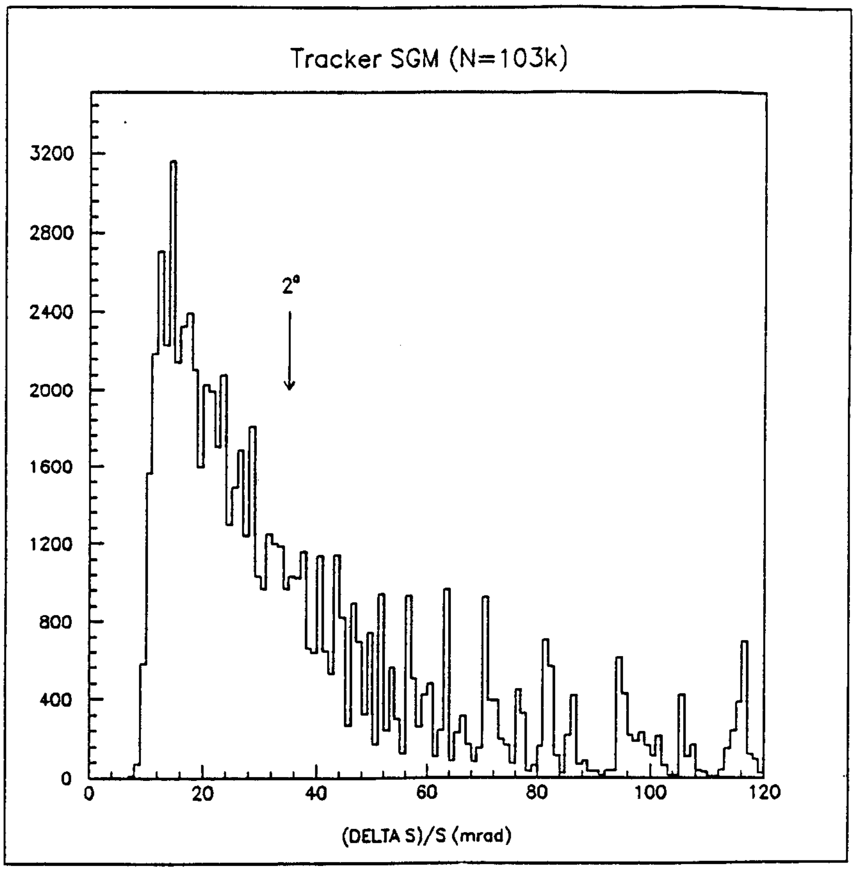

Fig. 4-10. Single Muon Tracking Resolution. The relative errors in track slopes are plotted in milliradians for both projections. The overall track resolution is about 2°.

data sample to be 0.756×10^{-2} Hz. An expanded view of the 0–100 s range of the data set, shown in Fig. 4-12, shows no inconsistencies for short periods. The bin size in this latter plot is 0.5 s.

The single muon distribution in azimuthal angle, A, is shown in Fig. 4-13. The bin size in the plot (1°) was chosen to expose the inefficiencies in the trigger seen at the compass points where the probability for a muon to pass through undetected is highest (*i.e.*, through the crack regions). The distribution shows a minimum for muons from the northwest direction (−60°) and a maximum for muons from the southeast direction (150°). A slight enhancement is noted at about 20°. The asymmetry in this plot is due almost entirely to the acceptance of the Tracker and not to overburden. As can be seen in Fig. 4-9,

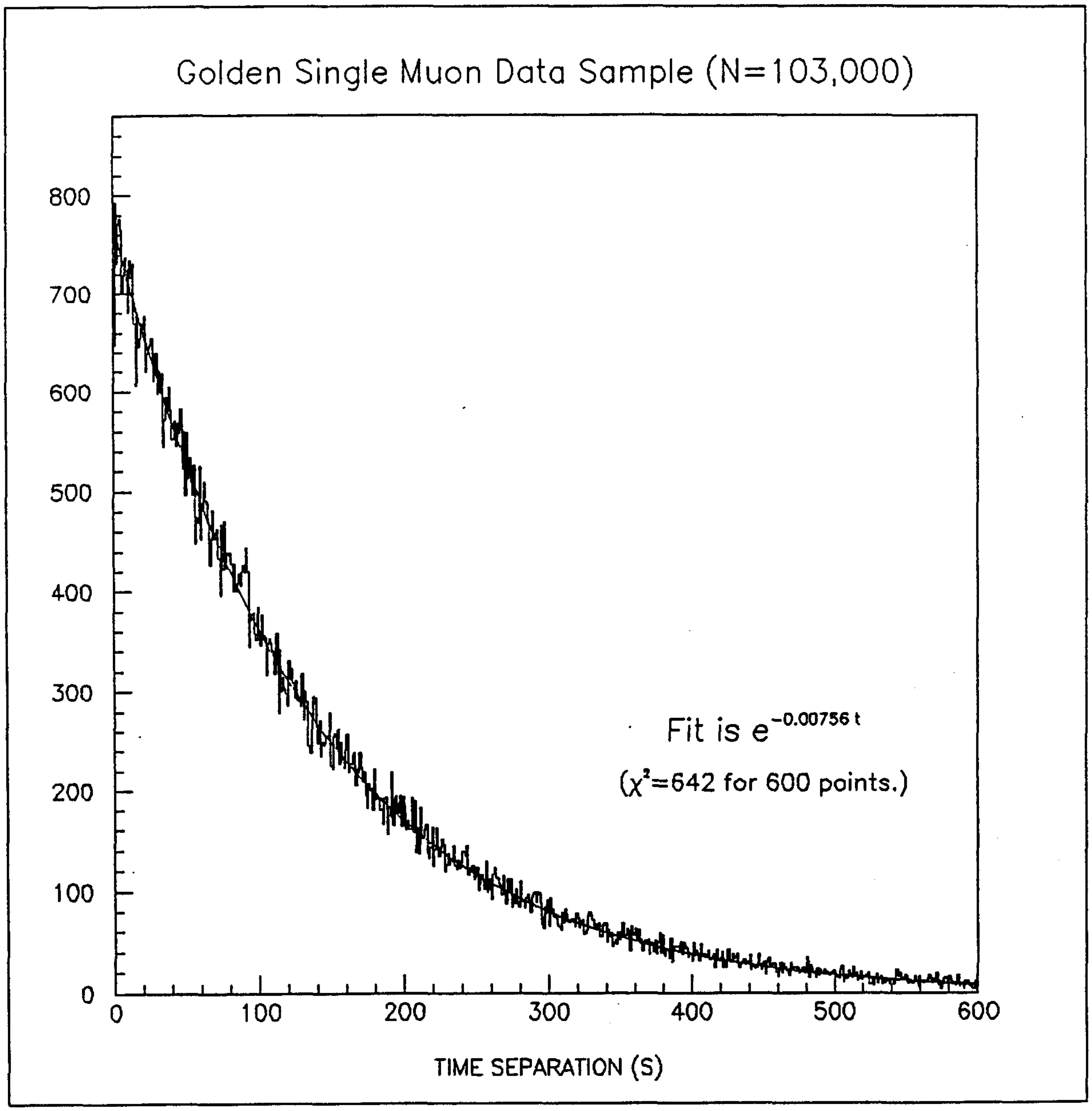

Fig. 4-11. Time Separation for Golden Single Muons. The vertical scale is in seconds and shows the time between golden single muon triggers. The solid curve is an exponential fit to the data.

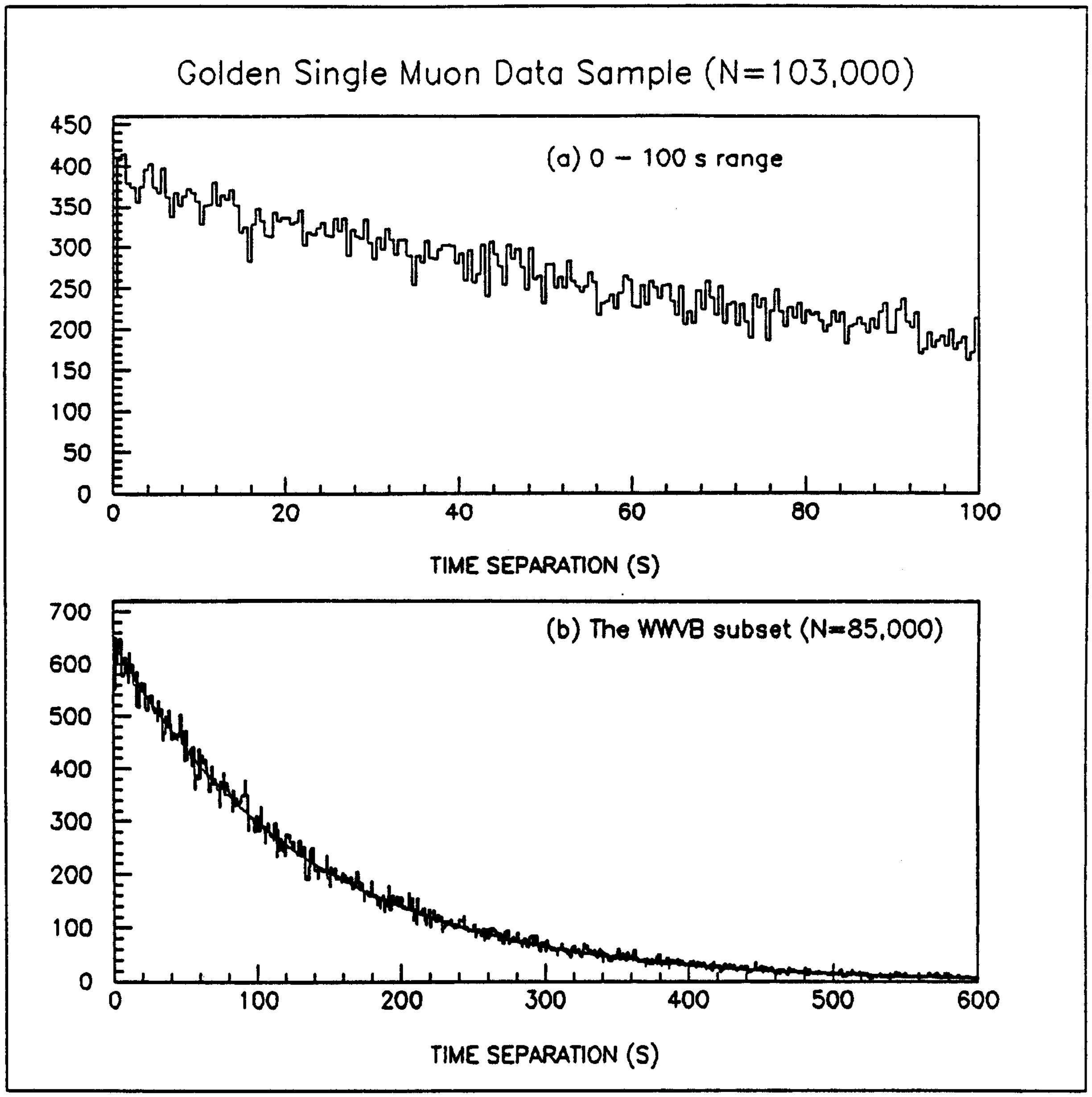

Fig. 4-12. (a) The 0–100 s Range of Fig. 4-11. (b) Time Separation in the WWVB Subset.

layer L1 is shifted north relative to layer L3 and layer L2 is shifted west relative to layer L4. This favors muons from the southeast direction.[6]

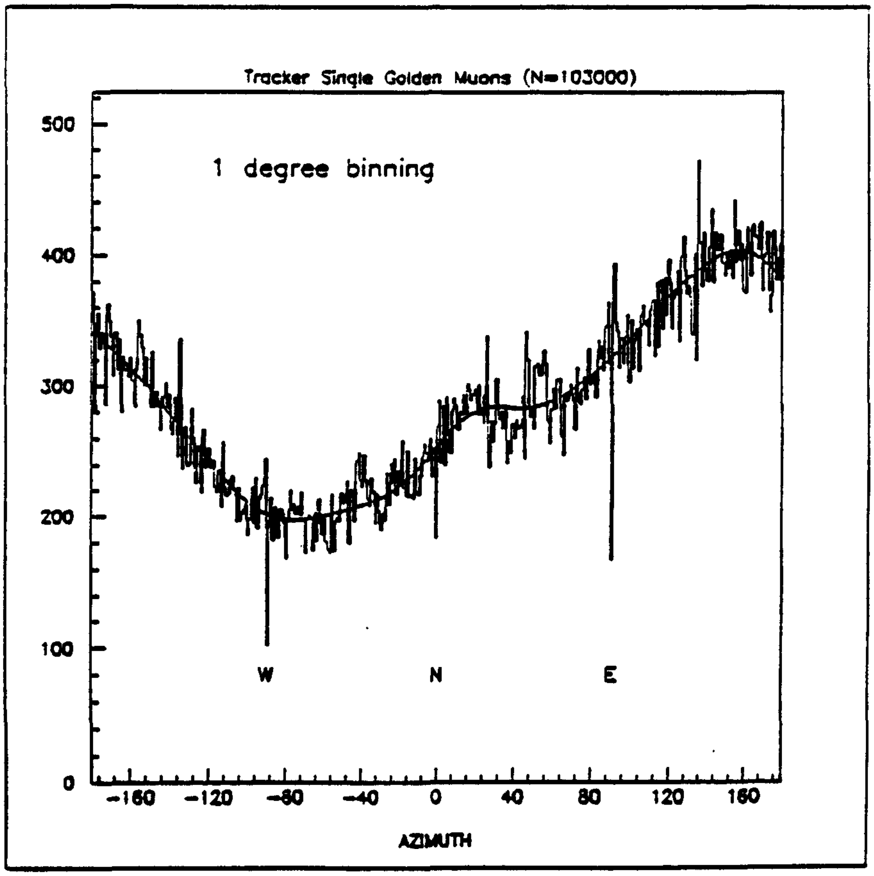

Fig. 4-13. Azimuthal Angle Distribution. The azimuthal angles, A, of all muons in the golden single muon data sample are shown.

The single muon distribution in zenith angle, θ, is shown in Fig. 4-14. The bin size in the plot is 1°. The average zenith angle is 15°, and no muons are observed for $\theta > 43°$.

Comparisons With the Single Muon Monte Carlo Model

The single muon Monte Carlo calculations were described in Chapter 3. Differential muon distributions were generated according to equation 3.6 for the cases $n = 1$, $n = 2$ and $n = 3$. In each model, all muons were generated in a 100 m^2 plane above the Tracker and then tracked through each individual layer.

---

[6] Although this shift was unintentional and built into the detector only because structural steel was in the way, it has provided a check since distributions in hour angle (at a particular right ascension) and declination should show the same trend that favors muons from the southeast.

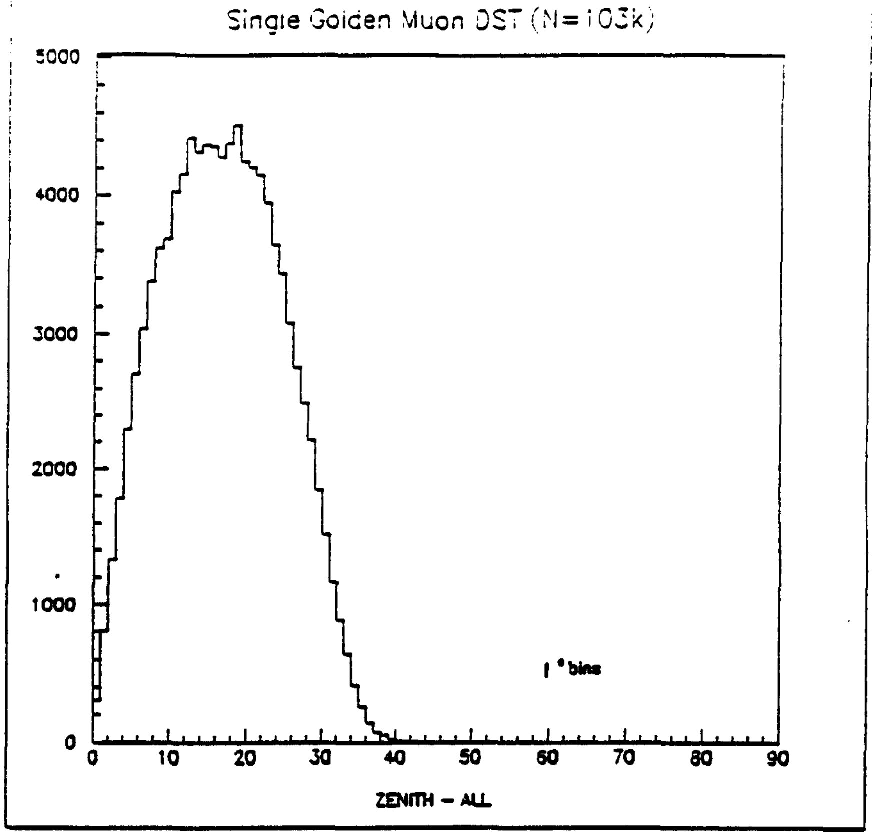

Fig. 4-14. Zenith Angle Distribution. The zenith angles, θ, of all muons in the golden single muon data sample are shown. The effect of detector acceptance is evident.

Figure 4-15 shows the resulting zenith angle ($\cos\theta$) distributions for the data and the three models. A logarithmic scale has been chosen for the vertical axes in order to compare the shapes of the distributions at low zenith angles where most of the muons are found. Each of the models has been normalized to the number of events in the data over the range $0.995 \leq \cos\theta \leq 1.000$.

Based on the data, 65 % of all muons arrive with zenith angles such that $\cos\theta \geq 0.94$ and 90 % arrive with zenith angles satisfying $\cos\theta \geq 0.90$. The range [0.94, 1.00] has been expanded and is shown in Fig. 4-16. The solid line in the figure is the data and the hatched areas show the difference between the data and the model $n = 2$. A quantitative comparison between the data and each model has been performed over the range [0.94, 1.00]. The comparison is made using a χ^2 calculation for two binned sets

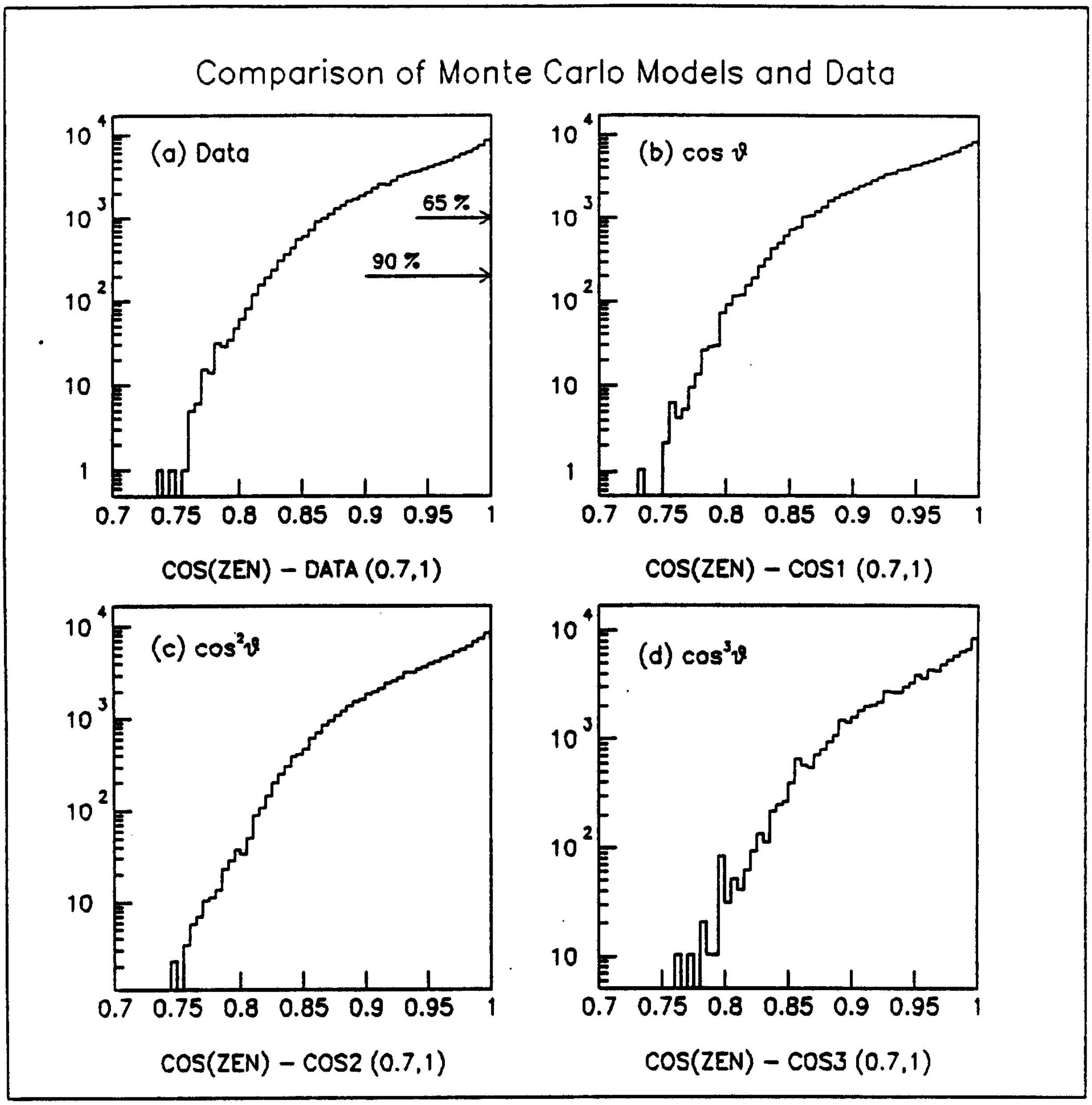

Fig. 4-15. $\cos\theta$ Distributions for the Data and the Single Muon Monte Carlo Models. The distributions show the total acceptance of the Tracker for the data and the models $\cos^n\theta$, n=1,2,3. From the data, it is seen that 90 % of all muons arrive with $\cos\theta \geq 0.90$ and 65 % arrive with $\cos\theta \geq 0.94$.

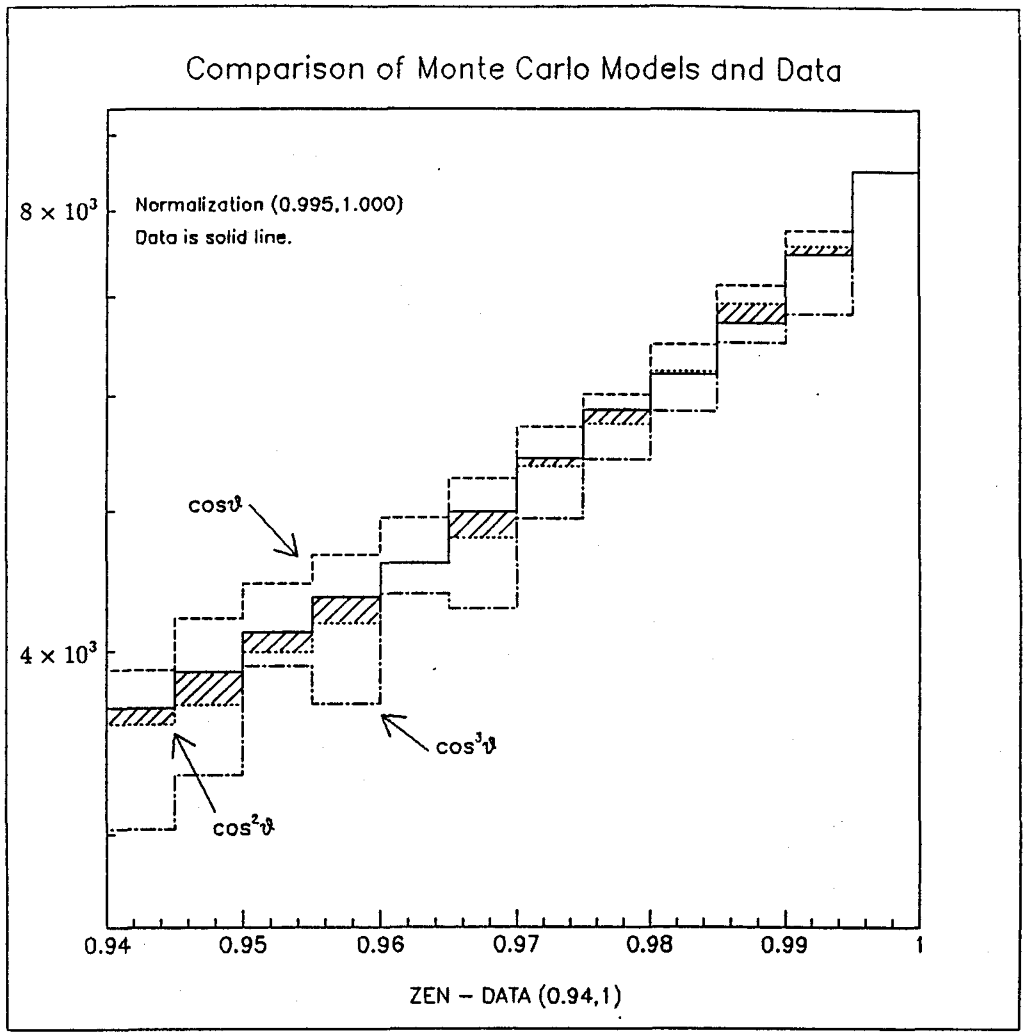

Fig. 4-16. Comparison of the Data and Single Muon Monte Carlo Models for the Range $0.94 \leq \cos\theta \leq 1.0$.

of data since neither the data nor any of the models are believed to be exactly correct.[7] In each comparison, the number of degrees of freedom is 12 (the 12 bins in the plot). The results are as follows: for the case $n = 1$, $\chi^2 = 97.2$, $Q \sim 10^{-15}$, for the case $n = 2$, $\chi^2 = 21.8$, $Q = 0.039$, and for the case $n = 3$, $\chi^2 = 313$, $Q = 0$, where Q is the χ^2 probability function. Based on the χ^2-fits, the $n = 2$ model is a better representation of the true distribution than are the other two cases although the low probability (0.039) indicates that a better representation likely exists (*i.e.*, some non-integral power of $\cos\theta$). The $n = 2$ model is used in all further comparisons of Monte Carlo results and data.

---

[7] See Numerical Recipes, p. 469 [6].

For the case $n = 2$, a total of 23.1×10^5 muons were generated and required to pass through the 100 m^2 plane. Of these, 10^5 satisfied the on-line trigger and 0.853×10^5 were tracked through all four layers. The miss ratio for layer L4 (1-T1·T2·T3·S4/T1·T2·T3, where S4 signifies that at least one single hit was recorded in layer L4) is therefore 0.147. The factor that will be used to scale the observed trigger rate in the detector, to a horizontal plane of 100 m^2, is 23.1.

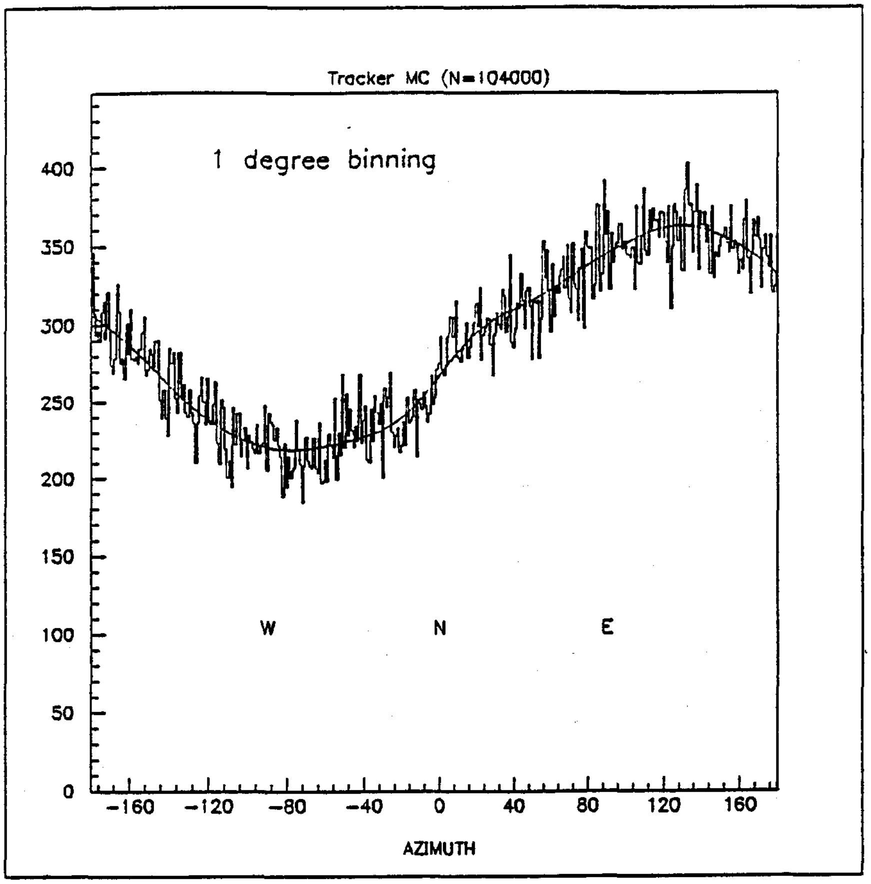

Fig. 4-17. Monte Carlo Azimuthal Distribution (n=2).

Figure 4-17 shows the azimuthal angle distribution for muons in the model and the bin size is 1°. Note that the inefficiencies observed in the data at the compass points is not evident in the Monte Carlo result. The minimum in the plot at −70° is close to that observed in the data. A maximum is observed in the southeast direction at 120°, but the height of this maximum relative to the average for the plot is not as pronounced as it is in the data. The small peak at 20° is also not as pronounced. In general though, the shape of this distribution agrees with that observed in the data.

4.4 The Golden Multiple Muon Data Sample

General Features of the Data Sample

A total of some 900 very good multiple muon events were extracted from the total data set. The breakdown of the multiplicity classification for these is shown in Table 4-3. For each of the multiple muon events, at least one pair of parallel tracks was found in each of the projections. The distribution of muon multiplicities for the subset and the total set are shown in Fig. 4-18. Also shown in the figure are results from the Homestake [7] (d = 4200 mwe, effective area of 113 m^2) and Soudan 1 [8] (d = 1800 mwe, 9 m^2) experiments. The curves drawn between the data points are only intended to guide the eye. The shapes of the golden multiple muon sample and the total multiple muon sample are similar. The Soudan 1 data indicates a slower fall-off in the number of muons of a given multiplicity than does the Tracker data. The distributions for Tracker data are not corrected for inefficiencies in the tracking algorithm. Studies using Monte Carlo generated 2–muon events (see below) indicate that at best, the algorithm is only $\sim$ 30 % efficient at finding a pair of tracks in the detector.

A total of 638 golden two–muon events were extracted from the 900 total and reconstructed for further analysis. Distributions in azimuth and zenith for two–muon events are similar to the ones shown for the single muon data set and will not be repeated.

Figure 4-19 is a plot of the difference in slopes between parallel tracks for both projections. The shape of the plot is due to the granularity of the detector; the enhancement at 0.5°, is at the angle subtended by half a module width (0.093 m over the 10 m separation). The rms width of this plot is 8.1 mrad. The error in muon direction is therefore $\sqrt{2} \times 8.1 = 11.5$ mrad or 0.7°.

MULTIPLICITY ARRAY

(Parallel Pairs per Projection)

Z

← Number of parallel pairs in Z

		1	2	3	4	5
	1	638	89	8	2	0
	2	82	33	8	2	1
X	3	15	9	4	1	0
	4	2	3	0	0	0
	5	1	0	0	0	0

↑

Number of parallel pairs in X

Table 4-3. Multiplicity Array. The number of parallel pairs found in each projection of the Tracker is given for all events in the golden multiple muon sample (N=898).

The distribution of the separation, s, between two–muon events in the the Tracker is shown in Fig. 4-20 (solid line). The horizontal scale is the muon separation in centimeters. The average separation is $s = 2.17\ m$ with an rms width of $1.26\ m$. The low statistics and granularity of the detector account for the peaks and troughs.

Comparisons With the Two-muon Monte Carlo Model

As described in Chapter 3, two–muon separation in the Tracker was studied using the two simulations given by equations 3.10 and 3.11. In the first case, the distribution in muon separation, s, was chosen to be random between 0 and 10 m while in the second case, it was chosen to be proportional to $1/s$. In both cases the distribution in zenith angle falls as $\cos^2\theta$ as determined by the single muon Monte Carlo. For those muon events which survive the on-line and off-line trigger requirements, a data file is written containing all the hits in the Tracker. The data file is read by a program that uses the same pattern-recognition and

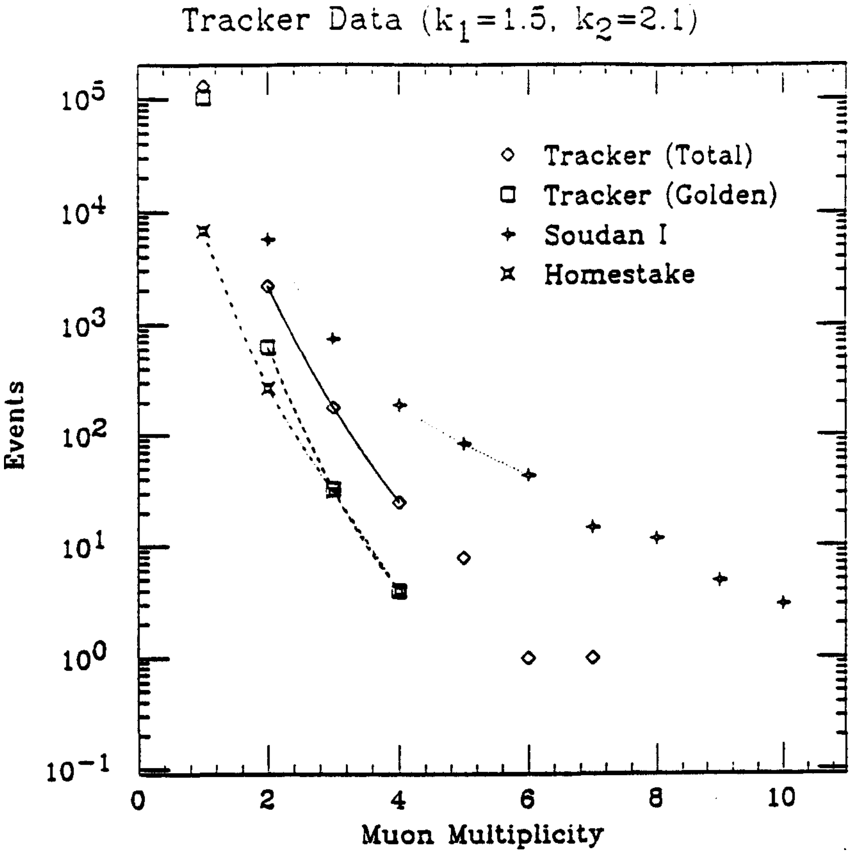

Fig. 4-18. Muon Multiplicity Distribution. The number of muons having event multiplicities M_μ is shown for Tracker data and two other experiments. Inefficiencies in the pattern recognition and track fitting algorithms are not accounted for in the Tracker data.

track fitting algorithms applied to the data. The separation between muons is calculated for those events which are reconstructed by the track fitting algorithm.

For comparison, the results of both attempts are plotted in the same figure as the data. Monte Carlo results have been normalized to the total number of events in the data (N=638). Once again, we used a χ^2 calculation for two binned sets of data as a maximum likelihood estimator. For both comparisons, the number of degrees of freedom (*df*) is 56 and is equal to the number of bins with data in the range [40 cm, 600 cm].

For the random case, 970 muons (before normalization) from a sample of 2085 within the acceptance survived the tracking algorithm. Their average separation is 2.71 m and the width of the distribution is 1.21 m. From the broad shape of the plot we see that this is a poor description of the actual distribution ($\chi^2 = 115$, $Q = 5.6 \times 10^{-6}$, 56 *df*).

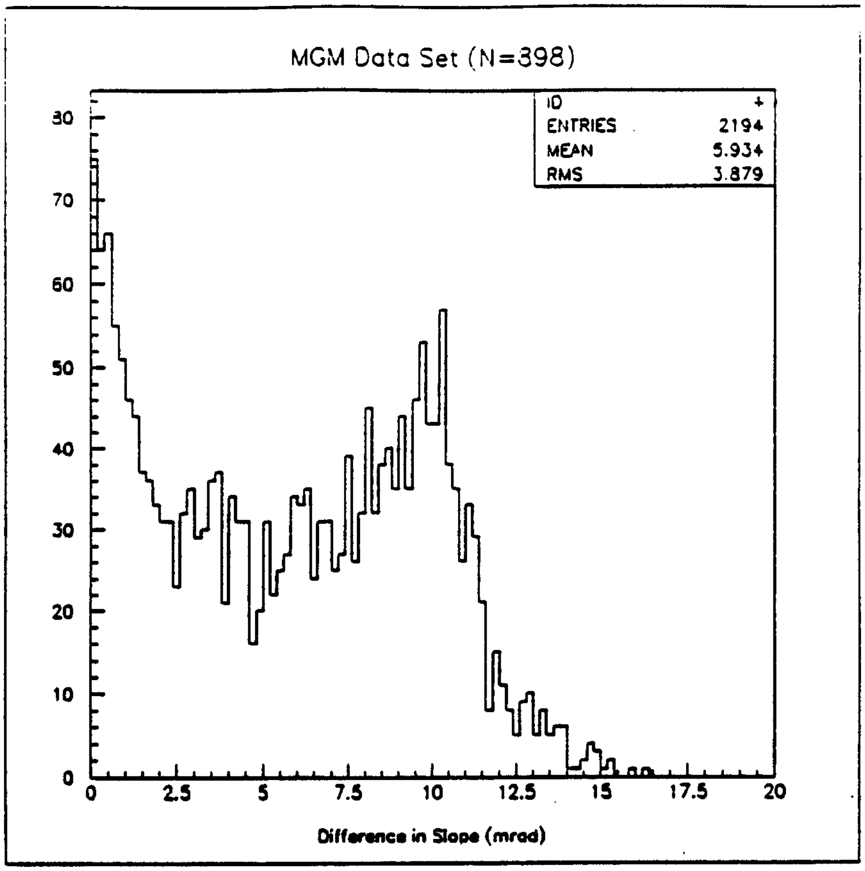

Fig. 4-19. The Difference in Slopes for Parallel Muons. The differences for both projections is plotted in milliradians. Based on the rms width of this distribution, the overall angular resolution for track pointing is 0.7°.

For the 1/s case, 2105 muons (before normalization) out of 6410 were reconstructed. The average separation is 2.05 m and the width of the distribution is 1.12 m. Although this distribution is slightly narrower than the data, the similarity between this model and the data seems remarkable considering its simplicity ($\chi^2 = 43,\ Q = 0.90,\ 56\ df$).

For completeness, the difference in slopes between muons in this model (for both the XY and ZY projections) is shown in Fig. 4-21. The rms width of the plot is 8.4 mrad, in agreement with the data.

4.5 The Muon Flux at 2100 Meters of Water Equivalent

The Vertical Muon Flux

A semi-empirical expression for the muon flux ($m^{-2}s^{-1}$) as a function of detector

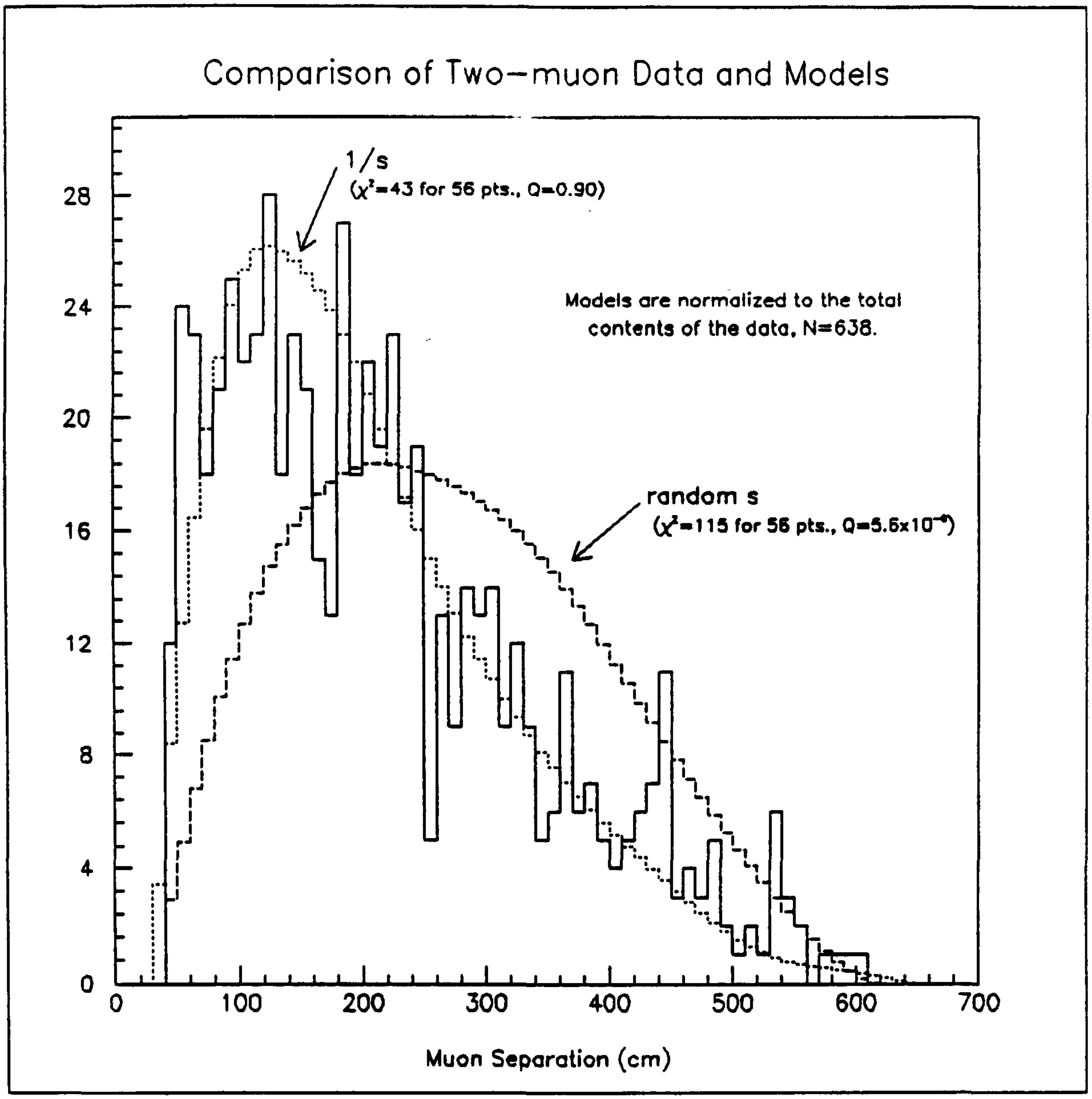

Fig. 4-20. Comparison of Two-muon Separation in the Data and the Monte Carlo Models.

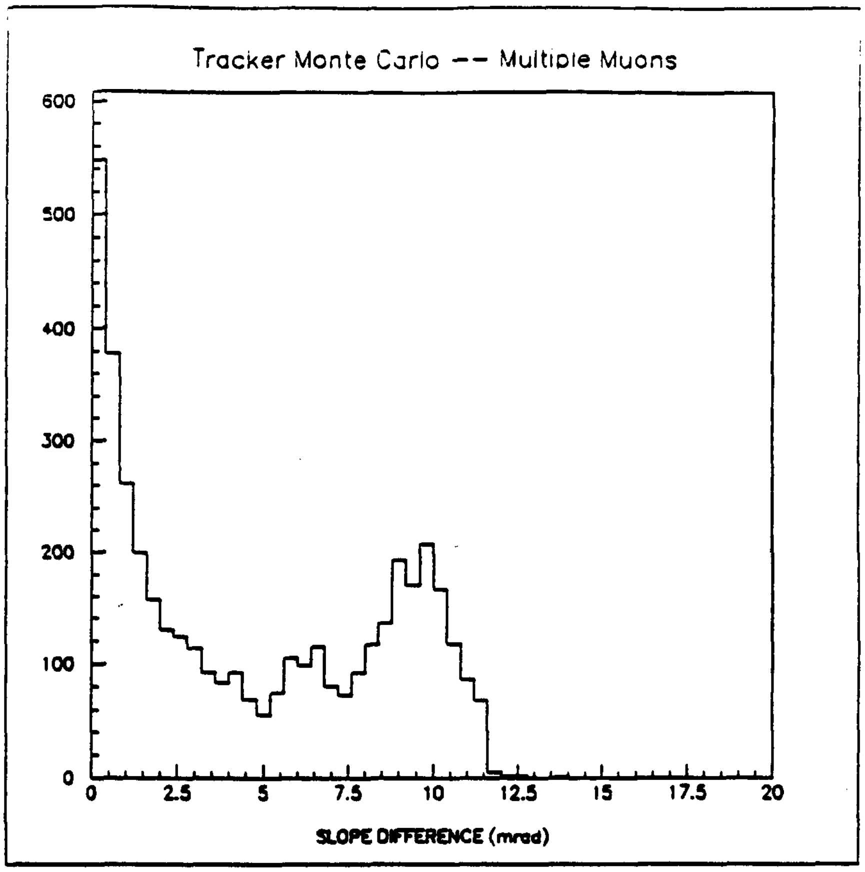

Fig. 4-21. Monte Carlo Slope Differences.

depth and muon zenith angle has been given by Miyake [9]:

$$I(d,\theta^*) = \frac{174}{d\sec\theta^* + 400}(d + 10\sec\theta^*)^{-1.53}\frac{d+75}{d+50+25\sec\theta^*}e^{-0.0008(d+10\sec\theta^*)} \qquad (4.1)$$

where θ^* is the zenith angle at production[8] and d is the detector depth in mwe (2100). The muon flux has been calculated using the vertical depth at the Tracker site and is found to be $1.05 \times 10^{-3} m^{-2} s^{-1}$. A compilation [10] of experimentally measured vertical muon rates as a function of detector depth shows agreement with the Miyake prediction.

The single muon Monte Carlo model will now be used to calculate the vertical muon flux at 2100 mwe from the trigger rate in the Tracker.

---

[8] $\cos\theta^* = \sqrt{1-\sin^2\theta^*}$, $\sin\theta^* = \sin\theta \cdot (R_e - d)/(R_e + a)$ where R_e is the radius of the Earth, a is the height of the atmosphere and θ is the zenith angle of observation.

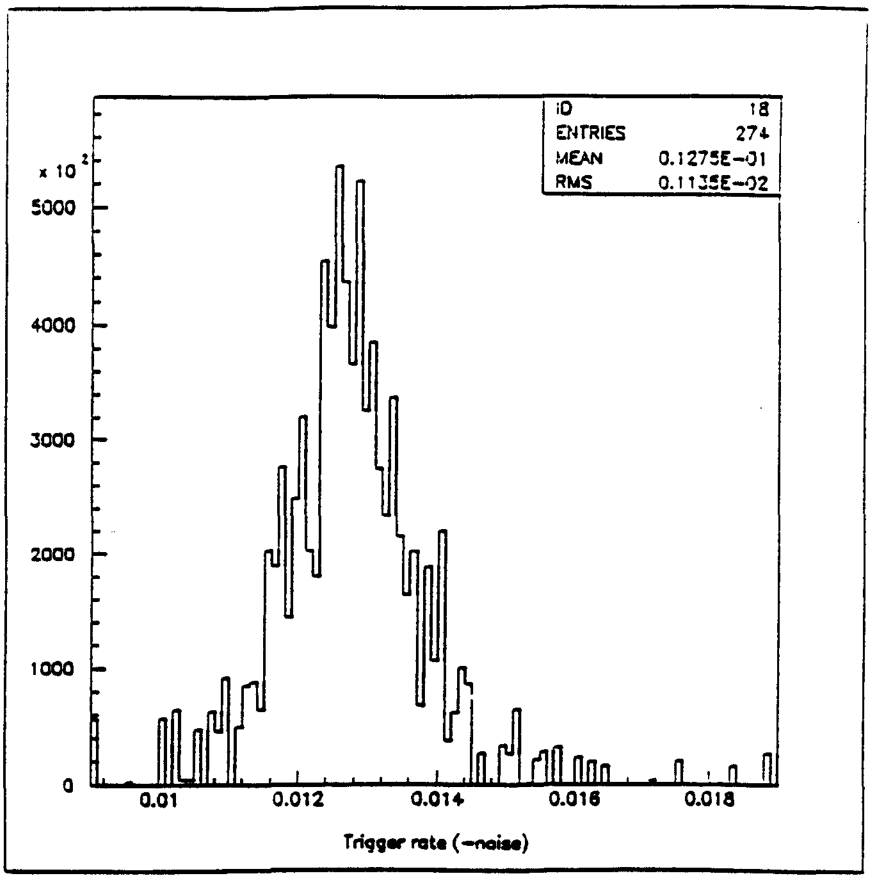

Fig. 4-22. Trigger Rate for Cosmic Ray Runs. The trigger rate in Hz for runs occuring before the installation of the Tracker extension is shown. Each entry is weighted by the amount of elapsed time in the run. The average trigger rate from this plot is 1.28 × 10^{-2} Hz.

It is necessary to include a measurement of the efficiency for detection of $0{\cdot}1 + 1{\cdot}2 + \cdots + 62{\cdot}63$. The efficiency is 0.970 ± 0.002. The trigger requires three layers to be in coincidence so the measured rate must be scaled by a factor of 0.970^{-3}.

It is likely that many real muons were removed from the analysis because of the cut placed on triggers with bad data buffers; 17,153 triggers were thrown out in this cut alone. Since most of these are believed to be real muons, we will set an upper limit on the flux based on the total number of triggers accumulated in a run minus the number of noise triggers (8534 total), since these are not believed to be real muon events. The trigger rate for runs prior to the installation of the extension are shown in Fig. 4-22. Entries are weighted by the amount of elapsed time in the run. The average trigger rate is 1.28×10^{-2} Hz.

Let N be the total number of triggers recorded per unit time by the Tracker. Then,

$$N = \int_{\Omega} \left(\frac{dN}{d\Omega}\right)_{\nu} \cos^2\theta \, d\Omega \, . \tag{4.2}$$

The quantity in parentheses represents the vertical muon intensity in units of $m^{-2}s^{-1}sterad^{-1}$ which is what we wish to measure. The integral over solid angle gives a factor of $2\pi/3$. The vertical muon flux is then given by

$$\left(\frac{dN}{d\Omega}\right)_{\nu} = \frac{3}{2\pi} \times N. \tag{4.3}$$

Scaling this by the ratio of the number of hits in the 100 m^2 plane to the number of hits detected in the trigger for the Monte Carlo and correcting for efficiency gives us an *upper limit on the vertical muon flux*:

$$\left(\frac{dN}{d\Omega}\right)_{\nu} = \frac{3}{2\pi} \times 0.0128 \times \frac{23.14}{100} \times (0.970)^{-3} = 1.55 \times 10^{-3} \; m^{-2}s^{-1}sterad^{-1} \; . \tag{4.4}$$

The time history showing the rate for *reconstructed events* satisfying the trigger requirement (T1·T2·T3) is given in Fig. 4-23. The decrease in performance noted in the singles rate measurement is also evident but to a smaller extent. As stated before, the exact number of real muons in the triggers with bad data buffers is not known for sure. A value for the vertical muon flux can be derived by using the muon rate inferred from the time separation distribution of muons in the golden single muon data sample. This rate is 0.76×10^{-2} Hz. Using the number of triggers that satisfied the trigger requirement after reconstruction sets a *lower limit on the vertical muon flux*:

$$\left(\frac{dN}{d\Omega}\right)_{\nu} = 0.92 \times 10^{-3} \; m^{-2}s^{-1}sterad^{-1}. \tag{4.5}$$

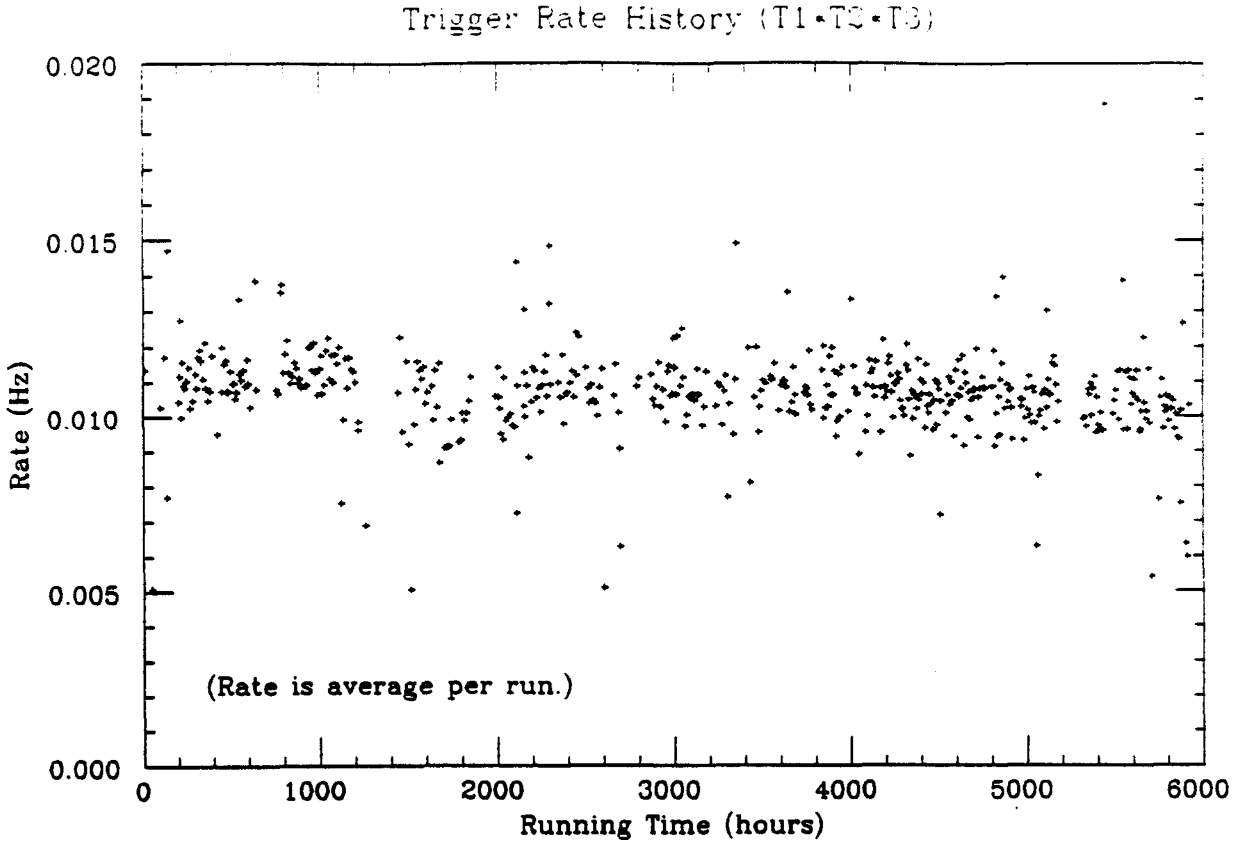

Fig. 4-23. Time History for Reconstructed Event Rates. The slight drop in rate for singles shown in Fig. 4-3 is not as evident in reconstructed events.

Variations in the Muon Rate

It has been postulated that time variations in surface cosmic ray intensity exist at the level of a few tenths of a percent but no clear period, amplitude or phase has been established [11]. A simple study was carried out to see if *any* variations could be detected in the Tracker data. The study made use of a sample of data which included those triggers that satisfied all cuts applied before the pattern–recognition and track fitting algorithms. The average number of muons per hour was calculated for all muons in the sample. Shown in Fig. 4-24 is the muon rate per hour for each hour of the day weighted by the amount of livetime for that hour. The average rate is $36.8 \pm 1.2\ h^{-1} = (1.02 \pm 0.03) \times 10^{-2}$ Hz. Note that this rate is less than the trigger rate in the detector but greater than the rate for totally reconstructed tracks in the golden single muon sample. No sinusoidal variation is evident in the data at the level of a few percent. Larger fluctuations are observed in the daytime hours when system checkout and debugging was going on.

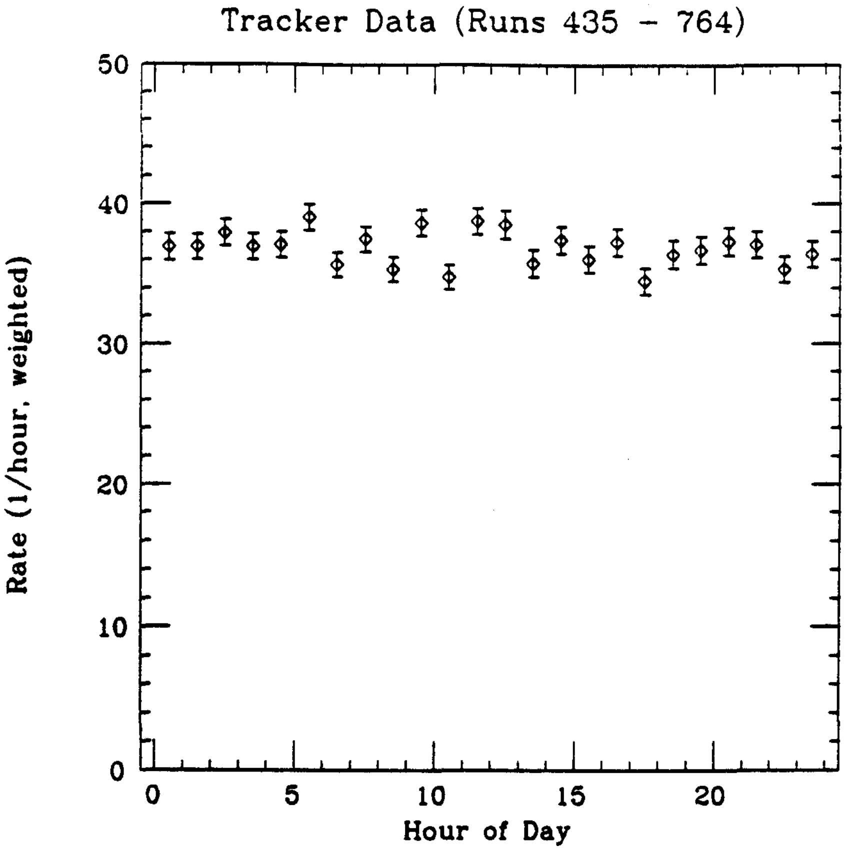

Fig. 4-24. Muon Rate per Hour.

Chapter 4 References

[1] Barr, G. D., 'The Separation of Signals and Background in a Nucleon Decay Experiment', Ph.D. Thesis, Michaelmas Term, 1987.

[2] Ruddick, K., 'Estimates of Natural Background Activity in Soudan I/II (non cosmic ray)', PDK–96, Jan, 1984.

[3] Ruddick, K., 'Radioactivity in the Soudan', PDK–114, Mar, 1984.

[4] Ruddick, K., 'Final Report on Natural Radioactivity in the Soudan Mine', PDK–194, April, 1985.

[5] Kochocki, J. A. and Oliver, W. P., 'Pattern Recognition and Track Fitting from Hit Patterns in the Tracker', Tufts Internal Memo, Oct, 1988.

[6] Press, W., H., *et al.*, Numerical Recipes, (Cambridge University Press, 1986).

[7] Bartelt, J., *et al.*, Phys. Rev. D 32, 1630 (1984).

[8] Cherry, M. L., *et al.*, Phys. Rev. D 27, 1444 (1983).

[9] Miyake, S., Rapporteur Talk 13th Int. Cosmic Ray Conf., Denver, (1973), Vol. 5, p. 3638.

[10] Menon, M. G. K. and P. V. Ramana Murthy, Progress in Elementary Particle and Cosmic Ray Physics, edited by J. G. Wilson and S. A. Wouthuysen (John Wiley, New York, 1967), Vol IX, p. 188.

[11] Montgomery, D. J. X., Cosmic Ray Physics, (Princeton University Press, 1949).

CHAPTER 5. CYGNUS X–3 MUON ANALYSIS RESULTS

As described in the previous chapter, the strict cuts placed on the data yielded a sample of golden single muons which represents slightly less than half of the total data collected. The subset of this sample which contains muons from the Cyg X–3 direction will be used to determine the excess muon flux from that direction. We will begin with a description of the golden single muon data sample in terms of celestial coordinates. The concepts and mathematical tools necessary to carry out the transformation from the local lab coordinate system to the celestial coordinate system are used extensively and are described in Appendix C.[1] Once the basic algorithms for achieving the transformation are specified, the actual mapping is straightforward and one can quickly determine which muons in the set come from the source direction (within certain cuts of course). Next, the detector sensitivity as a function of the position of Cyg X–3 will be described since this is important in the most difficult part of the calculation, the background for the signal. That is, if the primary cosmic rays arrive isotropically, how many muons do we expect to observe in a patch of the celestial sphere centered at some right ascension, α, and declination, δ. In this analysis, the patch will always be a cone centered about a source or background direction with a given half-angle size. In an attempt to improve the signal-to-background ratio for this analysis, we will make use of the ephemerides, as determined by X–ray analysis, of the (presumed) orbital period of the source. Using the arrival times of muons at the solar system barycenter (SSBC) and an ephemeris of the source, the Cyg X–3 phase of each muon will then be calculated. The flux of excess muons from the source direction will be determined with use of the Monte Carlo simulation described in Chapter 3. Finally, the same analyses performed on a small set of golden multiple muons extracted from the data will be briefly described.

---

[1] A set of general references [1–6] found to be very useful in this work is listed at the end of this chapter.

5.1 Celestial Mapping

By application of the principles set forth in the Appendix C, we are able to determine the distribution of muons as a function of celestial coordinates α and δ. The mapping to be performed takes local coordinates on the Earth and maps them to the fixed celestial sphere:

$$(\theta, \phi, t) \rightarrow (\alpha, \delta). \tag{5.1}$$

Distributions in δ and α are shown in Figs. 5-1 and 5-2 for muons in the golden sample. Neither distribution shows any significant peaks or "hotspots". The distribution in δ has a maximum at 46°, just shy of the latitude of the detector (47.7°) and indicating an acceptance that favors muons from the direction of the celestial equator (*i.e.*, south). Again, this is due to the asymmetry built into the geometry of the detector. It is seen that the acceptance of the Tracker limits the amount of the sphere that can be viewed; no muons come from either the celestial equator or from the north celestial pole. The distribution in α is statistically flat as one would expect for an isotropic background. A three–dimensional plot of α vs δ is shown in Fig. 5-3. The bin size in the plot is 2° in $\delta \times 4^\circ$ in α, close to the resoultion of the Tracker.

5.2 Detector Sensitivity and the Overburden at the Cygnus X–3 Declination

Detector Sensitivity

To calculate the total livetime of the detector, a scan was made of the total data set to extract the begin-run and end-run times for each run that recorded at least one cosmic ray trigger. The elapsed time per run was summed for years 1987 and 1988, a total of 0.50 year over the course of about 8 months. This number has been corrected for computer deadtime using a nominal value of ~ 1 % (see Fig. 5-4). The begin-run and end-run times were tabulated for later use.

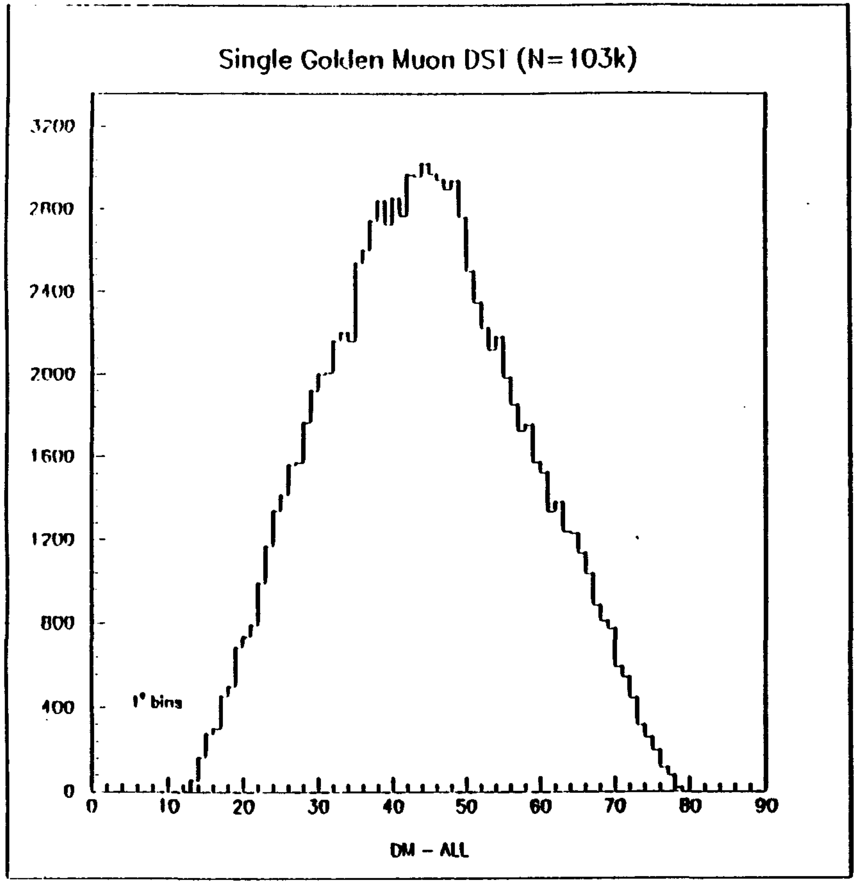

Fig. 5-1. Declination of Muons in the Golden Single Muon Sample. Because of the limited acceptance of the Tracker, muons from the directions of the celestial equator ($\delta = 0°$) and the north celestial pole ($\delta = 90°$) are not detected.

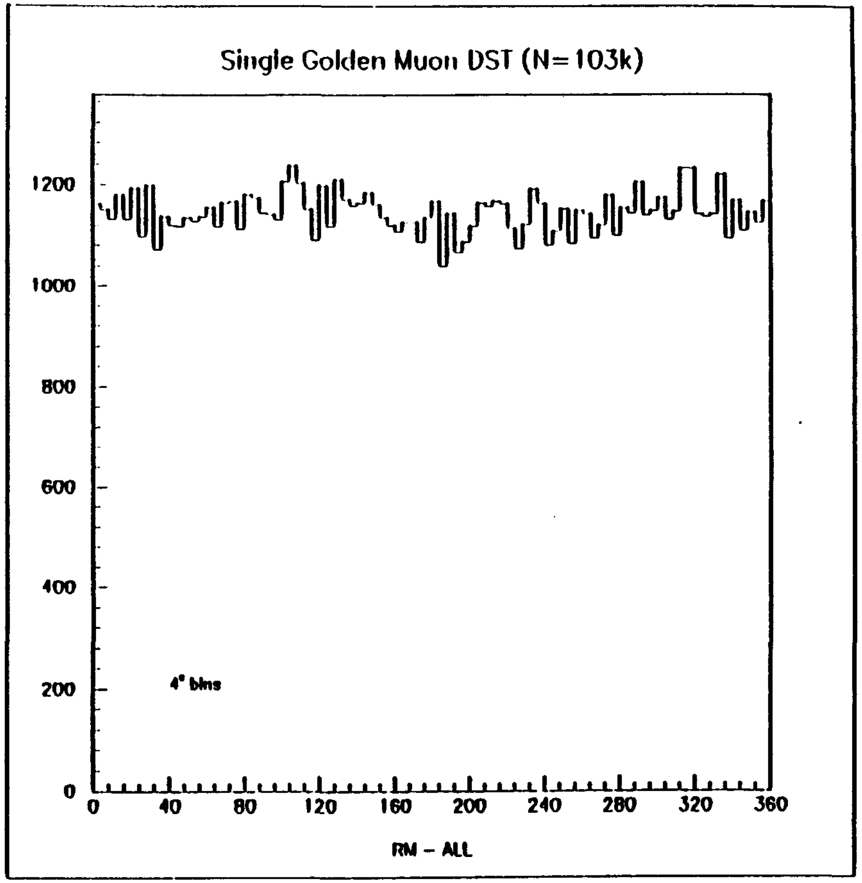

Fig. 5-2. Right Ascension of Muons in the Golden Single Muon Sample. For an isotropic cosmic ray background, one expects a flat distribution in α as seen here. The origin of longitudinal measure ($\alpha = 0$) is the vernal equinox, Υ.

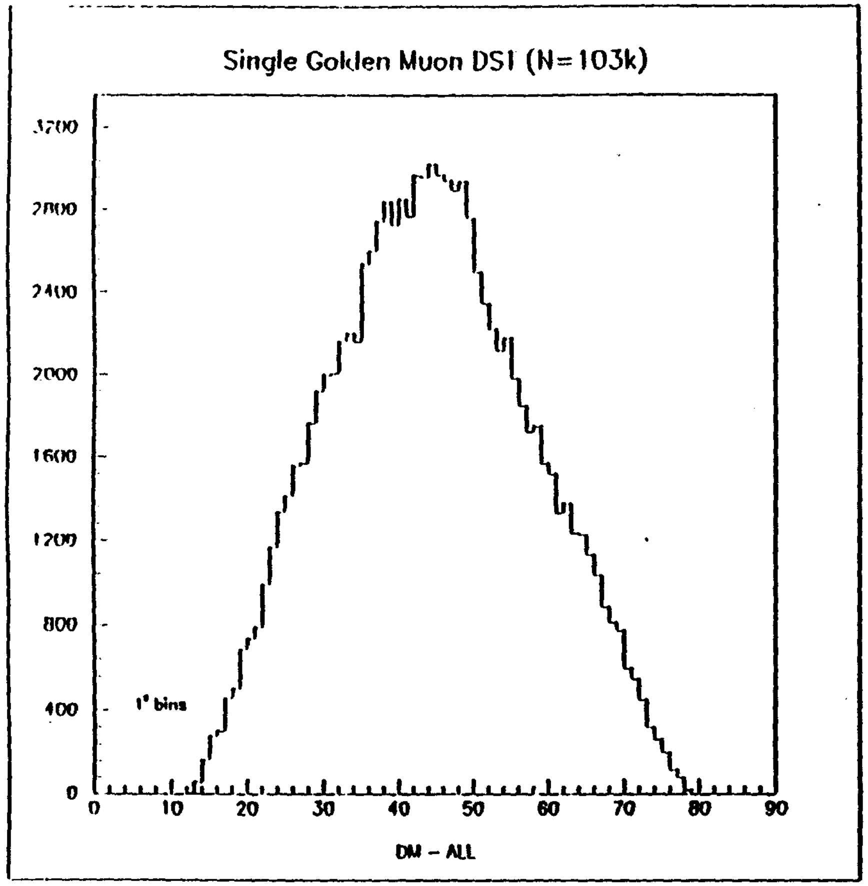

Fig. 5-1. Declination of Muons in the Golden Single Muon Sample. Because of the limited acceptance of the Tracker, muons from the directions of the celestial equator ($\delta = 0°$) and the north celestial pole ($\delta = 90°$) are not detected.

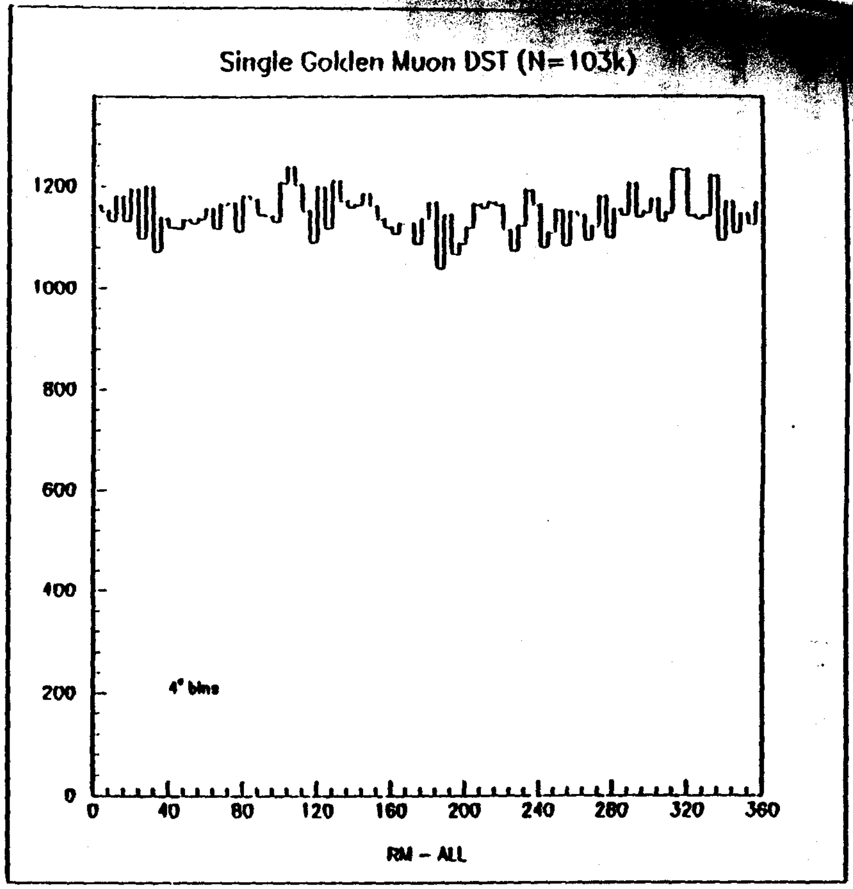

Fig. 5-2. Right Ascension of Muons in the Golden Single Muon Sample. For an isotropic cosmic ray background, one expects a flat distribution in α as seen here. The origin of longitudinal measure ($\alpha = 0$) is the vernal equinox, Υ.

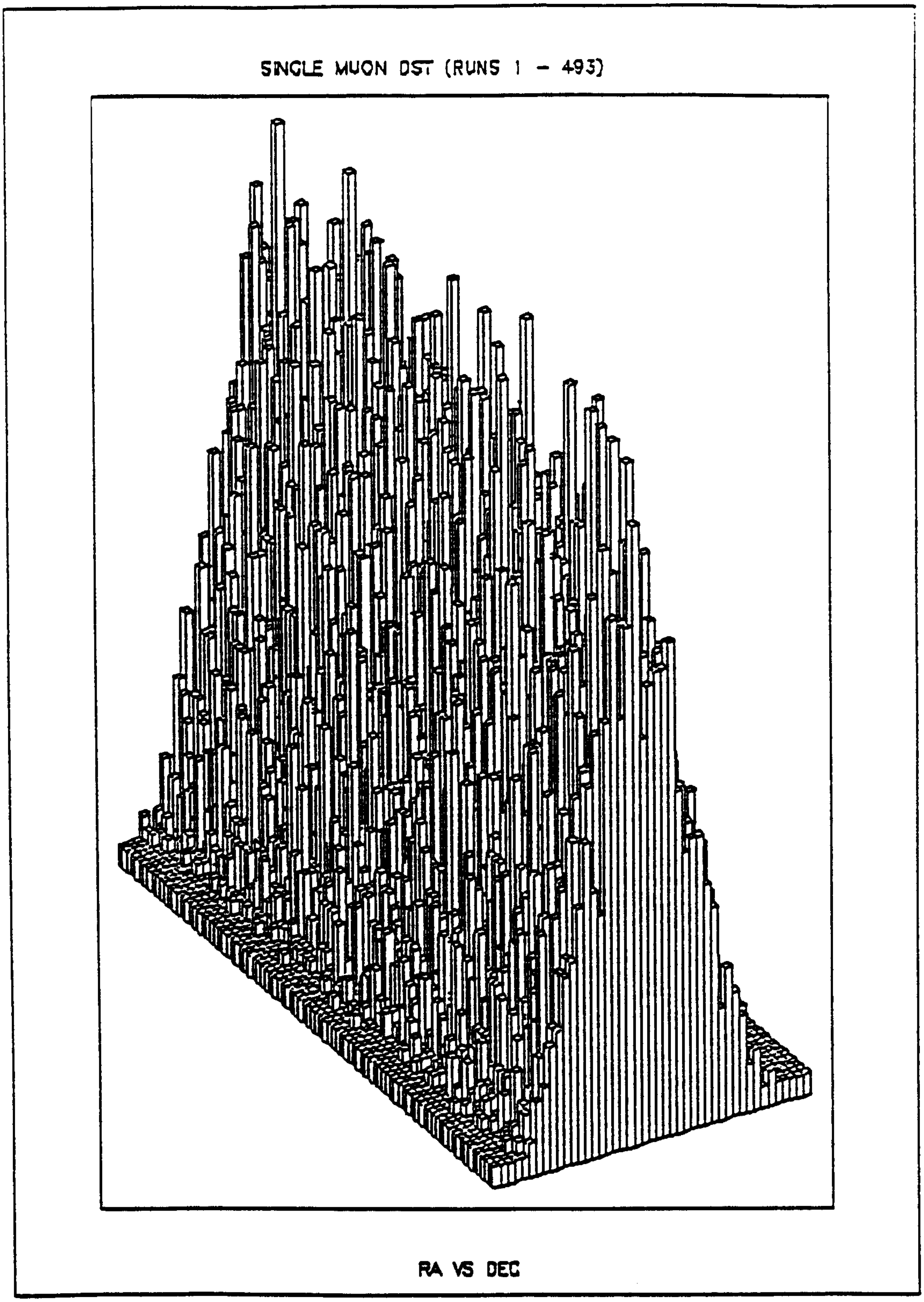

Fig. 5-3. α *vs.* δ.

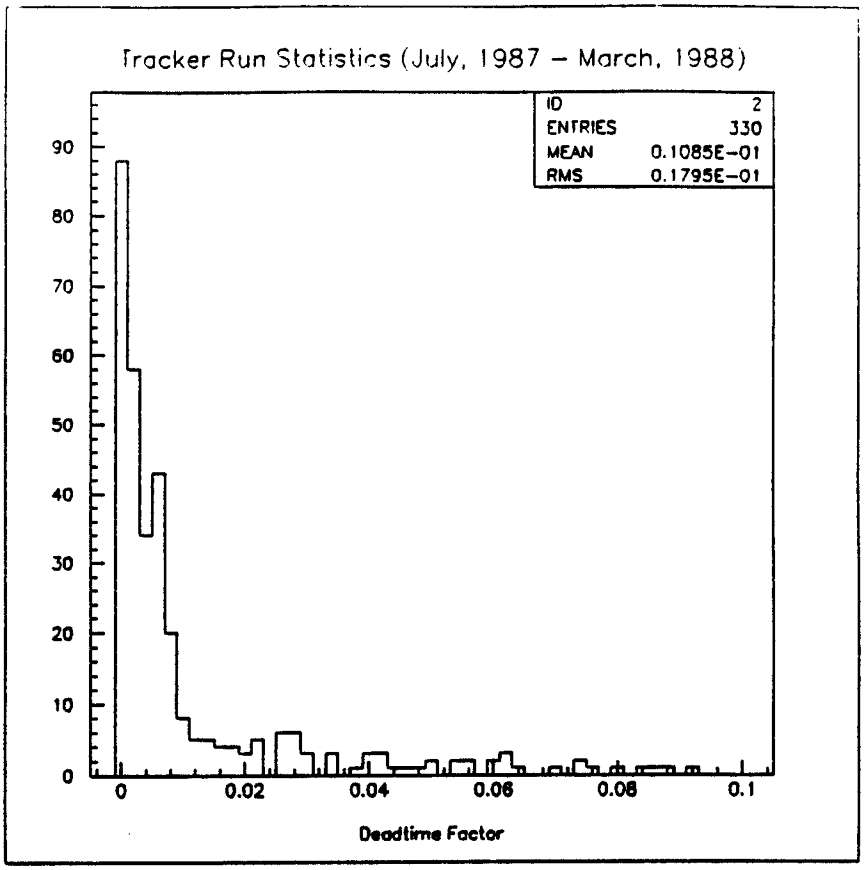

Fig. 5-4. Deadtime Factor for Cosmic Ray Runs. A scaler, not under computer control, counted the actual number of triggers which occurred during a run. The difference between the number of recorded triggers and the scaler count allowed us to determine the deadtime during a run (~ 1 %).

We will now study the sensitivity of the detector as a function of the position of Cyg X-3. There are a number of ways to examine this problem. We chose to calculate the livetime as a function of the hour angle (h_{Cyg}) of the source. The hour angle represents the time until ($-$) or since ($+$) transit of an object on the celestial sphere with the celestial meridian of the observer. The hour angle is expressed in degrees with $-180 \leq h \leq +180$. Any deviation from a flat distribution signals a favoring of certain hour angles over others and this will have to be corrected. An algorithm was designed to determine the detector livetime as a function of the hour angle of Cyg X-3. An internal (software) clock was created with t_0 equal to the begin-run time for the very first run and increment $\delta t = 60$ s. At the center of each bin in time, the program calculates h_{Cyg} and increments the appropriate bin (with care taken for those time intervals which split two bins). Stepping through each run, the program summed the amount of livetime for each portion of the celestial sphere as shown in Fig. 5-5. The plot is centered on the Cyg X–3 right ascension and uses bin widths of 6°. (To allow for the bin at $h_{Cyg} = 0$ to be centered at the exact right ascension of Cyg X–3, the bin centered at $h_{Cyg} = 180°$ has been split in two. This can be seen in the plot where the sum of the contents of the bins at $h_{Cyg} = \pm 180°$ is equal to the total expected for a single bin at that angle.) The plot is not flat and shows less sensitivity for most directions away from Cyg X–3. The maximum variation in sensitivity with h_{Cyg} is 10 %. Since the increment for the internal clock was set at 60 s, each entry in the sensitivity distribution represents that amount of livetime, so that a sum over all bins produces the total experimental livetime. This plot will be used normalize the livetime for all directions.

Overburden

Figure 5-6 is a distribution of the overburden as a function of h_{Cyg} as seen by muons which arrive from the same declination as Cyg X–3. This has been derived from a scan of the overburden data. Knowing α and δ for some source, one can then use the transformation equations 3.7–3.9, to calculate the local coordinates of the source as it tracks across the sky. The vertical scale shows the amount of overburden in mwe at each hour angle. Superimposed on the overburden plot is the distribution of the number of muons as a function of hour angle (at the time of observation) for the data sample. The same vertical scale also represents the number of muons detected at each hour angle. The detector acceptance limits hour angle values to $|h| \leq 50°$. The overburden seen by muons is essentially constant (2100 mwe) for all hour angles within the acceptance.

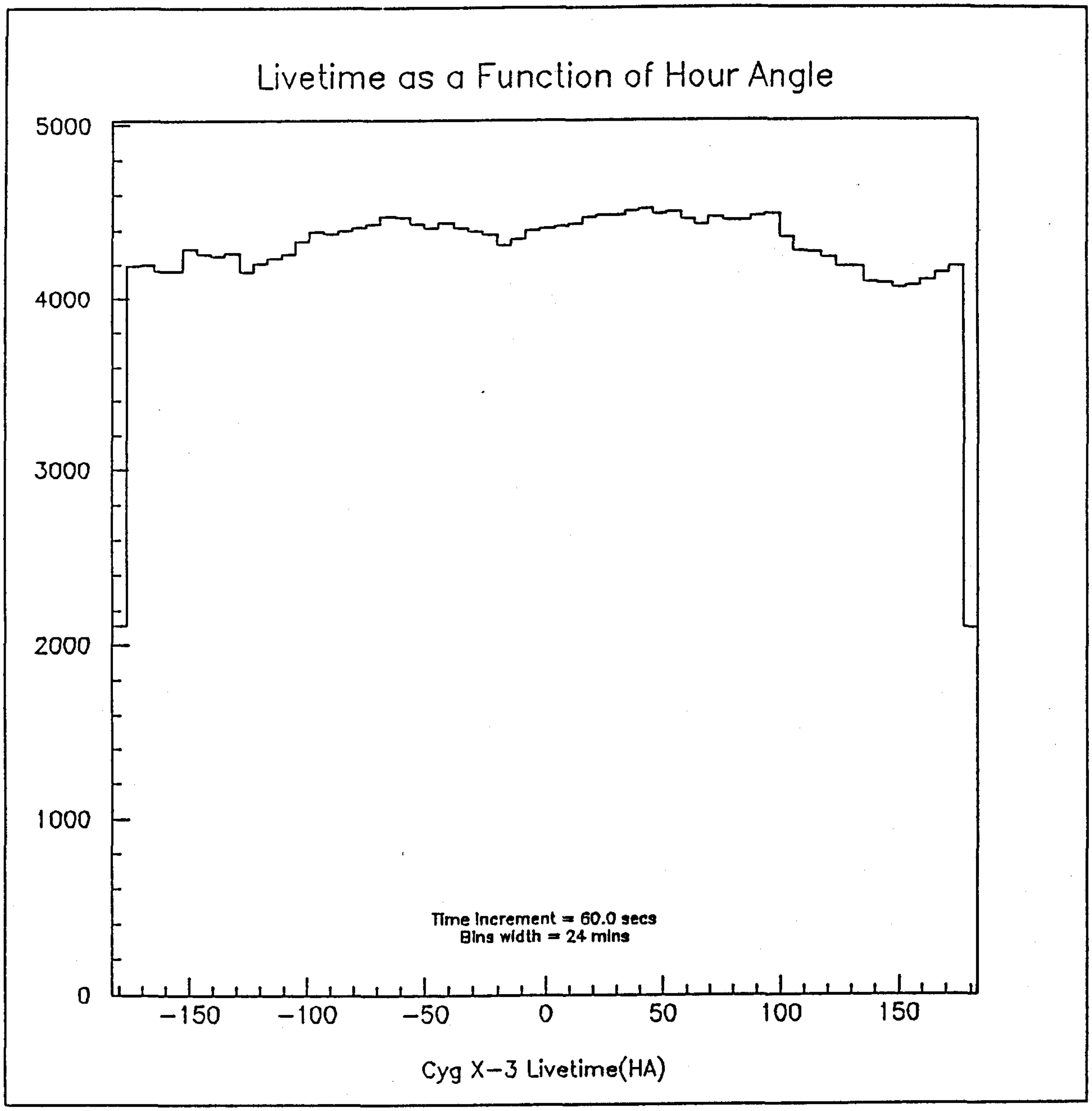

Fig. 5-5. Livetime as a Function of Cyg X-3 Hour Angle. The plot shows the sensitivity of the detector as a function of the hour angle of the source, h_{Cyg}. The bin at $h_{Cyg} = 0°$ is centered on the right ascension (1987.5) of Cyg X-3 and the bin at $\pm 180°$ has been split in two. Note that the bin width is $6°$ and each entry in the plot corresponds to 1 minute of livetime.

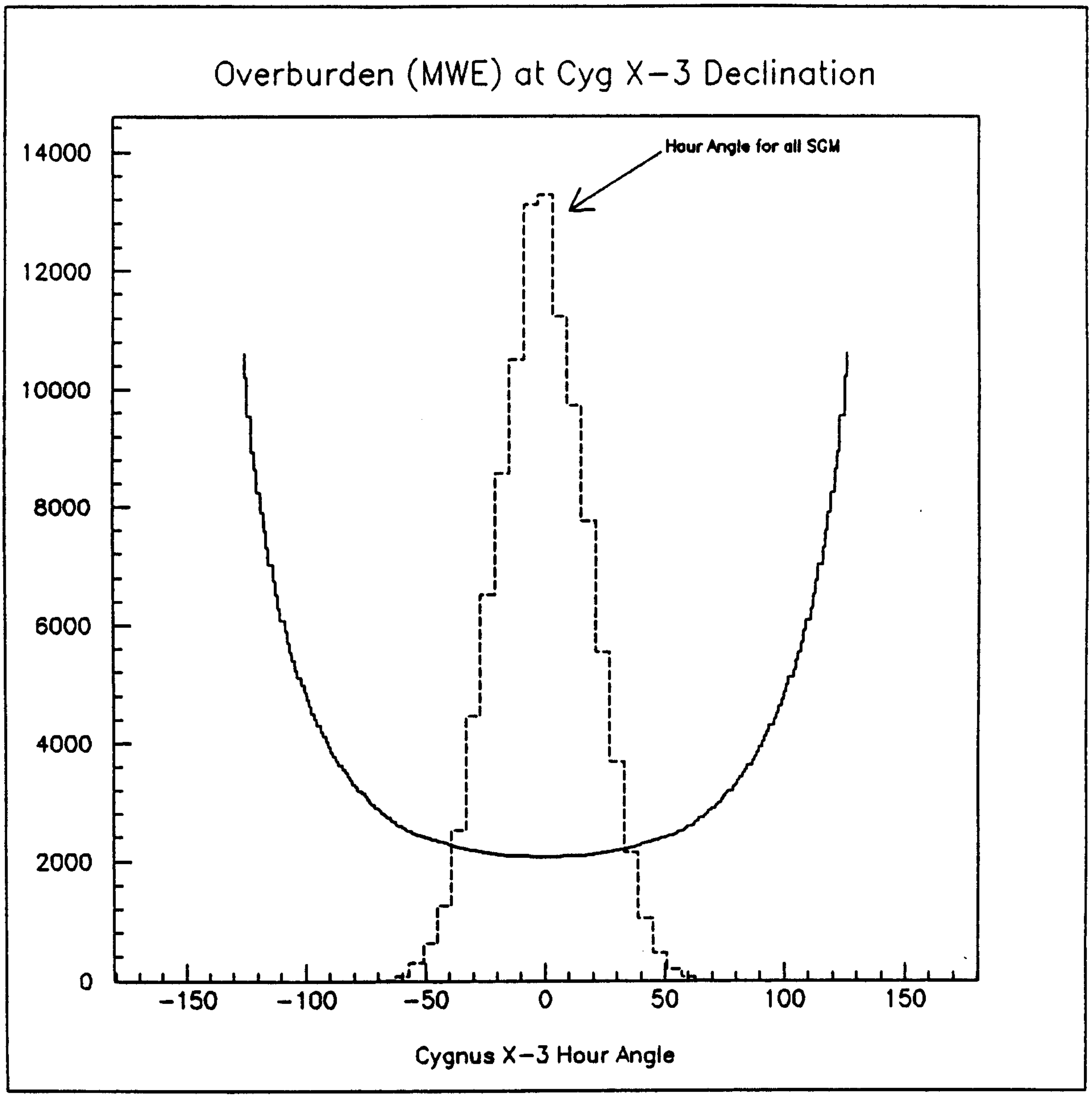

Fig. 5-6. The Amount of Overburden (MWE) Between the Detector and the Surface in the Cyg X-3 Direction. The vertical scale indicates the amount of overburden traversed by a muon at a given hour angle of the source. The hour angle of all muons in the golden single muon sample is superimposed over the overburden description. The same vertical scale indicates the number of muons at each hour angle. The overburden is essentially constant for muons within the Tracker acceptance.

5.3 The 3° Half-angle Cone Cut

Time-independent Background and Source Analysis

The goal of this calculation is to determine the number of muons to be expected from the Cyg X–3 direction within a 3° half-angle cone. The background for the Cyg X–3 direction has been studied using 29 3° half-angle cones, centered at the same declination as Cyg X–3 and spaced every 12° in right ascension. With this spacing there is no overlap between cones. (The on-source cone is centered on the 1987.5 coordinates of Cyg X–3, $\alpha = 307.99583°$ and $\delta = 40.91500°$.) A scan is made of the golden single muon data sample. From the track slopes in both projections, the latitude of the detector, and the time of observation, the declination and hour angle for each muon is determined. Knowing the longitude of the detector, the right ascension of the muon can be determined by first calculating the Greenwich mean sidereal time (GMST) and then the local sidereal time (LST) of the event.[2] The celestial direction cosines of the muon are formed. A loop over the 29 background directions is then executed. From the direction cosines of the muon and the chosen cone direction, a dot product is formed from which the angular separation of the two directions can be determined. If the angular separation falls within the prescribed cut about one of these cones, the muon is accepted. Muons falling outside the cut are rejected.

The hour angle distribution for muons in the Cyg X–3 cone are shown in Fig. 5-7. Plots of the hour angle of each muon in each of the 29 cones in the background scan are shown in Fig. 5-8. The first plot in the figure is for the source cone. The horizontal axis is the hour angle of the muon and the vertical axis is the number of muons per bin. Note that the bin size of 6° in these plots is exactly the same as that used in the livetime calculation above. All the plots show essentially the same (normal) shape. (Incidentally, each of the hour angle distributions has a negative mean value ($\sim -1°$), once again a result of the shift between the upper and lower overlap regions in the detector.)

---

[2] See the example in Appendix C.

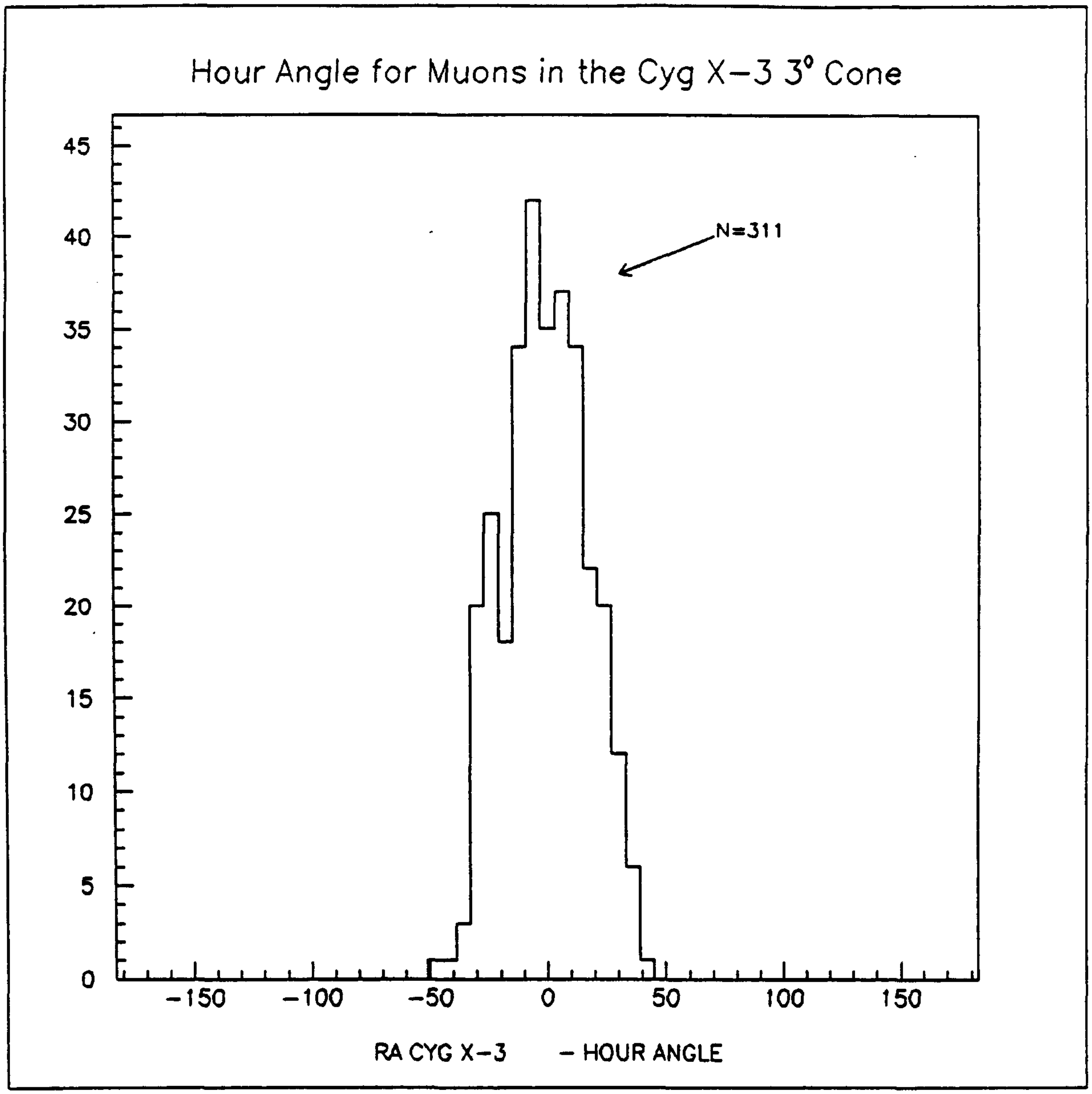

Fig. 5-7. The Hour Angles for Muons in the Cyg X-3 3° cone. A total of 311 muons were found in the source cone.

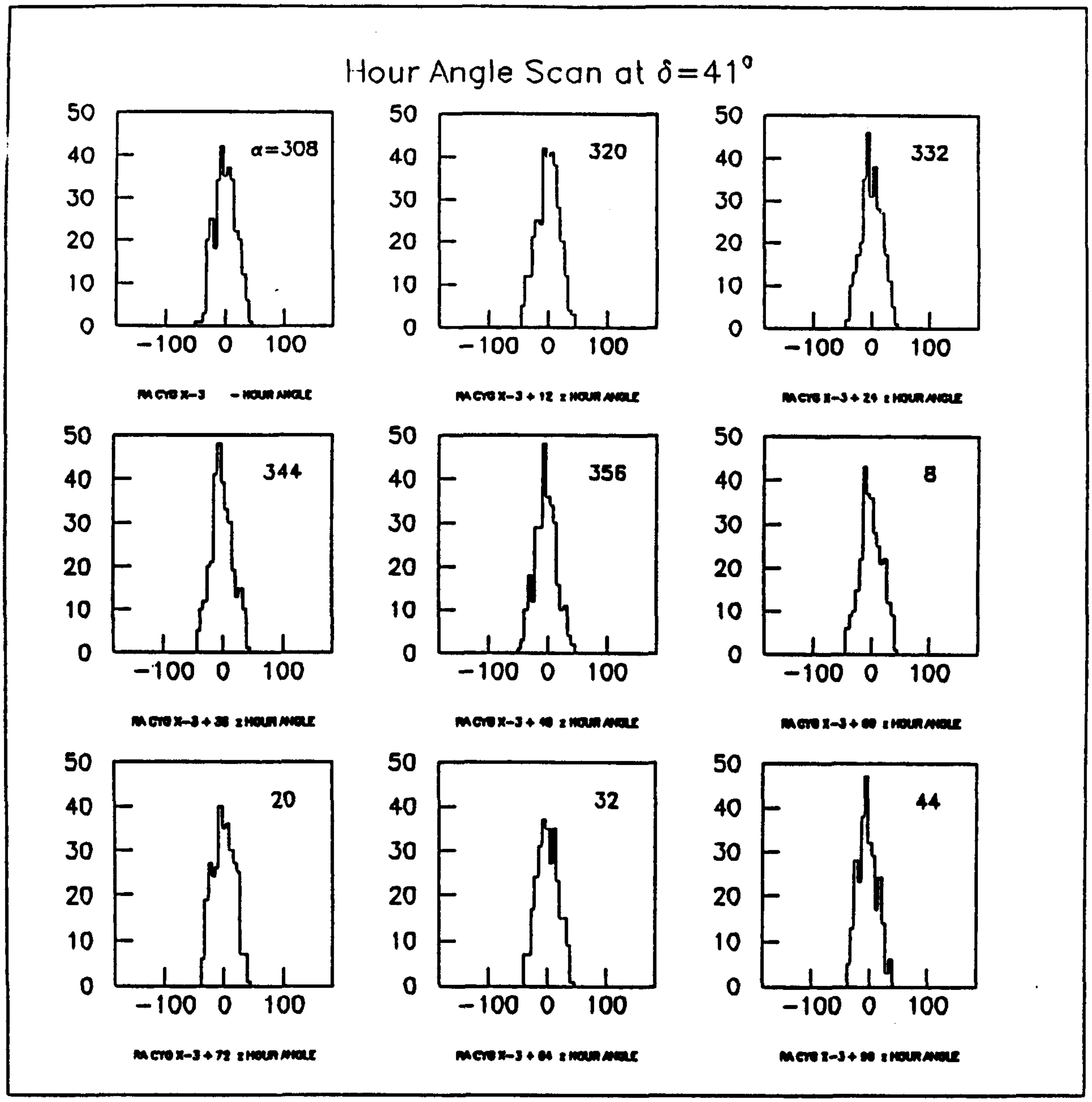

Fig. 5-8. Hour Angle Plots for the Source + 29 Background Directions. The first distribution in the set is for the source at $\alpha = 308^\circ$ and the others are for the 29 background directions spaced every 12 degrees in right ascension. These distributions are not corrected for detector sensitivity.

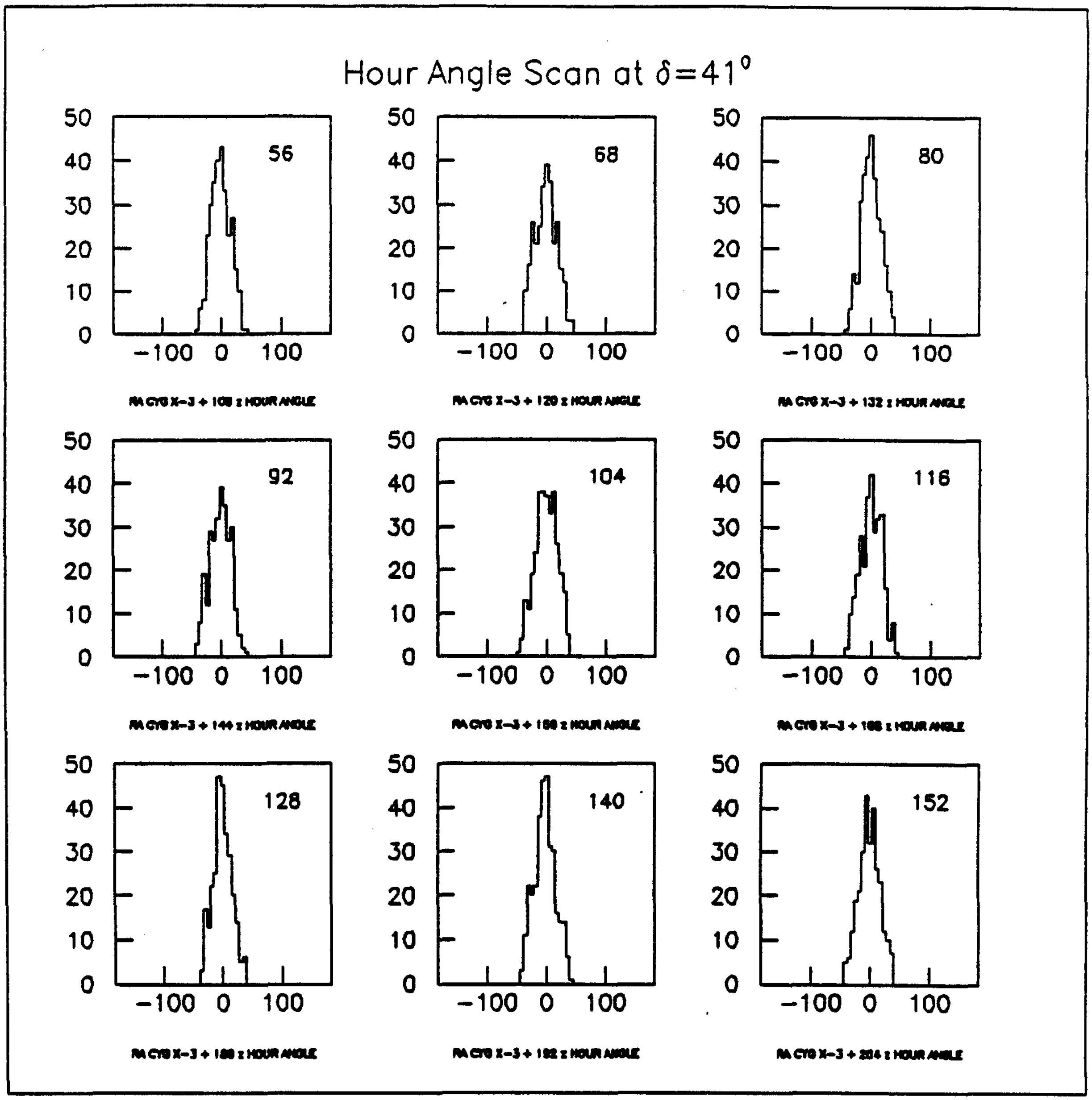

Fig. 5-8 continued.

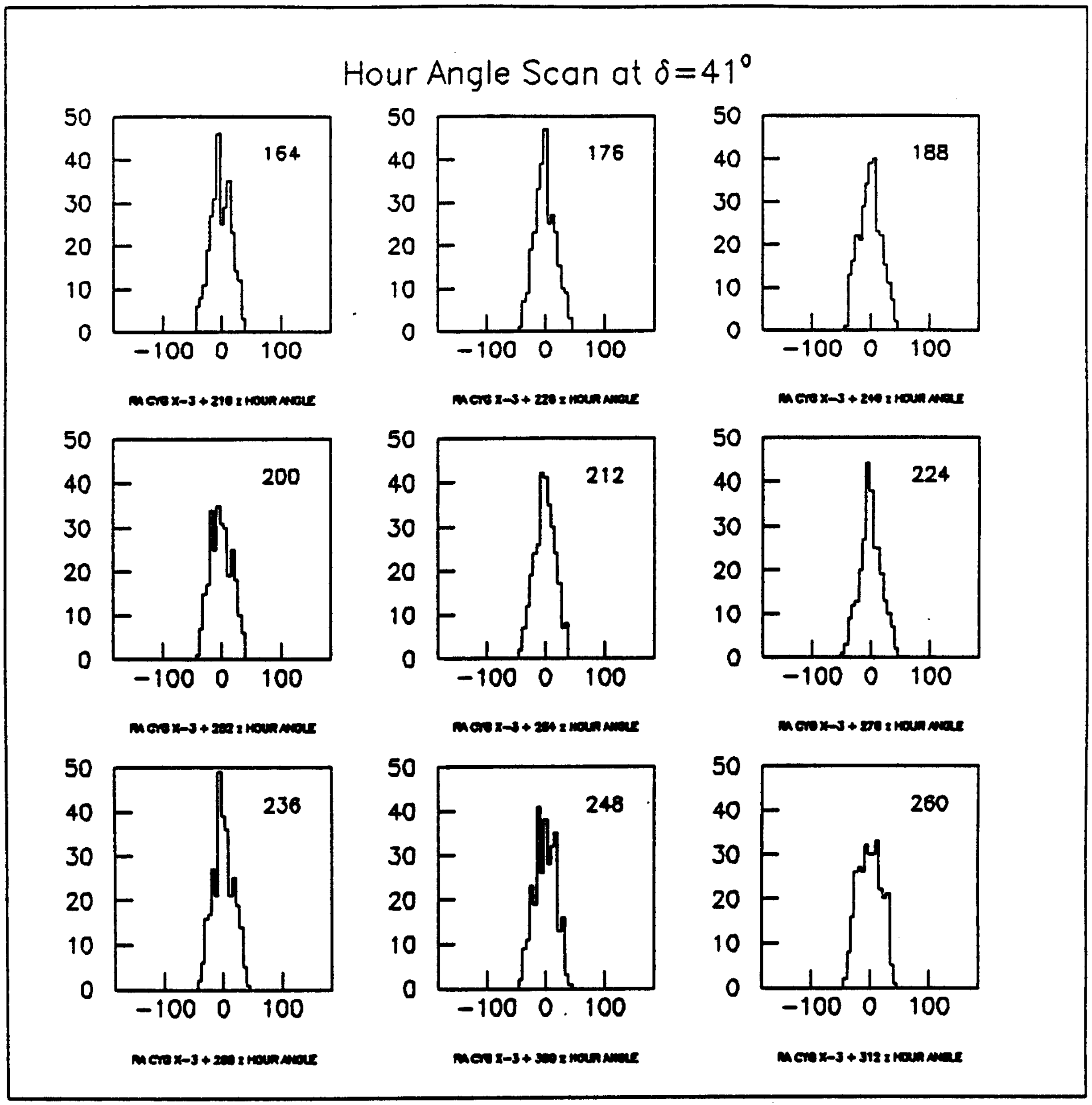

Fig. 5-8 continued.

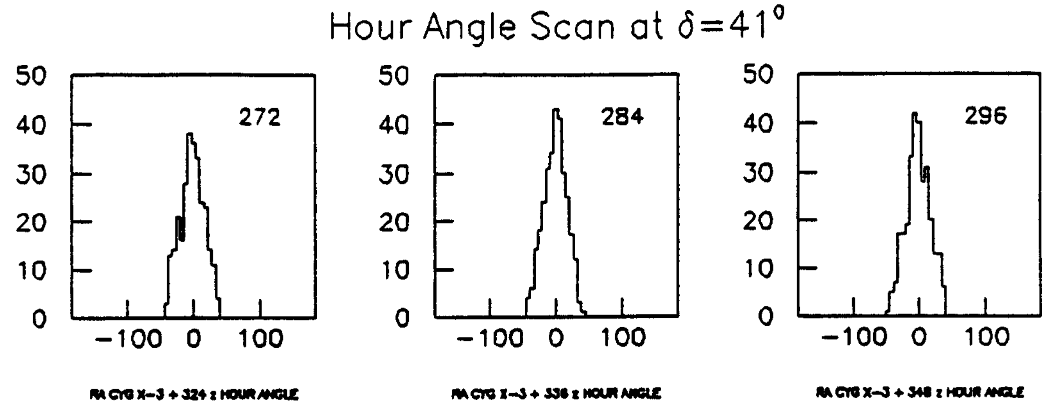

Fig. 5-8 continued.

The distribution of the number of muons in each 3° half-angle cone as a function of right ascension is shown in Fig. 5-9. The source cone is highlighted and indicates a slight (insignificant) excess above the expected background. The average number of muons per *background* cone, uncorrected for detector sensitivity, is 293.0. The solid line is at 301.3 muons per cone and this indicates the background after correction is made for detector sensitivity. The background calculation will next be described.

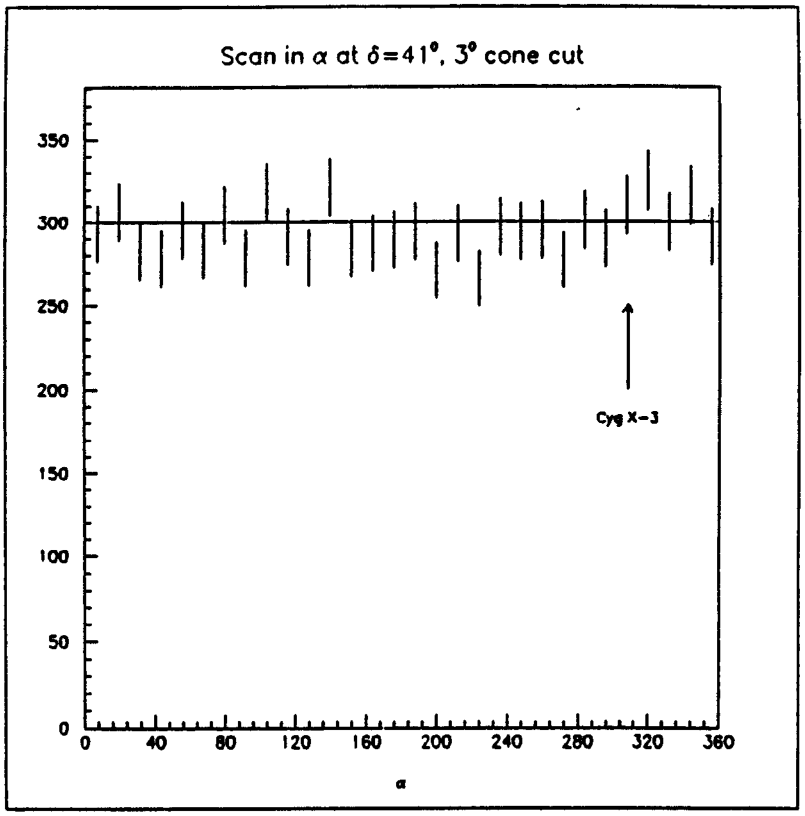

Fig. 5-9. The Number of Muons per 3° Cone. The source cone is seen to have a small excess (10) of muons above the livetime-corrected background of 301.3 which is indicated by the solid line in the plot.

We now wish to determine what effect, if any, the variation in detector sensitivity has had on these distributions. Since the detector appears to have more sensitivity for the Cyg X-3 direction, we expect the background number of muons to increase. The calculation is performed by normalizing the number of muons in each hour angle bin by an appropriate amount of livetime. The normalization for the bin centered on the source is chosen to be 1. Then, each hour angle bin in the 29 plots gets its amount weighted according to the livetime in each bin of the livetime vs hour angle plot (Fig. 5-5).[3] Since each plot is centered on a different right ascension, care must be taken here to remember that hour angle increases as right ascension decreases. Recalling that the time increment in the livetime plot is 60 s, we may calculate the flux of muons from each of the 29 background directions by dividing the number of muons in each bin in hour angle by the livetime for that bin. An average background flux per 3° cone is then calculated by summing the flux in each hour angle bin over all 29 background directions and dividing by the total number of directions. The product of the average background flux in each hour angle bin and the detector sensitivity for the corresponding Cyg X–3 hour angle bin, gives the expected number of muons ber bin. By summing over all bins, we arrive at the total expected number of muons in the 3° half-angle on-source cone: 301.3. The Cyg X–3 cone therefore has a small, insignificant excess of muons: 311 ± 18 were found when 301.3 ± 17 were expected.

Time-dependent Background and Source Analysis

To remove effects caused by the orbit of the Earth about the Sun, the arrival time of all muons in each of the 3° cones at a plane which crosses the SSBC, and has a normal unit vector in the Cyg X–3 direction, was calculated using an ephemeris interpolation program provided by the Jet Propulsion Laboratory (JPL) [7]. The JPL ephemeris uses the J2000.0 epoch for determination of the Earth's position relative to the Sun.[4]

We now use knowledge of the source obtained in some of the various ephemerides mentioned above as determined by the X-ray data.

---

[3] The changes are small and do not call for a repeat of all 29 plots.

[4] To be precise here, the JPL package allowed one the option of choosing either the location of the center of our Sun or the location of the barycenter of our solar system relative to Earth. We chose the latter in this calculation.

Let $\Omega(t)$ represent the frequency of the binary orbit and Ω_0 be the frequency at time T_0. Expanding $\Omega(t)$ to second order in time yields:

$$\Omega(t) \simeq \Omega_0 + \dot{\Omega}(t - T_0) + \frac{1}{2}\ddot{\Omega}(t - T_0)^2. \tag{5.2}$$

Then, the phase at time t, $\phi(t)$, is given by

$$\phi(t) \simeq \phi_0 + \Omega_0(t - T_0) + \frac{1}{2}\dot{\Omega}(t - T_0)^2 + \frac{1}{6}\ddot{\Omega}(t - T_0)^3 \ ; \ \phi_0 = \phi(t = T_0). \tag{5.3}$$

We can express this in terms of the period and its derivatives:

$$\phi(t) \simeq \frac{t - T_0}{P_0} - \frac{\dot{P}}{2}\left(\frac{t - T_0}{P_0}\right)^2 + \frac{1}{6}(2\dot{P}^2 - \ddot{P}P_0)\left(\frac{t - T_0}{P_0}\right)^3. \tag{5.4}$$

The distributions in phase for muons in each of the 3° cones have been determined using the vdkBB-88 ephemeris and are shown in Fig. 5-10 on the following pages. In order to test the hypothesis that the background is an isotropic source of primary cosmic rays, the difference between the expected value and the actual value of the 580 phase bins of the 29 background directions was calculated in units of standard deviation based on a normal distribution about a mean value of 14.65 (293/20). The histogram, shown in Fig. 5-11, has a slight skewness toward the negative end indicating an excess of muons above the expected value. The skewness prompted us to explore the possibility that we were approximating a Poisson process with low statistics ($\sim$ 15 per phase bin) by a normal one. Using the same expectation value, a histogram of the difference between the expected value and the observed data points was accumulated as shown in Fig. 5-12. Superimposed on this is the (content normalized) Poisson distribution for a mean value of 14.65. It is seen that the data is slightly broader at the tail ends of the distribution, but in general, the distributions agree very well ($\chi^2 = 11.7$, $Q = 0.998$, $df = 29$). Fluctuations in the data are very likely due to variations in sensitive time for the different cones.[5]

---

[5] Unfortunately, this effect is very difficult to correct for since the muons in these cones come from different runs, each of about 500 muons. The sensitive time for some of these was decreased in many cases by false or noise triggers caused by the overhead crane in the experiment.

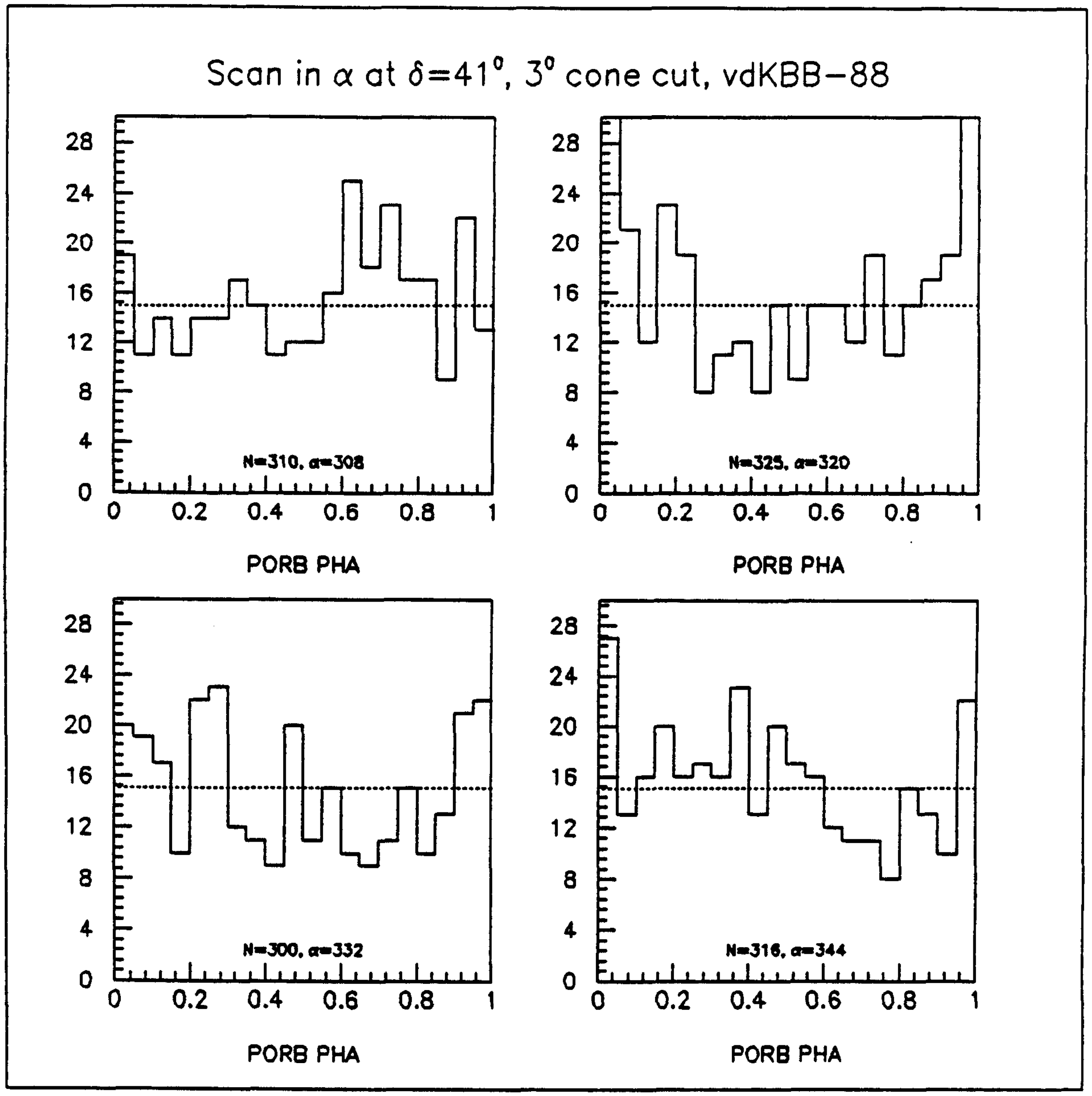

Fig. 5-10. Phase Plots for the Source + 29 Background Directions. The time-dependent calculation was made using the vdKBB-88 ephemeris as described in Chapter 5. The first plot is for the Cyg X-3 cone. The number of entries and the right ascention of each cone is given. All of the background 3° cone phase plots are given for comparison with the source cone phase plot.

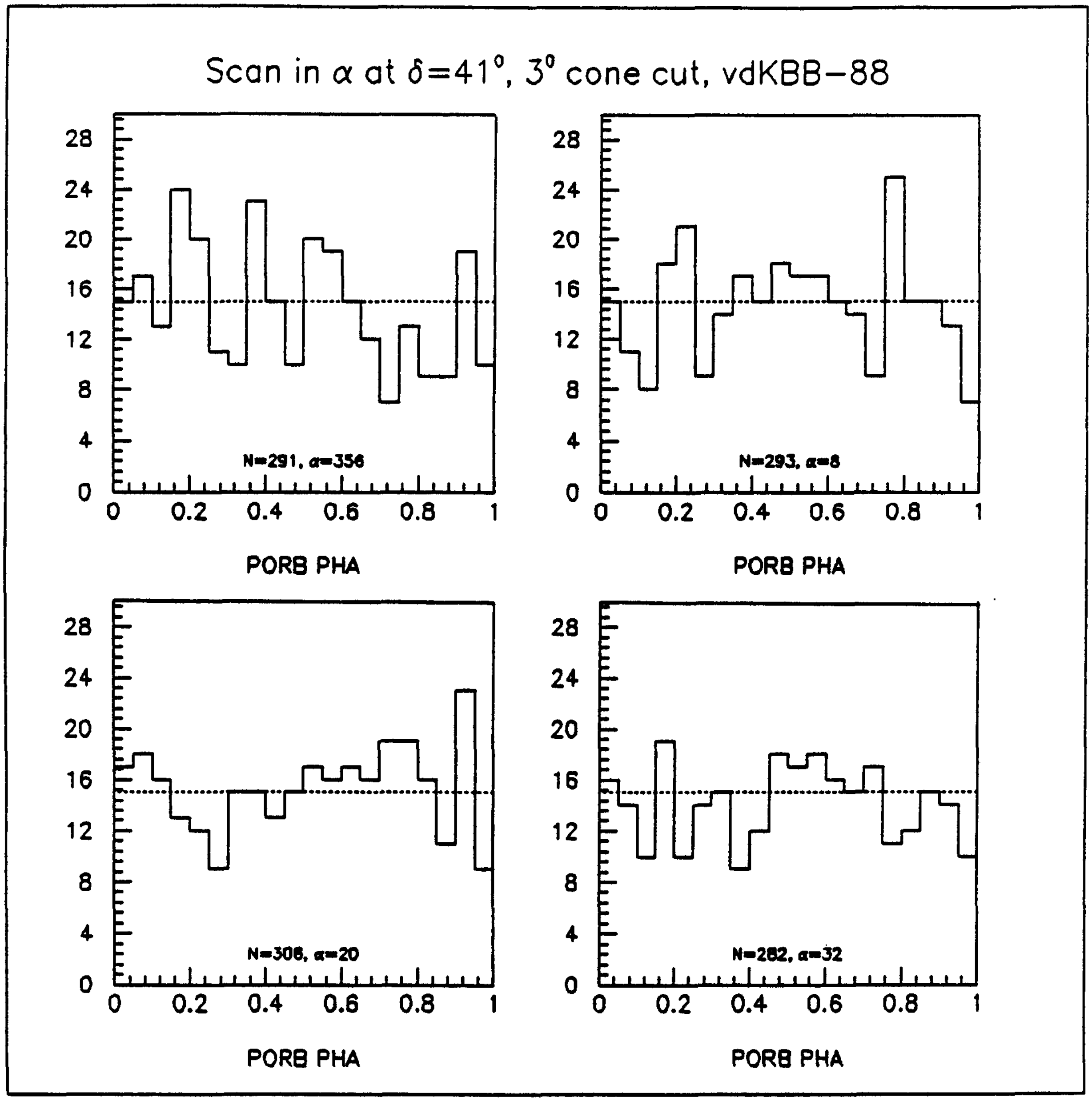

Fig. 5-10 continued.

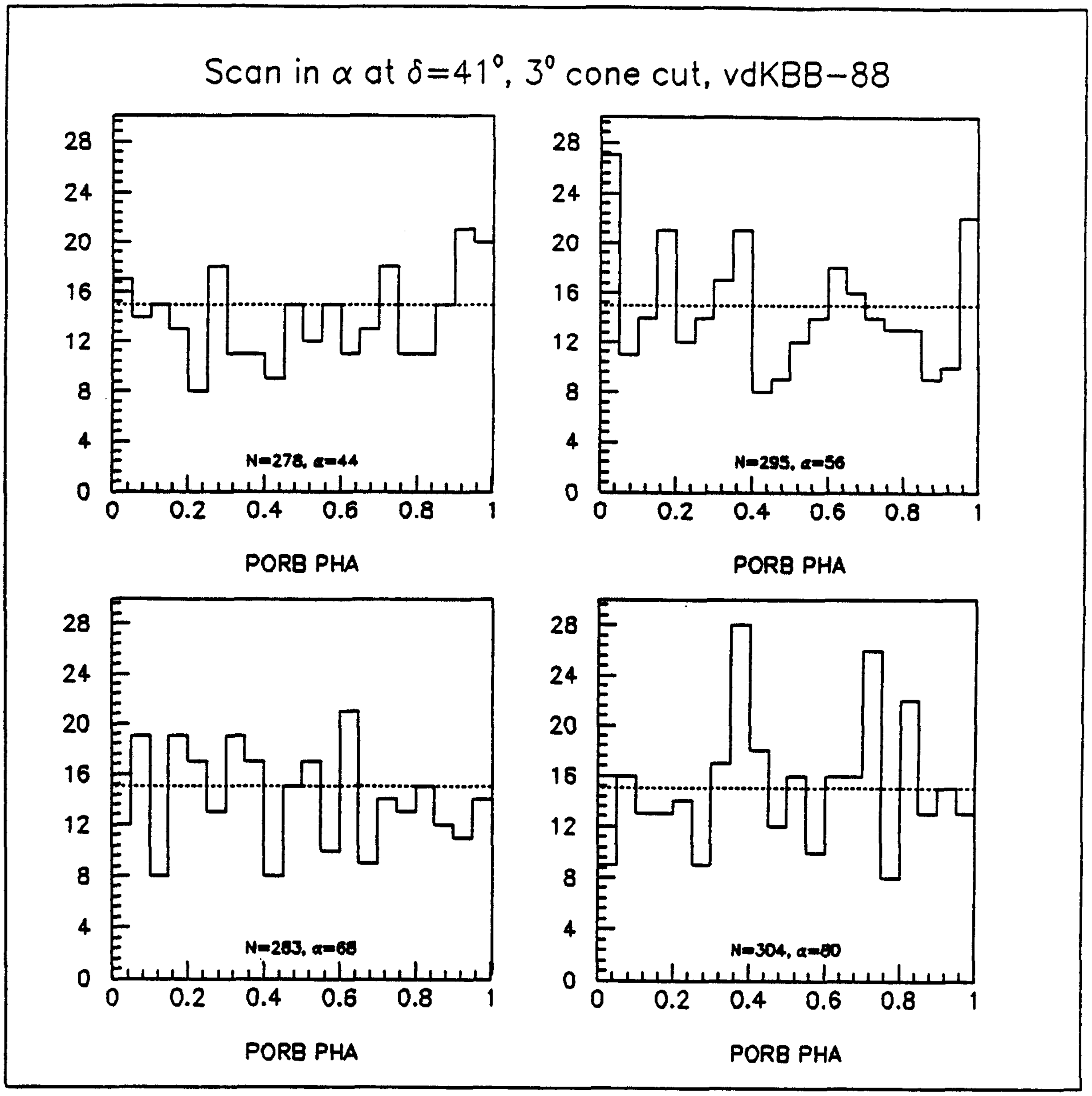

Fig. 5-10 continued.

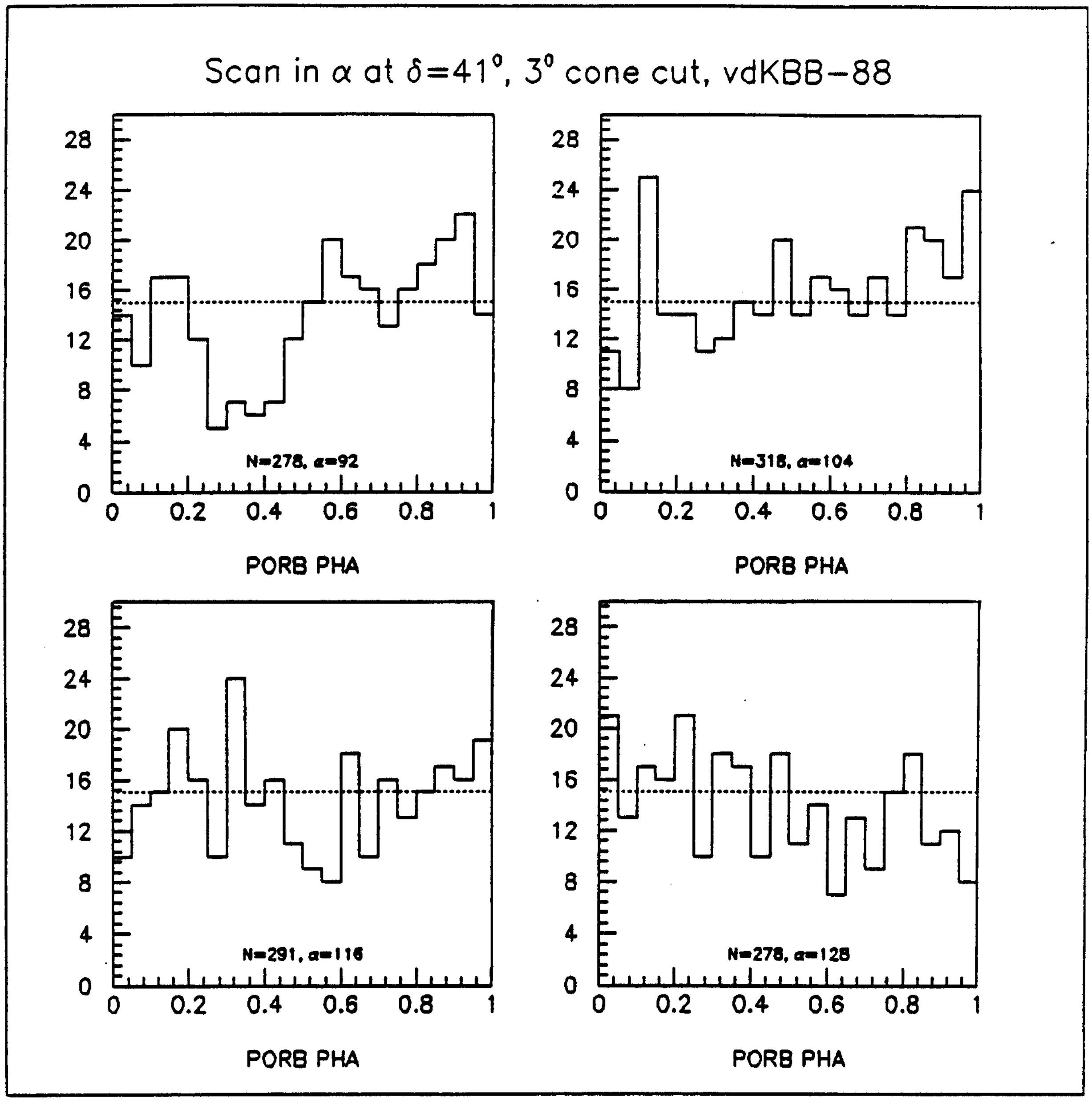

Scan in α at δ=41°, 3° cone cut, vdKBB-88

Fig. 5-10 continued.

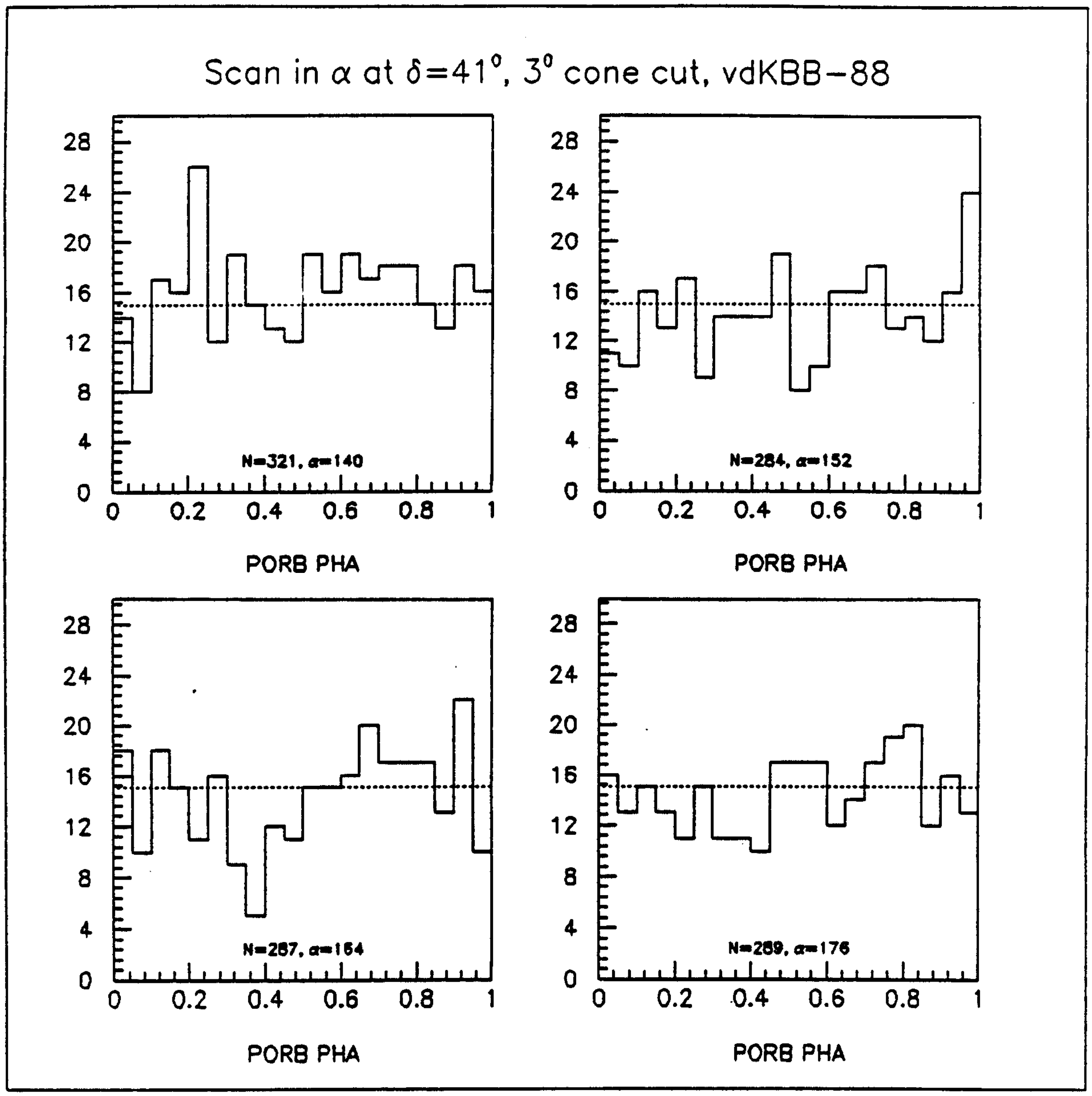

Fig. 5-10 continued.

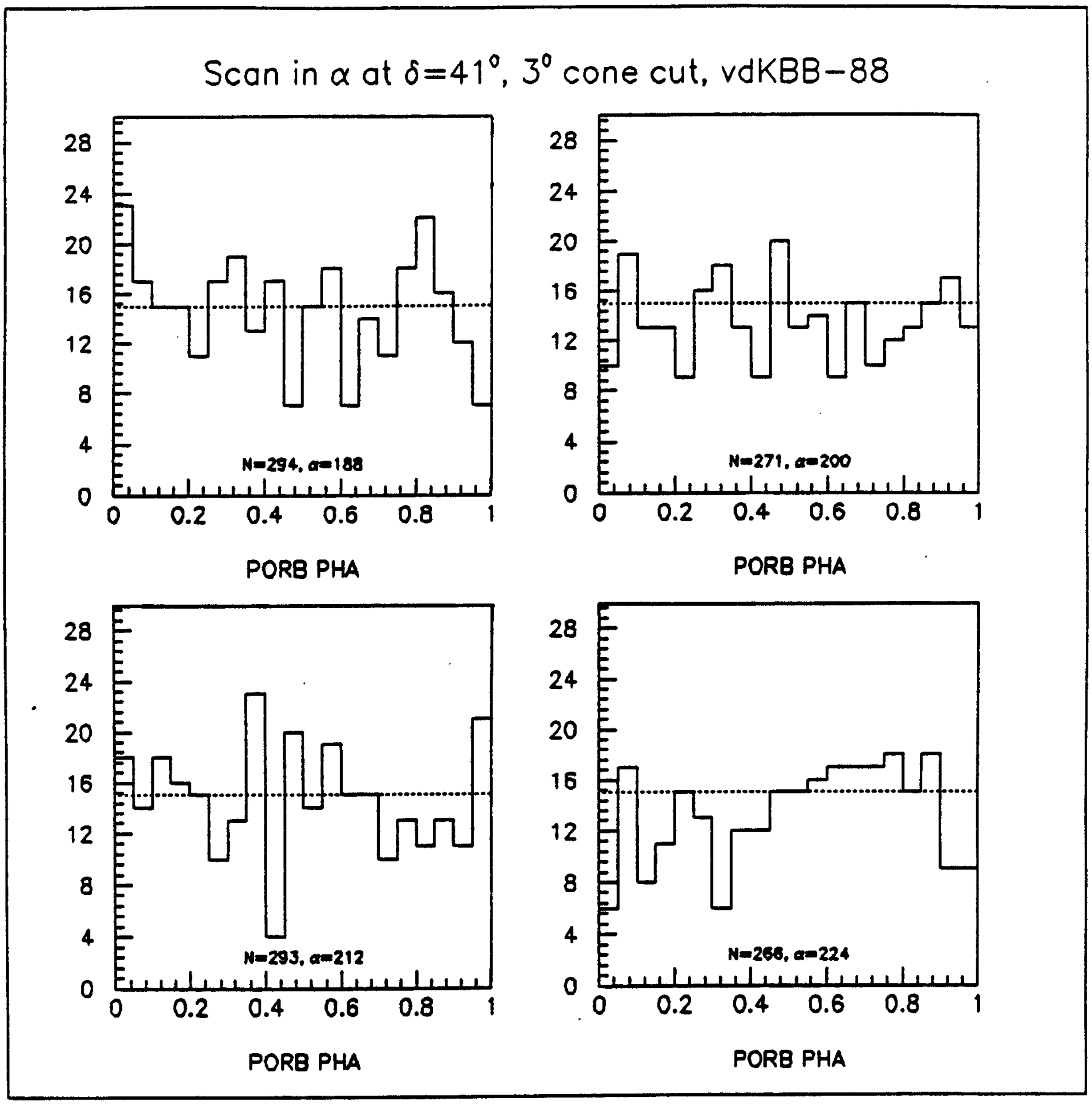

Fig. 5-10 continued.

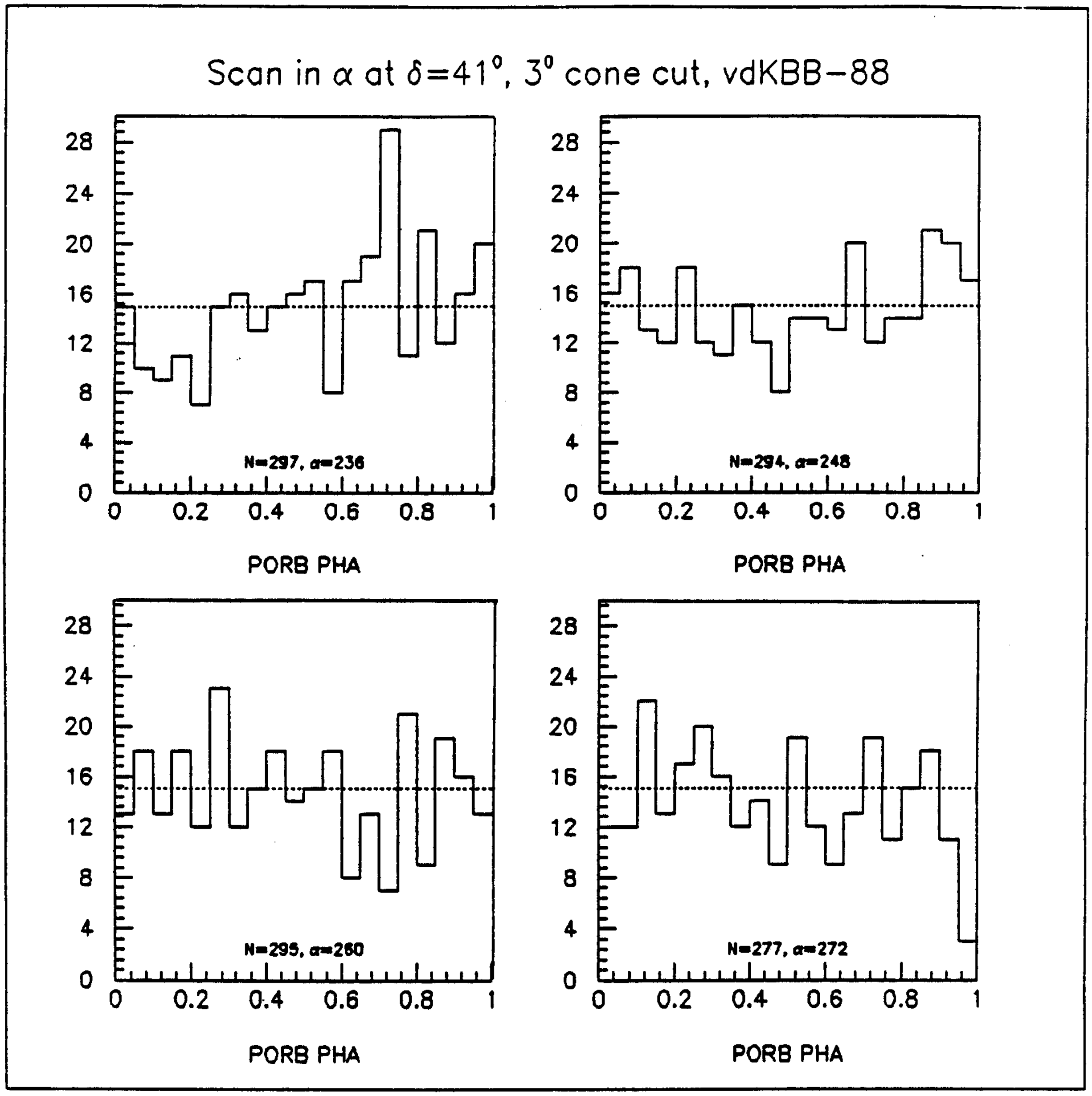

Fig. 5-10 continued.

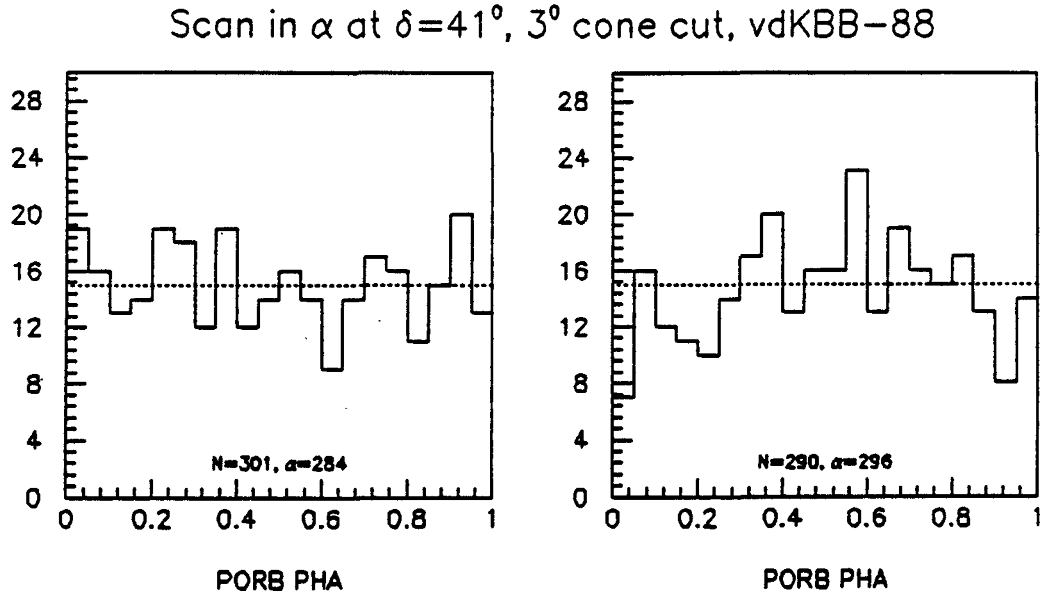

Fig. 5-10 continued.

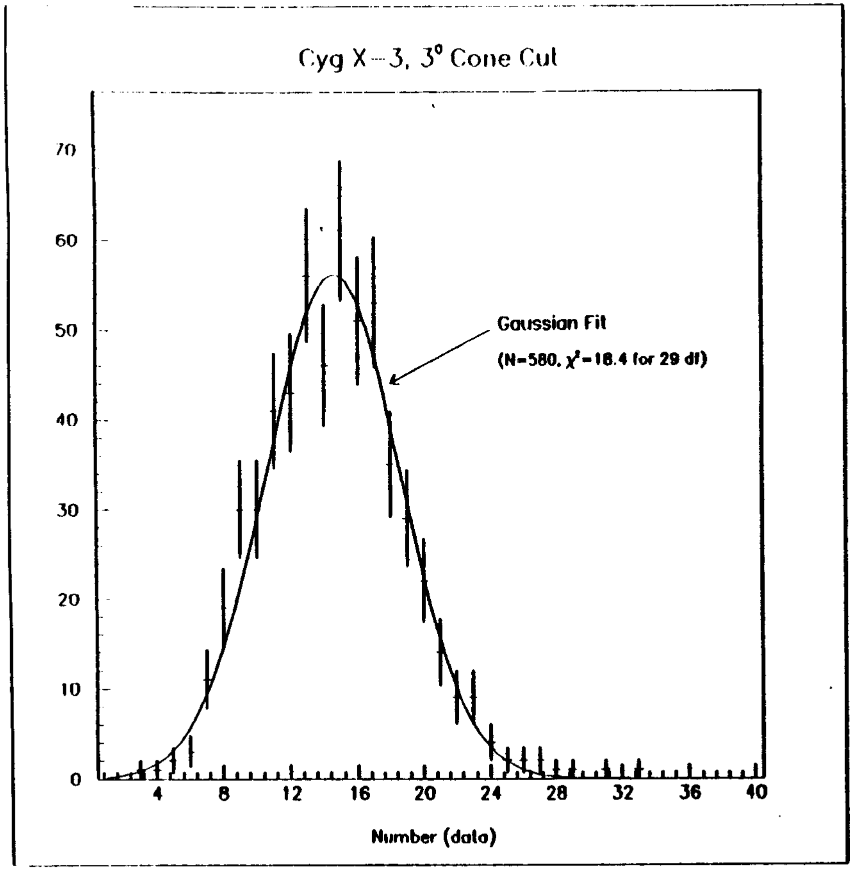

Fig. 5-11. Deviations from the Expected Background. Each of the 20 bins in the 29 background phase plots is compared to the expected number of muons per bin $(x_i - \bar{x})$. The average (uncorrected) background per phase bin is 14.65 muons (see text). The solid curve is a Gaussian fit normalized to the total number of entries (580). The data shows a positive skewness.

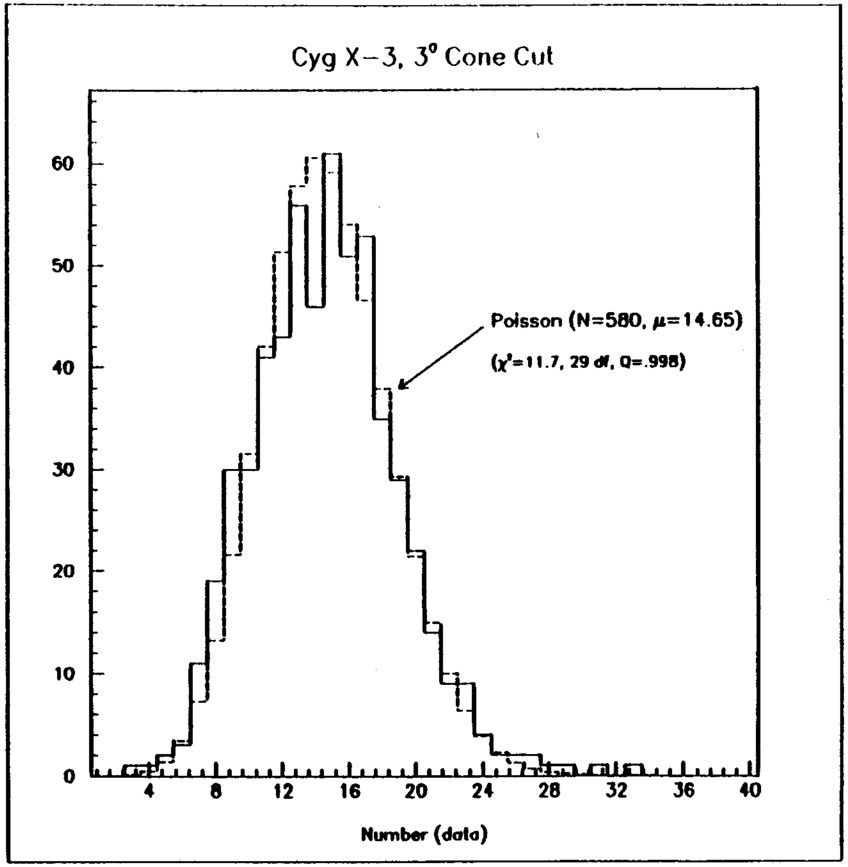

Fig. 5-12. Poisson Fit to the Background Deviation. The Poisson distribution is normalized to N=580 and has mean, $\mu = 14.65$.

The actual location of the projected position of all muons within a 5° cone is shown in the scatter plot of Fig. 5-13 and the subset in the peak phase region [0.60, 0.80] are shown in Fig. 5-14. (The 3° cone is obviously just a subset of these.) The vertical axis in both plots is declination and the horizontal axis is right ascension. No abundance at any given location in the cone is evident.

The distribution in phase of the 311 muons in the Cyg X–3 cone are plotted in Figs. 5-15 and 5-16 for the vdKBB-88 and Mason 1986 ephemerides. The bin size in both plots is 0.05 in phase. A comparison of commonly used ephemerides is shown in Table 5-1. The difference in phase between the Mason and vdKBB-88 ephemerides is 0.018 at the beginning of 1988. The difference is smaller than the width of a phase bin but is believed responsible for the differences in shape between the two phase distributions. We note a total of 83 muons above a background of 60.3 (4 bins × 301.3/20) in the narrow phase region [0.60,0.80], an excess of 23 events. For a χ^2 of 11.5 with 4 degrees of freedom, the probability that this is a fluctuation above a normal background is 2.1×10^{-2}. Table 5-2 summarizes the results of the time-dependent analyses for both the Mason and vdKBB-88 ephemerides. The hour angle distribution for muons in the narrow phase region is shown in Fig. 5-17.

<u>COMPARISON OF VARIOUS EPHEMERIDES</u>

Ephemeris	Jan-1981	Jan-1988	Jan-1989
vdKBB-81	0.825	0.741	0.577
vdKBB-88	0.830	0.845	0.713
Mason-86	0.850	0.863	0.717
Molnar	0.836	0.814	0.662

Table 5-1—A Comparison of Various Ephemerides. The table compares the phase of signals at various epochs for four ephemeris measurements of the source Cyg X–3. The comparisons were made at 0 hour on the first day of the indicated year.

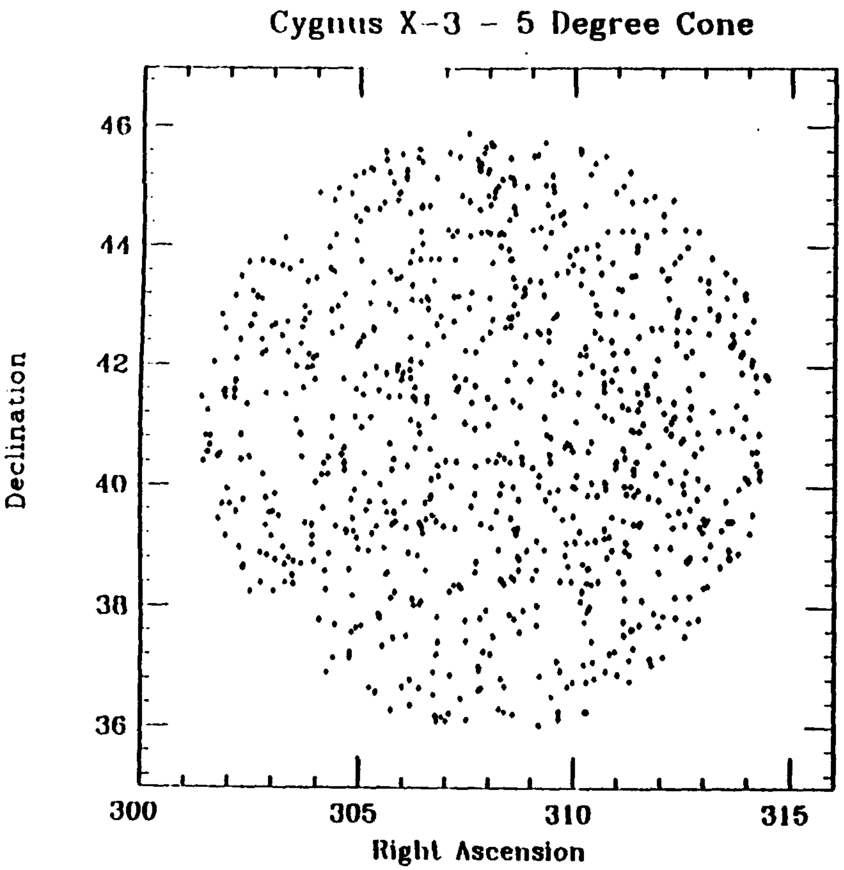

Fig. 5-13. Scatterplot (α *vs.* δ) for All Muons in a 5° Cone About Cyg X-3.

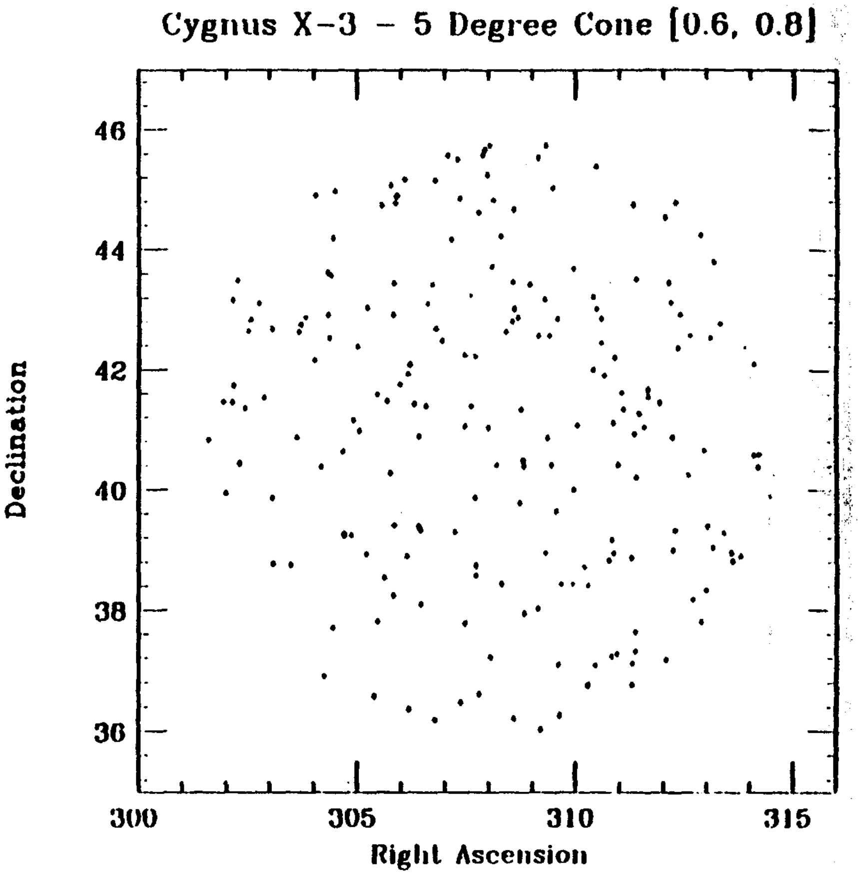

Fig. 5-14. Scatterplot (α *vs.* δ) for Muons in the [0.60,0.80] Phase Cut.

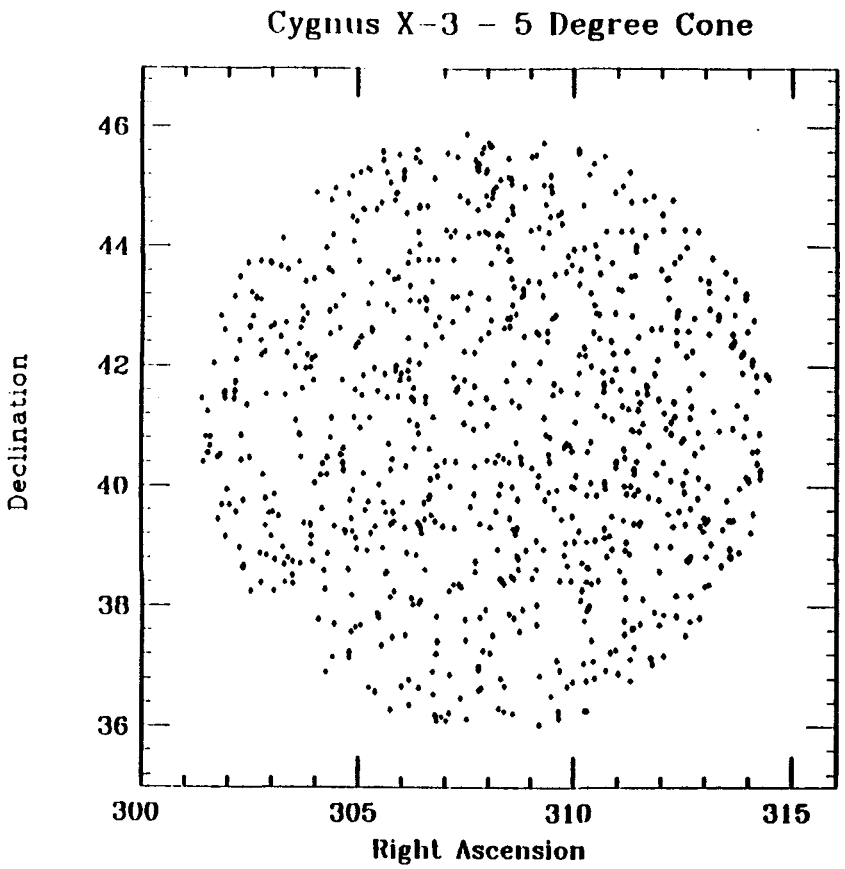

Fig. 5-13. Scatterplot (α *vs.* δ) for All Muons in a 5° Cone About Cyg X-3.

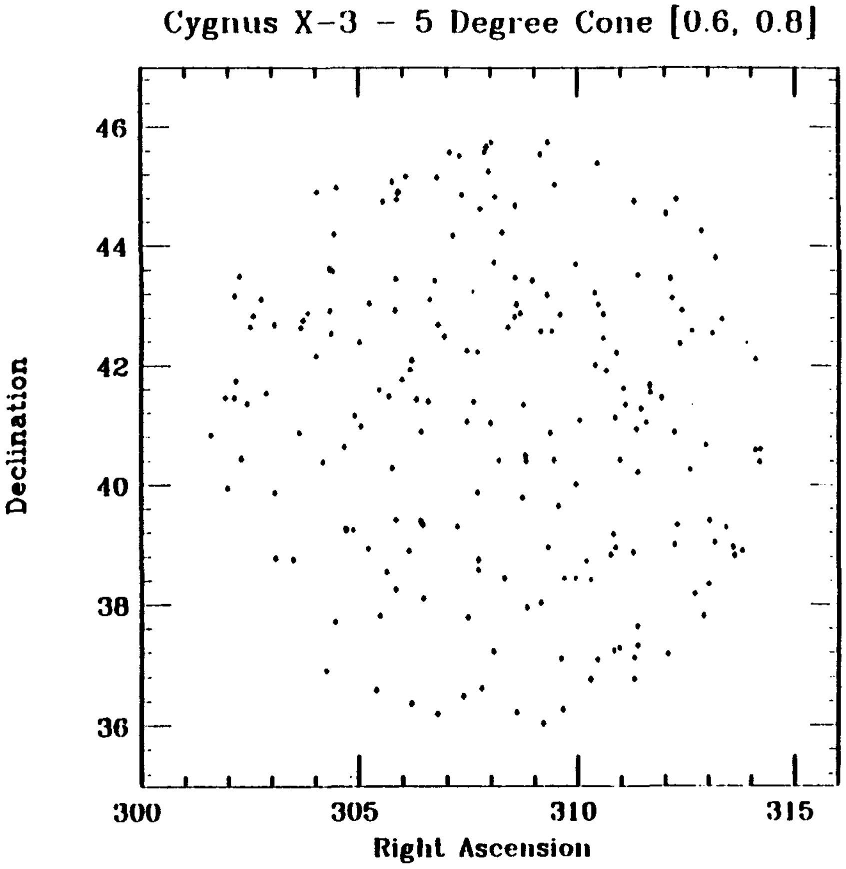

Fig. 5-14. Scatterplot (α *vs.* δ) for Muons in the [0.60,0.80] Phase Cut.

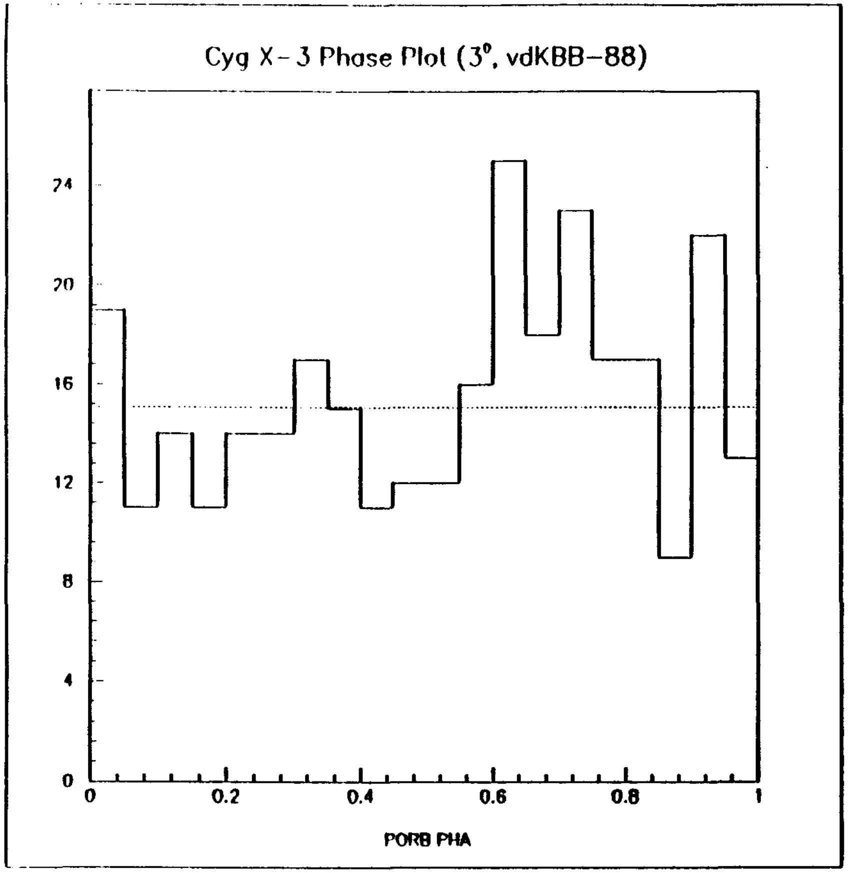

Fig. 5-15. Phase Plot for Muons in the 3° Cone Using the vdKBB-88 Ephemeris.

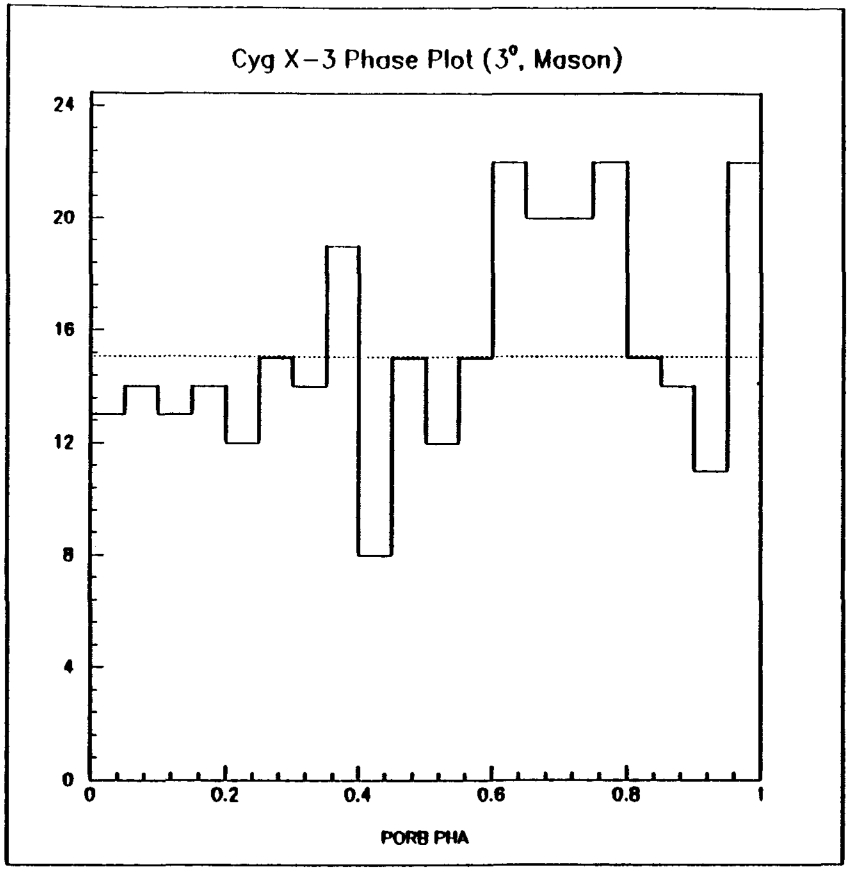

Fig. 5-16. Phase Plot for Muons in the 3° Cone Using the Mason Ephemeris.

TIME-DEPENDENT PHASE ANALYSIS RESULTS [0.60, 0.80]

Ephemeris	Excess Events	Signal-To-Background	χ^2	Q
(3° Cone)				
vdKBB-88	23	83/60.3	11.5	2.12×10^{-2}
Mason-86	24	84/60.3	9.6	4.77×10^{-2}
(5° Cone)				
vdKBB-88	30	198/168	7.2	0.126
Mason-86	28	196/168	7.6	0.109

Table 5-2—Time-dependent Phase Analysis Results. The significance of the excess events in the narrow phase region [0.60, 0.80] is shown for each of the vdKBB-88 and Mason ephemerides in the 3° and 5° half-angle cone analyses. In each case the number of degrees of freedom in the χ^2 analysis is 4. The χ^2 probability is the incomplete gamma-function, Q.

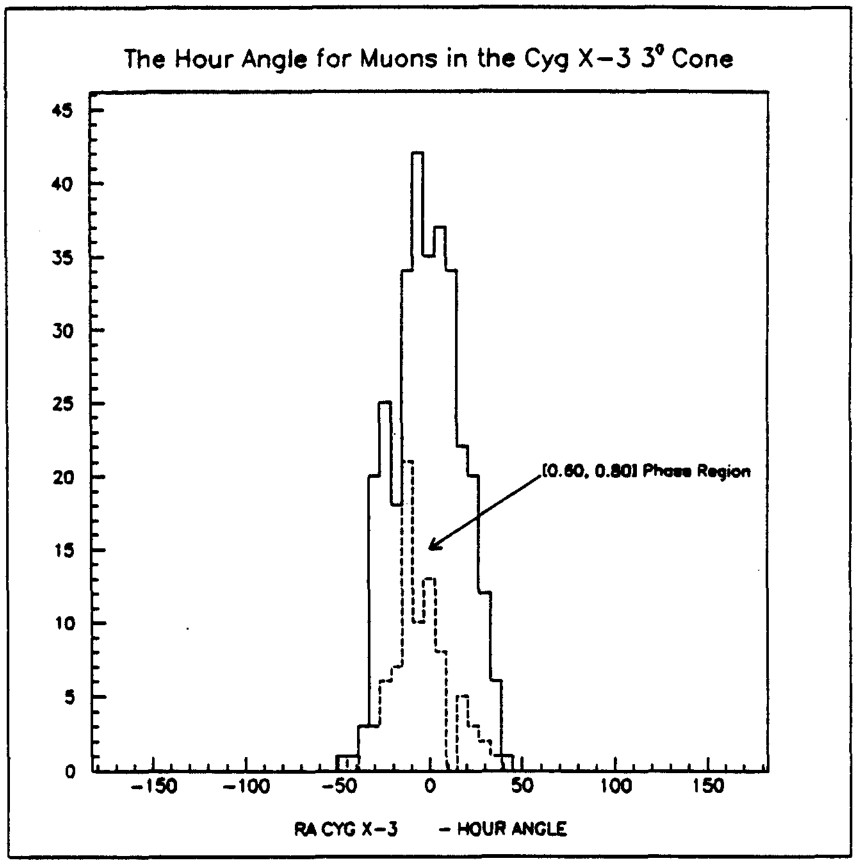

Fig. 5-17. Hour Angle Distribution for Muons in the [0.60,0.80] Phase Cut.

5.4 The 5° Half-angle Cone Cut

The same analysis has been performed using a 5° cone in order to increase the statistics in the phase bins. Figures 5-18 through 5-21 show the analogous distributions for the 5° cone that were arrived at in the 3° analysis.

The careful study of the background using detector sensitivity was not carried out in this case however. As an approximation to the correct number of muons per 5° cone, we simply use the percentage change between the measured average number of muons per cone in the 3° analysis and the number of muons expected after correction for detector sensitivity $((301.3 - 294)/301.3 = .0275)$. The average number of muons observed in the 5° analysis is 823 as shown in Fig 5-18. The corrected number is $(1 - 0.0275) \times 823 = 846.3$ per cone or 42 per phase bin.

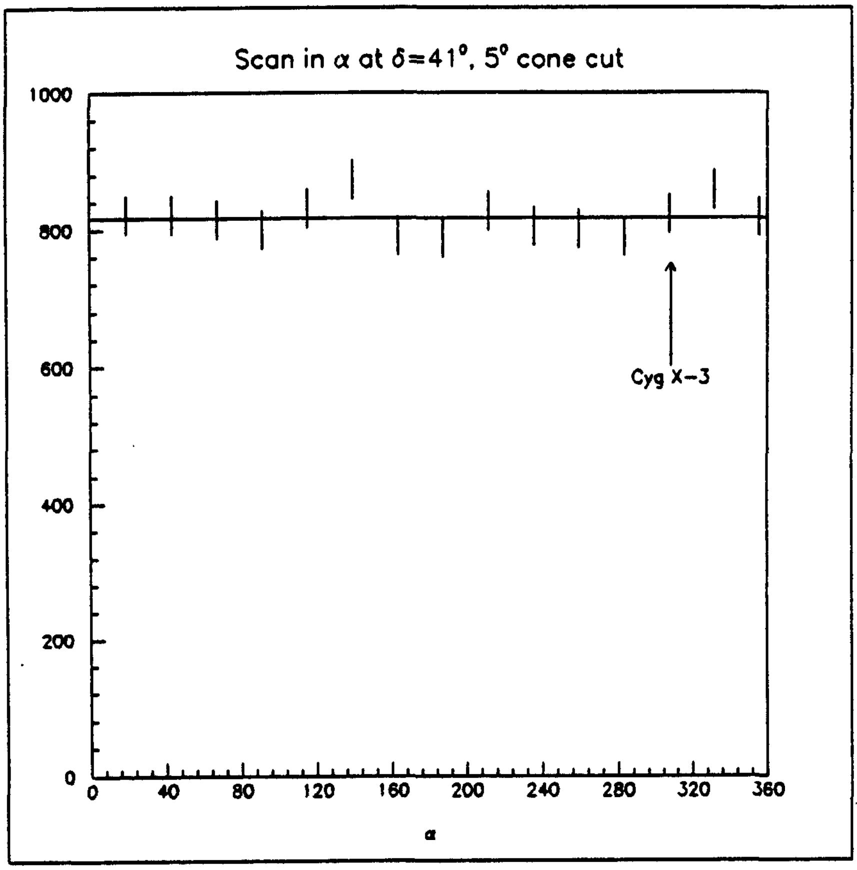

Fig. 5-18. The Number of Muons per 5° Cone. The 5° analysis used 1 source + 14 background directions spaced every 24° in α.

Phase analysis was carried out using the vdKBB-88 ephemeris. The deviation from the expected background for the $14 \times 20 = 280$ background phase bins is shown in Fig 5-19.

The solid curve in the figure is a Gaussian fit to the data with $\chi^2 = 36.5$ for $39 - 1 = 38$ df. The mean number of muons per phase bin is 41.3 before the livetime correction is made.

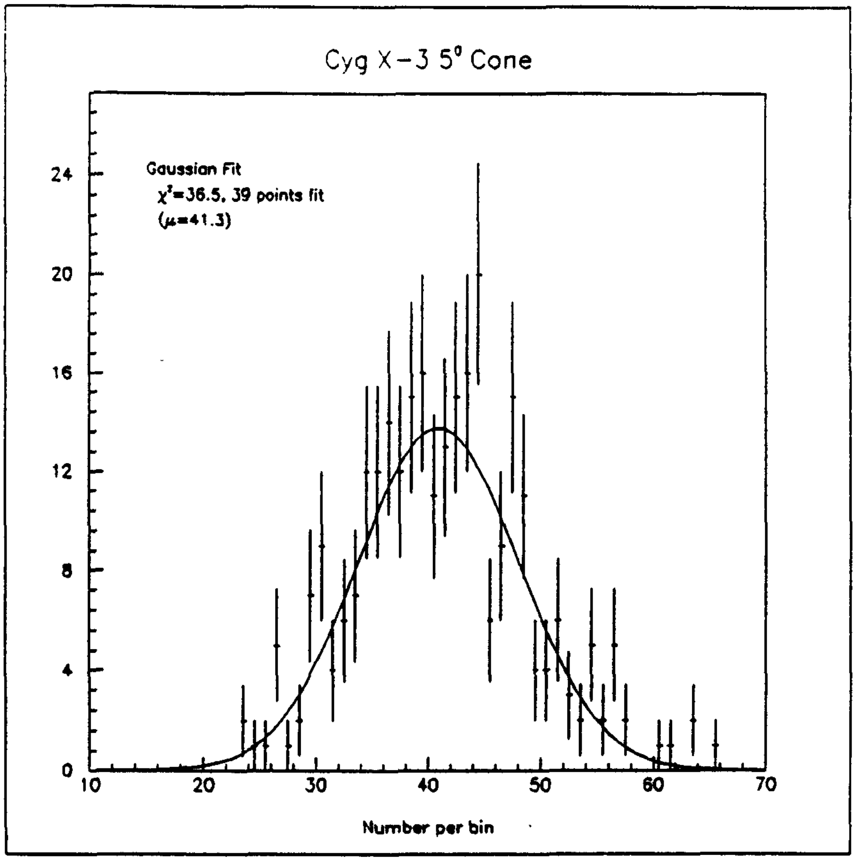

Fig. 5-19. Deviations from Expected Background for Muons in the 5° Cone Analysis. The solid curve is a Gaussian fit to the data.

Phase plots for the 5° cones based on both the Mason and vdKBB-88 ephemerides are given in Figs. 5-20 and 5-21 and the results are summarized in Table 5-2. For the Mason ephemeris, 28 excess muons are observed above a backgrond of 168 in the [0.60,0.80] phase region. For the vdKBB-88 ephemeris, 30 excess muons are observed. We note that the difference between the number of excess muons found in the 5° and 3° cone analyses is smaller than that which would be expected for an isotropic flux given the decrease in solid angle.

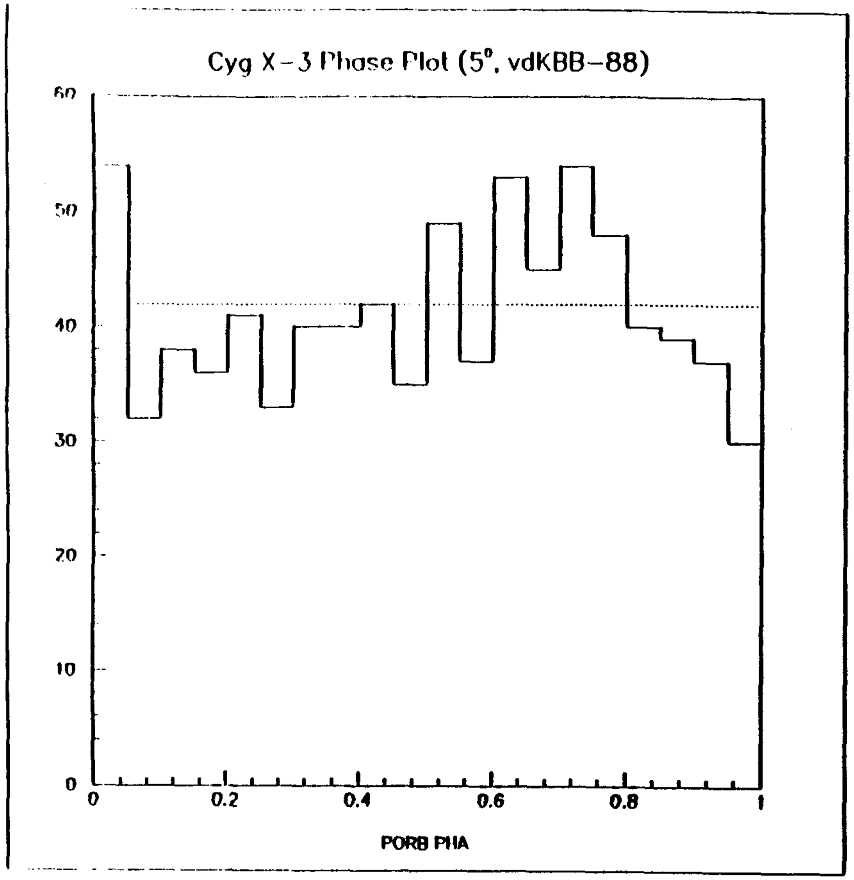

Fig. 5-20. Phase Plot for Muons in the 5° Cone Using the vdKBB-88 Ephemeris.

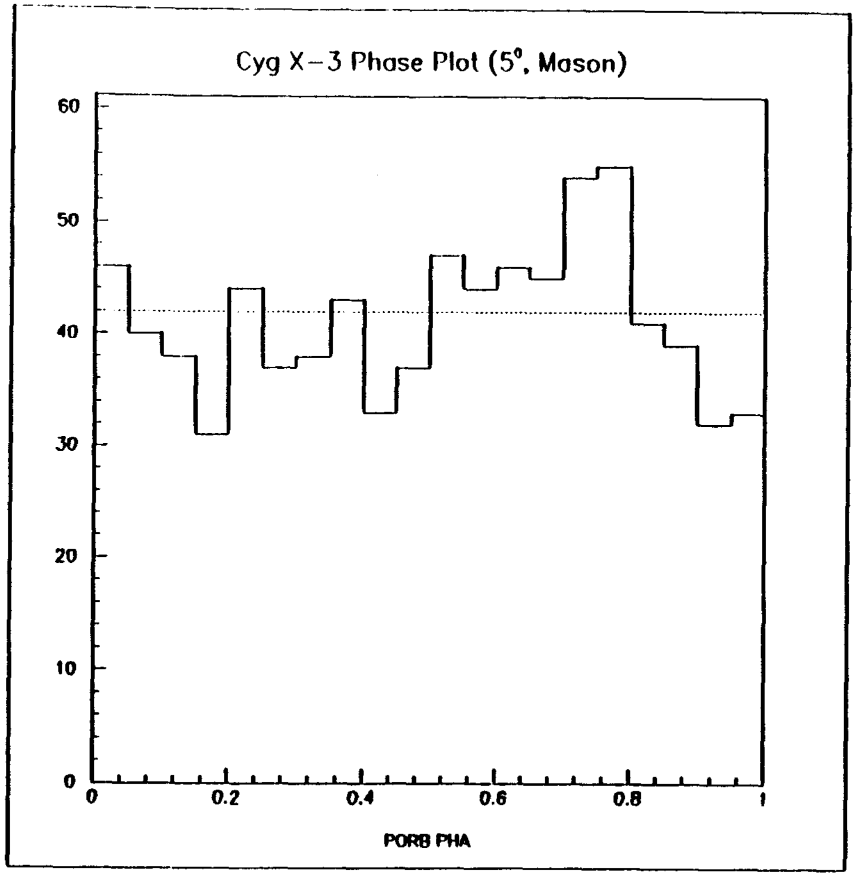

Fig. 5-21. Phase Plot for Muons in the 5° Cone Using the Mason Ephemeris.

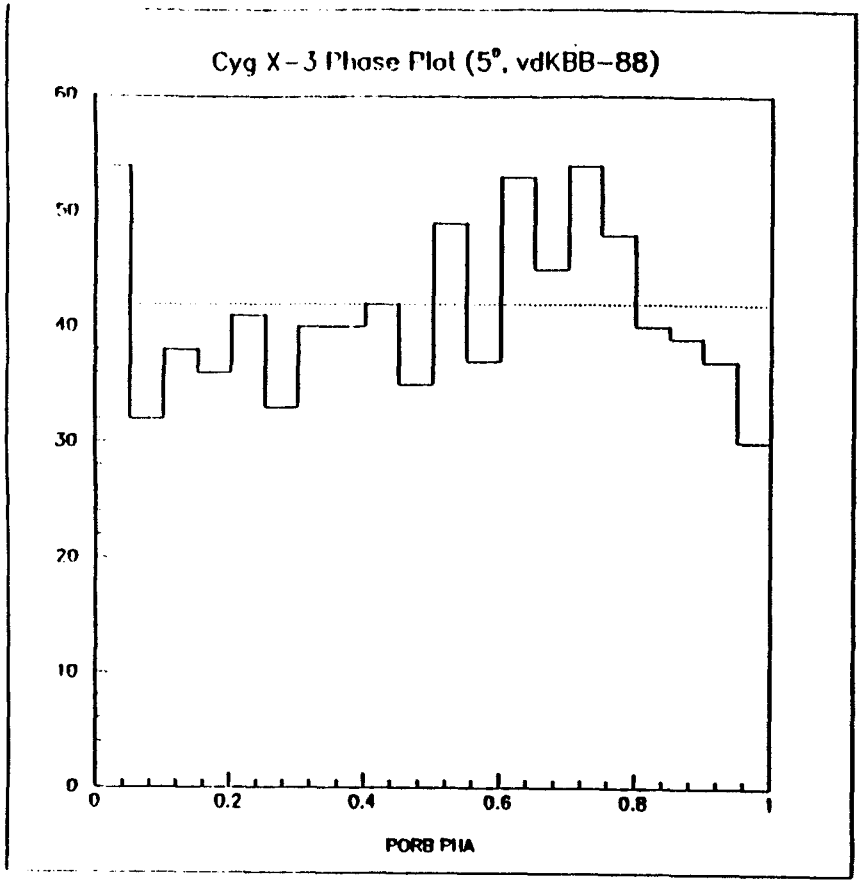

Fig. 5-20. **Phase Plot for Muons in the 5° Cone Using the vdKBB-88 Ephemeris.**

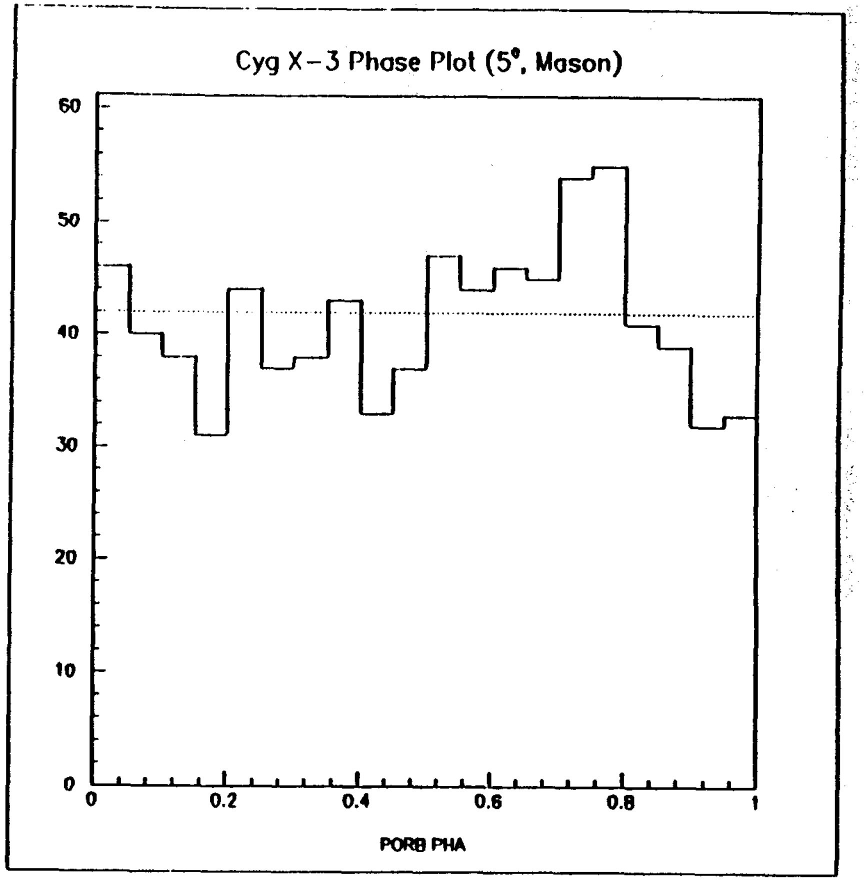

Fig. 5-21. **Phase Plot for Muons in the 5° Cone Using the Mason Ephemeris.**

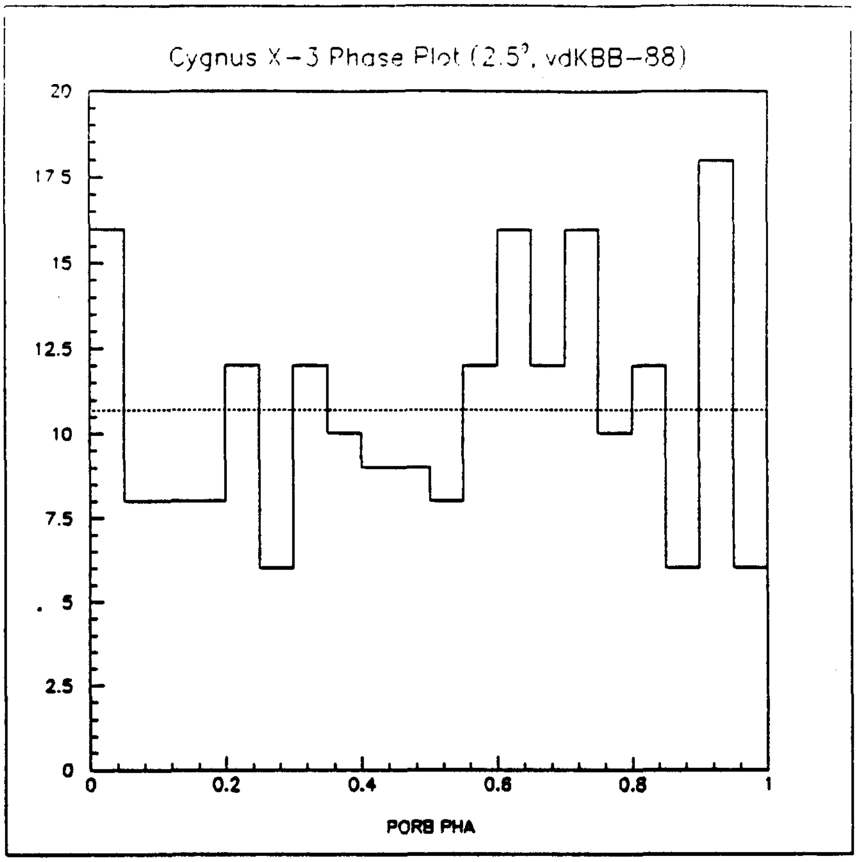

Fig. 5-22. Phase Plot for Muons in the 2.5° Cone Using the vdKBB-88 Ephemeris.

Also, a 2.5° analysis was performed on the data sample. The phase plot is shown in Fig. 5-22. The average number of muons per bin is 11. No significant peaks are observed.

5.5 Flux Calculation

The Monte Carlo calculation described in Chapter 3 will now be used to determine an upper limit for the flux of muons from the Cyg X–3 direction. It will be recalled that the simulation generated a set of muons from the Cyg X–3 direction with random hour angles. Those muons that are within the detector acceptance have their hour angles weighted by $\cos\theta$ in order to correct for solid angle as described previously. The weighted hour angle distribution for these muons is plotted in Fig. 5-23. Note that the bin size in these plots is the same as in the livetime *vs.* hour angle plot described above. Also, the shape of the distribution agrees with that observed in the data. The mean value in the hour angle distribution for the model is 1° more negative than the mean in the data. This is likely due to the fact that all muons in the model were generated with exactly the same declination whereas muons in the data have a declination that is within 3° of $\delta = 41°$. The ratio of the total number of muons generated to the (weighted) number within the acceptance for bins with non-zero content only is $86.3/8.1 = 10.7$. Summing the total sensitive time in each of these same bins and recalling that all muons were generated in a 100 m^2 plane above the detector, the excess flux, Φ_e, can then be determined from the number of excess events in the peak region, N_e, according to:

$$\Phi_e = N_e \times \frac{10.7}{100 \times 10^4} \times 4.00 \times 10^6 \ s^{-1} cm^{-2}. \tag{5.5}$$

These 23 events in the peak region correspond to an excess peak flux of $6.1 \times 10^{-11} cm^{-2} s^{-1}$.

5.6 Multiple Muons

The golden multiple muons data sample was scanned for muons from the Cyg X–3 direction. A total of three muons was found within a 3° cone about the source and a total of seven in a 5° cone. None of these muons appears within the narrow phase region of [0.60,0.80]. Since the size of the golden multiple muon sample is ~ 1 % that of the golden single muon sample, the number of multiple muons observed (7) in the 5° cone agrees with the number expected (10).

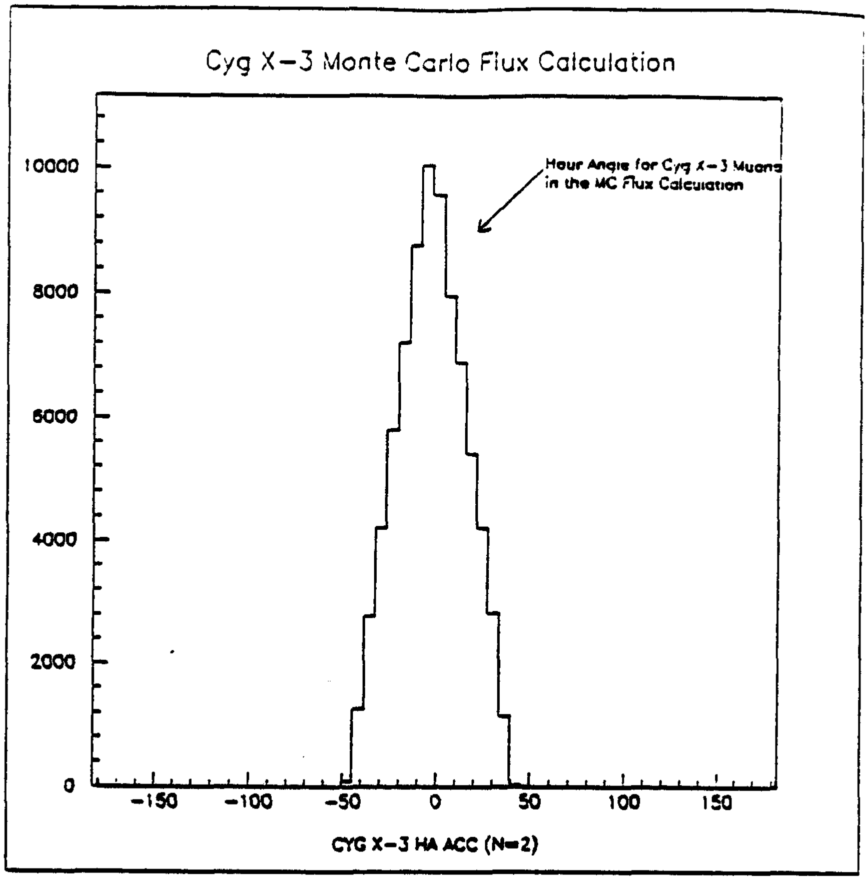

Fig. 5-23. Hour Angle Distribution of Muons in the Cyg X-3 Monte Carlo Flux Calculation. A total of 3.23×10^6 muons were generated in a 100 m^2 plane above the Tracker. Of these, 83.7×10^3 satisfied the on-line (T1·T2·T3) and off-line (any hit in L4) trigger requirements.

Chapter 5 References

[1] The Astronomical Almanac, Washington: U.S. Government Printing Office, London: Her Majesty's Stationery Office, (1988).

[2] Supplement to the 1984 Astronomical Almanac, Washington: U.S. Government Printing Office, London: Her Majesty's Stationery Office, (1984).

[3] Duffett-Smith, P., Practical Astronomy With Your Calculator, Cambridge University Press (1979).

[4] Goldstein, H., Classical Mechanics, Addison Wesley (1980).

[5] Taff, L. G., Celestial Mechanics, John Wiley & Sons (1985).

[6] Smith, E., and Jacobs, K. C., Introductory Astronomy and Astrophysics, W. B. Saunders Co. (1973).

[7] The JPL ephemeris fitting package was provided by Dr. Ken Johns of the University of Minnesota.

CHAPTER 6. DISCUSSION AND SUMMARY

6.1 Results of Observations Made with the Tracker

As was stated in Chapter 2, the goals of the Tracker experiment were: "to provide a testing of the complete veto shield design, to serve as an unbiased muon trigger to the main detector, to provide a detector close to the Soudan 1 depth for muon astronomy, and to provide physics data at an early stage."

In the process of satisfying these goals, much has been learned about the installation and operation of the the Soudan 2 active shield. Problems discovered early-on in the set up of the Tracker have been remedied so that installation for the rest of the shield should now flow smoothly. Methods have been shown for identifying operational problems as well. Measurements of natural radioactivity in the mine provide a means for checking the operation of the shield on a daily basis. Benchmark measurements of singles rates and coincidence rates were firmly established by the Tracker and they set standards for proper operation of the rest of the shield.

As an independent experiment, the operation of the Tracker proved to be useful to the main experiment as well. During the entire livetime of the experiment, it served as an unbiased muon trigger for the central calorimeter. The Tracker helped in diagnosing newly installed main modules, and it provided an initial data set for studying the detector response to penetrating muons. Measurements of the singles rates, coincidence rates and photon attenuation length from the Tracker also confirmed predictions about the background flux due to natural radioactivity expected to be observed by the central calorimeter.

From measurements of the muon rate in the Tracker, we have set upper and lower limits on the vertical muon flux at the Soudan 2 depth (see equations 4.2 through 4.5).

Our best estimate of the vertical flux at 2100 mwe is:

$$\left(\frac{dN}{d\Omega}\right)_\nu = (1.2 \pm 0.3) \times 10^{-3}\ m^{-2} st^{-1} s^{-1}\ .$$

This number is in agreement with theoretical predictions.

6.2 Cygnus X-3 Muon Analysis Results

During the period July, 1987 through March, 1988 (livetime 0.50 years), the Tracker experiment, at a depth of 2100 mwe, collected a very clean sample of ~ 103,000 single muons and a smaller sample (~ 1%) of multiple muons. Using the methods explained in Chapter 5, we have analysed the single muon sample background to determine the expected number of muons in a 3° half-angle cone centered on the celestial coordinates of Cyg X-3. We report that in a narrow range of phase of this source, namely, [0.60,0.80], an excess of 23 ± 8 muons corresponding to an excess flux of $(6 \pm 2) \times 10^{-11} cm^{-2} s^{-1}$ was observed. The possibility that this signal is due to a chance fluctuation above a random background is ~ 2 %. We note that our choice for the phase cut, [0.60, 0.80], is not the same as that selected by the Soudan 1 group, [0.65, 0.90], and was chosen to maximize the signal. Our results are in agreement with those of the Soudan 1 collaboration at the stated level of significance. The known variability of the source may account for the shift in the peak range between the time of the original Soudan 1 observation and this one. This may also explain the null result reported by the Kamiokande collaboration. Should the recent reports by air-shower arrays of an anomalously high muon content in their data be correct, further support will have been gained for underground experiments, such as this one, which report high energy muon signals from the Cyg X-3 direction.

Finally, this experiment and the Soudan 1 detector ran concurrently during the above period. A similar, though less significant $(1 - 2\ \sigma)$ effect is seen in their data during this period[1].

---

[1] M. Marshak, private communitcations.

APPENDIX A

The Soudan 2 Collaboration

Argonne National Laboratory

I. Ambats, D. S. Ayres, L. J. Balka, W. L. Barrett,
J. W. Dawson, T. H. Fields, M. C. Goodman, N. Hill,
J. H. Hoftiezer, D. J. Jankowski, F. V. Lopez,
E. N. May, L. E. Price, J. L. Schlereth, J. L. Thron

University of Minnesota

P. Border, H. Courant, B. Dahlin, U. DasGupta,
K. Heller, S. Heppelman, K. Johns, T. Joyce, M. Lowe,
M. L. Marshak, W. Miller, E. A. Peterson, D. Roback,
D. B. Rosen, K. Ruddick, D. Schmid, M. Shupe, S. Werkema

University of Oxford

W. W. M. Allison, G. D. Barr, C. B. Brooks, J. H. Cobb,
L. M. Kirby–Gallagher, R. H. Giles, D. H. Perkins,
P.D. Shield, M. A. Thomson, N. West

Rutherford–Appleton Laboratory

G. J. Alner, D. J. A. Cockerill, V. W. Edwards,
C. Garcia–Garcia, P. J. Litchfield,
G. F. Pearce, E. W. G. Wallace

Tufts University

D. Benjamin, B. Ewen, T. Kafka, J. A. Kochocki,
W. A. Mann, R. Milburn, A. Napier, W. P. Oliver,
B. Saitta, J. Schneps, N. Sundaralingam

APPENDIX B

The Veto Shield Pulser and Tracker Trigger CAMAC Modules

PDK–315

March 3, 1987

J. Kochocki

Veto Shield Pulser

Introduction

The veto shield pulser is a CAMAC design module used to test shield preamp channels. It provides variable width test pulses, in advance of a trigger, to any or all of 32 twisted pair lines. The trigger pulse is of fixed width and is carried over a twisted pair to the XTRIG input of shield readout modules in a crate. All lines are terminated in 100 Ω.

In normal operation, it is expected that each crate with readout modules in it will have a single pulser module as well. At the beginning and at the end of a run, the pulser will strobe the test inputs of the veto shield preamps allowing the readout modules to identify inactive channels. For diagnostic purposes, the pulser can bypass the preamps and strobe the inputs to a readout module directly to verify proper operation of the back end electronics. (See the attached overview of the CAMAC crate.)

The pulser module can also be used to provide stand–alone software triggers to readout modules in a crate. This is useful for debugging shield electronics and also for measuring singles rates. This software trigger may be random if so desired.

General Description

The module has a 2MHz oscillator and uses 47 chips. It is housed in a double–width CAMAC module and under normal circumstances should draw less than 1 ampere at +5 volts.

The trigger pulse is delivered over a twisted pair that is daisy–chained to up to 16 readout modules in a crate. The delay between the time data gets latched onto the 32 test lines and the arrival of the trigger pulse is programmable between 0 and 255 μs in steps of 1 μs. (*N.B.* The digital readout modules only scan the 128 μs previous to the trigger.)

The test pulses can be delivered to the test inputs of the shield preamps, or they can be delivered directly to the inputs of the readout modules. In the former case, each twisted pair is daisy–chained to 32 shield tubes. Since the rising edge of the test pulse strobes one set of channels while the falling edge of the pulse strobes the other set, each twisted pair can test up to 64 channels. In the latter case, a different cable is used and the 32 twisted pairs are fed directly into 32 of the 64 inputs on a readout module (*e.g.* channels 0–31 which are to be tested). A separate output port on the front of the pulser module is available to turn off (or on) the other 32 inputs on the readout module which are not being tested. The cables can then be swapped to test the other 32 channels (32–63) and to turn off (or on) the previously tested channels. The test pulse width is programmable between 0 and 15 μs.

Pulser Operation

The pulser is a write–only module that operates in a single mode. It is initialized by a crate–wide Z or C command and responds to N and A specific F(16) and F(10) commands only. The module generates a Q in response to an N·F(16).

Any of the 32 test lines can have a signal on it in advance of the trigger. To achieve this, the module requires two CAMAC writes; one to N·A(0) and one to N·A(1).

The first write is executed when the condition $\mathrm{N}\cdot\mathrm{F}(16)\cdot\overline{\mathrm{A1}}$ is true at S1 time. The condition, $\mathrm{N}\cdot\mathrm{F}(16)\cdot\overline{\mathrm{A1}}\cdot\mathrm{S1}$ true, generates $\overline{\mathrm{WLR}}$. $\overline{\mathrm{WLR}}$ enables latches L1 and L2 latching the inverted data W1 through W16 into the low register. This data now appears at the inputs of the SN74183 line drivers LD1–LD8. In addition, a pulse $\overline{\mathrm{WLR}}$, is used to load (asynchronous) data from lines W17–W20 onto the outputs of counter C1. The data, W17–W20, contain the pulse width in μs. The range of this number is 0 to 15 μs.

The second write is executed when the condition, $\mathrm{N}\cdot\mathrm{F}(16)\cdot\mathrm{A1}$ true, is satisfied at S1 time. This condition generates $\overline{\mathrm{WHR}}$. $\overline{\mathrm{WHR}}$ enables latches L3 and L4, latching the inverted data W1 through W16 into the high register. This data now appears at the inputs to line drivers LD9–LD16. In addition, the pulse $\overline{\mathrm{WHR}}$ loads (asychronous) preset data W17–W24 onto the outputs of counters C2 and C3. The data, W17–W24, contain the intended trigger delay in μs. The range of this number is 0 to 255 μs.

At the arrival of S2 during the second write, the condition, $\mathrm{N}\cdot\mathrm{F}(16)\cdot\mathrm{A1}\cdot\mathrm{S2}$ true, causes STROBE to go high. The transition of STROBE clocks latch PL1. The output of this latch (PL1), has been low since the last pulse latch reset, $\overline{\mathrm{PLRST}}$ low. This occurred during the last initialization (RST) or at the end of the last pulse (PC0). Because $\overline{\mathrm{PLRST}}$ is now high, STROBE clocks data (high) onto the output, PL1. PL1 being high causes PULSE to go high at the next uptick of the MC clock. One half–cycle later, an uptick of $\overline{\mathrm{MC}}$ causes ENPC to go high at the output of PL3 since the data there (PULSE) is now high. $\overline{\mathrm{ENPC}}$ low enables counter C1 to count the pulse width. With each clock tick, C1 counts down from the preset pulse width, PC0–PC4, to zero. When the counter reaches zero it enters an underflow condition causing PC0 to go high for one cycle of the clock. PC0 high generates PLRST. $\overline{\mathrm{PLRST}}$ low causes PL1 and PULSE to be reset to zero at latches PL1 and PL2 respectively. Since PULSE is now low, the next uptick of $\overline{\mathrm{MC}}$ (one half–cycle later) causes ENPC to go low disabling counter C1. While PULSE is high, any line drivers with data high at pins 1 and 2 or pins 10 and 11 of the SN75183's will strobe the differential outputs, Y and Z, with test pulses of the correct width.

The transition of STROBE also clocks data (high) onto the output of TL1. TL1 high at the data input of TL2 causes ENTC to go high on the next uptick of MC. $\overline{\text{ENTC}}$ low enables the counters, C2 and C3, that will count out the trigger delay (0–255 μs). These counters also count down from their preset values, TD0–TD7, to zero. When both counters are about to reach zero, the ripple–clock output from C2 clocks C3. Since C3 is now in an underflow state, it sets TCO high for one clock cycle. TCO high generates XTRIG and TLRST. $\overline{\text{TLRST}}$ low resets both latches TL1 and TL2. XTRIG appears at the input to an SN75174 line driver causing XTRIGIN to be sent out on twisted pair to all digital readout modules in the crate. (If one is testing a single readout module, a special cable is used to bus XTRIG, TRIG, and ABORT to that readout module only.)

As an example, consider the test shown in the *Pulser Timing* diagram and assume the crate has been previously initialized. This test requires a 5 μs wide test pulse to strobe data onto the twisted pairs with a follow–up trigger 3 μs after the test pulses are placed on the outputs of the line drivers. The binary value of 5, 0101, is loaded onto the outputs of counter C1 during S1 of the first write. In an analogous way, the binary value of 3, 00000011, is loaded onto the outputs of counters C2 and C3 during S1 of the second write. The strobe at S2 of latch PL1 sets data high on latch PL2. The same strobe at latch TL1 sets data high at TL2. At the next uptick of MC, PULSE is generated and the trigger delay counters, C2 and C3, are enabled. One half–cycle later, an uptick of $\overline{\text{MC}}$ causes $\overline{\text{ENPC}}$ to go low enabling C1. All three counters count down from their preset values to zero. When counters C2 and C3 reach zero, the pulse TCO is generated which resets the trigger latches and generates a 1 μs wide trigger pulse, XTRIG. Counter C1 continues to count out the pulse width until it reaches the underflow condition and generates PC0. PC0 generates PLRST. $\overline{\text{PLRST}}$ low resets PL1 and PL2 and in one half–cycle, C1 is again disabled since $\overline{\text{ENPC}}$ goes high. The module is now reset and waiting for its next instruction.

The module generates a LAM on receipt of an XVETO signal during testing of a single digital readout module. The presence of a LAM tests the XVETO feature of the readout module. (XVETO is generated for an IN·OUT coincidence.)

The module responds to an N·F(10) instruction by clearing any LAM generated by the module. The condition N·F2·F8·S2 at the quad–input NAND gate generates $\overline{\text{CLAM}}$. $\overline{\text{CLAM}}$ is inverted and OR'ed with RST to generate LRST. $\overline{\text{LRST}}$ low causes a reset of the latch that generates L. L appears at the input of a triple–input NAND gate that generates $\overline{\text{LAM}}$ on the dataway. It also appears at a front panel LED. The module can be prevented from generating LAMs by using a side panel switch, SW0, to disable the XVETO line receiver.

Three other side panel switches, SW1–SW3, are used to respectively turn off (or on) the TRIGIN and ABORT signals at the digital readout module and an unused line driver. This is useful during testing of a single readout module.

CAMAC Functions

C or Z	Initialize Module and Clear LAM
N·F(10)	Clear LAM.
N·F(16)·A(0)	Write to low register on S1. Respond Q=0. W1–W16 contain the bit pattern of test channels T0–T15 respectively. The test channel is strobed if the corresponding write line is set.

	W17–W20 contain the pulse in μs. W17 is LSB.
N·F(16)·A(1)	Write to high register on S1. STROBE on S2. Respond Q=1 W1–W16 contain the bit pattern of test channels T16–T31 respectively. The test channel is strobed if the corresponding write line is set. W17–W24 contain the trigger delay in μs. W17 is LSB.

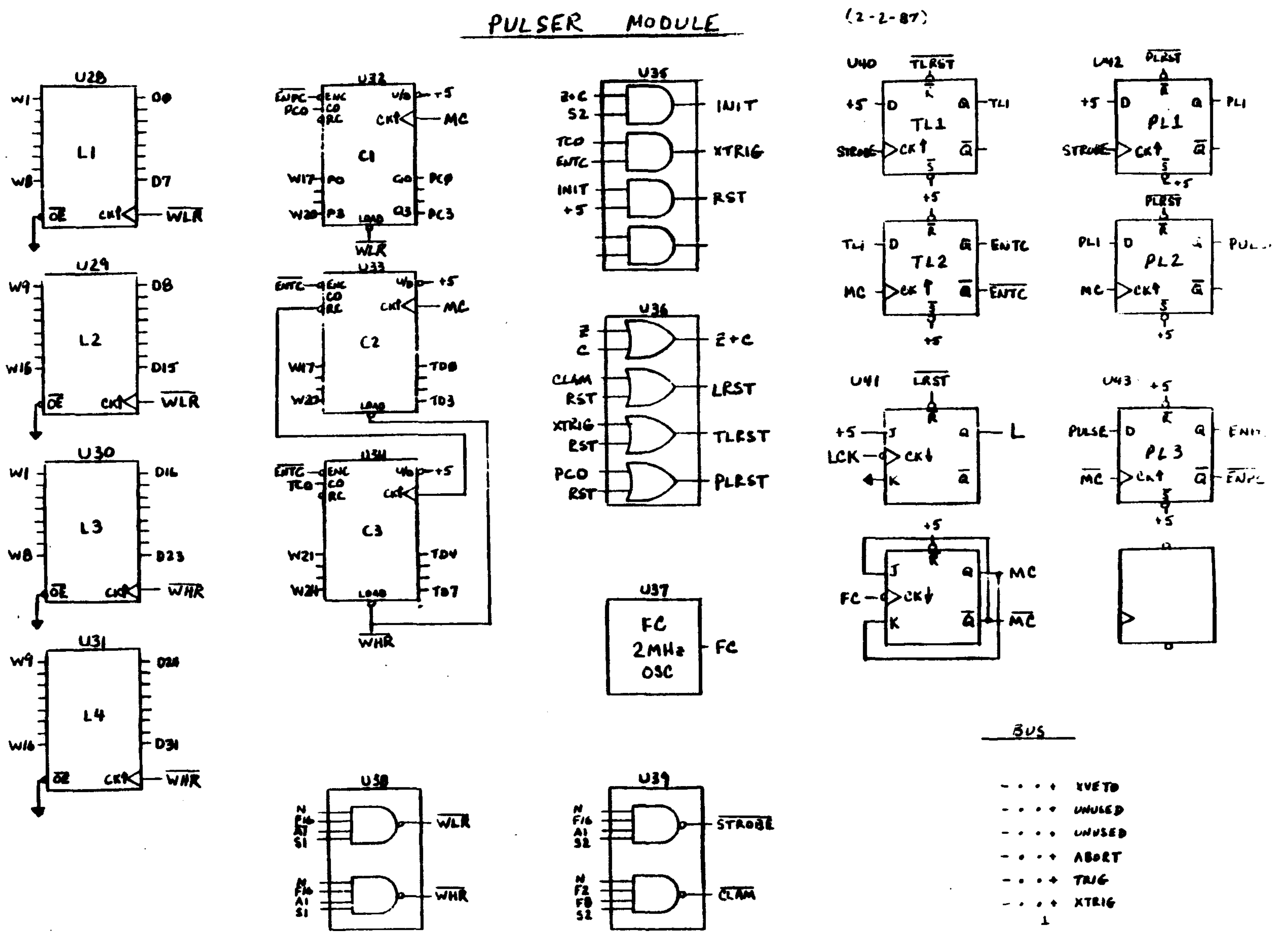

Fig. B-1 Pulser Schematic

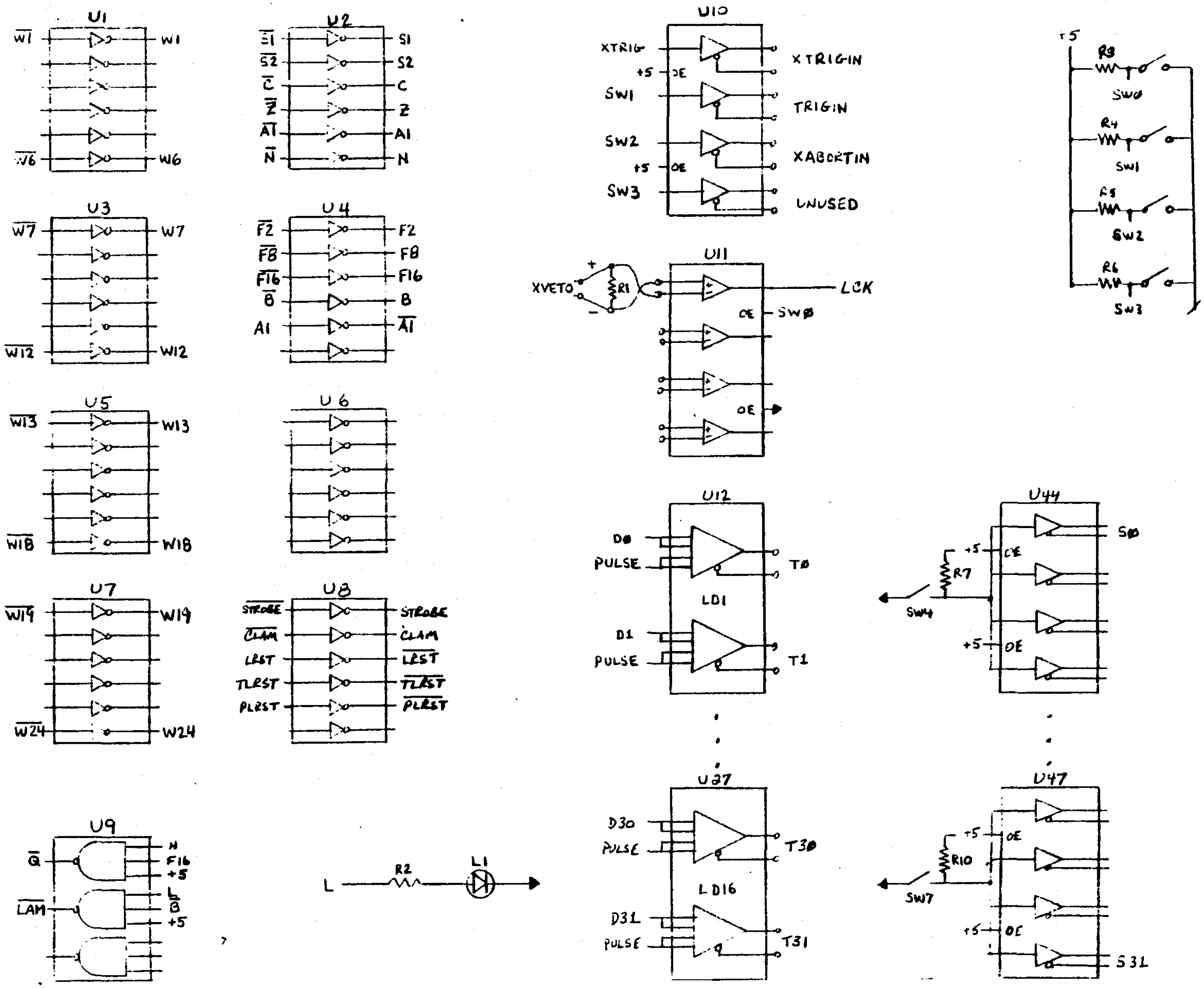

Fig. B-1 Pulser Schematic – continued

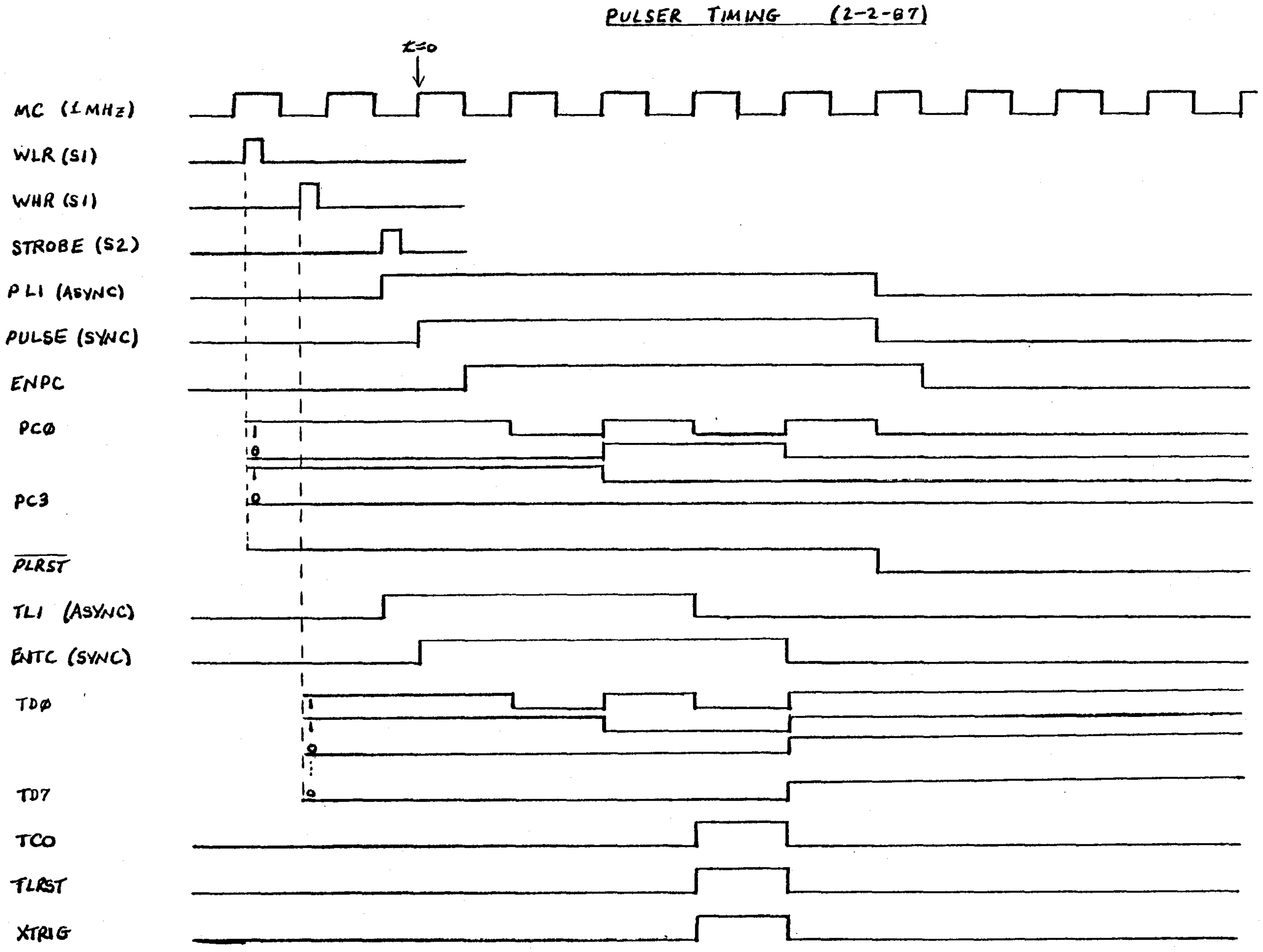

Fig. B-2 Pulser Timing

TRACKER CAMAC CRATE

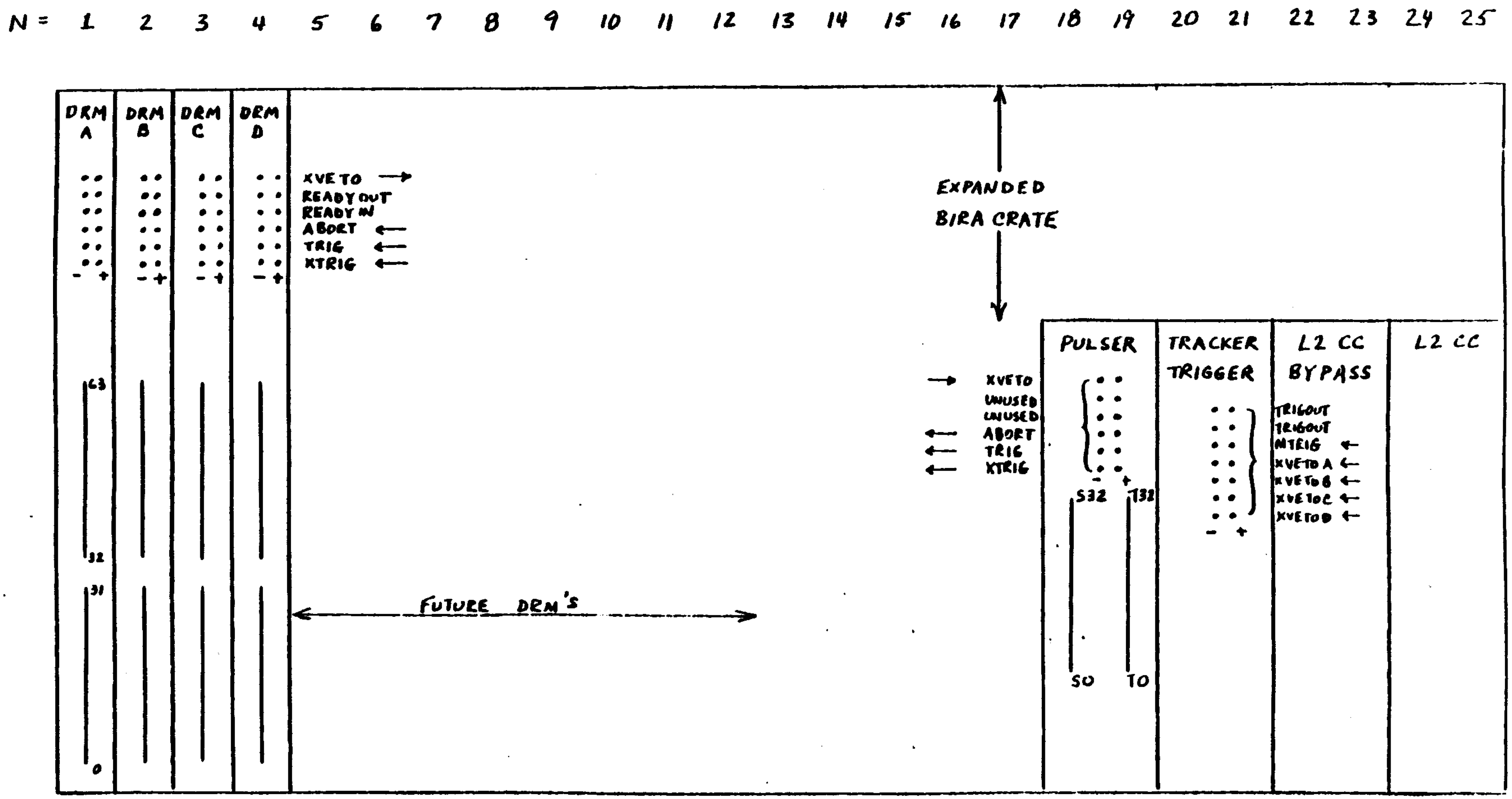

DRM = PROTOTYPE DIGITAL READOUT MODULE

Fig. B-3 CAMAC Crate

PDK–314

January 28, 1987

J. Kochocki

W. Oliver

Tracker Trigger

Introduction

The Tracker Trigger is a CAMAC module used to form a coincidence between any or all of the four layers of the veto shield tracker system. Each tracker layer consists of two sub–layers, IN and OUT. A single digital readout module (W. Oliver, PDK–289) is used to read out each tracker layer (64 channels). When a coincidence occurs between the IN and OUT sub–layers of a particular tracker layer, the corresponding readout module generates a 5 μs–wide XVETO signal. The Tracker Trigger allows one to form a coincidence of the XVETO signals from the four readout modules in the tracker system.

The Tracker Trigger can generate a trigger in response to a signal from the main experiment. Normally, a trigger from the main experiment would be carried directly to the veto shield readout modules in a crate. The Tracker Trigger allows one to logically OR the trigger generated by the tracker system and the trigger generated by main modules before carrying a trigger to the four readout modules in the tracker system.

In addition, the Tracker Trigger can provide a trigger signal to the main experiment's trigger processor. This trigger will be useful in determining main module efficiency since the tracker can provide an independent source of muon triggers.

General Description

The Tracker Trigger is a wire–wrapped, double–width CAMAC module using 20 chips.

The module has been built and tested, and it works as described. The XVETO signals from each of the four readout modules are carried over twisted pairs to a front panel connector where they are terminated in 100 Ω. Through software, one is allowed to choose which layers of the tracker will be required to form the coincidence signal. The coincidence signal is bussed to the TRIG inputs of the four readout modules. (XTRIG on all readout modules is reserved for the veto shield pulser module – J. Kochocki, PDK–315). Upon receipt of TRIG, the readout modules perform their data scan and set LAMs when ready for readout.

In normal operation it is anticipated that the Tracker Trigger module will be the only module in the crate allowed to generate demands on the serial highway. Once the trigger module generates a LAM, it is prevented from generating another until it receives a clear–LAM instruction. Furthermore, the readout modules in the crate can receive no further trigger pulses while they are waiting to be read out. Once the last module has been read out, a clear–LAM instruction must be generated allowing further triggers to generate demands on the serial highway. Note that although triggers are not allowed to generate demands once a LAM has been set, they may nevertheless occur. These triggers are transparent to the computer and cannot cause readout modules to enter the data–scan state. They may, however, be scaled.

The trigger signal, TRIGOUT, is available at two front panel bus connectors. One of these connectors is used to carry TRIGOUT to the readout modules as described above. The other connector is used to carry TRIGOUT over a twisted pair to the main experiment's trigger processor. (A third connector was later provided so that one could promptly latch the WWVB time using the same TRIGOUT signal.)

The Tracker Trigger also accepts triggers from the main experiment. A signal MTRIG, can be carried over twisted pair to a front panel connector on the module. This signal is logically OR'ed to the trigger generated by the tracker itself, CTRIG. A software bit allows one to enable/disable MTRIG.

The Tracker Trigger can be enabled and disabled by the computer. This enable/disable feature can be used to prevent unwanted tracker trigger pulses when the system is being tested with the veto shield pulser module.

An internal (8 bit) register on the module can be read out through CAMAC. This register contains the required coincidence level set in the software, the type of trigger(s) enabled/disabled (main module trigger and/or coincidence trigger), and the trigger type for the last trigger generated.

A front panel lemo connector is available to scale the trigger pulses.

Trigger Operation

Upon receiving a CAMAC C, Z or F(24) (disable), the module generates a pulse DSBL at S1 time. $\overline{\mathrm{DSBL}}$ low resets the LS279 enable latch, turns off ENTR and prevents any OTRIG pulses at the JK flip–flop.

Upon receiving an F(26) (enable), the module generates a pulse ENBL at S1 time. $\overline{\mathrm{ENBL}}$ low at the LS279 latch sets ENTR. ENTR high allows the formation of the signal OTRIG whenever TRIG comes TRUE. TRIG is the logical OR of MTRIG and CTRIG. TRIG is fanned out to a line driver and a front panel LED. The line driver is used to drive a lemo connector for scaling the trigger count.

An N–specific F(16) command is used to write 6 bits of information into the trigger module. The first four bits, $\overline{\mathrm{CL1}}$–$\overline{\mathrm{CL4}}$, appear on dataway lines $\overline{\mathrm{W1}}$–$\overline{\mathrm{W4}}$ and are used to specify which of the four tracker layers are required in the coincidence. (Layer n is required if $\overline{\mathrm{CLn}}$ is low.) The other two bits, $\overline{\mathrm{ENCT}}$ and $\overline{\mathrm{ENMT}}$, appear on dataway lines

$\overline{W5}$ and $\overline{W6}$ respectively. These signals individually enable/disable trigger formation by a coincidence trigger and/or a main module trigger. Data must be present on these six lines during S1 when they are latched onto the outputs of the LS374's D–type flip–flops by the signal, WCL.

Once latched, the first four bits appear at the inputs of one of the LS32 OR gates and at the inputs of the LS240 buffer. These bits must contain the complement of the intended coincidence level. (E.g. If one requires layers 3 and 4 only in the coincidence, then lines $\overline{CL1}$ and $\overline{CL2}$ must be high while lines $\overline{CL3}$ and $\overline{CL4}$ are low.) For a coincidence to form, XV1'–XV4' must all be TRUE. This condition generates the signal PCTRIG. CTRIG is the logical AND of PCTRIG and ENCT. ENCT is the complement of the fifth bit written into the module. Only when ENCT is on can CTRIG be formed. TRIG is the logical OR of MTRIG and CTRIG. When the module is enabled, ENTR is high and a signal, OTRIG, is formed at the LS73 JK flip–flop whenever TRIG comes TRUE. The signal, OTRIG, is fanned out to two line drivers and to an input of an LS12 triple–input NAND. The two drivers generate the signals, TRIGOUT, described above. The LS12 is used to generate LAM's on the dataway.

A signal, MTRIGIN, is expected to be formed by the main experiment and carried over twisted pair to the Tracker Trigger. MTRIGIN generates a signal, PMTRIG, at the 75175 line receiver. PMTRIG is AND'ed to ENMT, the complement of the sixth bit written into the module. MTRIG is generated only when both ENMT and PMTRIG are TRUE. This signal, like CTRIG, generates the signal TRIGOUT to be carried over twisted pair to readout modules and/or to the main experiment's trigger processor. The signal, MTRIGIN, should be 5 long.

An N–specific F(0) command is used to read the internal status register of the Tracker

Trigger. The 8 bits in this register will be available on the CAMAC read lines R1–R8 whenever N is on. The register contains the complement of the four bits used to specify the coincidence level (CL1–CL4), the two bits used to specify which trigger(s) is active (ENCT and ENMT), and two more bits to specify which trigger fired last (CTSTAT and MTSTAT).

When the module is enabled, the falling edge of a TRIG pulse clocks the data present, ENTR, at the J–input of the LS73. If a trigger has already occured, OTRIG will be high and there will be no change in the state of the output, Q1. If a trigger has not occured, OTRIG will be low from the last Z or clear LAM command. The falling edge of TRIG will clock ENTR onto the output of the flip–flop. The signal, OTRIG, generates a LAM at the LS12 NAND. OTRIG also generates the response, Q=1, whenever a test LAM command occurs.

An N–specific F(8) command is used to test the status of the LAM line. The module generates a response, Q=1, for the duration of the command if a LAM is present. If a LAM is not present, the response is Q=0.

An N–specific F(10) command or a crate–wide Z can be used to clear LAMs generated by the module. The condition $\overline{\text{CLAM}}$ low or Z low will cause the signal $\overline{\text{LRST}}$ to go low. $\overline{\text{LRST}}$ low resets the LS73 flip–flop causing OTRIG to go low.

CAMAC Functions

C or Z	Initialize module – disable trigger pulses.
N·F(0)	Read Tracker Trigger Status Register. (MTSTAT, CTSTAT, ENMT, ENCT, $\overline{\text{CL4}}$, $\overline{\text{CL3}}$, *ovl*CL2, $\overline{\text{CL1}}$) These bits appear on R1–R8 during N of this command. $\overline{\text{CL1}}$ corresponds to R1.

N·F(8)	Test LAM. Respond Q=1 if LAM present.
N·F(10)	Clear LAM.
N·F(16)	Write Tracker Trigger Coincidence Level and Enable/Disable bits (ENMT, ENCT, CL4, CL3, CL2, CL1) These bits must appear on dataway lines W1–W6 during S1 of this command. CL1 corresponds to W1.
N·F(24)	Disable module.
N·F(26)	Enable module.

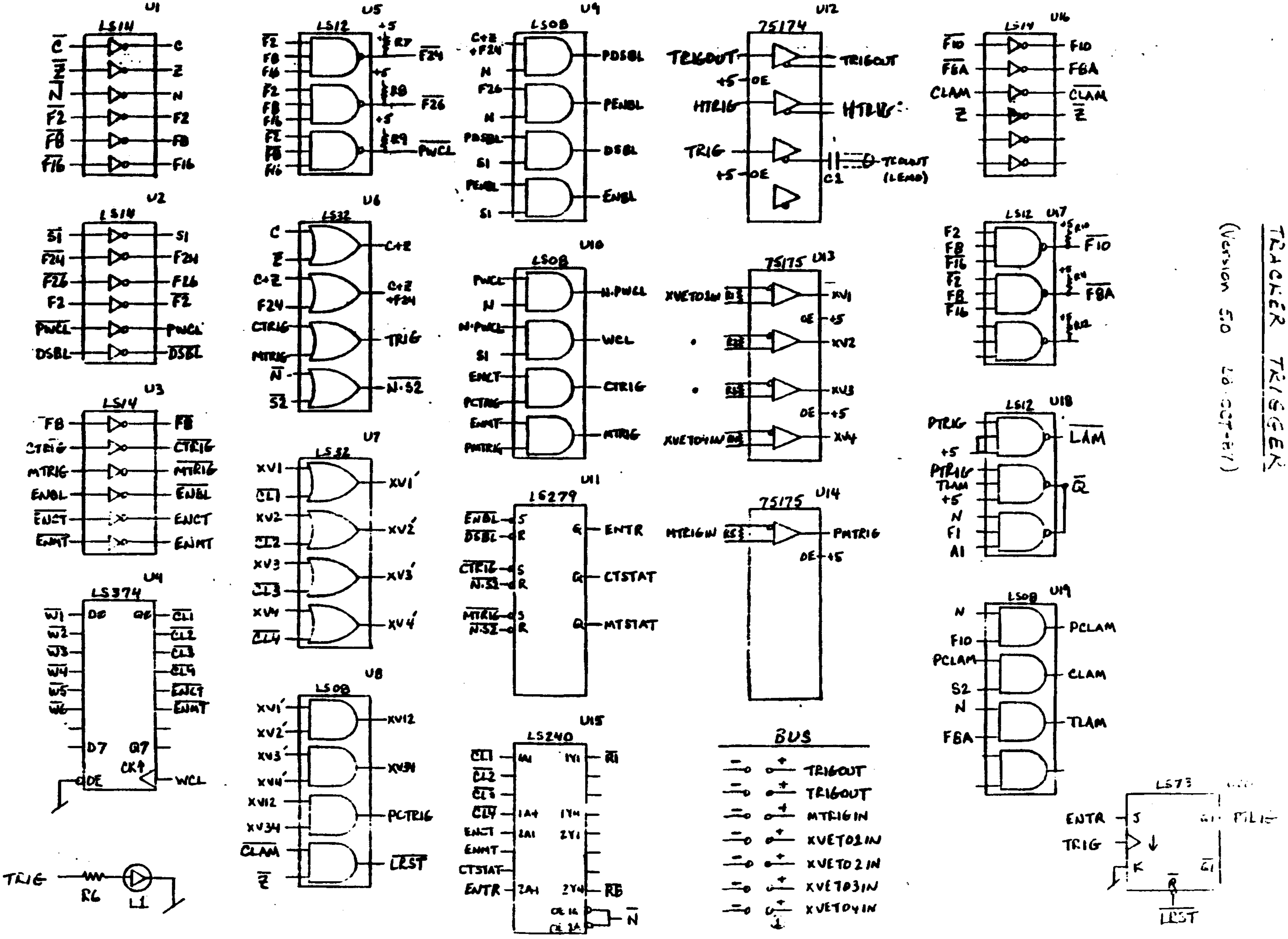

Fig. B-4 Trigger Schematic

APPENDIX C

A Review of Relevant Astronomy

Coordinate Systems

There are four celestial coordinate systems in common use by astronomers and astrophysicists. These are the horizon, equatorial, ecliptic, and galactic coordinate systems. Spherical coordinate systems such as these are defined in terms of a fundamental or reference (great) circle, a particular point on this circle (origin of longitudinal or azimuthal coordinate), one of the poles of this circle (origin of colatitude), and a sense of helicity. Both righthanded and lefthanded systems are used. Furthermore, coordinate systems are labeled as topocentric, geocentric, or heliocentric depending on whether the coordinate system is centered on the observer, the Earth, or the Sun, respectively.

The celestial sphere is the imaginary surface on which we wish to map the entire visible universe. The radius of this sphere is hence arbitrary. This sphere will now be defined (see Fig. C-1). The Earth rotates on its axis in the center of the celestial sphere. The extension of the Earth's equator into space defines the celestial equator (CE). One of the normals to the plane so formed is in the direction of the north celestial pole (NCP); again, this is an extension into space of the Earth's north pole (not the magnetic one). Having defined a plane and a normal to that plane, one more direction will allow us to define a coordinate system. Consider the *apparent* path of the Sun about the Earth as projected on the celestial sphere. This path is known as the ecliptic. The path forms a plane that is inclined with the celestial equator by an angle of $\sim 23.5°$ as shown in Fig. C-1. (Since the Sun rises in the east and sets in the west, the Earth must rotate in a counterclockwise fashion when viewed by an observer looking *down* the NCP.) There are two points at which the ecliptic and celestial equators intersect, and these are known as the equinoxes.

In the northern hemisphere, the autumnal equinox marks the beginning of fall and the vernal equinox marks the beginning of spring. At the vernal equinox, the Sun passes through the celestial equator in the direction of the north pole. That direction, as the Sun crosses the celestial equator during the vernal equinox, when projected onto the celestial sphere, gives us the third direction, Υ. Historically, this direction is known as the Rising of Aries because when first observed, the direction was in the constellation of Aries. It is no longer in that direction due to the precession of the Earth (see below). Note that the vernal equinox moves on a fixed ecliptic as shown by the arrows in the figure. Υ marks the direction of the vernal equinox today. In about 13,000 years, Υ will have rotated by π radians and will be pointing in the direction of the present autumnal equinox.

This gives us a general description of celestial coordinate systems. Next, precise ways of mapping the location of objects on the celestial sphere are presented for four different systems.

The first system is topocentric and the fundamental circle is the observer's horizon (H). The formal definition of the horizon is the plane normal to the direction of the local gravitational field. The horizon is seldom planar however, and is best approximated by an observer on a ship in a calm sea. A point, P, on the celestial sphere is defined by two angles, the altitude, a, and the azimuth, A (see Fig. C-2). The origin of azimuthal measurement is the observer's celestial meridian, CM, a great circle which passes through the observer's zenith and the north direction.[1] Note that the helicity in this system is left; A is measured positive eastward. The altitude is the angular distance above the horizon

---

[1] In some books, the origin of azimuthal measure is defined as the intersection of the horizon with the great circle which passes through the observer's zenith and south directions.

at which the point, P, lies. ($0 \leq a \leq 90°, 0 \leq A < 360°$) There is a fundamental limitation to this coordinate system. Since the Earth rotates on its axis, a point on the celestial sphere specified by (a,A) moves with time so that (a,A) is correct only for an instant. (By knowing the time of observation and the transformation to a fixed system, this problem can be solved.)

The fundamental circle in the equatorial system is the celestial equator, CE. A point, P, on the celestial sphere is defined by two angles, the declination, δ, and the right ascension, α (see Fig. C-3). (In the figure, ϵ is known as the *obliquity* of the ecliptic ($\epsilon \sim 23.5°$).) The origin of azimuthal measure is given by the Rising of Aries, Υ. α is measured positive eastward from this direction making this a righthanded coordinate system. δ is the angular measure above (+) or below (−) the celestial equator. ($0 \leq \delta \leq \pm 90°, 0 \leq \alpha < 360°$) In astronomical terms, α and δ are measured in sexagesimal hours and degrees, respectively ($24^h = 360°$). For example, the coordinates of the Sun at noon time (12^h UT) in Greenwich, England on June 21, 1988 are $\alpha = 6^h 01^m 23^s.63, \delta = 23°26'30''.48$.

The ecliptic system is a heliocentric system and the fundamental circle is the ecliptic (see Fig. C-4). A point, P, on the celestial sphere is located by its angular distance above the ecliptic, β, and its angular distance, λ, measured from the direction Υ. The north ecliptic pole makes an angle of $\sim 23.5°$ with the NCP. Note that λ is measured positive eastward so that this system, too, is righthanded. It is easy to locate objects in our solar system like the planets since they move in a plane close to the ecliptic.[2]

In the galactic system (see Fig. C-5), the fundamental circle is defined by the plane of our galaxy. The circle formed by the projection of the edge of this plane on the celestial sphere forms the galactic equator, GE. The galactic plane is inclined w.r.t the celestial equator by an angle of $\sim 63°$. In equatorial coordinates, the north galactic pole is located

---

[2] Our Moon (in its orbit about the Earth) also travels in the plane of the ecliptic to within $\sim 5°$.

at $\alpha = 12^h 49^m, \delta = +27°24'$ (as of 1950). The Sun and the center of our galaxy lie in the galactic plane. The location of a point, P, in this system is given by two angles, B and L. B, the galactic latitude, is the angular height (+) above or (−) below the galactic equator. The galactic longitude is the angle, L, measured eastward about the line joining our Sun to the galactic center as shown in the figure.

A comparison of these celestial coordinate systems is shown in Fig. C-6.

Time Systems

One of the earliest time pieces used was the sundial. The sundial marks the transit of the Sun from day to day; *i.e.* the instant at which the Sun crosses an observer's celestial meridian. To this day, we keep local time on Earth with respect to the Sun. We require that the Sun is overhead at noontime – every day. (One can imagine the difficulties in scheduling were this not true.) The difference between time measured with respect to the Sun, (*solar time*), and time measured with respect to the distant stars, (*sidereal time*), arises from the fact that the Earth is revolving about the Sun[3] in its orbit as it rotates about its axis. There are 24 solar hours in a solar day. If an observer detects the transit of the Sun at some arbitrary time and waits 24 solar hours, the Sun will once again be in transit. Suppose now that 12 hours after this second observation one sees a distant star in transit in the night sky. Will that same star be observed to transit exactly 24^h later? No. Solar time is useful for keeping track of the location of the Sun but not so useful for keeping track of most other celestial objects. Each day of the year, as the Earth revolves about Sun it moves $\sim 1°$ or 4 solar minutes of arc with respect to the fixed stars. Had the observer noted the second transit of the nighttime star in solar hours he would have seen that slightly less than 24^h had elapsed. The situation is depicted in Fig. C-7. (The

---

[3] **Actually, the Earth and the Sun as well as the rest of the planets and other debris in our solar system are in orbit about the center of mass (barycenter) of our solar system, located about 5 lightseconds outside of the Sun.**

Earth is moving down in the figure. A solar day is shown as B; a sidereal day is shown as A.) A sidereal day is simply the time between two successive transits of a distant, fixed star (measured in whatever units are most useful). A solar day is the time between two successive transits of the Sun. One sidereal day is equal to $23^h 56^m 4^s.09$ of mean solar time. Why *mean* solar time? The Earth travels in an elliptical orbit about the Sun. During perihelion, when the Earth is closest to the Sun, it is travelling faster in its orbit than at aphelion, when it is furthest from the Sun. Assuming a constant rate of rotation of the Earth, a solar day measured at aphelion will differ from one measured at perihelion due to the change in the relative location of the Sun with respect to the Earth. By averaging the solar day over the course of a year (or longer) we arrive at the meaning of a *mean solar day.*[4]

If we wish to measure time with a clock, we need to know two things: how long is each 'tick' of the clock (its scale) and when did the clock start (its zero reading or *epoch*). The most precisely determined time scale on Earth is the international atomic time scale (TAI). It is based on analyses of worldwide atomic measurements performed in Paris at the Bureau International des Poids et Mesures. The fundamental unit of TAI is the SI second defined as the duration of 9192631770 periods of the radiation corresponding to the transition between two hyperfine levels of the ground state of the cesium 133 atom. In terms of TAI, atomic time started at the instant when $TAI = 0$. It is necessary to know what solar time and sidereal time are at $TAI = 0$ in order to relate these measurements of time.

As explained above, sidereal time is based on measurements of the fixed stars. More formally, a mean sidereal day is the time between successive upper transits of the mean equinox of date relative to a fixed meridian on Earth. The instant of transit is called

---

[4] The difference between apparent and mean solar time is known as the equation of time.

sidereal noon. Sidereal time on the Greenwich Meridian (where *longitude* $= \lambda = 0$) is known as Greenwich Sidereal Time (apparent (GAST) or mean (GMST) depending on whether the true or mean position of the equinox of date is used).[5] Finding the local sidereal time (LST) at longitude λ is then simple; just subtract the longitude from the Greenwich time: $LST = GST - \lambda$ (λ is measured positive westward.) LST is also known as the *Hour Angle of the Vernal Equinox.* This is shown in Fig. C-8. An observer in the lab at L observes a star at P that some time earlier (τ) crossed his meridian. The hour angle of the star is simply equal to this time ($h = \tau$ measured in degrees or hours of arc). When the star was on the observer's meridian, its hour angle was 0^h and

$$LST = GST - \lambda. \tag{C.1}$$

The hour angle is measured positive westward (0^h *to* $+12^h$) and negative eastward (0^h *to* -12^h) about the equator, and describes how long ago an object was in transit (+) or how soon before the object will be in transit (−).

Universal time (UT) is the time scale on which all civil timekeeping is based. The unit of time in the UT scale is the SI second. UT and sidereal time are determined from observations of the diurnal motion of stars. UT is defined formally by a mathematical formula that relates UT to GMST as follows:

$$GMST\ of\ 0^hUT = 6^h41^m50^s.54841 + 8640184^s.812866T + 0^s.093104T^2 - 6^s.2 \times 10^{-6}T^3 \tag{C.2}$$

where T is measured in Julian centuries of 36525 days of UT1 (see below) from 2000 January 1, 12^h UT1 (JD 2451545.0 UT1).[6] "The measure of sidereal (hence Universal)

---

[5] The difference between the apparent and mean sidereal times, GAST–GMST, is known as the equation of the equinoxes.

[6] The Julian Calendar: The fundamental epoch in the Julian Calendar is noontime (12^h UT), January 1, 4713 B.C. where the hours are measured in mean solar time measure. At that instant, JD=0. Note that the Julian Calendar does not specify a scale. In the Julian Calendar there must be 36525 days in a century but the length of the day is not specified (therefore the scale UT1 was chosen). This epoch was chosen to be so far in the past that negative Julian Days could not occur when reducing astronomical observations.

time at any particular location on the Earth is represented by the sum of (1) the measure at some epoch, (2) the integral of the true angular speed of rotation of the Earth with respect to a uniform time scale from the initial epoch to the current instant, (3) the general precession in right ascension, (4) the equation of the equinoxes, (5) the motion of the pole (maximum $\sim 0^s.035$), and (6) the variations in the astronomical vertical."[7] Sidereal time is determined by star transits and depends on the place of observation. Universal time derived from this time (by the above formula) is called UT0. When UT0 is corrected for polar motion, it is called UT1.[8] Unless otherwise specified, $UT = UT1$. UT tabulations in the *Astronomical Almanac*, for example, are of the time UT1. Since January 1, 1972, national time services have transmitted what is known as coordinated universal time or UTC. The difference, $DUT1 = UT1 - UTC$, is always maintained to within $0^s.90$ by the addition of integral, leap seconds. Normally, these leap seconds are inserted at the end of June or December. The difference between UTC and UT1 is usually an integral number of tenths of seconds that is available (after the fact) on broadcast signals.[9]

Finally, two other time scales need mentioning. These are the terrestrial dynamical time scale (TDT) and the barycentric dynamical time scale (TDB). Irregularities in the Earth's rate of rotation cause the sidereal and universal time scales to be nonuniform. Ephemeris time scales are independent of the Earth's rate of rotation and become the independent argument of ephemerides and equations of motion. TDT is the time scale that fulfills this need. TDT was introduced in 1984 by the International Astronomical Union (IAU) and it replaces ephemeris time (ET) (see the *Supplement to the Astronomical*

---

[7] see Celestial Mechanics by Laurence G. Taff, p. 99

[8] A small periodic wobbling of the Earth's axis of rotation (mostly due to the gravitational attraction by the Moon) is known as nutation.

[9] The signal detected by a WWVB receiver is UTC. The format for reading this time can be adjusted to reflect the local time at the place of observation. Therefore, one must be careful to subtract the zone correction in order to derive UT from the broadcast signal. For example, 6^h UTC in central standard time is actually 6^h-(-6^h)=12^h UTC.

Almanac 1984). "At the instant 1977 January $01^d00^h00^d00^s$ TAI, the value of the new time scale for apparent geocentric ephemerides is 1977 January $1^d.0003725$ exactly." Also, "the unit of this time scale is a day of 86400 SI seconds at mean sea level." (Further details of the Improved IAU System are discussed in the above reference.) So, the relation between atomic time and TDT is

$$TDT = TAI + 32^s.184. \qquad (C.3)$$

To remove variations in gravitational potential around the Earth's orbit, TDB was introduced as the independent argument of ephemerides and equations of motion that are referred to the barycenter of the solar system. The variations between TDT and TDB are periodic only (by definition of TDB) and the magnitude of the difference is less than $0^s.002$. The difference between the time scales is given as follows:

$$TDB \;=\; TDT \;+\; 0^s.001658 \sin g + 0^s.000014 \sin 2g \qquad (C.4)$$

where

$$g \;=\; 357^\circ.53 + 0^\circ.98560028(JD - 2451545.0) \qquad (C.5)$$

and JD is the Julian Day (see p. B5 of the *Astronomical Almanac*).

Unfortunately, none of the above coordinate systems used by astronomers are inertial ones. The best nearby approximation to an inertial system is one defined with the barycenter of our solar system as the origin. The problem with any Earth based celestial coordinate system is that the Earth is moving with time. Although the equatorial system may seem to be inertial, it is defined using the Earth's pole and equator and the direction of the equinox and these, too, move with time. The reason is simple and is shown in Fig. C-9. The Earth precesses on its axis just like a top due to its oblate shape (see Fig. C-1 also). The only way to define an inertial equatorial system then is to define it at some instant. This is what has been done. The fundamental epoch of astronomical observation (designated J2000.0) is 2000 January 1.5 TDB which is JD 2451545.0 and the new standard equinox corresponds to this instant. In the past, there have been other standard epochs (J1900.0 and J1950.0 for instance) and these are now replaced by J2000.0. By doing this, we fix the direction of the NCP and Υ in space at some instant of time and refer all measurements to this coordinate system. Formulas for the reduction of precession are given in the *Astronomical Almanac* on p. B18. (Nutation was mentioned briefly above and is rigorously treated in many texts on celestial mechanics as well as in the *Astronomical Almanac.*)

A Worked Example of Celestial Tracking

Suppose you are faced with the following problem: You are quietly sitting in your lab in northern Minnesota watching muons go by. At the instant July 26, 11:00 am (UTC) central standard time, a muon goes by and makes an angle with the zenith direction defined as follows: the zenith angle between the up ($\hat{y}$) and West ($\hat{x}$) directions is 10°, and the zenith angle between the up and North ($\hat{z}$) directions is 5°. Someone (your advisor no doubt) asks, "where *did* that particle come from?" What are the equatorial coordinates of the point in the sky from which the muon came (α, δ)? (The lab is located at latitude $\phi = 47°47' \ N$ and longitude $\lambda = 92°.2 \ W$.)

The general picture is shown in Fig. C-10. (C is the unprimed lab system (x,y,z) and C' is a primed system (x', y', z') which will be described shortly.) P represents the point on the celestial sphere from which the particle came. Let θ_x and θ_z represent the angles described in the above problem. To solve this problem, we will first transform θ_x and θ_z into horizon coordinates (a, A). Next, by representing the point, P, in both the primed and unprimed systems, a transformation will be derived which will allow us to represent P in celestial equatorial coordinates (δ, h). Then, given the local time (UTC), we will calculate the local sidereal time (LST) for the event. Since LST is the hour angle of the vernal equinox, it follows that $\alpha = LST - h$.

Let θ represent the zenith angle. Then, the altitude is $a = \frac{\pi}{2} - \theta$. From the figure, it is easy to see that

$$\tan\theta_x = \frac{-x}{y} \quad ; \quad \tan\theta_z = \frac{z}{y} \tag{C.6}$$

so that

$$\tan^2\theta = \tan^2\theta_x + \tan^2\theta_z \tag{C.7}$$

and

$$\tan A = \frac{\tan\theta_x}{\tan\theta_z}. \tag{C.8}$$

Next, perform a counterclockwise rotation about the x-axis by the angle $\frac{\pi}{2} - \phi$ to arrive at the primed system C'. In the primed system, $\hat{y}$ is in the direction of the NCP and $\hat{z}$ is in the direction of the Earth's axis of rotation; $\hat{x}$ and $\hat{x}'$ are unchanged. The declination, δ, in the system C', is simply related to the height above the xz plane by $\sin\delta = y'$. The hour angle, h, is just the angular distance from the lab's celestial meridian to the meridian that includes the object. Now, the point, P, can be represented in system C or C' as follows:

$$\hat{P} = \begin{pmatrix} x \\ y \\ z \end{pmatrix} = \begin{pmatrix} -\cos a \sin A \\ \sin a \\ \cos a \cos A \end{pmatrix} \tag{C.9}$$

and

$$\hat{P}' = \begin{pmatrix} x' \\ y' \\ z' \end{pmatrix} = \begin{pmatrix} \cos\delta \sin h \\ \sin\delta \\ -\cos\delta \cos h \end{pmatrix} \tag{C.10}$$

The transformation matrix is $R_x(\psi)$ for a rotation about the x-axis by $\psi = \frac{\pi}{2} - \phi$. The entire transformation is then

$$\hat{P}' = \begin{pmatrix} 1 & 0 & 0 \\ 0 & \cos\psi & \sin\psi \\ 0 & -\sin\psi & \cos\psi \end{pmatrix} \cdot \hat{P}. \tag{C.11}$$

The transformation equations are symmetric under $(a, A) \rightleftharpoons (\delta, h)$:

$$\cos\delta \sin h = -\cos a \sin A \tag{C.12}$$

$$\sin\delta = \sin a \sin\phi + \cos a \cos A \cos\phi \tag{C.13}$$

$$\cos\delta \cos h = \sin a \cos\phi - \cos a \cos A \sin\phi \tag{C.14}$$

It is then straightforward to calculate the declination and hour angle given the local description of the coordinates of a celestial object ($\delta = +51^\circ.66, h = +16^\circ.14$).

Next, it is necessary to calculate the time of the observation. To begin, we note that the measured time is central standard time. Correct this by subtracting the zone correction, -6^h. The UTC time since 0^h is $39600^s.0 - (-21600^s.0) = 61200^s.0$. Next, add the appropriate number of leap seconds to bring UTC to TAI (see p. K9 of the 1988 *Astronomical Almanac* and note that an additional leap second has been added since 1985, July 1.) $\Delta AT = TAI - UTC = 24^s.00$ so

$$TAI = UTC + 24^s.00 = 61224^s.00$$

Now, knowing the zero reading for TDT given above, we can calculate the terrestrial dynamical time:

$$TDT = TAI + 32^s.184 = 61256^s.184.$$

ΔT, the difference between TDT and UT is tabulated on the same page in the *Astronomical Almanac* for each year since 1820. This reduces the TDT scale to UT:

$$UT = TDT - \Delta T = 61256^s.184 - 56^s.0 = 61200^s.184$$

So, we see that $\Delta UT = UT - UTC = 0^s.184$. Next, the relation between GMST and UT is used to calculate GMST for day 208 of year 1988 (a shortcut is given on page B6 in the *Astronomical Almanac* for this year):

$$GMST = 6^h.5926498 + 0^h.0657098242d + 1^h.00273791t \tag{C.15}$$

where

$$d = 208 \quad and \quad t = 17^h.00005112$$

giving

$$GMST = 13^h.306889.$$

Since $LST = GMST - \lambda$ with $\lambda = 92^\circ.2W = 6^h.146666$, $LST = 7^h.16022$ and $\alpha = LST - h = 6^h.0840$. Finally, we've arrived at the (less significant than implied) answer:

$$\alpha = 6^h05^m2^s.4 \quad , \quad \delta = 51^\circ39'36''.0$$

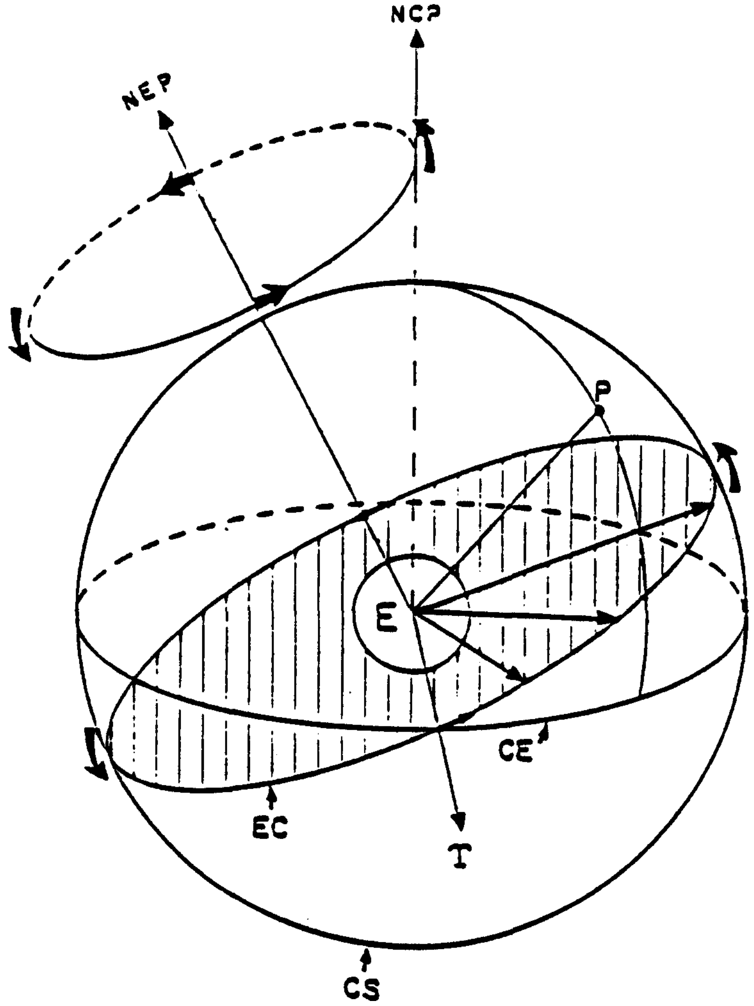

Fig. C-1. Celestial Coordinate Systems. The celestial sphere, CS, is shown with the fundamental circles, CE, the celestial equator and EC, the ecliptic. A point, P, on the celestial sphere lies on a meridian formed by the great circle which passes through P, the north celestial pole, NCP, and the south celestial pole (not shown).

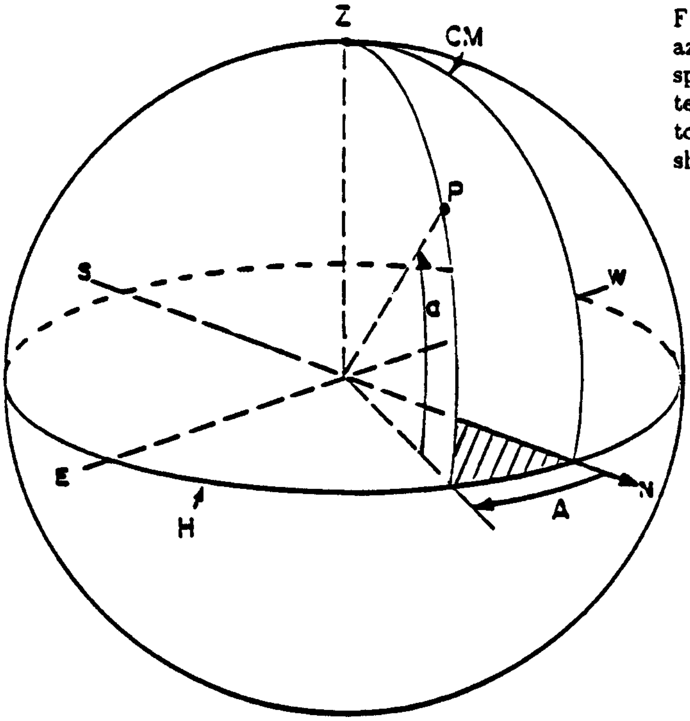

Fig. C-2. The Horizon System. The altitude. a. and the azimuth, A, define the location of a point, P, with respect to the observer's celestial meridian, CM. In some texts, A is defined from south to west. The zenith, Z, to the observer is directly overhead and his nadir (not shown) is directly below.

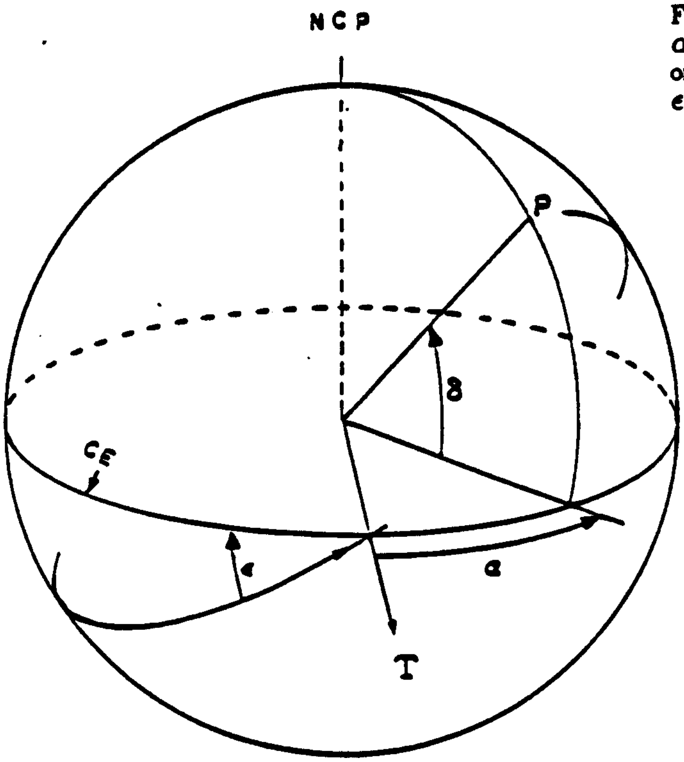

Fig. C-3. The Equatorial System. The right ascension, α, and declination, δ, define the location of a point, P, on the celestial sphere. The obliquity of the ecliptic is $\epsilon \sim 23.5°$.

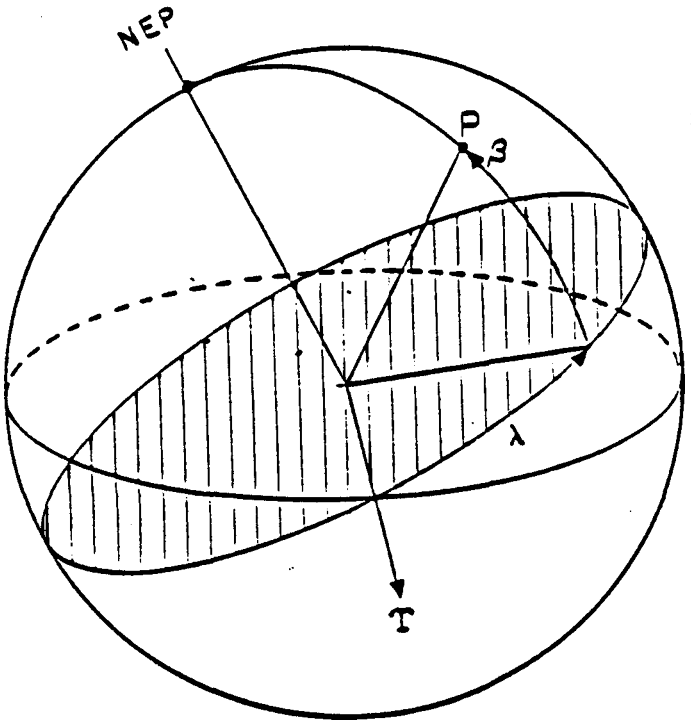

Fig. C-4. The Ecliptic System. The ecliptic latitude, β, and longitude, λ, define the location of a point, P, in this system.

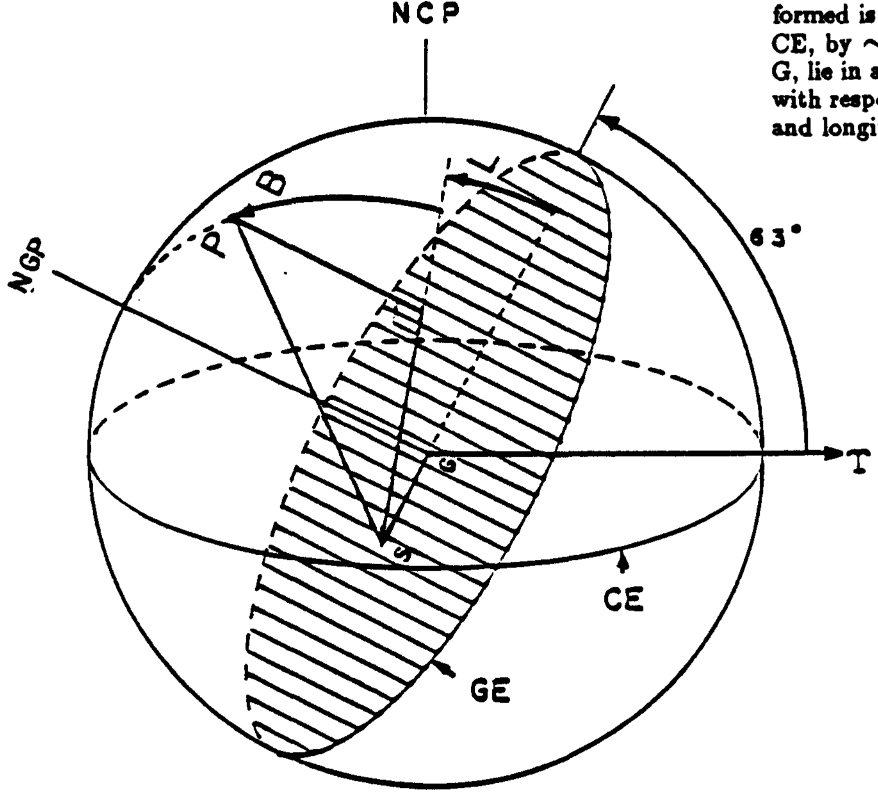

Fig. C-5. The Galactic System. The fundamental circle is the galactic equator, GE. The plane (highlighted) so formed is inclined with respect to the celestial equator, CE, by ~63°. The Sun and the center of our galaxy, G, lie in a plane and the location of a point, P, is given with respect to these. B and L are the galactic latitude and longitude respectively.

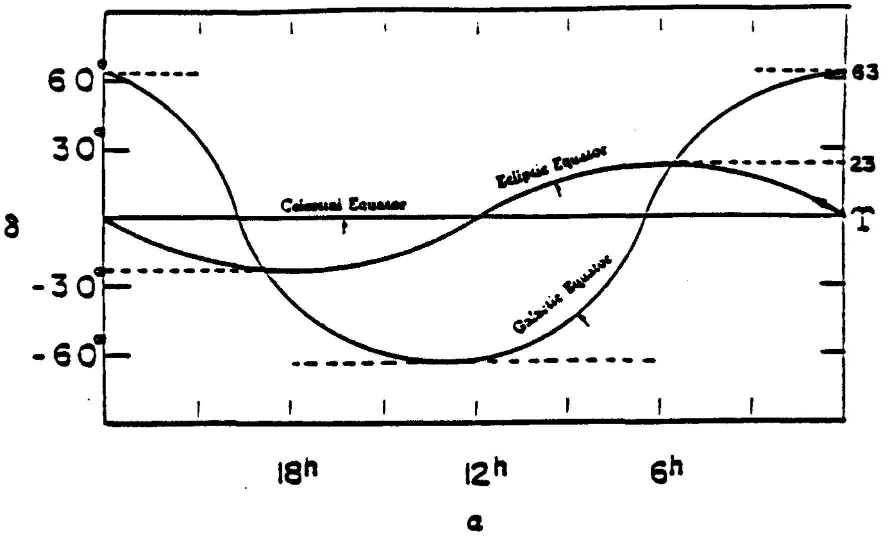

Fig. C-6. A Comparison of Systems. A plot of the declination, δ, vs. right ascension, α, is shown for the ecliptic and galactic equators. The celestial equator of course has $\delta = 0$.

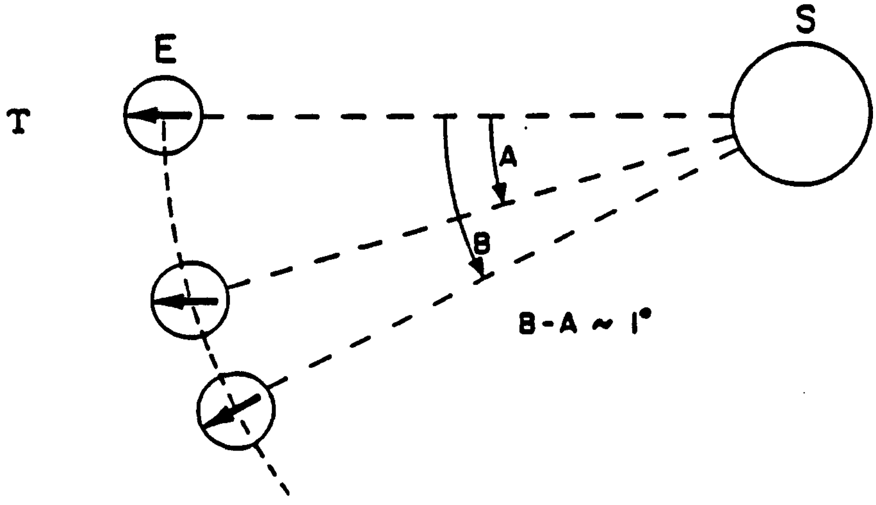

Fig. C-7. Sidereal Time vs. Solar Time. The Earth, E, is depicted in its orbit about the Sun, S. The difference between a sidereal day, A, and a solar day, B, is about 1° of arc or 4 solar minutes.

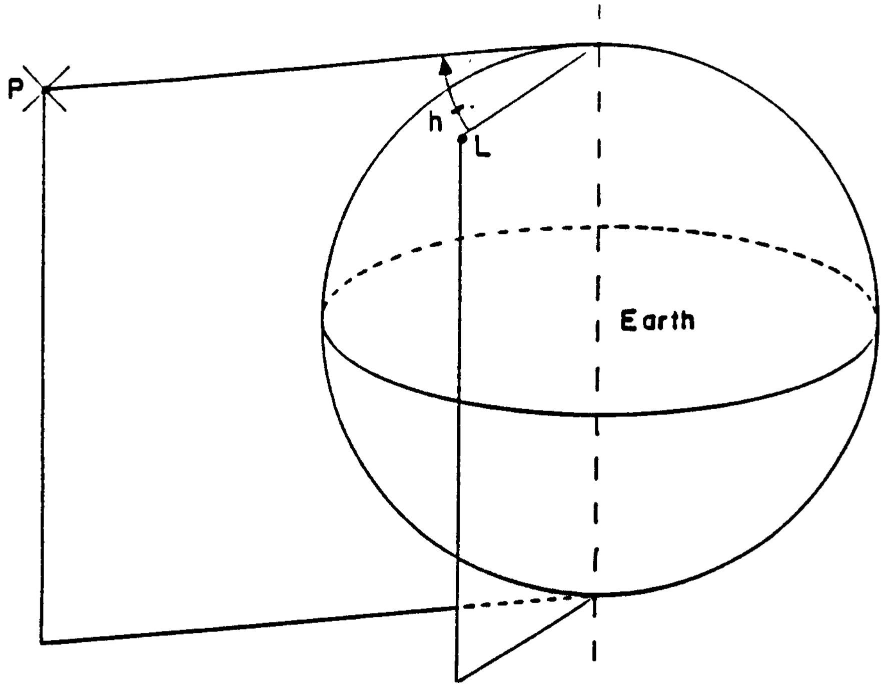

Fig. C-8. The Hour Angle. The angular distance between the planes formed by the intersection of a celestial object, P, and the axis of the Earth and an observer's coordinates, L, and the same axis forms the hour angle h, measured positive westward.

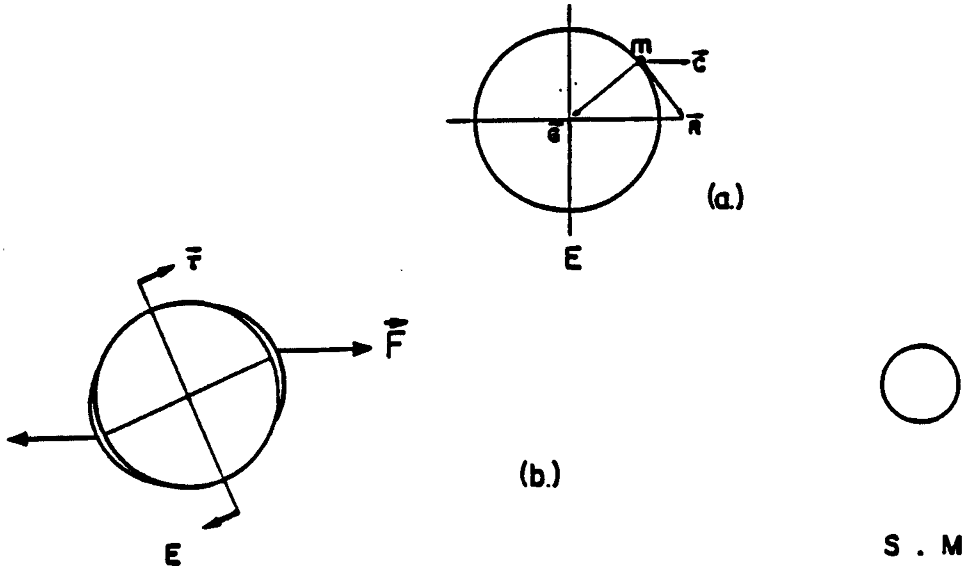

Fig. C-9. The Origin of Precession. (a.) Mass m is pulled toward the equator due to the resultant force $\vec{R}$ created by a centripetal acceleration $\vec{C}$ and a gravitational attraction $\vec{G}$. (b.) The accumulation of masses around the equator gives the Earth an oblate shape on which the Sun, S, and Moon, M, exert a gravitational force $\vec{F}$ giving rise to a torque $\vec{\tau}$.

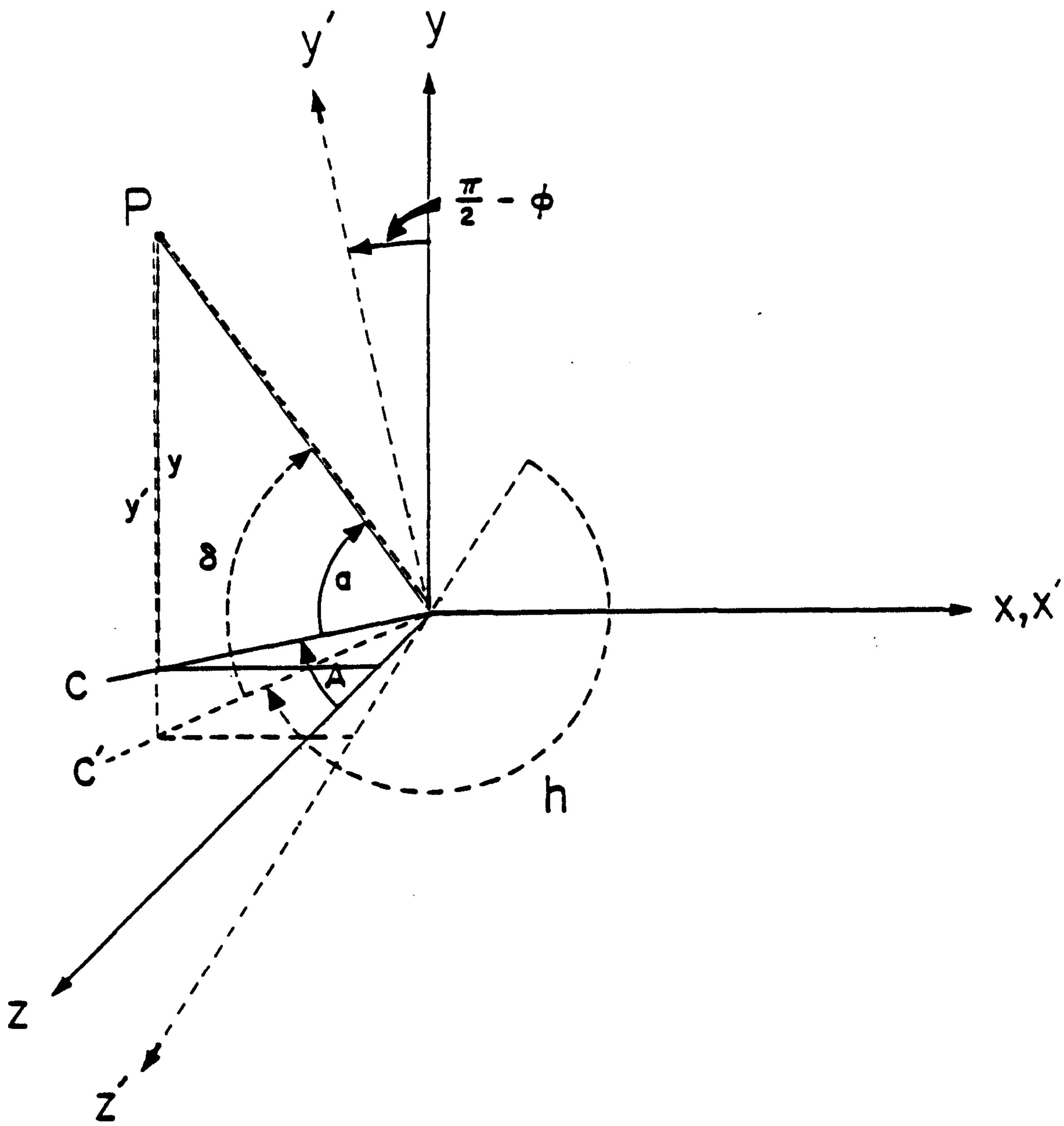

Fig. C-10. The Transformation from Lab to Celestial Coordinates. The coordinate system, C, is the lab system located at latitude ϕ. $\hat{Y}$ is in the direction of the observer's zenith while $\hat{Z}$ points north. A transformation about the X axis by $\pi/2 - \phi$ brings one to the primed system, C'. Now, Y' points to the north celestial pole and Z' points toward the axis of the Earth. The point, P, can now be expressed in horizon coordinates (a,A) or in equatorial coordinates (δ,h).